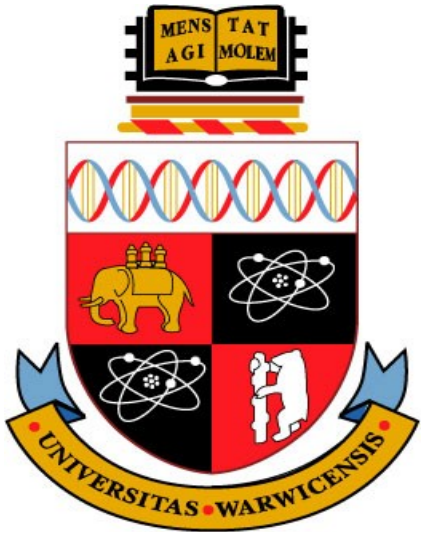

A Predictive Model of Bacterial Cell Division

Claire Elizabeth Broughton

MOAC Doctoral Training Centre

January 2016

A thesis submitted to the University of Warwick for the degree of Doctor of Philosophy

Contents

List of Figures

1 Acknowledgements

I would like to thank my project supervisors: Professor Alison Rodger of the Department of Chemistry, Dr David Roper of the School of Life Sciences and Dr Hugo van den Berg of the Mathematics Institute, University of Warwick. Many thanks also to our collaborators: Professor Tim Dafforn, University of Birmingham, and Dr Ravi Jagadeeshan, Monash University, Australia, and to my advisory panel: Dr Corinne Smith, Professor Matthew Turner and Dr Andrew McAinsh, University of Warwick.

Many thanks to my colleagues in both the Structural Biology and Biophysical Chemistry research groups. In particular to Alan Wemyss, Joseph Jones and Dr Nikola Chmel for sharing their knowledge of linear dichroism, circular dichroism and dynamic light scattering, and for always providing help and support, and to Amy O'Reilly for her advice and friendship. Many thanks also to Ian Hands-Portman for providing training in the use of the electron microscope and for his invaluable guidance. I am extremely grateful to my colleagues at the MOAC Doctoral Training Centre for sharing the highs and lows of research life, and for the fun and friendship along the way.

Thanks must also go to my family for all their support throughout this project, to Charlotte, Mandy and Carly. To my mum, who instilled in me a determination to succeed despite the obstacles and who encouraged me to indulge my love of learning and to work hard to achieve my goals. To my husband, for his endless love, support and encouragement and for his eternal optimism. Finally, thank you to Nigel for always listening when things went wrong, and for reminding me what really matters.

2 Declaration

This thesis is submitted to the University of Warwick for the degree of Doctor of Philosophy. It has been composed by the author and has not been submitted in any previous application for any degree.

The work presented (including data generated and data analysis) was carried out by the author, except where indicated in the text. For example, the publications were co-authored with supervisors, colleagues and collaborators.

3 Abstract

A mathematical model of the formation and contraction of the prokaryotic Z-ring *in vivo* was developed, based on the polymerisation and membrane anchor binding activity of the FtsZ protein as measured *in vitro*. From a set of kinetic parameters that are estimated from the experimental literature, the model, which is referred to as *Critical Accumulation of Membrane-bound FtsZ Fibres* (CAM-FF), predicts one of three cell division outcomes: i) division proceeds to completion, ii) division is initiated but stalls prior to completion, and iii) division is not initiated. CAM-FF was validated by the accurate prediction of the effect of deletion of the membrane anchor proteins ZipA and FtsA, and was used to predict an order of efficiency of the biochemical targets for antibacterial drug design as follows: FtsZ polymerisation > ZipA/FtsA availability > FtsZ GTP-binding. The temperature-sensitivity of the *ftsZ84* mutant was also analysed using CAM-FF and it was found that an acquired ATPase activity of the FtsZ84 protein (FtsZ G105S) could explain the temperature-sensitivity of cell growth. At lower temperatures where the ATPase activity is low, a functional Z-ring is able to form and contract. However, at 42 °C the increase in the ATPase rate causes the Z-ring to disassemble and cell division is inhibited. On purification of the FtsZ G105S mutant protein, a significant ATPase activity was observed *in vitro* that was absent in the wild-type FtsZ protein. Therefore, the ATPase activity is not an experimental artifact, as was previously thought. The ZapA and ZipA proteins were also purified, and the FtsA protein was overexpressed for subsequent purification, in preparation for crystallography and *in vitro* cell division reconstitution studies. A set of linear DNA molecules with defined length and GC content was designed and produced for the investigation of polymer hysteresis in flow.

4 Abbreviations

3-MBA	3-Methoxybenzamide
ADP	Adenosine-5'-diphosphate
ATP	Adenosine-5'-triphosphate
ATPase	Adenosine-5'-triphosphatase
ATP-γ-S	Adenosine-5'-[γ-thio]triphosphate
BAC	Bacterial artificial chromosome
B. subtilis	*Bacillus subtilis*
C. crescentus	*Caulobacter crescentus*
CD	Circular dichroism
ChIP	Chromatin immunoprecipitation
CMO	Chief Medical Officer
DEAE-dextran	Diethylaminoethyl-dextran
DNA	Deoxyribonucleic acid
E. coli	*Escherichia coli*
EM	Electron microscopy
EMSA	Electrophoretic mobility shift assay
FLM	Fluorescence light microscopy
FRAP	Fluorescence recovery after photobleaching
Fts	Filamentous temperature-sensitive
GC	Guanine/cytosine
GDP	Guanosine-5'-diphosphate
GFP	Green fluorescent protein
GlcNAc	N-acetyl glucosamine
GMPCPP	Guanosine-5'-[(α,β)-methyleno]triphosphate
GTase	Glycosyl transferase
GTP	Guanosine-5'-triphosphate
GTPase	Guanosine-5'-triphosphatase
LD	Linear dichroism
Lpp	Braun's lipoprotein
M. jannaschii	*Methanococcus jannaschii*
MRSA	Methicillin-resistant *Staphylococcus aureus*
MTS	Membrane targeting sequence

MurNAc	N-acetyl muramic acid
M. tuberculosis	*Mycobacterium tuberculosis*
NO	Nucleoid occlusion
ODE	Ordinary differential equation
PBP	Penicillin-binding protein
PCR	Polymerase chain reaction
P. aeruginosa	*Pseudomonas aeruginosa*
RNA	Ribonucleic acid
S. aureus	*Staphylococcus aureus*
SMA	Styrene maleic acid
SMALP	Styrene maleic acid lipid particle
S. pneumoniae	*Streptococcus pneumoniae*
SPR	Surface plasmon resonance
Ter	Termination region
TPase	Transpeptidase
UDP	Uridine-5'-diphosphate
UMP	Uridine-5'-monophosphate
YFP	Yellow fluorescent protein
Zap	Z-associated protein
Zip	Z-interacting protein

5 Introduction

Antimicrobial drugs arguably represent the biggest success of medical science in the 20th century (1). From the time of acceptance of the germ theory of disease, following key work by Pasteur and the definition of Koch's postulates (2) in the late 19th century, the search for the "magic bullet" drug began (3). Following the early successes of synthetic agents Salversan and the sulfa drugs (3–5), effort shifted towards natural compounds with the demonstration of the antibacterial properties of Penicillium by Fleming and the subsequent purification of the active compound penicillin, in sufficient quantity, by Florey and Chain in 1940 (6). The identification of many classes of natural antibacterial compounds followed in the so-called "golden era" of antibiotic drug discovery from 1940 to 1960. Around 1970 to 1980 the focus then shifted to the chemical modification of the antimicrobial compounds already in use (3).

Although additional chemical structures have come to use in the clinic through chemical modification strategies, as can be seen in Figure 1, no novel antimicrobial chemical class has been discovered since daptomycin in 1987 (7). The continuation of this antibacterial discovery void is a major issue due to the emergence of antibacterial resistance among populations of clinically relevant bacteria. As resistance becomes widespread, there are no new drugs in the pipeline to replace those becoming ineffective in treatment.

Resistance is an issue rapidly gaining momentum. In 2013 the Chief Medical Officer (CMO) of the UK, Dame Professor Sally Davies, recommended that antimicrobial resistance be put on the UK national risk register for civil emergencies. This was one of 17 recommendations put forward in the CMO Annual Health Report to address the emerging crisis (1). Although the incidence of the well-publicised "superbug" methicillin-resistant *Staphylococcus aureus* (MRSA) has been in decline in the UK since its peak in 2003 due to improved hospital procedures, MRSA and other drug-resistant strains are still of major concern. Carbapenem-resistant Enterobacteriaceae, penicillin-resistant *Streptococcus pneumoniae*, vancomycin-resistant *Enterococci*, and multidrug-resistant *Mycobacterium tuberculosis* and *Neisseria gonorrhoeae* have been highlighted as serious threats (1,3,8).

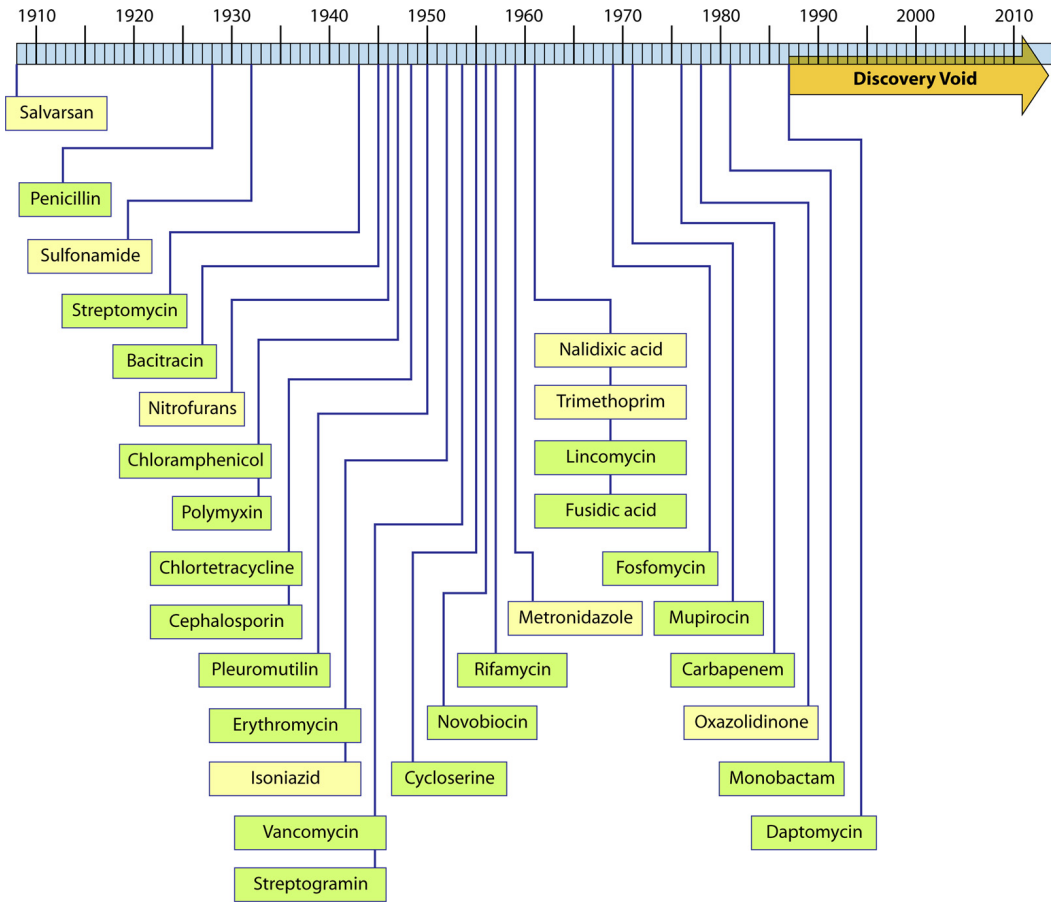

Figure 1: Antimicrobial drug discovery timeline. Dates indicate initial discovery or patent registration (7).

Current antibacterial drugs mainly target deoxyribonucleic acid (DNA) synthesis (DNA topoisomerase inhibitors: fluoroquinolones), ribonucleic acid (RNA) synthesis (RNA polymerase inhibitors: rifamycins), protein synthesis (50S inhibitors: macrolides, amphenicols; 30S inhibitors: tetracyclines, aminoglycosides), and cell wall synthesis (Penicillin binding protein (PBP) inhibitors: beta-lactams; transpeptidase inhibitors: glycopeptides), but as yet drugs targeted to the prokaryotic cell division machinery have not reached the market (9).

The prokaryotic cell division machinery comprises a set of at least 20 proteins that form a large complex referred to as the "divisome" (10). This complex assembles at the midcell from just inside the plasma membrane when the FtsZ protein self-assembles into polymers and forms a ring that spans the cell circumference, referred to as the Z-ring (11–13). Z-associated proteins (Zap

proteins) provide structural organisation (14–16) and the Z-ring is attached to the plasma membrane via interactions with ZipA and FtsA (17).

This protein scaffold then recruits the enzymes that will hydrolyse and synthesise peptidoglycan on the opposite side of the plasma membrane in the periplasm. Further protein-protein interactions connect the scaffold to the outer membrane in Gram-negative bacteria such as *Escherichia coli*. This ensures that the entire cell wall is remodelled in a concerted manner when the Z-ring contracts to pull opposite sides of the cell membrane together in cytokinesis – the final step in the division of a parent cell into two daughter cells (11–13). A simplified diagram of the core divisome components is shown in Figure 2.

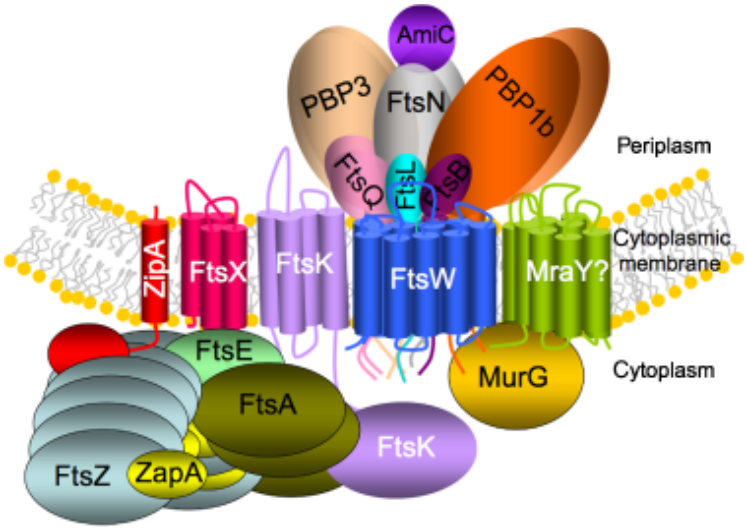

Figure 2: The prokaryotic divisome. A schematic representation of the complex of proteins that orchestrates cytokinesis in prokaryotic cells (10). Cylinders represent transmembrane domains.

An ideal antibacterial target is essential to life, is well conserved across a range of pathogens with little functional redundancy and has no homologue in mammalian cells (7). Several proteins of the divisome complex meet these criteria (18). Understanding bacterial cell division is therefore key to our ability to design and develop the antibacterial drugs of the future. The aim of this project was to investigate the formation and contraction of the Z-ring in *E. coli* by a combination of mathematical modelling and biophysical investigation of the

component proteins. The project began with the development of a kinetic model of FtsZ polymerisation and membrane binding, and a phenomenological model of Z-ring contraction. This lead to the definition of a contraction parameter which could be used to predict one of three cell division outcomes: i) division proceeds to completion, ii) division is initiated but stalls prior to completion, and iii) division is not initiated. The model was used to predict the division outcome on deletion of the membrane-anchoring proteins ZipA and FtsA and on inhibition of FtsZ activity, due to mutation or the presence of a chemical inhibitor. The model solutions were also used to predict the optimum biochemical targets for antibacterial drug design. The temperature-sensitivity of the *ftsZ84* mutant was also analysed using the model.

In concurrent work, a set of the cytoplasmic divisome proteins was cloned, expressed and purified for biophysical characterisation. Based on the simulation results for the *ftsZ84* mutant from the modelling work, the FtsZ G105S mutant protein was also purified and investigated. Significantly, an adenosine-5'-triphosphatase (ATPase) activity was confirmed.

5.1 The prokaryotic cell wall

The cell wall of the Gram-negative bacterium *E. coli* consists of an inner plasma membrane, a 3–6 nm thick single-molecule net-like peptidoglycan layer and an outer membrane (19), as shown in Figure 3. The peptidoglycan cell wall is required for the cell to withstand the large internal turgor pressure and to maintain cell morphology. However, it must also allow for growth by the addition of new material and it must be separated in two during cell division (20). In newborn cells, following a previous division, the rod-shaped cell elongates while the diameter remains constant. Once the length has doubled, the cell divides by the controlled invagination and separation of all three cell wall layers (21). It has been suggested that in addition to the contraction of the Z-ring, the synthesis of peptidoglycan at the midcell contributes a force for cytokinesis (22).

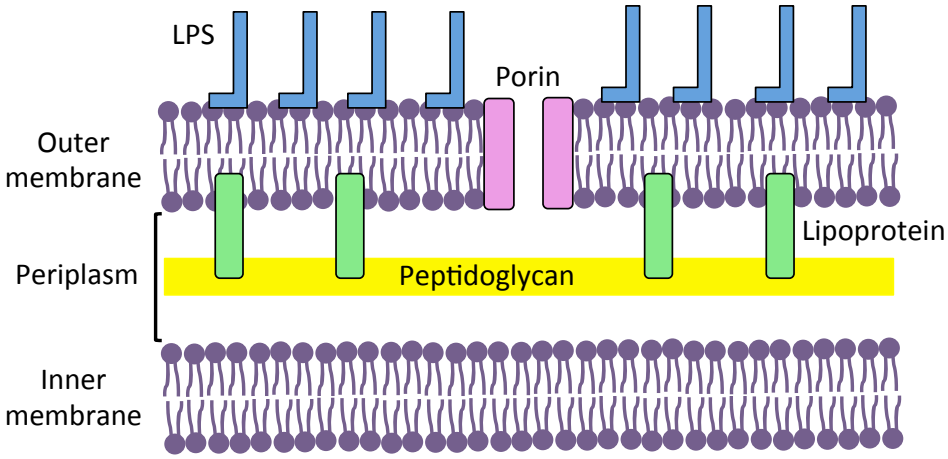

Figure 3: The cell wall of Gram-negative bacteria. LPS: lipopolysaccharide. Adapted from Cabeen and Jacobs-Wagner (20).

The peptidoglycan cell wall has been extensively studied over several decades. It consists of glycan chains that are covalently cross-linked by peptides. Electron cryotomography indicates that the peptidoglycan network of the *E. coli* cell wall forms a single layer that lies parallel to the cell surface. The structure was found to be fairly disordered, but the glycan chains are mainly perpendicular to the long axis of the cell. This structure is shown in Figure 4 (23).

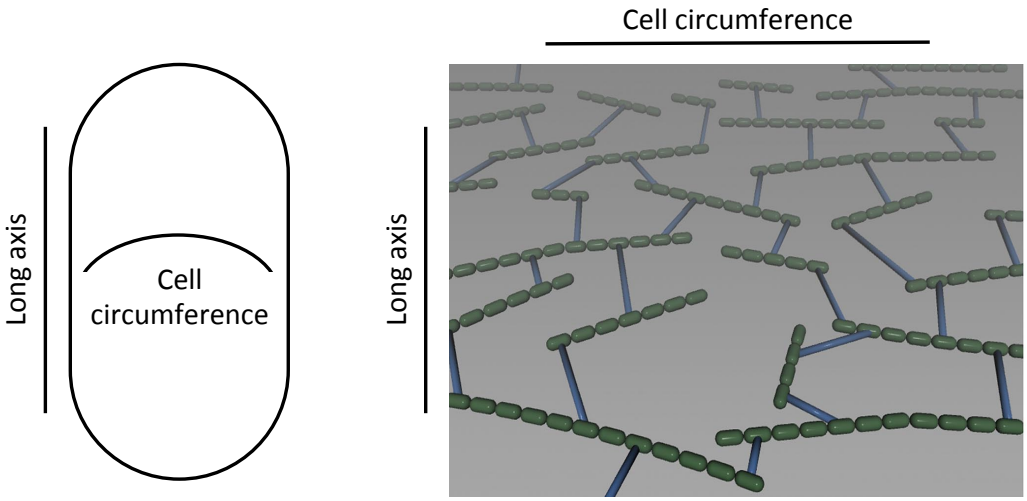

Figure 4: The organisation of the peptidoglycan cell wall in *E. coli*. Glycan strands shown in green are organised approximately perpendicular to the long axis of the cell. The structure is predicted to be fairly disorganised. Peptide cross-links are shown in blue. Adapted from Gan *et al*. (23).

The glycan chains of peptidoglycan contain alternating units of N-acetyl-glucosamine (GlcNAc) and N-acetyl-muramic acid (MurNAc) linked by a β-1,4-glycosidic bond. A peptide bond links a pentapeptide side chain to the MurNAc subunit and adjacent pentapeptides are covalently cross-linked to form an extended peptidoglycan network (24). Peptidoglycan synthesis begins in the cytoplasm where a series of enzymes generates uridine-5'-diphosphate (UDP)-GlcNAc from fructose-6-phosphate. MurA and MurB enzymes then catalyse the formation of UDP-MurNAc from UDP-GlcNAc (13,19,25) as shown in Figure 5.

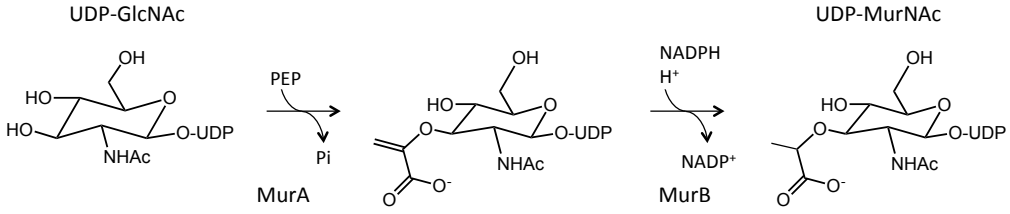

Figure 5: The synthesis of UDP-MurNAc from UDP-GlcNAc by MurA and MurB. Adapted from Barreteau *et al.* (26).

The enzymes MurC–F then sequentially add the pentapeptide stem to the carboxyl group of the lactoyl moiety of MurNAc. MurC adds L-alanine and MurD follows adding D-glutamate. MurE then adds meso-diaminopimelic acid (an intermediate in lysine biosynthesis) to the γ-carboxylate group of the D-glutmate and MurF then adds the D-Ala-D-Ala dipeptide previously dimerised by Ddl (26). The phosphorylated MurNAc-pentapeptide precursor is then transferred to the membrane acceptor undecaprenyl-phosphate by MraY to give inner membrane bound undecaprenyl-pyrophosphoryl-MurNAc (lipid I) with the release of uridine-5'-monophosphate. Finally in the cytoplasmic stage of peptidoglycan synthesis, MurG catalyses the transfer of GlcNAc from UDP-GlcNAc to lipid I to give undecaprenyl-pyrophosphoryl-MurNAc-pentapeptide-GlcNAc (lipid II) with the release of UDP (27). The steps of the peptidoglycan synthesis process that occur at the inner membrane are summarised in Figure 6. The identity of the inner membrane protein that transports lipid II across the membrane into the periplasm is disputed. Mohammadi *et al*. reported that FtsW was required for the transport of lipid II in FRET- and fluorescence-based assays

using *E. coli* membranes and reconstituted lipid vesicles respectively (28). However, Sham *et al*. reported that MurJ is the lipid II "flippase" in work using the toxin protein ColM to cleave newly transported lipid II (29).

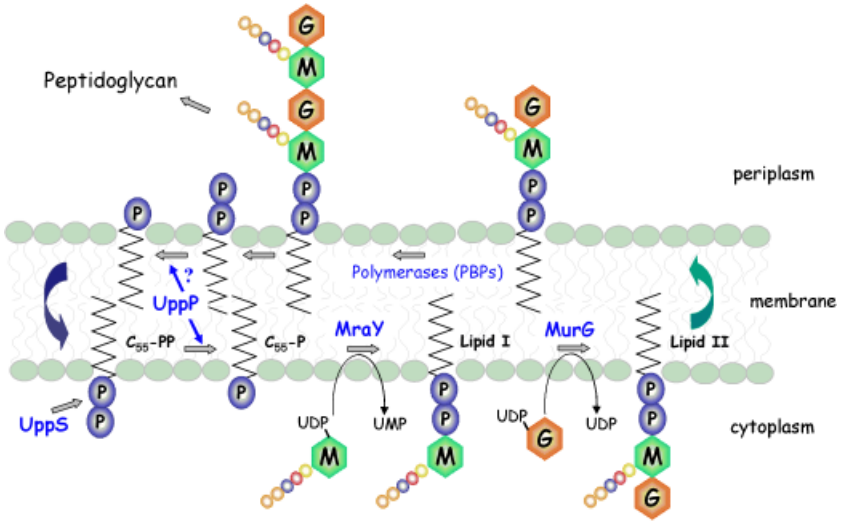

Figure 6: Peptidoglycan synthesis at the inner membrane. M and G correspond to MurNAc and GlcNAc respectively. The pentapeptide stem is represented as coloured beads. C_{55}-PP and C_{55}-P correspond to undecaprenyl-pyrophosphate and undecaprenyl-phosphate respectively (27).

Once lipid II has been transported to the periplasmic face of the inner membrane, glycosyltransferase enzymes (GTases) catalyse the addition of the GlcNAc-MurNAc disaccharide to a growing glycan chain and transpeptidases (TPases) catalyse the peptide crosslinking reactions. The usual peptide crosslink seen in *E. coli* cell walls is shown in Figure 7 and consists of a peptide bond between the carboxyl terminus of the D-Ala of position 4 and the free amino group of meso-diaminopimelic acid. The terminal D-Ala of the original pentapeptide stem is lost. All of the peptidoglycan synthases are anchored to the inner membrane (13,19,25).

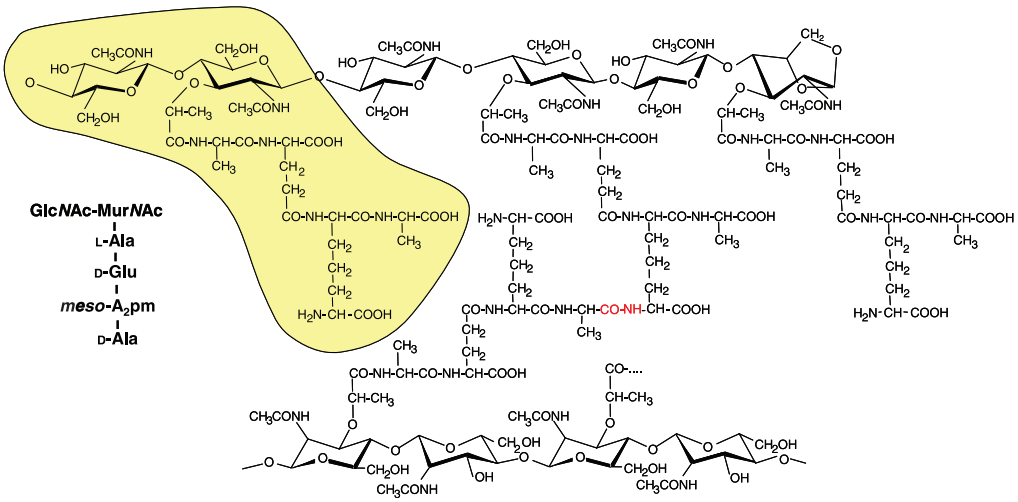

Figure 7: The chemical structure of *E. coli* peptidoglycan from Vollmer *et al.* (25). Highlighted in yellow is the basic GlcNAc-MurNAc-tetrapeptide disaccharide subunit or peptidoglycan "monomer". The typical peptide crosslink is shown in red.

There are three classes of peptidoglycan synthase enzymes, the monofunctional GTases, the monofunctional TPases and the bifunctional GTase and TPases (30). The proteins were originally identified as binding partners of penicillin and are still referred to as the penicillin-binding proteins (PBPs) (31,32). *E. coli* has three class A bifunctional PBPs: PBP1A, PBP1B and PBP1C and two monofunctional TPases: PBP2 and PBP3. PBP1A and PBP2 have been shown to interact and are thought to be involved in cell elongation in the growth phase and also in an early phase of cell division (30). A direct interaction between PBP1B and PBP3 has also been observed and this pair of enzymes is involved in late cell division (33).

The presence of either PBP1A or PBP1B is essential for life (34). Although PBP1A has been shown to act in elongation and PBP1B in cell division, each protein can compensate in the absence of the other. PBP1C is non-essential and its over-expression cannot compensate for the loss of both PBP1A and PBP1B (35). The monofunctional GTase, MtgA is non-essential in *E. coli* and may also have a role in cell division (36).

The peptidoglycan wall is also linked to the outer membrane via Braun's lipoprotein (Lpp), a small 58-residue protein with an S-glycerylcysteine at the N-terminus, which is modified with 3 fatty acids. These are embedded in the outer

membrane *in vivo*. The C-terminal lysine residue is covalently attached to peptidoglycan via a peptide bond between the ε-amino group of the lysine side chain and the α-carbonyl of mDAP (37,38).

5.2 Prokaryotic cell division

Work to understand bacterial cell division began in the 1960s with the isolation of *E. coli* mutant cells that were able to replicate and segregate chromosomal DNA but were unable to divide. Under certain conditions, the cells formed long filaments that eventually died and the mutants were referred to as "*fts*" for filamentous temperature-sensitive (39,40). Since then, an extensive body of research has been generated with the most notable advances coming from developments in fluorescence microscopy, and in gene fusion and two-hybrid assays in the 1990s. A large number of component proteins and their specific interactions have been shown to be required for cell division and the large macromolecular complex is referred to as the divisome (41). The study of the division process was slowed for several years by the very nature of the problem – the difficulty of the study of membrane proteins, and the fact that many of the component proteins are essential for life. That is, investigation of the effect of loss of function is not possible if the result of gene deletion is cell death. The observed temperature-sensitivity of several key mutants has been extensively utilised to analyse the effects of protein loss. Cells may be grown at the so-called permissive temperature then are shifted to a temperature at which the protein of interest is no longer functional. The window of opportunity for observation, before cell death, may then be exploited (17,41–44).

Cytokinesis is the final step in cell division. Following chromosome replication and segregation, the parent cell is divided into two daughter cells by the contraction of a large protein ring that forms at the midcell. *E. coli* uses a constrictive mode of cell division in which the invagination of the inner and outer membranes and the synthesis of new peptidoglycan occur simultaneously. This is in contrast to many Gram-positive bacteria in which the new cell wall is synthesised along the midcell before membrane invagination (10,11,13).

In 1991 FtsZ was identified as the first and most abundant component of the cell division machinery using immuno-electron microscopy (45). A ring of FtsZ was shown to be localised to the midcell and it remained at the leading edge throughout the contraction of the cell wall. Since this discovery, numerous reports of the behaviour of FtsZ and of the subsequent assembly of the divisome complex have been published. The Z-ring is highly dynamic with the continuous exchange of FtsZ with the cytoplasmic pool. The half life of recovery of a photo-bleached region of the Z-ring was found to be 10–30 seconds with fluorescence recovery after photobleaching (FRAP) (46–48).

FtsZ remains the first protein known to localise to the midcell in the initiation of cell division and it is required for the localisation of all downstream proteins. At least 20 other proteins have been shown to contribute to the cell division process. A subset of these proteins are essential in *E. coli*: FtsZ, ZipA, FtsA, FtsK, FtsQ, FtsL, FtsB, FtsW, FtsI/PBP3 and FtsN. Additional proteins including ZapA–E, FtsEX, and AmiC localise to the midcell and play a role in cell division but are non-essential (41).

A linear order of recruitment to the midcell has been elucidated using fluorescent labelling of each component with green fluorescent protein (GFP) and visualisation of the localisation pattern on depletion of each of the other proteins in the complex. FtsZ localises first, followed by FtsA and ZipA which localise independently of each other (17), followed by FtsEX (49,50), FtsK (51,52), FtsQ (53), FtsL/FtsB (54), FtsW (55), FtsI/PBP3 (56) and finally FtsN (52). The assembly of the divisome complex is thought to occur in two stages with early division proteins FtsZ, ZipA, FtsA FtsEX and ZapA–E localising to form the preliminary Z-ring structure. This is followed by a phase of pre-septal peptidoglycan synthesis at the future division site. Divisome maturation refers to the arrival of the late proteins from FtsK to FtsN (57).

The linear system of recruitment reflects the inability of each protein to localise in the absence of at least one other upstream protein. Although it appears relatively simple, the precise assembly mechanism may be very complex. In the simplest case, each new recruit may interact directly with the latest upstream protein. Alternatively, each protein could form interactions with the previous recruit and one or more others. Protein-protein interactions may cause a modification which then allows the further recruitment of the next protein (58).

A combination of all three mechanisms may be at work in reality. Evidence for a complex interaction network certainly exists. For example, FtsW and FtsI/PBP3 have been shown to interact independently of the other proteins (59) and there is evidence that FtsQ, FtsL and FtsB form a complex prior to midcell localisation (60). Furthermore, when a ZapA fusion protein was used to prematurely target FtsQ to the midcell, FtsL and FtsB were recruited in the absence of FtsA or FtsK. The FtsQ fusion was also able to back-recruit FtsK and to forward recruit FtsI/PBP3. Interestingly, FtsN was not recruited in the absence of FtsA (58).

Although many of the components of the divisome are essential for life, there is evidence for overlap and redundancy of function. For example, cell viability can be restored on deletion of *ftsK* by overexpression of FtsAZ, FtsQ, ZipA, FtsB and FtsN. The loss of the FtsK protein was also compensated by the mutant protein FtsA R286W (also referred to as FtsA*) (61). However, it should be noted that as for many other examples of division recovery, although the cells are viable on overexpression of another division component, the wild-type phenotype is not fully restored and some defect remains.

5.2.1 FtsZ

FtsZ is a 40 kDa guanosine-5'-triphosphatase (GTPase), with a guanosine-5'-triphosphate (GTP) binding motif almost identical to that found in eukaryotic tubulin: GGGTGTG in FtsZ compared to G/AGGTGSG in α-, β- and γ-tubulins (62,63). When the structures of FtsZ (64) and tubulin (65) were solved in 1998, it was found that the proteins have essentially the same fold, despite amino acid sequence similarity of only 10–18%. FtsZ spontaneously forms head-to-tail polymers in the presence of GTP and, on polymerisation, a GTPase active site is formed when a catalytic aspartate residue (D212 in *E. coli*) on the T7 loop of the C-terminal domain of one subunit inserts into the N-terminal GTP-binding pocket of the adjacent subunit (66,67). The subsequent depletion of GTP by hydrolysis leads to polymer dissociation *in vitro* (68). The structure of the FtsZ monomer of *Pseudomonas aeruginosa* and the predicted polymer structure are shown in Figure 8 (69).

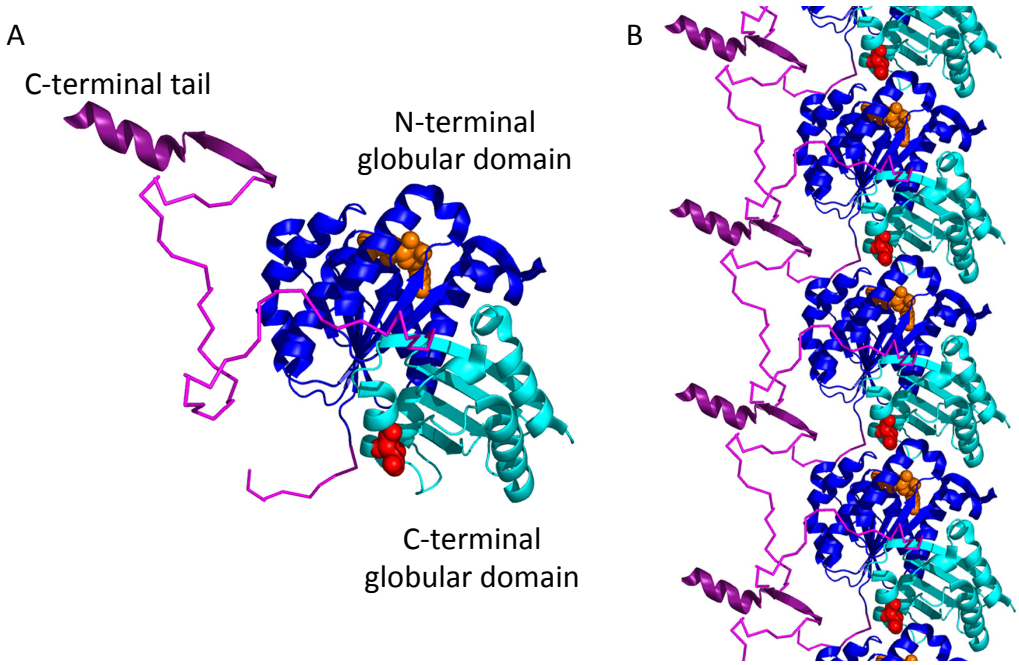

Figure 8: FtsZ structure from *Pseudomonas aeruginosa*. (A) The crystal structure of the FtsZ monomer (PDB file 1OFU (70)) with bound GDP shown in orange and the catalytic aspartate residue equivalent to D212 in *E. coli* highlighted in red. (B) The predicted structure of an FtsZ polymer based on monomer stacking (69).

Various FtsZ structures have been reported. For example, in the presence of GTP and diethylaminoethyl-dextran (DEAE-dextran) (71) or GTP and Ca^{2+} (72), straight polymers of FtsZ formed and collected into flat sheets. With excess guanosine-5'-diphosphate (GDP), tubes formed where the FtsZ polymers curve into a helix (68,71,73). The polymerisation of FtsZ is also enhanced by the presence of potassium and magnesium ions in the solution buffer (62,63,74). Subsequent *in vitro* mimicking of the crowded conditions of the cell indicated that GTP-bound FtsZ forms flat single-polymer thick ribbons by lateral FtsZ interactions and that the rate of polymerisation of GDP-bound FtsZ is very low (75). In another crowding study, FtsZ formed bundles, helices, rings of 200 nm diameter and toroids (76). The precise structure of the Z-ring *in vivo* remains unclear but single-chain GTP-bound polymers are thought to form the basic subunits.

5.2.2 Isodesmic *vs* co-operative assembly of FtsZ filaments

In isodesmic polymer assembly, the addition of each monomer in the elongation reaction has the same rate or affinity as the next addition. Polymers can form at low protein concentrations and the average polymer length at equilibrium gradually increases with protein concentration (77). In contrast, in co-operative polymer assembly a critical concentration is observed below which all subunits exist of monomers. Above the critical concentration, the protein exists in distinct populations of long polymers and monomers at equilibrium. There are few intermediates and polymers assemble until the monomer concentration falls below the critical concentration. A time delay in polymerisation is also a hallmark of co-operative assembly and the extent of polymerisation measured over time is sigmoidal (78).

In several studies, co-operative behaviour of FtsZ has been reported including a critical concentration for polymerisation, where the precise concentration is dependent on the buffer composition. For example, Huecas *et al*. reported that the critical concentration of *E. coli* FtsZ in the presence of GTP is 0.88 μM at pH 6.5 and 1.57 μM at pH 7.5. Single-stranded linear polymers were observed above the critical concentration using cryo-electron microscopy. However, above a concentration of 1.7 μM, FtsZ double filaments were also observed (77). Caplan and Erickson used isothermal titration calorimetry and reported a critical concentration of 0.31 μM at pH 6.5 with 2.5 mM magnesium and this increased to 2.9 μM in the absence of magnesium (79). Mukherjee and Lutkenhaus reported a critical concetration of FtsZ of 1 μM using polymer centrifugation and 2 μM using light scattering (68). These values are considerably lower than the predicted concentration of FtsZ in *E. coli* of 3.5–15 μM (80–82).

Since light scattering and centrifugation assays under-report small polymers, Chen *et al*. used the fluorescent *E. coli* FtsZ L68W mutant which gives an increase in fluorescence on polymerisation that is proportional to the number of FtsZ interfaces (74). They found the critical concentration of polymerisation to be between 0.1 and 2.8 μM, dependent on the buffer pH and composition, and polymerisation was favoured at pH 6.5 compared to pH 7.7 and in the presence of magnesium and potassium ions at 5 mM and 100 mM

respectively. Electron micrographs indicated that the polymers were single filaments of between 20 and 100 subunits long with an average length of 60 subunits. On addition of GTP to FtsZ L68W in a stopped-flow device, following a time lag, the fluorescence signal increased rapidly then reached a plateau (74). This suggests a co-operative polymerisation mechanism.

In further support of a co-operative mechanism, when purified *E. coli* FtsZ was polymerised with the addition of a GTP-regenerating system, sedimentation-velocity analysis revealed a bimodal distribution of FtsZ. At low concentrations FtsZ was slow to sediment and the solutions contained FtsZ monomers and dimers. Above the critical concentration, FtsZ existed with a narrow distribution of very fast sedimenting species (83).

Initially, it was unclear how the formation of single-stranded polymers could result in co-operative kinetics. Co-operative polymerisation had been previously explained for helical or multi-stranded polymers by the slow formation of a dimer nucleus with favourable trimerisation and further elongation since the elongating monomer, shown in blue in Figure 9, interacts with more than one subunit simultaneously after the formation of the dimer nucleus (84).

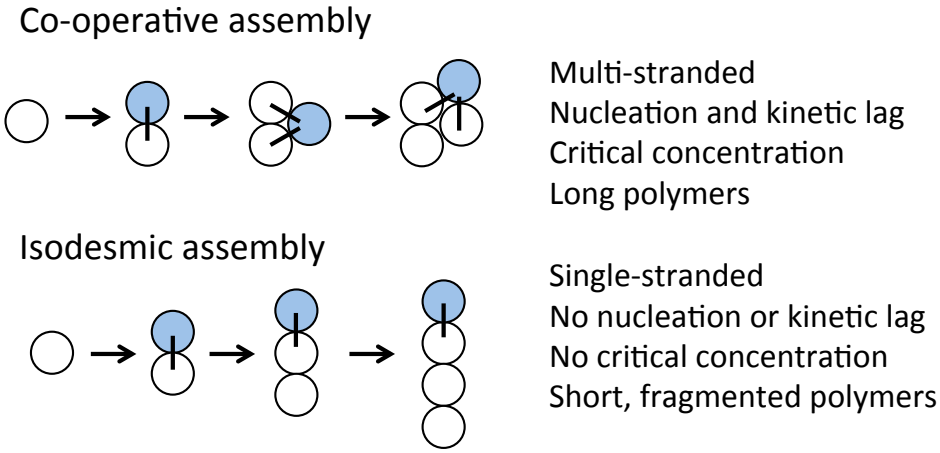

Figure 9: A traditional view of co-operative and isodesmic polymerisation mechanisms. Adapted from Romberg *et al*. (78).

Chen *et al*. fitted the fluorescence data of the FtsZ L68W mutant using a kinetic model that included monomer activation, dimer nucleation and elongation steps only (74). Although the formation of a dimer occurred at the same rate as the subsequent dimer elongation, the dimer was weak with a fast dissociation rate. The fit suggested that the time lag for the polymerisation reaction is due to the requirement for the release of GDP that is still bound to FtsZ on purification, before GTP binding. The results also suggested that the dimer is more stable in the presence of magnesium. However, the model did not include the effect of GTP hydrolysis (74).

Further modelling work by Huecas *et al*. (77) and by Miraldi *et al*. (84) support the explanation of co-operativity by a dimer nucleation mechanism, where there are two possible states of the monomer, inactive and active. These states do not necessarily directly relate to GDP- and GTP-bound FtsZ respectively. The system will be co-operative if the nucleation reaction requires an unfavoured monomer activation step since dimerization will require two such activation steps, whereas the subsequent elongation requires only one (84). The subunit activation may occur before or after the association of the two interfaces and the binding of GTP may lower the energy difference between the inactive and active states. Alternatively, the conversion to the active state may be driven by the polymer contacts (77). The possible pathways to the formation of an active dimer in a nucleation process are shown in Figure 10. Formation of the dimer nucleus requires two activation steps and one binding step. Subsequent elongation requires a single activation and a single binding step.

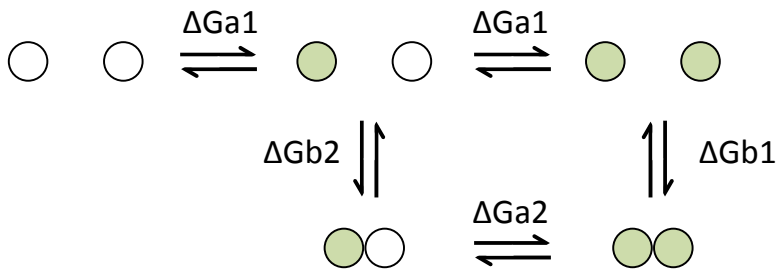

Figure 10: Dimer nucleation with the requirement for subunit activation. White indicates inactive monomers, green indicates activated monomers. ΔGa refers to the energy of monomer activation and ΔGb to the energy of binding. Adapted from Huecas *et al*. (77).

5.2.3 Structure of the Z-ring *in vivo*

The first study to demonstrate the localisation of FtsZ to the Z-ring *in vivo* used immuno-gold labelling and visualisation with electron microscopy (EM) (45). Figure 11 shows the localisation of FtsZ to the midcell and its persistence at the leading edge of constriction. The density of the cytoplasm prevents visualisation of the Z-ring by EM without specific labelling and the cell must be fixed and stained. The resolution is limited and the visualisation of Z-ring dynamics in live cells is not possible.

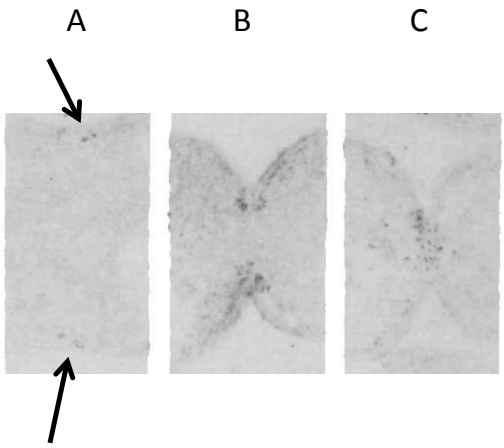

Figure 11: Electron micrographs of the localisation of FtsZ to the midcell in *E. coli*. (A) Arrows indicate the localisation of FtsZ to the midcell membrane prior to the initiation of constriction. (B) and (C) demonstrate that FtsZ remains localised at the leading edge until constriction is complete (45).

Fluorescence light microscopy (FLM) was next utilised and the Z-ring was visualised using a low level of expression of FtsZ fused to GFP from a plasmid, since replacement of the chromosomal copy of FtsZ with an FtsZ-GFP fusion is non-viable. Examples of the early images of the Z-ring from FLM are shown in Figure 12A and Figure 12B. The Z-ring was shown to form from a single nucleation point, seen as a dot of fluorescence, which extended with bidirectional synthesis as an arc along the cell periphery and eventually formed a closed ring structure (85). The Z-ring was shown to be approximately 100 nm wide but the structure of individual filaments of FtsZ were not resolved (86).

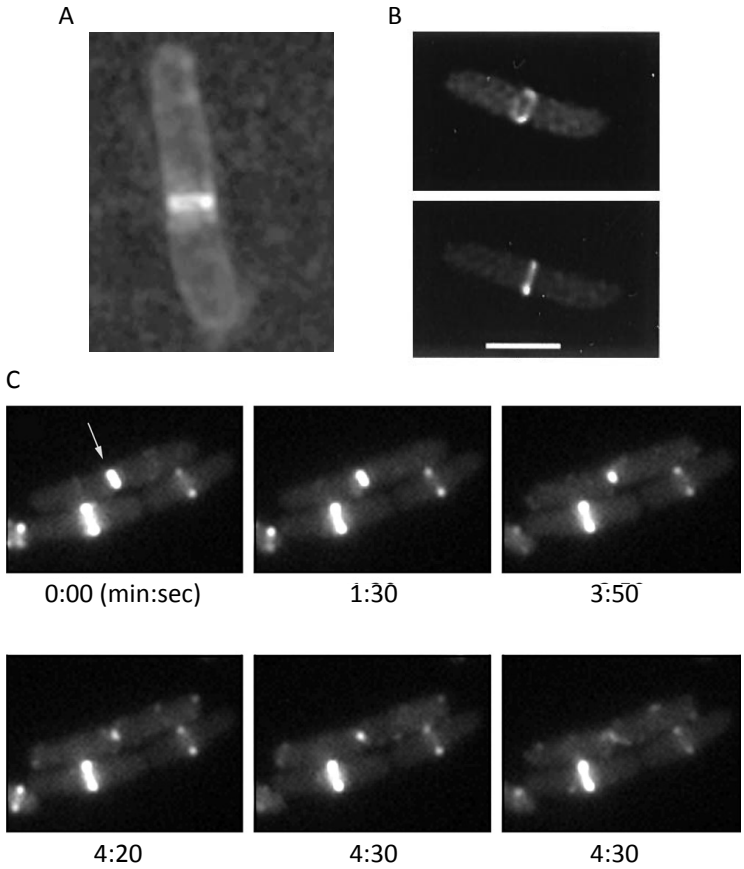

Figure 12: The Z-ring visualised by fluorescence light microscopy with an FtsZ-GFP fusion protein. (A) From Sun and Margolin (87). *E. coli* FtsZ-GFP with additional staining of the cell membrane with FM4-64. (B) From Ma *et al*. (88) with alternative viewing angles to demonstrate the ring structure. Scale bar represents 1 μm. (C) A time course experiment from Erickson *et al*. (69) to demonstrate the constriction and disassembly of the Z-ring (shown in the upper cell of the image) during cell division.

As shown in Figure 12C, the Z-ring contracts and disassembles as it divides the cell into two. New Z-rings were also shown to begin assembly at the ¼ and ¾ positions before the previous cell constriction is complete (87). When FtsZ-GFP was overexpressed, spiral and helical structures were observed that were non-functional for division (88). In 2004, Thanedar and Margolin reported that GFP-labelled FtsZ forms mobile helical rings that complete wave-like oscillations in *E. coli* and it was thought that these structures were Z-ring precursors that may condense or coalesce into functional Z-rings (89). A similar observation was made for FtsZ in *Bacillus subtilis* as it was shown to form a dynamic helix that spans the length of the cell and then condenses into the midcell ring at the appropriate time (90). The presence and significance of FtsZ

helices has been further reported in more recent studies using high resolution imaging of FtsZ both in *B. subtilis* (91) and *E. coli* (86,92). However, using photoactivated localization microscopy (PALM) imaging of FtsZ in *E. coli*, the tendency to form helical structures, as shown in Figure 13, increased with FtsZ over-expression and the extended helical structures were not observed with up to 2–3-fold excess of the wild-type concentration (86). The relevance of the helical structures in wild-type cells is therefore unclear. It has also recently been suggested that the helical pattern may be an artifact of the fluorescent labelling (93,94).

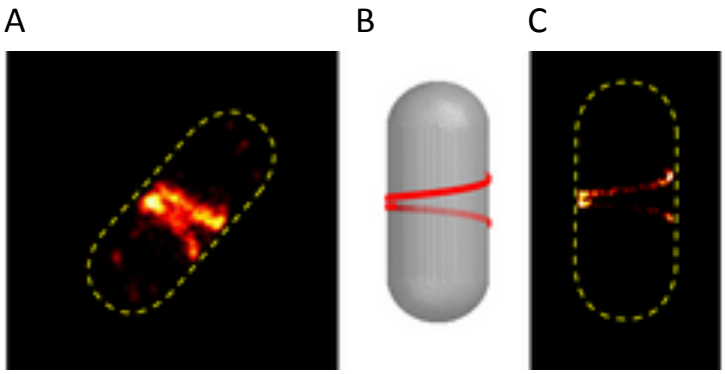

Figure 13: PALM imaging of helical structures of FtsZ in *E. coli* from Fu *et al*. (86). (A) High-resolution PALM image of FtsZ labelled with mEos2. The cell boundary is indicated. (B) Modelled helical structure and (C) the simulated PALM image expected from the modelled structure.

Indeed, using three-dimensional structured illumination microscopy (3D-SIM) in *E. coli*, and immunofluorescence with wild-type cells to ensure any observed pattern was not due to an effect of FtsZ over-expression or an artifact of the GFP labelling, Rowlett and Margolin did not observe helices but patches of FtsZ with randomly oriented short filaments. In addition, large gaps were observed within Z-rings that lacked or contained low concentrations of FtsZ (95). As shown in Figure 14A, a similar pattern was observed on labelling of FtsA or ZipA with GFP. Under 3D-SIM, the Z-rings of *B. subtilis* and *S. aureus* were also heterogeneous with some regions lacking fluorescence. The Z-ring had a bead-like structure with regions of high FtsZ concentration linked by regions that contained little or no FtsZ. This is also shown in Figure 14B. The bead structure

was dynamic both before and during constriction (96). Using high throughput 3D-PALM of synchronous *Caulobacter crescentus* populations the Z-ring was again shown to be patchy and discontinuous. Complete, high-density, persistent rings that did not constrict were seen in response to DNA damage (97). This suggests that the observed gaps are required for Z-ring constriction to proceed.

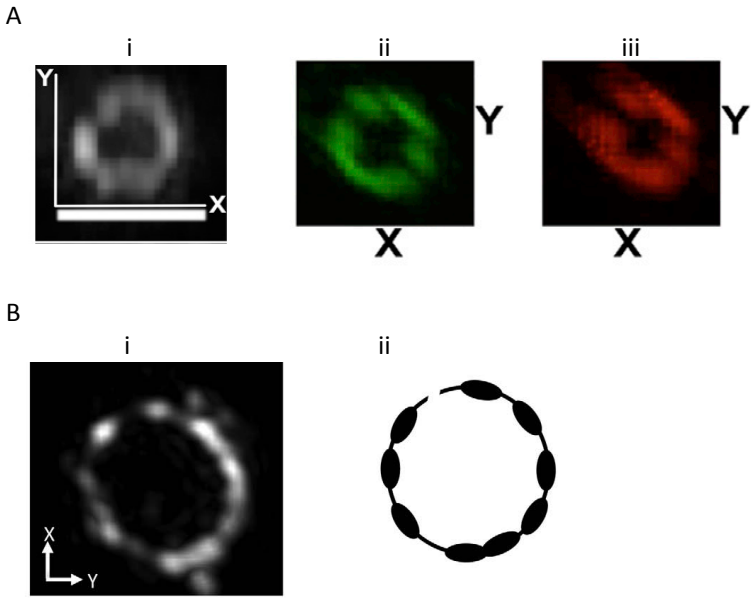

Figure 14: Local heterogeneity in functional Z-rings revealed by 3D-structured illumination microscopy (3D-SIM). (A) Z-rings in *E. coli* contain large gaps and local discontinuities when (i) FtsZ, (ii) FtsA or (iii) ZipA is labelled with GFP (95). Scale bar indicates 1 μm. (B) Under 3D-SIM, the Z-ring of *B. subtilis* (i) shows a bead-like structural arrangement with gaps. A representation of the structure is given in (ii) (96).

A key study into the fine organisation of the FtsZ filaments in the Z-ring *in vivo* was published in 2007 (98). Electron cryotomography of the marine bacterium *C. crescentus* indicated that the Z-ring is composed of a sparse arrangement of short (approximately 100 nm), independent FtsZ filaments with a single or double thickness. As shown in Figure 15, the filaments were adjacent to the inner membrane with a somewhat erratic arrangement, although most of the filaments observed were perpendicular to the long axis of the cell. The number of filaments in the width of the Z-ring was low at only 2–3 and this is not be consistent with the high level of FtsZ found in the Z-ring in other studies. However, these images remain the most highly resolved of the arrangement of

FtsZ filaments *in vivo* to date (98). The model of the Z-ring shown in Figure 16 in which short FtsZ filaments are arranged perpendicular to the long axis of cell without direct lateral contacts is generally accepted.

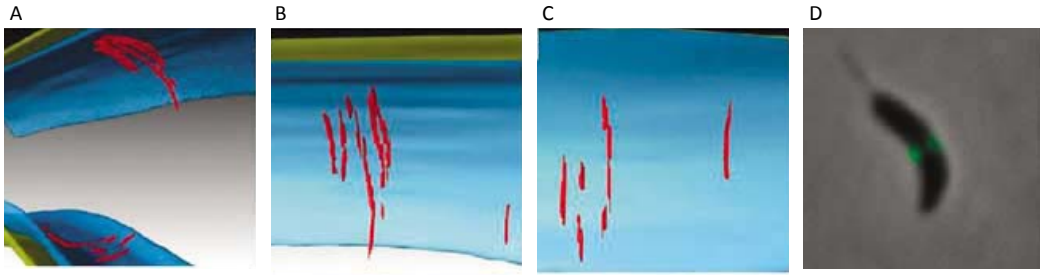

Figure 15: FtsZ filaments in *C. crescentus* visualised by electron cryotomography. (A–C) False colour images of the FtsZ filaments aligned on the inner cell membrane, perpendicular to the long axis of the cell. (D) Fluorescence light microscopy image of the cell expressing FtsZ-YFP (98).

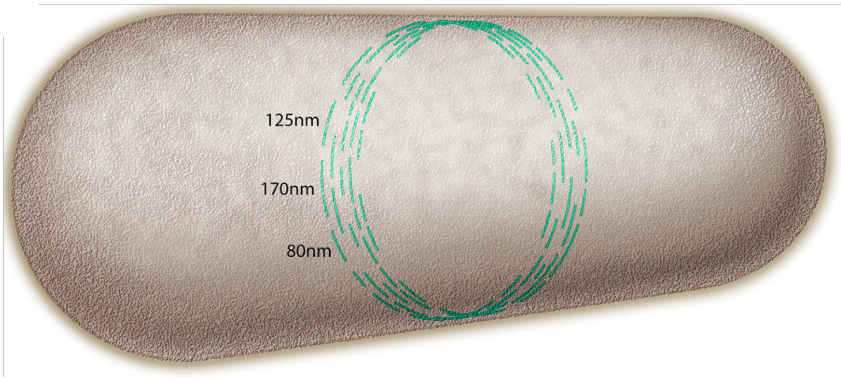

Figure 16: A model of the Z-ring structure, based on the length of FtsZ filaments observed *in vitro* and the perpendicular arrangement of FtsZ in *C. crescentus* (69).

5.2.4 Reconstitution of the Z-ring *in vitro*

In 2008, Osawa *et al*. demonstrated that at least the initial contraction force of the Z-ring is due to the intrinsic biochemical activity of FtsZ (99). Membrane indentations were observed in tubular, multi-lamellar vesicles on the addition of a membrane-targetted FtsZ protein, fused to yellow fluorescent protein (YFP). The construct contained the membrane targetting sequence (MTS) of the MinD protein at its C-terminus to replace the membrane-anchoring function of ZipA and FtsA *in vivo*. In the presence of GTP, the FtsZ inside the

vesicles formed mobile ring structures that coalesced and then pinched the membrane inwards. Examples are given in Figure 17. When GTP was depleted by hydrolysis, the contracted Z-rings relaxed and slowly disappeared. The contraction did not proceeded to completion which indicates the requirement for additional factors in the completion of membrane or cell division (99).

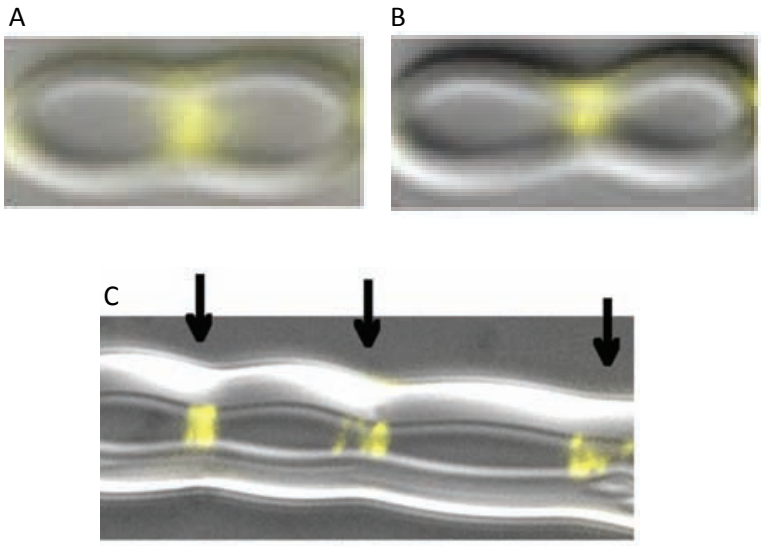

Figure 17: Z-rings constrict multi-lamellar liposomes *in vitro* from Osawa *et al*. (99). FtsZ-YFP-MTS organises into functional Z-rings in the presence of GTP. The fluorescence of FtsZ is superimposed onto a differential interference contrast image of the liposome. (A) An example Z-ring and (B) the contraction observed 6 minutes later. (C) An example of multiple Z-rings formed in a tubular liposome.

In subsequent work by Osawa *et al*., the localisation of the FtsZ-YFP-MTS fusion protein to the outside of liposomes caused concave membrane depressions in the presence of GTP (100). This is shown in Figure 18A. Furthermore, when the MTS was moved from the C-terminus to the N-terminus to give MTS-FtsZ-YFP, as shown in Figure 18B, the membrane indentations on the liposome surface became convex. This suggests that the FtsZ filament forms a particular defined curvature and that the membrane is pulled to match it. Interestingly, the position of the membrane targetting sequence determined the effect on the membrane. This suggests that the linker region at the native C-terminal membrane tether is able to confer the FtsZ filament bend onto the membrane (100).

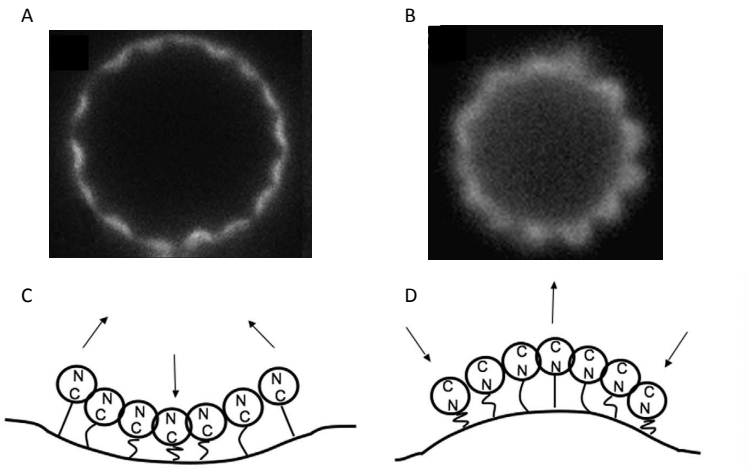

Figure 18: Membrane deformations in lipid vesicles due to membrane-targetted FtsZ polymers. (A) C-terminal FtsZ-YFP-MTS constructs localised to the outside of the liposome resulted in concave depressions of the membrane. (B) N-terminal MTS-FtsZ-YFP constructs localised to the outside of the liposome resulted in convex depressions of the membrane. (C) and (D) Diagrams of the possible structures of FtsZ polymers that explain the observed membrane structures for C-terminal and N-terminal MTS tags respectively. Adapted from Osawa *et al*. (100).

The MTS-FtsZ-YFP fusion protein also formed Z-rings on the outside of the tubular liposomes and these were termed "inside-out" Z-rings. These rings generated forces that pinched the liposome inwards. The rings could also move laterally and coalesce. Using the non-hydrolysable GTP analogue guanosine-5'-[(α,β)-methyleno]triphosphate (GMPCPP), constrictions did still occur but they did not progress as far as with GTP. The Z-rings formed with GMPCPP were also less mobile. Subunit exchange was prevented and photo-bleached spots did not recover in the presence of GMPCPP, compared to a recovery half time of 30 seconds with GTP. The reconstitution experiment gives further evidence that gaps are required for constriction to proceed. In the absence of subunit turnover with GMPCPP, once the Z-ring becomes completely closed with no visible gaps, constriction was blocked (101). EM imaging of the inside-out Z-rings revealed closely packed ribbons of FtsZ filaments with small gaps, suggestive of lateral FtsZ interactions (102).

5.2.5 Z-ring contraction mechanism in cytokinesis

In eukaryotic cells, contraction in cytokinesis relies on the sliding force generated by the adenosine-5'-triphosphate (ATP)-dependent interaction of the motor protein myosin and the structural actin filaments within the ring (103). As yet no equivalent motor protein has been identified in prokaryotic cells and the *in vitro* reconstitution work suggests that at least the initial force of contraction is a function of the FtsZ itself (99). Lan *et al*. reported that the force required for contraction of the Z-ring is relatively small at 8 pN and this calculated value is of the same order of magnitude as the force measured with eukaryotic motor proteins of 2–50 pN (104).

In one proposed mechanism of Z-ring contraction, FtsZ polymers anneal to form one large polymer that spans the entire cell circumference at least once and contracts by filament sliding. This increases the extent of filament overlap and the number of lateral FtsZ interactions (69). However, the rapid turnover of FtsZ observed in FRAP studies (46–48) and the presence of regions of the ring that lack FtsZ (95–97) do not support this model. In addition, Erickson calculated that it would take an average of 1,200 seconds to break the existing lateral bonds of the Z-ring to allow sliding to take place. Such a mechanism would therefore be too slow to allow contraction of the Z-ring (105).

Based on the observed organisation of FtsZ polymers *in vivo* in *C. crescentus*, Li *et al*. proposed that FtsZ polymers bind to the inner membrane in a GTP-bound, straight conformation and that on hydrolysis of the GTP to GDP, the polymer changes conformation to exert an inward pinch on the local region of the membrane. The combination of small pulling forces around the entire Z-ring, and the subsequent depolymerisation and rebinding of FtsZ was termed the "iterative pinching" contraction model (98).

Further support of a force of contraction from filament bending comes from the observation of FtsZ polymer structures *in vitro* using electron and atomic force microscopies. From electron microscopy data, Lu *et al*. reported that FtsZ polymers form straight filaments as well as tubes and mini-rings when assembled in the presence of GTP and DEAE-dextran (106). With the non-hydrolysable GTP analogue GMPCPP and DEAE-dextran, polymers were exclusively straight and with GDP and DEAE-dexran FtsZ formed curved tubes

and mini-rings of 24 nm diameter (71,106). These results suggest that GTP-bound FtsZ filaments adopt a straight conformation, whereas GDP-bound filaments are curved. Later work using both electron and atomic force microscopies indicated an intermediate curvature of FtsZ. Rings of 160–200 nm diameter formed in the presence of GTP, GMPCPP or the GTP analogue GDP-AlF_3 (83,107).

Significant structural changes that could account for the filament curvature have not been found in the crystal structures of GDP-bound FtsZ monomers compared to GTP-bound FtsZ monomers. However, in 2013 Li *et al*. solved the crystal structure of FtsZ from *M. tuberculosis* and analysed the dimer interface for key hydrophobic interactions (108). The T3 loop region showed clear differences between the GTP- and GDP-bound states. In the GTP-bound state, the T3 loop is held in a tension or T state, whereas with GDP bound, the loop may be in the T state or in a relaxed or R state. Rather than a large-scale change to the FtsZ monomer structure, this small change could represent a hinge mechanism at the dimer interface, as shown in Figure 19. The corresponding interface residues were mutated in the *E. coli* FtsZ protein to confirm their relevance and on disruption of the interface, FtsZ no longer polymerised and the GTPase activity was dramatically reduced *in vitro* (108).

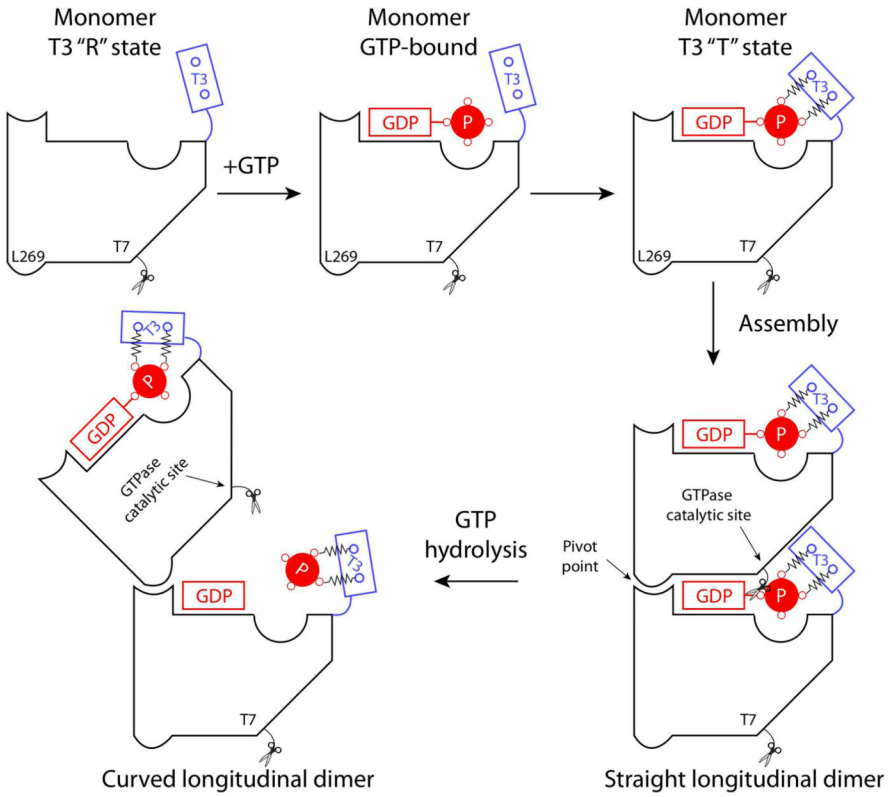

Figure 19: The hinge mechanism of Z-ring contraction. Li *et al*. suggest a GTP hydrolysis-mediated switch occurs at the FtsZ dimer interface due to a conformational change of the T3 loop region (108).

In subsequent molecular dynamics simulations (108), the differences in polymer conformation between the two nucleotide states were maintained over time. The GTP-bound polymer is slightly curved with a monomer-to-monomer angle of 170°. When the GDP-bound dimer transitions from the slightly curved state (170°) to the bent state with an angle of 135°, 7 kcal/mol is released and approximately 20 pN of force could be generated by this switch. The possible deformation of the inner membrane by a conformational change is shown in Figure 20. The GDP-bound interface was also shown to be weaker and more likely to dissociate (108).

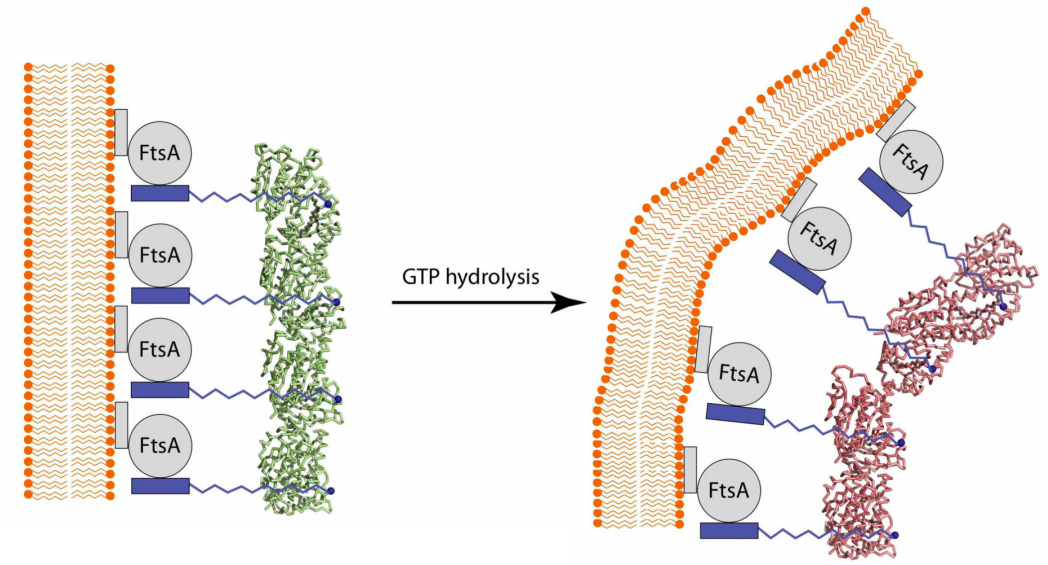

Figure 20: The transfer of the force of polymer bending through membrane anchor proteins may cause deformation of the inner plasma membrane (108).

Molecular dynamics simulation of the *Methanococcus jannaschii* FtsZ dimer also indicated that there was little difference between the individual monomer structures when bound to GTP or GDP (109). However, the GDP-bound dimer lost some monomer-monomer contacts compared to the GTP-bound dimer and thus was less stable. The "top" monomer tilted relative to the "bottom" monomer with GDP bound at the interface. When dimers were used to build larger filaments, the GDP-bound filament was more curved than the GTP-bound filament. The GDP-bound interface could exist in either the GDP-open or the GDP-closed state but GTP-bound interfaces existed exclusively in the GTP-closed state. Transitions from closed to open were estimated to produce 20–30 pN of force per FtsZ monomer. Significantly, the GTP-bound polymer was able to generate a smaller force of 10 pN in the absence of GTP hydrolysis (109).

The generation of a small pinching force by FtsZ in the GTP-bound state supports a mechanism in which FtsZ may partially constrict the membrane independent of GTP hydrolysis, as was observed in the reconstitution experiments (99–102). Full constriction of the membrane may require the additional force of the conversion of the FtsZ dimer interface from a closed to an open conformation following GTP hydrolysis. Furthermore, the role of GTP-hydrolysis may be to increase the likelihood of the dissociation of the FtsZ-FtsZ

interface, which may increase the turnover rate. This may allow the continuous formation of gaps in the Z-ring structure, which may then be closed as constriction proceeds. Indeed, fully closed Z-rings were shown to be blocked for further division (101).

In addition to the contractile mechanism of the Z-ring, peptidoglycan synthesis may contribute to the inward force that drives cytokinesis (69). For example, Meyer *et al*. found that peptidoglycan synthesis was localised to the leading edge of the engulfing membrane in the sporulation process of *B. subtilis* and that peptidoglycan synthesis provided the mechanism for membrane migration. They suggested that peptidoglycan synthesis may also be required to drive the membrane invagination that occurs in cell division (22).

However, it is argued that peptidoglycan remodelling is not required as a driving force for cytokinesis in *E. coli* since studies have shown that cell division continues in cells lacking certain proteins of the peptidoglycan remodelling machinery (110). For example, Denome *et al*. reported that *E. coli* mutants lacking various combinations of up to 8 PBPs (PBP1A, PBP1B, PBP4, PBP5, PBP6, PBP7, AmpC, AmpH and DacD) were viable and their growth rates, measured by the optical density at 550 nm, were equivalent to wild-type cells (111). Similarly, in a separate study by Heidrich *et al*., mutants of *E. coli* lacking the 6 lytic transglycosylase genes (*sltY*, *mltA*, *mltB*, *mltC*, *mltD* and *emtA*), or the 3 periplasmic amidase genes (*amiA*, *amiB* and *amiC*) or the 3 endopeptidase genes (*mepA*, *dacB* (PBP4) and *pbpG* (PBP7)) were shown to be viable. The growth rates, measured by the optical density at 578 nm, were unimpaired for the mutant cells, with the exception of cells lacking both the periplasmic amidases and the endopeptidases for which growth was inhibited (112).

However, it should be noted that there is significant redundancy of function. Therefore, it is possible that an essential function for the generation of force by peptidoglycan remodelling is provided by one or more other enzymes that are still active in the deletion mutants. In addition, although the mutant cells were viable in the work of Heidrich *et al*., a mutant phenotype was observed. The cells grew as filamentous chains with 3–100 cells per chain, dependent on the precise mutation. Therefore, cell division was impaired in these cells (112).

Direct evidence for the contribution of force by peptidoglycan synthesis is as yet lacking. It is difficult to separate the individual contributions made by

the Z-ring, and by the peptidoglycan synthesis enzymes PBP1A/PBP1B, PBP2 and PBP3 since their activities are all essential to cell viability (34). However, there is evidence that the constriction of the cell membrane and that of the peptidoglycan cell wall are uncoupled in some species (113,114). This could indicate that the Z-ring contraction force is required for membrane contraction, whereas the force of peptidoglycan constriction is provided by the PBPs. Specifically, Daniel *et al*. found that in *B. subtilis* cells depleted of PBP2B, cell membrane invagination proceeded to completion whereas cell wall synthesis stalled (113). In addition, Morlot *et al*. reported that the constriction of the Z-ring precedes the constriction of the PBPs in *S. pneumoniae* with a time delay of 5 minutes, which corresponds to a seventh of the generation time. They suggest that the assembled divisome complex separates into two or more subcomplexes which then constrict independently (114).

5.2.6 Control of FtsZ polymerisation and Z-ring localisation

The intracellular concentrations of FtsZ and its two membrane-anchoring proteins FtsA and ZipA have been shown to remain constant throughout the cell cycle (80). Therefore, the temporal control of FtsZ polymerisation and the spatial restriction of Z-ring formation to the midcell must depend on the interaction of FtsZ with other intracellular factors. A set of proteins has been identified including both positive and negative regulators of FtsZ activity and it is thought that additional factors remain to be discovered (115,116).

In *E. coli*, the expression of the SulA protein is induced on detection of DNA damage as part of a systematic stress response, referred to as the SOS response (117,118). The SulA protein inhibits the formation of the Z-ring to prevent cell division while the detected DNA damage is repaired (118–121). In a co-crystallisation study of the FtsZ and SulA proteins of *P. aeruginosa*, SulA was shown to bind to a surface of the C-terminal domain of FtsZ that contains the T7 loop and so the binding of SulA prevents FtsZ polymerisation (70). SulA has a half-life in the cell of just 1.2 minutes in *E. coli* (122). Therefore, once the DNA damage is resolved and the *sulA* gene is no longer expressed, recovery of cell division function is rapid (117,122).

In contrast to the inhibition of FtsZ polymerisation by SulA, which is induced only under certain conditions, there are at least two systems in continuous operation to restrict the formation of the Z-ring to the midcell. First, the Min system of proteins blocks Z-ring formation at the cell poles. Deletion of the *min* operon causes the "minicell phenoptype" where division at the cell poles generates small, anucleate cell bodies. The cells that retain the DNA are multi-nucleoid rods that are longer than wild-type cells (123). This suggests that the division machinery is limited to a single site per cycle (124,125).

The *min* operon encodes three Min proteins, MinC, MinD and MinE (126). MinD accumulates on the cell membrane within one half of the cell only and appears to oscillate from one half of the cell to the other, from pole-to-pole, in a cycle of membrane association and dissociation. On dissociation, the MinD polar cap shrinks towards the pole then re-accumulates from the opposite pole. The protein remains in one half of the cell for 10–30 seconds only. The oscillation of MinD is dependent on the presence of MinE and the ratio of MinD to MinE determines the oscillation cycles time (127).

MinE has been shown to accumulate into an annular structure at or near the midcell and to promote the dissociation of MinD from the membrane as a wave running from the midcell towards the cell pole. The accumulation of MinD at the opposite pole then follows and MinE reforms the ring at or near the midcell and then moves towards the opposite cell pole (128).

MinC follows the oscillation pattern of MinD but is not required for the establishment of the pattern of MinD and MinE (129). MinC is the effector of the Min system and has been shown to inhibit the polymerisation of FtsZ *in vitro* (130). Due to the spatial oscillation of the system, the time-averaged concentration of the inhibitor MinC is lowest at the midcell allowing FtsZ polymerisation and therefore Z-ring formation in this region only (129).

An overview of the oscillatory mechanism of the Min system is given in Figure 21. The Min proteins represent an example of self-organisation: a system that can establish a spatial pattern from random fluctuations in a homogenous solution, by coupling to nucleotide hydrolysis (126). MinD binds to ATP in the cytosol then dimerises and binds to the cell membrane (131,132) via a conserved C-terminal membrane targeting sequence that forms an amphipathic helix (133,134). MinD then recruits MinC from the cytosol (135). MinE subsequently

binds to the membrane-bound MinD which causes the release of MinC (136) and a 10-fold increase in the ATPase activity of MinD. ATP hydrolysis by MinD leads to its release from the membrane (135). MinE is then able to rebind to more MinD in its immediate vicinity but the released MinD must undergo nucleotide exchange before it rebinds to the membrane. This time delay is thought to underpin the oscillation pattern since MinD is able to diffuse through the cytosol while adenosine-5'-diphosphate (ADP)-bound (126,137).

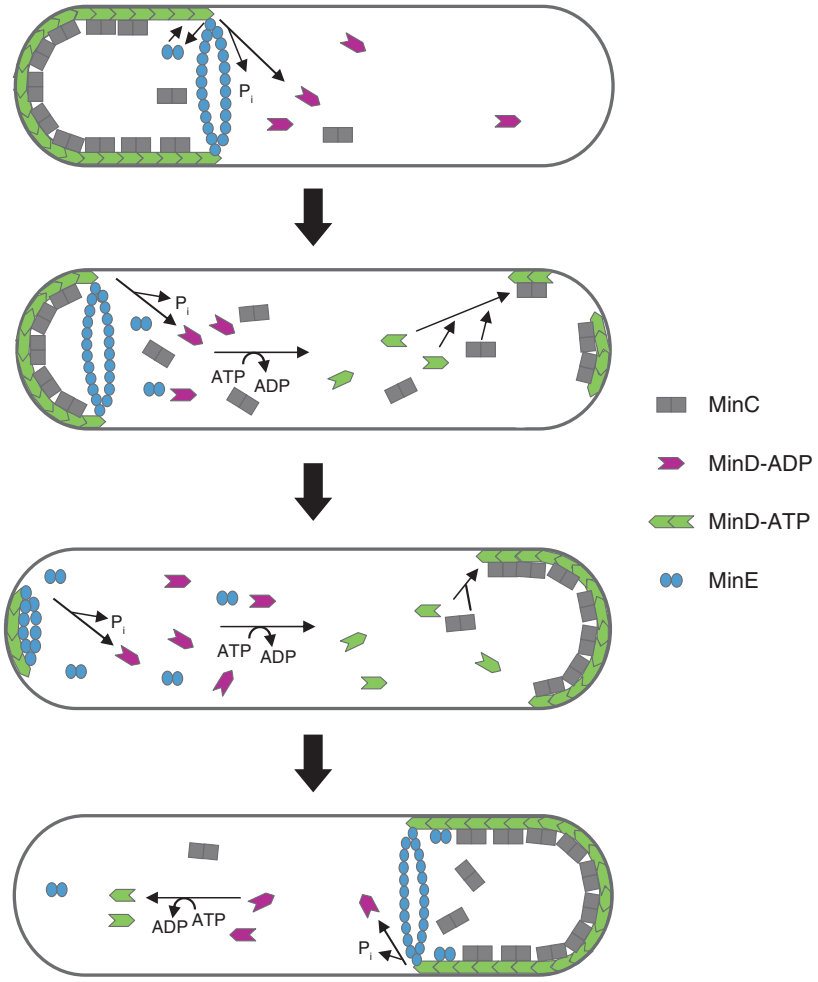

Figure 21: MinCDE oscillation in *E. coli*. MinD-ATP binds to the cell membrane as a dimer and recruits MinC. MinE forms a ring structure close to the midcell and causes the dissociation of MinC from MinD and an increase to the rate of ATP hydrolysis by MinD. MinD-ADP dissociates from the membrane. MinE rebinds to adjacent MinD and continues towards the cell pole. Nucleotide exchange in the cytosol allows MinD to reaccumulate at the opposite cell pole. The MinE ring reforms close to the midcell and the process is repeated towards the other cell pole (126).

The second mechanism known to restrict the localisation of the Z-ring is nucleoid occlusion (NO), which describes the inhibition of Z-ring formation in regions of the cell that contain the genetic material, referred to as the nucleoid. It is essential that chromosome replication and segregation are complete prior to cytokinesis else the DNA may be severed by the Z-ring on contraction (138). The *B. subtilis* protein Noc was the first nucleoid occlusion factor found (139) and SlmA was subsequently identified in *E. coli* (140), although the two proteins have no sequence or structural similarity and they contain different DNA-binding domains (138).

Noc and SlmA localise to their respective DNA consensus sequences that are found throughout the chromosome except in the replication termination region (Ter) and they locally inhibit the polymerisation of FtsZ. Since the Ter region is the last to be replicated and segregated, this suggests a mechanism by which the near completion of chromosome segregation is indicated: the concentration of the NO factor at the midcell region falls as the chromosomes are separated into the two halves of the cell (141,142).

The mechanism of inhibition of FtsZ polymerisation by SlmA is disputed (142–144). However, in the latest study, SlmA was shown to bind to the C-terminal tail of FtsZ and to further interact with FtsZ causing polymer destabilisation and breakage of the filament (145).

An additional DNA-binding protein, MatP has been shown to play a role in the positioning of the Z-ring in *E. coli*. It binds as a dimer to 23 *matS* DNA sequences within the Ter region of the chromosome (146). The MatP protein provides a link between chromosome segregation and cell division as it has been shown to interact with ZapB, in the presence of ZapA to provide a positive signal for Z-ring localisation (147).

5.2.7 FtsZ as an antibacterial target

An ideal antibacterial target is essential to life, is well conserved across a range of pathogens with little functional redundancy and has no homologue in mammalian cells (7). FtsZ is an ideal candidate as it is essential to life and is well conserved across most bacterial species. It is the first protein to localise to the midcell and is required for the downstream recruitment of all other cell division proteins (13). Therefore, an inhibitor of the function of FtsZ is likely to be highly toxic to the division process. Although FtsZ is a structural homologue of eukaryotic tubulin, there is expected to be sufficient difference in the amino acid sequences that it should be possible to design inhibitor molecules specific to FtsZ (18). A drug molecule could block FtsZ polymerisation by competition with GTP at the GTP-binding pocket. However, this strategy risks toxicity to other processes requiring GTP binding such as protein synthesis, signal transduction, and tubulin polymerisation in mammalian cells. Alternatively, a drug that mimics the SulA:FtsZ interaction at the T7 loop of FtsZ could block FtsZ polymerisation. A drug that stabilises polymers to prevent subsequent depolymerisation, or one that blocks the interaction of FtsZ with its binding partners through its C-terminal tail could also be toxic and active as an antibacterial agent (18).

The discovery of a specific inhibitor of FtsZ function is only part of the process, however. The drug pharmacokinetics, as well as access of the drug to the target in cells are issues to be addressed in drug development (7). This stage of the drug design process suffers from poor follow-up of previously reported inhibitors in the literature (148).

To date there have been several examples of success in the search for small molecule inhibitors of FtsZ. A selection of compounds found to have anti-FtsZ activity is given in Figure 22. Both naturally-derived and synthetic inhibitors have been identified using whole-cell filamentation tests, high-throughput FtsZ *in vitro* assays, as well as computational and structure-based design initiatives. Although an antibacterial drug active against the cell division machinery is yet to reach the market, the examples below demonstrate the potential for exploitation of this system in the design and development of the antibacterial drugs of the future (18,149).

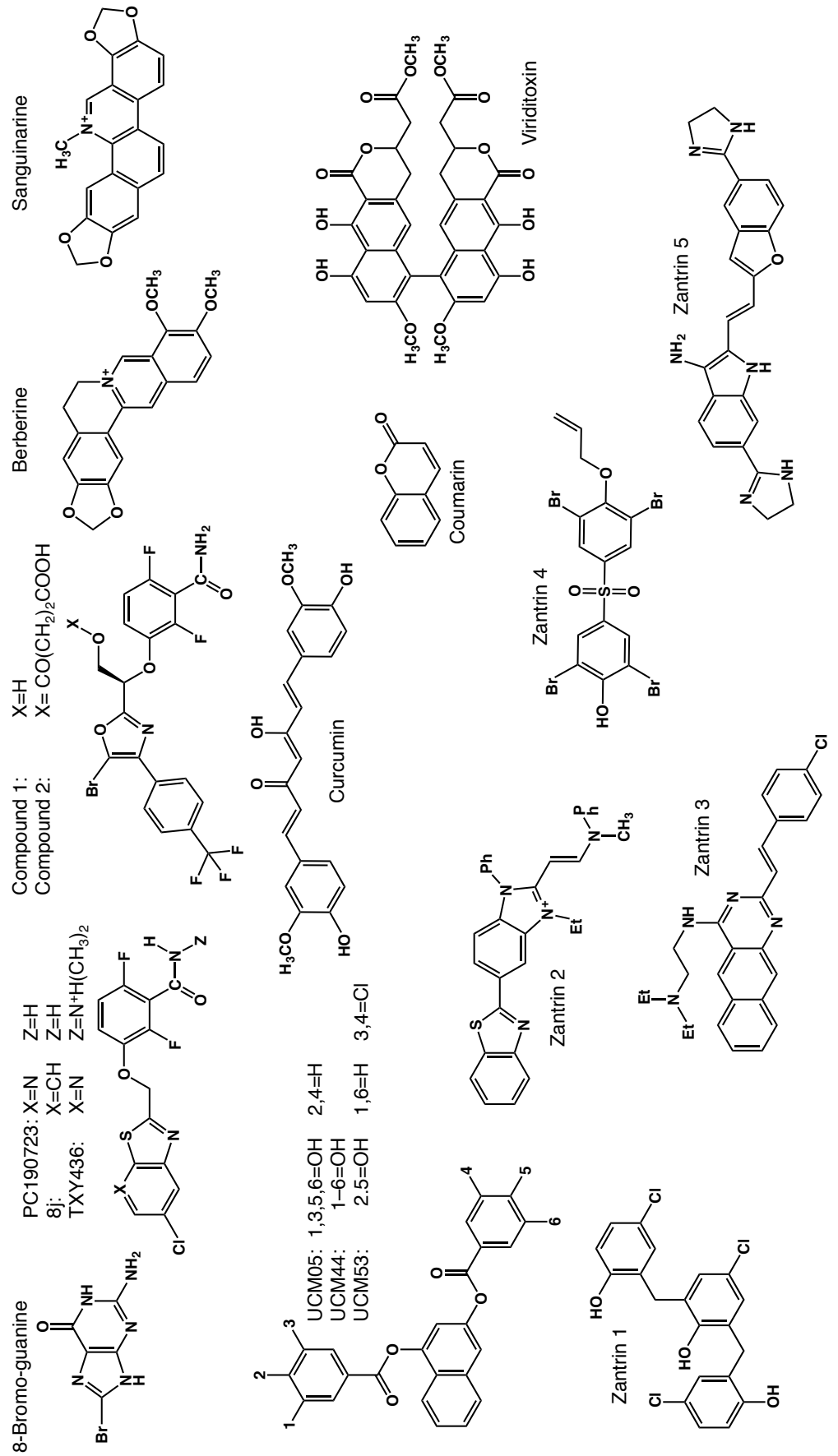

Figure 22: Small molecule inhibitors of FtsZ (149).

To block the GTP-dependent polymerisation of FtsZ, C8-substituted GTP analogues were tested and were shown to inhibit FtsZ polymerisation *in vitro* (150,151). The small substitutions did not inhibit tubulin assembly (151). Unfortunately, the C8-substituted guanine, guanosine, guanosine-5'-monophosphate (GMP) and guanosine-5'-triphosphates were later found to be ineffective antibacterial agents against *E. coli*, despite the strong inhibition of FtsZ polymerisation *in vitro* (152). As an alternative approach to blocking the N-terminal FtsZ polymerisation surface, Sorto *et al*. reported the design of T7-loop mimics by *in silico* docking of compounds into the T7 binding region of the SulA:FtsZ co-crystal structure from *P. aeruginosa* (70). The compounds were synthesised and work to test the activity is ongoing (153).

An inhibitor of ADP-ribosyltransferase, 3-methoxybenzamide (3-MBA), was found to cause filamentation of *B. subtilis* but the phenotype could be suppressed by mutations in the *ftsZ* gene. This suggested that the target of 3-MBA was the FtsZ protein (154). Subsequently, 500 analogues of 3-MBA were synthesised and tested for antibacterial activity against *B. subtilis* and *S. aureus*. Of these, the difluorobenzamide PC190723 (3-[(6-chloro[1,3]thiazolo[5,4-b]pyridin-2-yl)methoxy]-2,6-difluorobenzamide) was a potent inhibitor of both species and of single-drug-resistant and multi-drug-resistant *S. aureus* strains. The compound was also shown to be non-toxic to human hepatocytes (155,156). Furthermore, in a mouse model of *S. aureus* infection, 100% of mice survived with a single intravenous dose of PC190723 compared to a survival rate of 0% for infected mice without treatment (155).

In later work, PC190723 was shown to be more effective than vancomycin and linezolid against MRSA growth, with a minimum inhibitory concentration of 0.2 μg/mL, compared to 2 μg/mL for vancomycin and linezolid. PC190723 was also shown to act synergistically with imipenem and other β-lactam antibiotics *in vivo*. In a mouse model of MRSA infection, neither imipenem nor PC190723 (at higher doses than used in the original study) resolved the infection as a single agent. However, when co-administered, a significant reduction in the number of colony forming units in mouse thigh homogenates was observed (156).

FtsZ-CFP and GFP-FtsZ fusion proteins were shown to be mislocalised in MRSA and *B. subtilis* respectively on treatment with PC190723 and multiple

rings and arcs of FtsZ, not restricted to the midcell, were observed (155,156). PC190723 was shown to stabilise polymers of *B. subtilis* and *S. aureus* FtsZ and to reduce their GTPase activity. Curved structures, bundles, torroids and helices of FtsZ were also observed *in vitro* using electron microscopy. These effects were not observed for FtsZ purified from *E. coli* which is not susceptible to growth inhibition by PC190723 (155,157).

The binding of PC190723 to *S. aureus* FtsZ stabilises the active form to promote polymerisation. This reduces the concentration required for polymerisation and leads to loss of the critical concentration and co-operativity of FtsZ polymerisation seen in the absence of the compound (158). The crystal structure of *S. aureus* FtsZ in complex with PC190723, shown in Figure 23, revealed that the compound binds in the cleft between the interdomain helix H7 and the C-terminal domain with the benzamide moiety close to the T7 loop. The site is similar to the taxol binding site of tubulin (159).

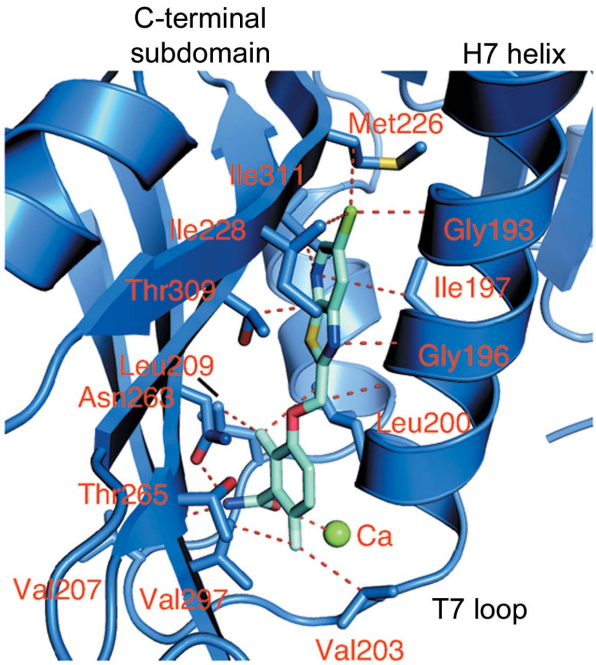

Figure 23: *S. aureus* FtsZ in complex with PC190723. The compound binds in the cleft between the interdomain helix H7 and the C-terminal domain (159).

Due to the low solubility of PC190723, which limits its use as an oral drug, a prodrug derivative referred to as TXY436 was developed. Whereas PC190723 was ineffective as an oral preparation, 100% of methicillin-sensitive *S. aureus* (MSSA)-infected mice that were treated with oral TXY436 survived, as did 67% of mice infected with MRSA, compared to 0% survival without treatment. The prodrug was also shown to be minimally toxic to monkey kidney epithelial cells (160). Compound 8j, shown in Figure 22, is closely related to PC190723 and was found to be more potent (161). An alternative 3-MBA derivative, referred to as compound 1 also displayed antibacterial activity as a single drug. Compound 1 and its succinate prodrug (referred to as compound 2) were both effective in the reduction of bacterial load in the murine model of *S. aureus* infection (162).

Several naturally-occurring molecules have also been shown to inhibit FtsZ activity. For example, in a screen of over 100,000 extracts of microbial fermentation broths and plants, viriditoxin was identified as an inhibitor of the polymerisation and GTPase activity of *E. coli* FtsZ *in vitro*. Viriditoxin was purified from an *Aspergillus viridinutans* fermentation broth and was found to inhibit the growth of all of the drug-sensitive and multi-drug-resistant strains of *Staphylococcus*, *Enterococcus* and *S. pneumoniae* that were tested (163). However, viriditoxin was later synthesised (164) but was found to be inactive against FtsZ from both *B. subtilis* and *E. coli*. The chemical stability of the preparation was thought to be an issue (149).

Plant-derived compounds have also been reported to be active against FtsZ including curcumin (1,7-bis-(4-hydroxy-3-methoxy-phenyl)hepta-1,6-diene-3,5-dione) which inhibits the growth of *E. coli* and *B. subtilis* and acts to disrupt FtsZ polymerisation by an increase in the rates of GTPase activity and the subsequent depolymerisation (165). However, curcumin has also been shown to inhibit other proteins including FabI in *E. coli*, as well as HIV integrase and human glyoxylase I and monoamine oxidase. This suggests that the compound is a promiscuous inhibitor and therefore may not be useful as a drug lead (7).

The plant-based, polyphenol coumarins were also shown to inhibit *B. subtilis* cell division and to inhibit *E. coli* FtsZ polymeristaion and GTPase activity *in vitro*. Docking studies suggested that they bind to the T7 loop of FtsZ.

These compounds were also shown to be non-toxic to NIH/3T3 mouse embryonic fibroblasts and to human embryonic kidney cell lines (166).

Berberine has also been shown to inhibit the growth of several species including, *E. coli*, *S. aureus* (including MRSA), *Streptococcus pyogenes*, *Vibrio cholerae*, *Clostridium perfringes* and multi-drug-resistant *M. tuberculosis*. The compound inhibited *E. coli* FtsZ polymerisation and GTPase activity by competition with GTP for binding to FtsZ (167). Plant compound sanguinarine was also found to inhibit the growth of several Gram-negative and Gram-positive species and to inhibit FtsZ polymerisation and GTPase activity *in vitro*. However, sanguinarine also inhibits tubulin *in vitro* and may be toxic to eukaryotic cells (168). Finally, cinnamaldehyde also inhibited *E. coli* FtsZ polymerisation and GTPase activity *in vitro* and was antibacterial against *E. coli* and *B. subtilis* (169).

Several high-throughput screens of chemical libraries have also yielded small molecule hits for activity against FtsZ. For example, the 5 chemically distinct Zantrins were identified in a screen of over 18,000 chemicals for inhibition of the GTPase activity of *E. coli* FtsZ. These compounds were also shown to inhibit the GTPase activity of FtsZ from *M. tuberculosis*. Zantrins Z1 and Z4 were shown to decrease the number and length of *E. coli* FtsZ filaments using electron microscopy, whereas, Z2, Z3 and Z5 stabilised the filaments. Growth of *P. aeruginosa*, *S. pneumoniae* and *Bacillus cereus*, was abolished by Z1. Z1 and Z2 killed *E. coli*, as did Z3 and Z5 in an *E. coli* strain lacking the major drug pump AcrAB. Z1–Z3 were active against *Shigella dysenteria* and *Vibrio cholera* and Z1–Z4 were active against MRSA. Zantrins were also shown to perturb Z-ring assembly in *E. coli* (170).

Competitive ligands UCM05, UCM44 and UCM53 were also identified from a chemical library screen but using FtsZ from *B. subtilis* and detection of competitive binding to FtsZ with mant-GTP. UCM53 was found to be active against *B. subtilis*, and drug-resistant strains of *S. aureus*, as well as ampicillin- and levofloxacin-resistant *Enterococcus faecium* (171). Finally, in a cell filamentation screen of 151 rhodanine compounds, compound CCR-11 was identified as an inhibitor of *B. subtilis*. CCR-11 was subsequently shown to cause mislocalisation of Z-rings in cells and to inhibit the assembly and GTPase activity of *B. subtilis* FtsZ *in vitro* (172).

There has also been some limited success in the search for small molecule inhibitors of the FtsZ:ZipA interaction. However, protein-protein interactions are difficult to disrupt using small molecules since large areas of the two protein surfaces are buried in the interaction (173). In a high-throughput screen of 250,000 compounds, 29 hits were found that compete for the FtsZ binding site of ZipA. The most successful competitor was co-crystallised with ZipA from *E. coli* and was found to bind to the FtsZ-binding cleft of ZipA (174). Lead compounds that were found to bind to different but overlapping sites of the ZipA cleft were chemically combined and the hybrid molecules were found to have increased potency. However, their antibacterial activity against Gram-positive bacteria suggests that the compound is acting on additional cell targets since ZipA homolgues have not been found in these species (175).

An NMR-based screen was also used to screen 825 compounds for binding to ZipA. 7 compounds showed binding to residues at the ZipA:FtsZ interface. From the highest affinity hit, a further 87 chemically similar molecules were tested with some improvement to ZipA affinity. However, the affinity was still too low at 2 mM (173).

5.2.8 The Z-ring membrane anchor proteins ZipA and FtsA

FtsZ is the first protein to localise to the midcell and is required for the localisation of all other essential and non-essential divisiome proteins (10). In the Gammaproteobacteria, FtsZ polymers are anchored to the inner membrane by the bitopic (single transmembrane domain) inner membrane protein ZipA, which localises to the Z-ring simultaneously to FtsZ and remains throughout the cell constriction (176). ZipA was shown to induce bundling of FtsZ polymers *in vitro* (177) but with no effect on the GTPase activity of FtsZ (178). In addition to its role as an FtsZ anchor protein, ZipA is required for the midcell localisation of the late division proteins (17).

The atomic-resolution structure of the C-terminal domain of ZipA has been solved by both X-ray crystallography and NMR spectroscopy (179,180). A 6-stranded antiparallel β-sheet forms a 20-Å cavity in which the C-terminal tail of FtsZ binds (180).

In addition to the membrane-anchoring function of ZipA, the C-terminal tail of FtsA contains a well-conserved amphipathic helix that acts as a membrane targeting sequence to tether FtsZ to the inner membrane (181). FtsA is also recruited to the midcell simultaneously to FtsZ (182) and while the Z-ring still forms in its absence, FtsA is essential for the downstream recruitment of the late division proteins and is therefore also essential to cell division (17,183).

FtsA is a member of a large family of ATPases and is an actin homologue (184). However, the existence of FtsA polymers *in vivo* and the role of the ATP-binding activity are yet to be demonstrated. An ATP-dependent polymerisation of FtsA from *S. pneumoniae* was reported to occur *in vitro* but no associated ATPase activity was detected (185). In contrast, an ATPase activity of an FtsA dimer from *B. subtilis* was found (186). In a crystallography study using FtsA from *T. maritima*, when co-crystallised with the non-hydrolysable ATP analogue adenosine-5'-[γ-thio]triphosphate (ATP-γ-S), the FtsA crystal contained continuous protofilaments (187).

In a reconstitution study, purified, fluorescently-labelled FtsA and FtsZ were applied to supported lipid bilayers and their positions were followed using total internal reflection fluorescence microscopy (188). In the presence of GTP and either ATP or ATP-γ-S, FtsZ formed bundles of polymers that moved across the bilayer in one direction. Vortices with a fixed diameter of 1.09 ± 0.24 μm also formed that always rotated clockwise, when viewed from the membrane. This dynamic activity of FtsZ was specific for the presence of FtsA; the large-scale organisation as seen for FtsA did not occur when FtsA was replaced with ZipA (188). This work suggests that FtsA has a specific role in the modification of the activity of FtsZ as compared to ZipA.

5.3 An introduction to mathematical modelling in biology

A model is merely a description of a system of interest. In a mathematical model, the system is described in terms of a set of algebraic or differential equations, which may subsequently be solved (189). Both the current knowledge of the system in question, and the scientific goal of the modelling effort will direct the mathematics used. The model may be continuous or discrete, static or

dynamic, spatially heterogeneous or spatially homogeneous, deterministic or stochastic. The mathematical descriptions may be derived from theory, based on a mechanistic insight of the system, or they may be phenomenological, that is based on descriptions of empirical observations rather than on a theoretical understanding (189).

In general, the aim of the mathematical modelling falls into one of three distinct categories, as shown in Figure 24. In prediction, for a given input and a given system, the expected output is generated. This output may then be compared to novel experimental data. In control, for a given system and a prescribed output, the aim is to define the required input. Finally, in identification, for a given input that produces a known output, the aim is to define the system (190).

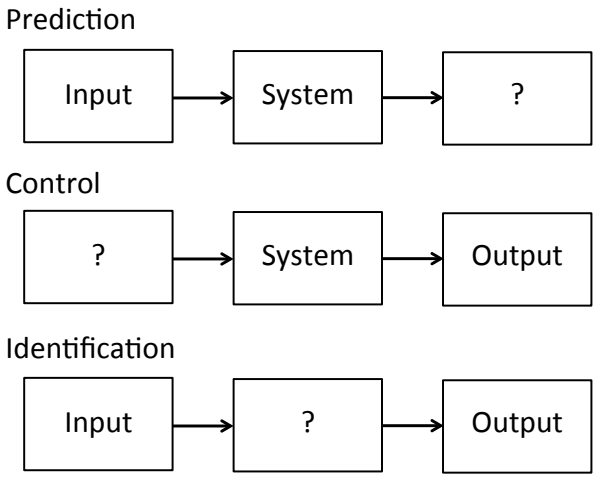

Figure 24: The three general problem types addressed with mathematical modelling. Prediction: The output is generated. Control: The input is found. Identification: The system is defined. Adapted from Doucet and Sloep (190).

The goal of the modelling effort will also determine the appropriate balance of three key factors. First is model precision, which refers to the accuracy of the model prediction compared to the real system (rather than the statistical concept of precision as the variability of a set of measurements). Realism is the second key factor, for which in addition to the generation of accurate predictions, the model equations must also be "correct" in that they reflect the true interactions between the objects of the real system. While

precision and realism are desirable, generality is also sought, which comes with model simplicity. There must always be a compromise. A precise, realistic model loses generality and can be used to describe and investigate specific biological systems or scenarios. Conversely, a simple, general model may be used to explore the behaviour of a variety of systems but it will lack predictive power for each individual scenario (191).

Mathematical modelling in biology is complicated by the large number of interacting molecules in any given system, the significant redundancy of function, and the quality of available experimental data (192). Therefore, the aim is to capture the key interactions that determine the system output rather than to explicitly account for each individual molecule. Simplicity is also sought for the ease of handling or solving of the equations. For a complex model with a greater number of variables and parameters, a better understanding of the system is required *a priori* and a greater volume or complexity of data is required for subsequent parameter fitting. When the model output does not fit the experimental data gathered, it can be difficult to determine which parameters or variables should be changed within a complex model in which several variables and parameters generate a single prediction. Furthermore, a model with a large number of variables and parameters can be forced to fit any data set. A good fit therefore does not indicate that the model reflects the system itself or that the parameter values are meaningful (190).

5.3.1 Mathematical models of FtsZ in the literature

There are several mathematical descriptions of FtsZ polymerisation and Z-ring formation available in the literature. Chen *et al*. used a set of ordinary differential equations (ODEs) to describe the activation, dimerisation and elongation of FtsZ over time (74). The equations were numerically solved to simulate the *in vitro* polymerisation of FtsZ on the addition of GTP. Multiple elongation equations were defined for the sequential addition of FtsZ monomers up to a subunit length of 6. On further elongation of the hexamer, the molecule was defined as a filament. Filaments further interacted with monomers, but the individual filament lengths were not explicitly followed. The model assumed that

FtsZ forms single thickness filaments, and it did not include the end-to-end annealing of FtsZ oligomers or the kinetics of GTP hydrolysis and the subsequent polymer destabilisation (48,74).

Initially, the equations were solved and the rate constants were determined by fitting to polymerisation data from a fluorescence-based assay of the FtsZ-L68W mutant. On polymerisation of the mutant, there is a 2.5-fold increase in the fluorescence at 350 nm due to the change in the environment of the tryptophan residue. The model fitting suggested that the polymerisation of FtsZ is nucleated by the formation of a weak dimer. However, using sedimentation assays, it was shown that polymerisation of the mutant protein has a lower critical concentration than that of the wild-type FtsZ protein. Therefore, it was unclear if the behaviour of the mutant protein could be used to infer the behaviour of the wild-type (74).

In a follow-up study, a FRET FtsZ polymerisation assay was developed in which a single cysteine residue was introduced for the covalent attachment of either the donor or the acceptor fluorophore to the FtsZ monomer. Although there were significant differences between the fitted rate constants from the FtsZ-L68W mutant fluorescence data and those from the FtsZ-F268C mutant in the FRET assay, the results again indicated the formation of a weak dimer nucleus (48). This is an example of the implementation of a model for identification. For a given input, that is the starting concentrations of FtsZ and GTP, and an output determined experimentally, the model is used to elucidate the details of the system.

With a different approach to the investigation of co-operative FtsZ polymerisation, Huecas *et al*. described a static, equilibrium model of FtsZ polymerisation in which the monomer must be activated, prior to dimerisation and elongation (77). The analytical solution for the total FtsZ concentration was identical to Oosawa's equation for condensation polymerisation (193). This suggested that FtsZ polymerisation could be co-operative for a strictly linear FtsZ polymer (77). Miraldi *et al*. used a similar description of FtsZ polymerisation at equilibrium (84). However, in contrast to the Huecas model in which only activated monomers are able to interact, Miraldi *et al*. explicitly modelled the polymerisation of both activated and non-activated monomers. The non-activated and activated monomers were assigned variables L and H

respectively with an equilibrium constant of activation of K_c. Four separate equilibrium constants were defined, K_{HH}, K_{LH}, K_{HL} and K_{LL}, one for each of the four possible dimer interactions. The values of the 5 equilibrium constants were systematically varied for a given total protein concentration and the maximum monomer concentration, and the polymer concentration and the degree of co-operativity were calculated using matrix algebra (84).

In agreement with the result of the simpler model of Huecas *et al*. (77), co-operativity was predicted when the non-activated monomer is more stable than the activated monomer (that is when the equilibrium constant for monomer activation is much less than 1), and when the favourable interaction of two activated monomers compensates for the energetic cost of activation. The greatest co-operativity was observed when the equilibrium constant for the dimerisation of activated monomers was large and the other 4 equilibrium constants were small (84). However, this appears to contradict the conclusion of the kinetic modelling work by Chen *et al*. that suggested that the dimer is unstable (48,74).

The evaluation of a different parameter set suggested that co-operative assembly would also be observed for a segregated assembly mechanism in which polymers form of one type of monomer only, either non-activated FtsZ or activated FtsZ (K_{LH} and K_{HL} set to 0). However, this also required that the equilibrium constants for both the monomer activation and the polymerisation of non-activated monomers were small compared to that for the polymerisation of activated monomers. The model does not suggest a unique mechanism to account for the observed behaviour of FtsZ *in vitro* (84).

As demonstrated by these examples, in identification, there may be several different mathematical models that generate the required output from a given input. Therefore, a good fit does not necessarily indicate that the model is a realistic representation of the system itself (190).

Other mathematical models have been designed to describe the formation of the Z-ring *in vivo*. For example, Allard and Cytrynbaum presented a kinetic model for the binding of FtsZ polymers from a distribution of sizes in the cytoplasm into the membrane-bound Z-ring (194). On the assumption that polymers in the Z-ring are held by lateral interactions, the binding surface was modelled as the outer edges of a barrel-shaped Z-ring. It was assumed that the

cytosolic pool of polymers contained only GTP-bound FtsZ but GTP hydrolysis was included for FtsZ within the Z-ring. The total force for a given Z-ring radius and FtsZ composition was generated based on a "hydrolyse and bend" contraction model in which it was assumed that GTP-bound interfaces are straight and that GDP-bound interfaces are bent at 22° (106). It was assumed that only GDP-bound FtsZ subunits at the end of a filament can dissociate from the Z-ring and return to the cytoplasmic pool (194).

The solutions of the equations defined by Allard and Cytrynbaum indicated that for a cell radius between 25 nm and 400 nm, the Z-ring generates a force significantly larger than the 8 pN that was calculated by Lan *et al*. as the force required to deform the bacterial cell wall (104). The large force is a result of the prediction of a high proportion of FtsZ subunits in the Z-ring in the GDP-bound state (0.53), since GDP-bound subunits are assumed to bend and to only dissociate from the filament ends. Although the restriction of subunit dissociation to the filament ends seems in contrast to the rapid turnover of subunits in the Z-ring observed *in vivo*, in support of the model assumptions, the average residence time in the Z-ring according to the model of 12 seconds is in agreement with the average time predicted by FRAP of 10–30 seconds (194).

In later work, Lan *et al*. took an entirely different approach (195). The inner membrane was conceptually divided into grid squares where each square may be empty or occupied by ZipA, FtsA, FtsZ, both ZipA and FtsZ, or both FtsA and FtsZ. The protein dynamics were captured by Monto Carlo moves and a change to the protein positions over the grid was accepted if the energy change in moving from the previous configuration to the new configuration was favourable. The energy was calculated based on the interactions of FtsZ with ZipA and with FtsA, and on the energy of longitudinal and lateral interactions for adjacent FtsZ-occupied grid squares (195).

ZipA and FtsA remained membrane-bound within the grid and their free diffusion was modelled as movement between grid squares. FtsZ from a pool of cytoplasmic monomers moved onto the membrane by the addition of FtsZ to a grid square occupied by ZipA or FtsA or to a grid square adjacent to another square occupied by FtsZ. Once membrane-bound, FtsZ monomers then moved between grid squares. FtsZ monomers were also released from the membrane

grid back into the cytoplasmic pool. The model was limited to the movement of individual protein monomers, which oriented at random on the membrane (195).

To model Z-ring contraction, the lateral interactions were assumed to become more favourable and the lateral bond energy was switched from $\Delta G = -0.2\ k_B T$ to $\Delta G = -1\ k_B T$. However, the biological relevance and the mechanism of this switch are unclear (105). In addition to the Monte Carlo moves of the formation of the Z-ring, in the contraction model, if an FtsZ monomer attempts to move to a square that is already occupied, the model will insert a new row and the Z-ring radius increases by 1 grid square or 5 nm. When a monomer is released into the cytoplasm, if an empty row is generated it is deleted and the radius decreases by 5 nm. Row deletion and therefore Z-ring contraction is favoured, since the deletion of an empty row is likely to introduce new FtsZ-FtsZ interactions, compared to row addition which may disrupt FtsZ-FtsZ interactions to allow for the insertion of a single FtsZ subunit (195).

A model published by Surovtsev *et al*. in 2008 included mathematical descriptions of the polymerisation of FtsZ, the formation of the Z-ring at the midcell and the contraction of the Z-ring in cytokinesis (196). The ODEs for FtsZ polymer kinetics included the end-to-end annealing of polymers, the hydrolysis of GTP to GDP and the subsequent polymer dissociation. In contrast to the model of Allard and Cytrynbaun (194), dissociation following GTP hydrolysis was assumed to occur at the same rate for all FtsZ-FtsZ interfaces within the polymer. The equations were defined and numerically solved for polymer lengths of up to 150 subunits (196).

The model of linear polymerisation represented a significant step forward in the mathematical modelling of FtsZ *in vitro*. However, it was also assumed that *in vivo* the Z-ring is composed of long, single-stranded FtsZ filaments that anneal end-to-end to form closed polymers. The model did not extend to a maximum FtsZ polymer size that could feasibly span the entire cell circumference (based on the cell radius of 0.4 μm and the diameter of a single FtsZ subnunit of 4 nm, a subunit length of 628 would be required), but it was assumed that the model solutions qualitatively represented the formation of the Z-ring *in vivo* (196). This FtsZ cyclisation model is in contrast to the current view that the Z-ring consists of short, overlapping FtsZ polymers (98).

In addition, the diffusion of FtsZ in the cell and the binding of FtsZ to the membrane at the midcell were not explicitly modelled. Rather, a polymer containing 3 or more FtsZ subunits was assumed to be in the midcell membrane "reacting zone" and therefore was assumed to be within the Z-ring. The concentrations were scaled based on the midcell reacting zone volume (the product of the cell circumference, 2.5% of the cell length and the size of an FtsZ dimer of 8 nm) as a proportion of the whole cell volume. The formation of long polymers in the *in vivo* model solutions is due to the artificial increase in the FtsZ concentration with the confinement of polymers to the midcell volume (196).

The scaling of polymer concentrations also caused a truncation artefact where the average linear polymer length is dependent on the maximum value of the subunit length in the model. For example, for a maximum subunit length of 150, as used by Surovtsev *et al*., the average open polymer length is 62 subunits whereas for a maximum subunit length of 200, the average open polymer length is 70 subunits. Inclusion of diffusion of FtsZ throughout the cell removes this truncation artefact and suggests that *in vivo* much shorter polymers than those seen in the Surovtsev model are formed. This again supports the model in which the Z-ring is composed of short polymers.

Following Z-ring formation, the contraction model of Surovtsev *et al*. was based on the optimal cyclisation length being set as equal to the average cyclic polymer length. Since the average cyclic polymer length is slightly lower than the optimum cyclisation length once equilibrium has been reached, setting the optimum length equal to the average length tends to decrease the average length over time. However, to induce significant Z-ring contraction, changes to the conditions were required such as a decrease in the GTP/GDP ratio or a decrease in the rate of FtsZ polymerisation (196). Neither of these has been shown to occur in the initiation of Z-ring contraction *in vivo*. Since the contraction model was based on a decrease in the average length of a set of cyclised polymers, and it is now accepted that the Z-ring is composed of short FtsZ polymers, the model of Surovtsev *et al*. does not reflect the behaviour of FtsZ *in vivo*.

In a follow-up study, Zhang *et al*. used a one-dimensional spatial model of the diffusion and accumulation of FtsZ at the midcell membrane that included the inhibitory effects of the Min system and nucleoid occlusion (197). Using the

reaction-diffusion equations of the Min system previously defined (137,198,199) and a step function to indicate the presence or absence of SlmA, the spatial accumulation of 7 different FtsZ species was modelled over time (197). Short cytosolic FtsZ filaments were evenly distributed along a line in the initial conditions. The short FtsZ filaments bound to the membrane with a specific rate and then interacted longitudinally to form long FtsZ filaments. Short overlapping FtsZ filaments also formed on the membrane due to lateral interactions, with either a single or double overlap. Long FtsZ filaments similarly overlapped. It was assumed that SlmA catalysed the dissociation of long FtsZ filaments to short FtsZ filaments and that MinCD catalysed the loss of FtsZ overlap or lateral interactions (197).

The model simulations demonstrated that the Min system prevents the accumulation of FtsZ at the cell poles. In the absence of the Min system, if the nucleoid occlusion system was active and the nucleoids had segregated, the model solutions resembled the minicell phenotype as the formation of Z-rings was accommodated at both at the midcell and at the cell poles. The formation of a single, precise Z-ring at midcell required both the Min system and nucleoid occlusion (197).

6 Contribution to knowledge of the research reported in this thesis

6.1 Mathematical modelling of FtsZ polymerisation, Z-ring formation and Z-ring contraction

A kinetic model of the formation of the Z-ring was developed with the *in vitro* kinetic model of Surovtsev *et al*. (196) as a starting point. Many of the flawed assumptions of the Surovtsev model were addressed including the removal of FtsZ polymer cyclisation and the inclusion of three distinct cell compartments: the cytosol, the midcell cytosol and the midcell membrane. The diffusion of FtsZ between the two cytosolic compartments was explicitly modelled, which removed the truncation artefact of the Surovtsev model.

The binding of FtsZ polymers in the midcell cytosol to a set of membrane anchor proteins was also included. Theoretically, an FtsZ polymer of length i subunits may bind up to i membrane anchor proteins, since the anchor proteins ZipA and FtsA have been shown to interact with the C-terminal tail of FtsZ (180,200,201). The surface density of the anchor proteins was used to calculate the probability that an FtsZ subunit in a membrane-bound polymer is adjacent to an anchor protein, and the expected number of FtsZ:anchor protein interactions for a given polymer length. The rate equation for the release of FtsZ polymers back into the cytosol was adjusted to allow FtsZ polymers attached by a single membrane anchor to be released.

GTP hydrolysis and subsequent polymer dissociation was included for both cytosolic and membrane-bound FtsZ polymers. For membrane-bound polymers, the probability that each of the resulting FtsZ species was no longer in contact with a membrane anchor was calculated. Release of FtsZ from the membrane into the cytosol was via FtsZ:anchor dissociation events for singly-bound polymers and via GTP hydrolysis and subsequent polymer dissociation.

An *in vivo* contraction model was also developed in which the total tension of the Z-ring was defined, as a function of the midcell radius and the cell surface tension. The maximum tension the Z-ring can withstand at a given radius was also calculated based on the population of FtsZ polymers at the membrane and the force of the interaction between FtsZ and a membrane anchor protein. It was assumed that a difference between these two values can drive contraction at

the midcell, if the maximum tension the Z-ring can withstand is greater than the total tension for the given radius. This assumption lead to the definition of a dimensionless contraction parameter χ, which is equal to the average membrane-bound FtsZ polymer length (in subunits) squared, multiplied by the total number of membrane-bound FtsZ polymers. This contraction parameter is compared to two threshold values, a contraction initiation threshold and a contraction completion threshold. The model is referred to as *Critical Accumulation of Membrane-bound FtsZ Fibres* (CAM-FF).

The result of the modelling effort is a prediction of the division outcome in cells, given a set of kinetic parameters predicted from the experimental literature, and the initial conditions where the cell complement of FtsZ is monomeric, GDP-bound and evenly distributed throughout the cytosol. One of three division outcomes is predicted: i) division proceeds to completion, ii) division is initiated but stalls prior to completion, and iii) division is not initiated. Implementation of CAM-FF for the deletion of either ZipA or FtsA gave predictions in accord with the experimental evidence. That is, on the deletion of ZipA, cell division is not initiated, whereas on the deletion of FtsA, cell division is initiated but stalls prior to completion (202).

In addition to the accurate prediction of scenarios previously reported in the literature, the model solutions have provided further insight to the effect of the inhibition or enhancement of particular biochemical activities, which may be difficult to analyse in isolation through experimentation. For example, the effect of perturbation of the rate constants for GTP binding, FtsZ polymerisation and GTP hydrolysis/FtsZ dissociation were investigated individually. It was shown that measurement of the overall GTPase activity is insufficient to predict cell division behaviour, as is often attempted in the experimental literature (203), since the resulting GTPase activity represents a combination of nucleotide exchange, FtsZ polymerisation, nucleotide hydrolysis and dissociation. Furthermore, it was found that the GTP binding site is a poor antibacterial target site as the affinity for GTP can be significantly reduced with no effect on the predicted outcome of cell division. This may explain why C8-substituted guanine, guanosine, guanosine 5'-monophosphate (GMP) and guanosine 5'-triphosphates have been found to be ineffective antibacterial agents against *E. coli*, despite the C8-substituted GTP analogues displaying strong inhibition of

FtsZ polymerisation *in vitro* (152,204) by competition for the GTP binding site. Based on the solutions of CAM-FF, the T7 loop region is a more effective target site. Indeed, inhibition of the growth of *B. subtilis* by coumarin derviatives and their inhibition of FtsZ polymerisation *in vitro* has been reported (166). Promisingly, *in silico* docking studies suggested that courmarin binds to residues of the T7 loop of FtsZ and prevents FtsZ polymerisation (166).

6.2 A possible explanation of the temperature-sensitivity of the *ftsZ84* mutant

The effect of the *ftsZ84* mutation has been analysed in detail both using CAM-FF and by experimentation. Previously it had not been clear why cells bearing the *ftsZ84* mutation appear to divide normally at 30 °C but are unable to divide at 42 °C. At 42 °C the Z-ring structure is lost and cell division is inhibited, which results in the filamentous phenotype (43,44,205,206). In the initial study of the purified *E. coli* FtsZ84 protein, which contains a single point mutation of glycine at position 105 to serine, a decrease in the GTPase activity of the mutant protein was reported, compared to the wild-type FtsZ protein. In addition, the mutation was found to introduce a significant ATPase activity that was not displayed by the wild-type FtsZ. Significantly, the ATPase activity was temperature-sensitive within the critical range of the switch from normal growth to cell filamentation. A two-fold increase in the ATPase activity was measured at 43 °C, compared to 30 °C (207).

However, since then, the crystal solutions of FtsZ proteins from other species have suggested that the equivalent glycine residue is adjacent to the phosphates of the nucleotide rather than the base (208), and the presence of an ATPase activity has been dismissed as an experimental artifact, perhaps due to contamination of another protein in the FtsZ preparation. However, on implementation of the original kinetic parameters (207) to CAM-FF, the ATPase activity could explain the temperature-sensitivity of the mutant protein. The ATPase activity acquired by the mutant FtsZ protein increases the concentration of the pool of activating nucleotides (GTP and ATP). At lower temperatures where the ATPase activity is low, a functional Z-ring is able to form and

contract. However, at 42 °C the increase in the ATPase rate causes the Z-ring to disassemble and cell division is inhibited.

To further investigate the behaviour of the *ftsZ84* mutant, the wild-type *ftsZ* gene from *E. coli* was cloned, and the wild-type FtsZ and mutant FtsZ G105S proteins were expressed and purified. Following several rounds of purification, and in the absence of major structural reorganisation of the FtsZ protein on introduction of the point mutation, a significant ATPase activity was measured for the FtsZ G105S protein that was absent for the wild-type. The mutation also caused a significant reduction in the GTPase activity, as previously reported in the literature (203,207). This confirms the findings of the original report (207). Further work is now required to elucidate the biochemical mechanism behind the observed catalytic activities.

6.3 Preparation of a set of purified early cell division proteins for reconstitution studies

As detailed in Appendix A, Appendix B and Appendix C, significant progress has also been made towards the production of a set of early division proteins for reconstitution into lipid vesicles. An N-terminal polyhistidine tagged construct of ZapA was designed and produced such that following purification of the protein using immobilised metal affinity chromatography, the polyhistidine tag may be removed by tobacco etch virus (TEV) protease. This results in a ZapA protein with only an additional glycine residue at the N-terminus of the purified protein. This strategy was taken in response to concerns raised by Mohammadi *et al*. (209) on the effect of the polyhistidine tag on the activity of ZapA both *in vivo* and *in vitro*.

An N-terminal polyhistidine tagged ZipA protein was also successfully purified. Styrene maleic acid (SMA) was used as an alternative to detergent for the solubilisation of the *E. coli* cell membranes. Encapsulation of the membrane protein into a styrene maleic acid lipid particle (SMALP) should retain the native lipid environment of the protein and should provide a simple method to reconstitute the protein into a lipid vesicle (210,211).

FtsA was also successfully cloned as an N-terminal polyhistidine tagged construct with the incorporation of a TEV protease cleavage site. As for ZapA,

subsequent removal of the polyhistidine tag following protein purification will leave a single additional glycine residue at the N-terminus. The FtsA protein was expressed in *E. coli* C43 cells and will be purified in future work using the SMALP system.

6.4 Design and production of a set of linear DNA molecules for polymer rheology studies

In addition to the work on bacterial cell division, in collaboration with Ravi Jagadeeshan of Monash University, Australia, a project was undertaken to design and produce a set of monodisperse, linear DNA molecules with defined size and guanine/cytosine (GC) content. The ultimate goal of this project was to produce a set of standards to facilitate quantitation of linear dichroism data, to provide better input parameters for the mathematical modelling of *E. coli* cell division. The more immediate aim was to establish protocols for the reproducible synthesis of sufficient concentrations of DNA for polymer rheology studies. The DNA is analysed with linear dichroism and dynamic light scattering for the validation of theoretical analyses of the hysteresis of polymers in flow (212). The target size range was 0.5 to 6 kbp and a GC content of 50% was selected. The *E. coli* K12 MG1655 genome sequence from the National Centre for Biotechnology Information (NCBI) database (NCBI Reference: NC_000913.3) was scanned to locate target sequences of the required length and GC content. The target region was amplified by the polymerase chain reaction (PCR) and the PCR product was cloned into the pBluescript KS+ DNA vector. A second round of PCR using the cloned vector as the template yielded DNA of the correct size with sufficient purity and yield for the planned experiments.

7 Introduction to publications

7.1 Mathematical modelling of Z-ring formation and contraction

The first paper published during this project was titled: "*A model of membrane contraction predicting initiation and completion of bacterial cell division*". The manuscript was accepted by the Royal Society of Chemistry journal *Integrative Biology* in February 2013. The mathematical detail of CAM-FF is described in full. The kinetic equations for the polymerisation of FtsZ and the formation of the midcell Z-ring are given, as are the derivations of the Z-ring contraction model. Demonstrations of the validity of CAM-FF are given including the correct prediction of cell division outcome on the deletion of membrane anchor proteins ZipA and FtsA. Note the paper was published under author name C.E. Dow. The author's name has subsequently changed to C.E. Broughton.

Full citation: Dow, CE, Rodger, A, Roper, DI and van den Berg, HA (2013) A model of membrane contraction predicting initiation and completion of bacterial cell division. *Integrative Biology*, 5(5) 778-795.

7.2 Biological insights from the predictions of the mathematical model of Z-ring formation and contraction

The second paper to be published during this project was titled: "*Biological insights from a simulation model of the critical FtsZ accumulation required for prokaryotic cell division*". The paper was accepted by the American Chemical Society journal *Biochemistry* in June 2015. The model solutions and the predictions of cell division outcome are described in detail for various scenarios including perturbations to the rates of nucleotide exchange, FtsZ polymerisation and GTP hydrolysis/dissociation. The effect of the FtsZ G105S mutation is also analysed in detail. Note the paper was published under author name C.E. Dow. The author's name has subsequently changed to C.E. Broughton.

Full citation: Dow, CE, van den Berg, HA, Roper, DI and Rodger, A (2015) Biological insights from a simulation model of the critical FtsZ accumulation required for prokaryotic cell division. *Biochemistry*, 54(24) 3803-3813.

7.3 Investigation of the ATPase activity of the FtsZ G105S mutant protein

This manuscript is in preparation for submission to *PLOS One* and is titled: "*A significant ATPase activity of the mutant cell division protein FtsZ G105S/FtsZ84 from Escherichia coli*". The purification procedure for an N-terminal polyhistidine tagged FtsZ is described in detail. The results of a phosphate release assay demonstrate that on substitution of a serine residue for the wild-type glycine at position 105 of the polypeptide chain, a significant ATPase activity is introduced. The results of a comprehensive analysis of the protein secondary structures using circular dichroism (CD) are also discussed which suggest that the introduction of the mutation does not lead to any major structural reorganisation of the protein. Therefore, the differences in the catalytic activity observed between the wild-type FtsZ and the FtsZ G105S can be attributed to the chemical difference at the active site.

7.4 Production of linear DNA molecules for linear dichroism

This manuscript is in preparation for submission to the American Chemical Society journal *Macromolecules* and is titled: "*Production of DNA molecules of defined length and GC content for linear dichroism and light scattering experiments*". The experimental procedure for the synthesis of linear DNA of the required length and GC content is described in full. The project motivation and the applications of the designed DNA molecules are also provided in detail.

8 Discussion and conclusions

The international community now recognises the re-emergence of bacterial infections as a serious threat to global public health in the post-antibiotic era (1). In 2013, the UK Government responded to the concerns of its Chief Medical Officer, with the publication of its Five Year Antimicrobial Resistance Strategy 2013–2018 (213) that detailed targets to improve public awareness of the issue, to conserve the currently available treatments, and to invest in new treatments. The strategy also includes targets to reduce the number of antibacterial prescriptions and to improve point-of-care diagnostics with genomic approaches to pathogen identification. The report also details a commitment to influence the EU regulatory landscape regarding the agricultural use of antibiotics, to promote research collaboration between academia and industry, and to address the financial incentives for research by the pharmaceutical industry (213).

Also in 2013, the Centers for Disease Control and Prevention (CDC), USA, described the consequences of antibacterial resistance as “catastrophic” and published details of their “Four Core Actions” in response to the situation. The focus is on the prevention of the spread of infection, improved surveillance of resistance, a reduction of the number of antibacterial prescriptions and further investment in new drugs and new diagnostics (214). In 2014, the World Health Organisation described the current antimicrobial resistance levels as “alarming”. Major gaps were identified in the surveillance and reporting of antibacterial resistance globally (215).

Several of the cell division proteins are essential to life and are well conserved across a range of pathogen species. Many also lack homologues in mammalian cells (7). Therefore, the divisome represents a target for antibacterial drug development that is currently unexploited (18). A thorough understanding of the cell division machinery and its function is therefore key to our ability to design the antibacterial drugs of the future.

8.1 A mathematical model of the formation and contraction of the Z-ring

The approach taken to advance the field in this work was to develop a mathematical model of the formation and contraction of Z-ring *in vivo*. The model, referred to as *Critical Accumulation of Membrane-bound FtsZ Fibres* or CAM-FF, predicted one of three possible cell division outcomes and was used to explore the efficiency of possible drug targets within the system *in silico*. CAM-FF accurately predicted the division outcome for cells in which the anchor protein ZipA or FtsA was depleted, which suggested that the model adequately captures the dynamics of the system *in vivo*. The order of efficiency of possible drug targets was found to be as follows: FtsZ polymerisation > ZipA/FtsA availability > FtsZ GTP-binding. The analysis therefore suggests that a competitive inhibitor of GTP-binding to FtsZ would be an inefficient antibacterial agent.

Surovtsev *et al*., the authors of a mathematical model of FtsZ from which the development of the equations of CAM-FF began, anticipate that the only viable path towards a whole-cell predictive model is via the collaborative development of individual modules to be added piecemeal to a global model (216). CAM-FF is therefore presented as a development of the Z-ring assembly and contraction module. The long-term goal is to link the current model with modules for: (i) membrane bending, (ii) peptidoglycan remodelling, and (iii) outer membrane remodelling.

As for all mathematical models, a set of assumptions on the behaviour of the system components was made when defining the equations of CAM-FF. For any biological system that is consistent with these assumptions, the model predictions are valid. Some of the simplifying assumptions of CAM-FF may be addressed in future iterations and their impact on the model predictions may be assessed. For example, a single diffusion constant was assumed for all lengths of FtsZ polymer. It is anticipated that accounting for the slower diffusion of longer FtsZ polymers and for the effect of molecular crowding on the rate constants will resolve the rapid Z-ring assembly predicted in the solutions of CAM-FF of 5 seconds compared to the assembly time of 1 minute observed experimentally (87,217).

It was also assumed that on GTP hydrolysis, the FtsZ polymer dissociates into three FtsZ species: a GDP-bound monomer and two GTP-bound polymers, one from either side of the released GDP-bound monomer. In future iterations of the model, the dissociation of the FtsZ polymer into two species: one GDP-bound polymer and one GTP-bound polymer could be introduced with subsequent GDP/GTP exchange to reactivate the GDP-bound subunit for further polymerisation. This will more accurately reflect the dissociation process occurring in reality, since the hydrolysis of GTP to GDP affects only the FtsZ-FtsZ interface that contains the bound nucleotide, rather than both the upper and lower interfaces as assumed in the model (108,109).

However, the implementation of this change to the model assumptions will almost double the number of model variables, and therefore the number of ODEs, required to track the concentrations of the different FtsZ species over time. Currently in CAM-FF, the concentrations of GDP-bound FtsZ monomers, GTP-bound FtsZ monomers and GTP-bound FtsZ polymers are defined by variables Z_D, Z_T and Z_i for $2 \leq i \leq i_{max}$ respectively, where i_{max} is the maximum length of FtsZ polymers in subunits. Therefore, in the current iteration of CAM-FF, the number of variables, and therefore the number of ODEs is equal to $i_{max}+1$, which is 151 for the value of i_{max} of 150 used in this work. In the revised model, the concentrations of GDP-bound FtsZ polymers must also be defined. Sets of variables, as well as ODEs, for both GTP-bound FtsZ species with length 1 to i_{max} and GDP-bound FtsZ species with length 1 to $i_{max}-1$ are required. Since GTP hydrolysis requires an FtsZ-FtsZ interface, the maximum length of a GDP-bound FtsZ species is $i_{max}-1$. Therefore, the total number of variables is equal to $2i_{max}-1$, which is 299 for the value of i_{max} of 150 used in this work. It is assumed that the exchange reaction of GDP for GTP for FtsZ polymers follows the same kinetics as for the FtsZ monomer. Therefore, the revised model does not introduce new control parameters.

To avoid unnecessary complexity, the described extension of the model was not included in this first iteration of CAM-FF and the simplifying assumption was retained. This is an important consideration in the balance of simplicity versus realism. In future iterations, the simplifying assumption will be addressed and the impact on the model predictions may be assessed. It may be

determined that the simplifying assumption is in fact sufficient to capture the dynamics of the system.

The Min and nucleoid occlusion systems were also assumed to be functional but they were not explicitly modelled. This limited the number of hypothetical scenarios that could be analysed. For example, *in vivo* high levels of FtsZ expression have been shown to overwhelm the midcell localisation mechanisms (124,125). However, this is not reflected in CAM-FF. The introduction of a spatial model for the midcell localisation could be used to address this assumption. However, this would add significant complexity to the model. The explicit modelling of the midcell localisation mechanisms may be better addressed as a separate module, which may then be linked to the Z-ring formation and contraction model of CAM-FF.

8.2 The prediction of cell division outcome

In the model of Z-ring contraction, the average membrane-bound FtsZ polymer length and the total number of membrane-bound FtsZ polymers are used to calculate the value of the contraction parameter for a given set of kinetic parameters for FtsZ polymerisation and membrane binding. The contraction parameter is then compared to two threshold values, an initiation threshold (α), and a completion threshold, for the prediction of cell division. The curve of the contraction threshold, with respect to the cell division progress fraction (ρ), is derived from a comparison of the total tension of the Z-ring during contraction and the maximum tension the Z-ring can withstand. Key to this derivation was the description of the tension required to maintain a given cell radius, based on the balance of the Z-ring and cell surface tensions and the internal pressure, where the cell wall is modelled as a thin-walled cylinder. The use of a cylinder as the starting point of the contraction model reflects the assumption that the cell elongation machinery is functional. The activity of the MreB protein and its associated factors drives the unidirectional growth of the peptidoglycan cell wall along the long axis, which maintains the cylindrical shape of *E. coli* (10,21). CAM-FF does not consider the internal forces generated within the cell wall on its deformation.

The total tension of the Z-ring during contraction is given by,

$$\tau_{\mathrm{Z}} = \tau_0 \left(1 + \frac{2r}{\omega}\rho\sqrt{1-\rho^2}\right) \ ,$$

where r is the cell radius, ω is the Z-ring width, ρ is the Z-ring radius as a fraction of the cell radius (which indicates the progression of cell division as ρ decreases from 1 to 0) and τ_0 is the cell surface tension. This leads to the definition of the contraction threshold, which is equal to $\alpha\rho(1+\gamma\rho\sqrt{1-\rho^2})$, for $0 \leq \rho \leq 1$, where $\gamma = 2r/\omega$, and the initiation threshold (α), i.e. the value of the contraction threshold for $\rho = 1$, is defined as,

$$\alpha = \frac{\tau_0 \omega r}{F \mathrm{P_a} l_0} \ ,$$

where, F is the force of the interaction between an FtsZ monomer and a membrane anchor protein divided by π^3, $\mathrm{P_a}$ is the probability that an FtsZ subunit at the midcell membrane is adjacent to an anchor protein, and l_0 is the length of an FtsZ subunit. The division completion threshold is the maximum value of the contraction threshold for $0 \leq \rho \leq 1$.

In CAM-FF, the radius of the cell (r), the width of the Z-ring (ω) and the length of an FtsZ subunit (l_0) are taken to be 0.4 μm, 0.1 μm and 4 nm respectively. These values were used in the analysis of the various biological scenarios presented in this work. The probability $\mathrm{P_a}$ is calculated from the division of the Z-ring surface area into grid squares of area l_0^2. The number of anchor proteins at the midcell surface (B), is then divided by the number of grid squares to give,

$$\mathrm{P_a} = \frac{B l_0^2}{2\pi r \omega} \ ,$$

and probability $\mathrm{P_a}$ is assumed to be constant throughout the division process.

The initiation threshold (α) may be directly calculated from the parameter values described. However, there is significant uncertainty in the numerical value

of both the cell surface tension (τ_0) and the force of the FtsZ-anchor interaction in the experimental literature. This leads to a high uncertainty in the calculated value of α. Indeed, various studies of cell surface tension using freeze front tracking, droplet sedimentation and adhesion contact angle measurement have reported values in the range of 62–72 mN/m for bacterial cells, including *E. coli* (218), as well as for eukaryotic cells such as lymphocytes, granulocytes and glutaraldehyde-fixed erythrocytes (219). However, using parallel plate confinement, the reported cell surface tensions are significantly lower at 0.11 mN/m for sea-urchin egg cells (220) and 0.2–1.6 mN/m for HeLa cells (221).

There has been no reported measurement of the force of the FtsZ-anchor protein interaction, but values in the region of 50–450 pN have been found for the high affinity interactions of biotin and streptavidin, of various antibodies and antigens (222) and for the aggregation of Aβ-amyloid and of α-synuclein (223). Calculated values of α, for various different values of the cell surface tension and of the force of the FtsZ-anchor interaction from the experimental literature are given in Table 1.

The effect of an increase in the surface tension is an increase in the initiation threshold, since a larger tension in the Z-ring is required. In contrast, if the force of the FtsZ-anchor interaction is increased, the threshold value decreases, since the maximum tension the Z-ring can withstand is increased. The large range of values of α shown in Table 1 demonstrates that currently the value of the initiation threshold (α) may not be directly calculated. Therefore in CAM-FF, α is set to 20,000 on the assumption that the wild-type contraction parameter value is sufficient to allow the completion of cell division with the capacity to lose 15% of its value before division behaviour is affected.

Table 1: Calculation of the initiation threshold α based on values of the cell surface tension (τ_0) and the force of the FtsZ-anchor interaction taken from the experimental literature, and with $\omega = 0.1$ μm, r = 0.4 μm, $P_a = 0.043$ and $l_0 = 4$ nm.

Cell surface tension (mN/m)	Force of the FtsZ-anchor interaction (pN)	Initiation threshold
0.11	25	31,727
0.2	25	57,686
1.6	25	461,489
62	25	17,882,690
72	25	20,766,995
0.11	50	15,864
0.2	50	28,843
1.6	50	230,744
62	50	8,941,345
72	50	10,383,497
0.11	100	7,932
0.2	100	14,422
1.6	100	115,372
62	100	4,470,672
72	100	5,191,749
0.11	150	5,288
0.2	150	9,614
1.6	150	76,915
62	150	2,980,448
72	150	3,461,166

The numerical parameters used in CAM-FF may differ to the true biological values. To assess the impact on the contraction threshold, a range of possible values was analysed. The value of α determines the magnitude of the contraction threshold for $0 < \rho \leq 1$, whereas the value of γ affects both the magnitude of the contraction threshold for $0 < \rho \leq 1$, and the value of ρ at the maximum of the contraction threshold curve, that is the point of the cell division process that requires the maximum tension in the Z-ring. However, α and γ do not change independently, since $\alpha \propto \omega r$ and $\gamma \propto r/\omega$.

The initiation threshold (α) is inversely proportional to the probability P_a and to the length of the FtsZ subunit (l_0). If the probability P_a increases, due to an increase in the number of membrane anchors (B), then the initiation threshold (α) and the magnitude of the contraction threshold curve decrease. For a greater density of membrane anchors, the maximum tension the Z-ring may withstand increases. If the length of the FtsZ subunit (l_0) is increased, the value of the probability P_a also increases. Both contribute to a reduction in the value of the initiation threshold (α) and overall, α is inversely proportional to l_0^3. The effects

of the variation of l_0, within a biologically reasonable range, on the probability P_a, on the initiation threshold (α) and on the contraction threshold curve are shown in Figure 25.

Variation in the values of the initial Z-ring dimensions, that is the cell radius (r) and the Z-ring width (ω), affect the values of both the initiation threshold (α) and the ratio γ. Therefore, both the magnitude of the contraction threshold and the value of ρ at the maximum of the contraction threshold curve will vary. As shown in Figure 25, on an increase in the value of the cell radius (r), the probability P_a decreases. Both contribute to an increase in the value of the initiation threshold (α). An increase in r also results in an increase in γ. The magnitude of the contraction threshold curve increases, and due to the increase in γ, the value of ρ at the maximum of the contraction threshold curve decreases slightly, for example, from 0.848 for a cell radius of 0.2 μm to 0.828 for a cell radius of 0.6 μm.

As shown in Figure 25, on an increase in the value of the Z-ring width (ω), the probability P_a decreases. As for an increase in the cell radius (r), both contribute to an increase in the value of the initiation threshold (α) and of the magnitude of the contraction threshold curve. In contrast to an increase in the cell radius (r), an increase in the Z-ring width (ω) causes a decrease in γ. As a result, the value of ρ at the maximum of the contraction threshold curve increases slightly, for example, from 0.825 for a Z-ring width of 0.05 μm to 0.882 for a Z-ring width of 0.5 μm. In sum, within reasonable biological limits for the parameter values, the general shape of the contraction threshold curve is stable and there is only a slight variation in the value of ρ at the maximum of the contraction threshold. However, there are large variations in the magnitude of the contraction threshold.

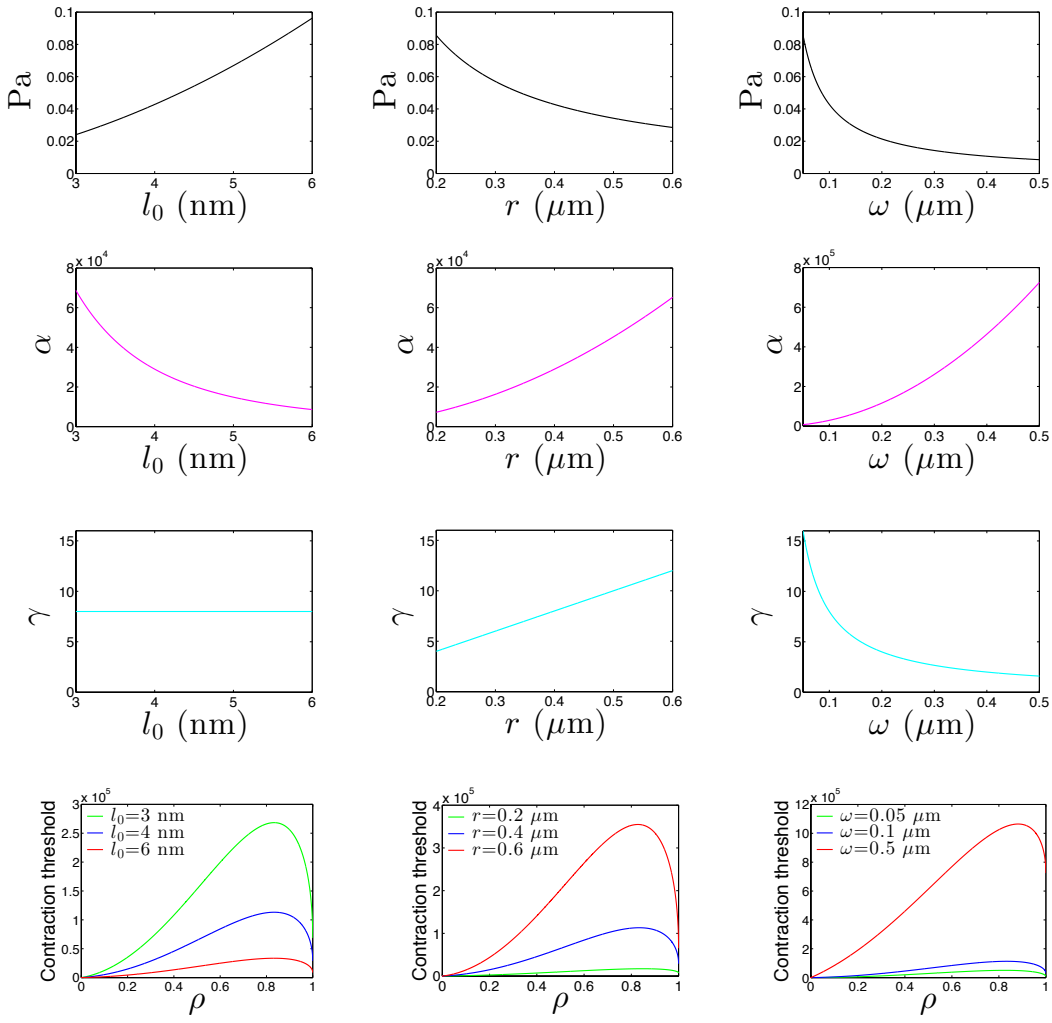

Figure 25: The effect of variation of the numerical parameters of CAM-FF. Three key parameters are shown: the length of an FtsZ subunit (l_0; left-hand column), the cell radius (r; central column) and the width of the Z-ring (ω; right-hand column). For demonstration, the cell surface tension was set to 0.2 mN/m and the force of the FtsZ-anchor interaction was set to 50 pN.

It should also be noted that the value of the contraction parameter was assumed to be constant in CAM-FF and was not updated to reflect the changes to the population of membrane-bound FtsZ polymers as contraction progresses. This is reasonable for the initial stages of division, which determine the division outcome prediction in CAM-FF since the peak of the threshold curve is reached early in the division process, when the cell radius is around 82–88% of its original length. Furthermore, the reconstitution studies have demonstrated that the initiation and the early stages of Z-ring contraction do not require GTP hydrolysis and the subsequent dissociation of FtsZ polymers (101,102).

However, the assumption that the contraction parameter is constant throughout cell division must be considered in the interpretation of the model solutions for certain scenarios. For example, a reduced rate of GTP hydrolysis promotes FtsZ polymerisation and Z-ring formation. Therefore, longer membrane-bound FtsZ polymers are formed and the value of the contraction parameter of CAM-FF increases. The model predicts that a reduction in the GTPase activity of FtsZ has a positive effect on the ability of the cell to initiate contraction. While this is true for the early stages of cell division, the Z-ring must depolymerise later in the cycle and a severe or complete loss of GTPase activity would arrest this process. The inhibition of the contraction process by a major loss of the GTPase activity is not captured in the current iteration of CAM-FF and will be addressed in future work.

The predictions of cell division outcome presented in this work for various biological scenarios were based on the numerical solution of the ODEs of CAM-FF from a single set of initial conditions, where FtsZ is monomeric, GDP-bound and localised to the cytosolic compartments (the cell caps and the midcell region) with a concentration of 12 μM. This set of conditions was chosen to reflect the distribution of FtsZ in the newborn cell (224). For a given total number of FtsZ molecules, the same steady state solution is reached for various different distributions of FtsZ over the three cellular compartments in the initial conditions. For example, the equilibrium solution is the same if the FtsZ is initially all monomeric and GTP-bound, or if FtsZ exists only as dimers, as trimers, as tetramers or as polymers with length i_{max}. Similarly, the same steady state is reached if the FtsZ is initially all bound to the midcell membrane, whether the molecules exist as GDP- or GTP-bound monomers, as dimers, as trimers, as tetramers or as polymers with length i_{max}. Other distributions of the FtsZ through the three compartments also lead to the same equilibrium solution. For example if 50% of the cell complement of FtsZ is cytosolic and GDP-bound and the other 50% is membrane-bound with length i_{max}.

Different steady state distributions of FtsZ are reached if overall the total number of FtsZ molecules in the cell is changed. If the total number of FtsZ molecules is reduced, the average FtsZ polymer length in all three compartments and the percentage of FtsZ that is membrane-bound at equilibrium both decrease, whereas the number of membrane-bound FtsZ polymers at equilibrium increases.

Conversely, if the total number of FtsZ molecules is increased, the average FtsZ polymer length in all three compartments and the percentage of FtsZ that is membrane-bound at equilibrium both increase, whereas the number of membrane-bound FtsZ polymers at equilibrium decreases.

CAM-FF makes no assumptions about the molecular mechanism of Z-ring contraction. A minimal force is required for contraction, perhaps generated by a conformational switch in the FtsZ-FtsZ interface on GTP hydrolysis (106,108,109,225), since as yet no motor protein has been found to associate with FtsZ. The bending of an FtsZ fibre on the hydrolysis of GTP and the subsequent dissociation of the GDP-bound FtsZ-FtsZ interface may create a ratchet mechanism whereby local movement of the membrane becomes locked in place. For example, as shown in Figure 26, the Z-ring may consist of a small number of layers of short FtsZ polymers that are linked by one or more scaffold proteins, such as the Zap proteins. If the hydrolysis of GTP causes a bend in the FtsZ fibre, and if this movement is directed towards the inside of the cell, then the new position of the fibre may be locked in place by the formation of new interactions with the FtsZ polymers below, via the scaffold protein. When the GDP-bound FtsZ-FtsZ interface then dissociates, the new position of the membrane becomes fixed, if the FtsZ-anchor interaction is sufficiently strong. Depending on the orientation of the FtsZ fibres on the membrane, the bending of the filament may not necessarily be directed inwards. However, a polymer bending outwards resulting in an outward push on the membrane would not be locked in place by the FtsZ network. On dissociation of the GDP-bound FtsZ-FtsZ interface the outward force would be lost. If the GTP hydrolysis occurs at a position on an FtsZ polymer without a membrane anchor either side, then on dissociation of the interface, one part of the FtsZ polymer is released back into the cytosol, without exerting a force on the membrane. The released FtsZ is then available to rebind to the Z-ring in another position.

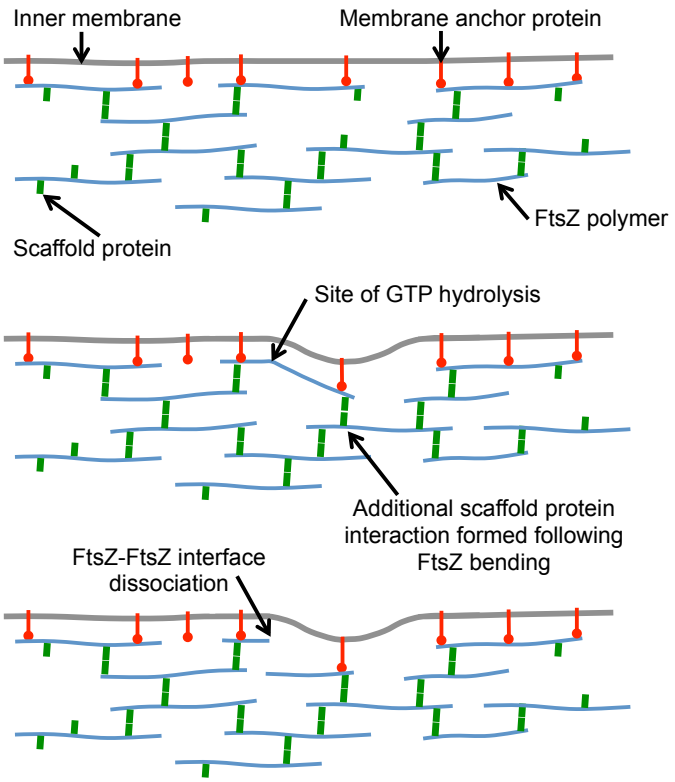

Figure 26: A possible ratchet mechanism where the bending of an FtsZ polymer on GTP hydrolysis exerts a pulling force on the cell membrane and becomes locked into place by the subsequent formation of a new FtsZ-scaffold interaction.

Despite the simplification of certain aspects of the biological process and the absence of the molecular mechanism of the contraction process, analysis of the contraction parameter from CAM-FF generates organism-level predictions based on the biochemical activity of FtsZ measured *in vitro*. The predictions have been verified against scenarios previously tested *in vivo*, such as the deletion of the membrane anchoring proteins ZipA and FtsA. A tool for the prediction of cell division on the perturbation of the biochemical activity of FtsZ is particularly important since specific small molecule inhibitors, commonplace in the laboratory for the study of the FtsZ structural homolgue tubulin, are absent. The search for potential drug interactions may be aided by evaluation of target efficacy *in silico*.

A key result from the modelling work was the finding that the ATPase activity of FtsZ G105S could explain the temperature-sensitivity of the *ftsZ84* mutant (43,44,205,206). Although the wild-type glycine residue has been shown to be adjacent to the phosphates of the nucleotide, rather than the base in the FtsZ

crystal structures solved to date (208), a significant ATPase activity was measured in this work, on replacement of glycine at position 105 of the polypeptide chain of FtsZ with serine. Further work is now required to confirm the biological significance of the ATPase activity of the FtsZ G105S mutant *in vivo* and to determine the biochemical explanation for the difference in the catalytic activity of the wild-type FtsZ and FtsZ G105S proteins.

A competition assay to measure the phosphate release from ATP with the addition of a non-hydrolysable GTP analogue will confirm whether the same active site is used by both nucleotides in the FtsZ G105S mutant. Further, the introduction of a second mutation to the protein to inhibit the hydrolytic activity, such as the D212A mutation, would also confirm that the ATPase activity is intrinsic to the FtsZ G105S protein if both the GTPase and ATPase activities are lost on the introduction of the second mutation. Crosslinking of radio-labelled nucleotides using ultraviolet light, followed by analysis using SDS-PAGE would also confirm that the ATPase is specific to the FtsZ protein and not the result of a contamination with an additional protein.

The nucleotide binding activity of the mutant protein may also be further investigated using surface plasmon resosnance (SPR). The purification protocol for an N-terminal polyhistidine tagged FtsZ construct was developed to allow binding of the protein to a nickel-coated SPR chip. In initial binding screens, the native, untagged FtsZ protein did not bind to a chip functionalised for amine coupling. The isoelectric point of the native protein is relatively low at 4.63 (226), and the amine coupling method requires that the protein is overall positively charged. For FtsZ, the protein precipitates at the low pH required for amine coupling. The N-terminal polyhistidine tagged wild-type FtsZ and FtsZ G105S proteins will be bound to a nickel coated SPR chip surface in future work.

The nucleotide binding activity of the FtsZ G105S protein, compared to the wild-type may also be explored using molecular dynamics simulation. This will help elucidate the biochemical explanation of the change to the nucleotide specificity and will determine if the FtsZ G105S structure is in a more open conformation compared to the wild-type protein, as suggested by the tryptic digest used in the original study of the FtsZ G105S protein (207) and by the dynamic light scattering results from this work. Analysis of the effect of temperature on the GTPase and ATPase activities of the mutant protein is also

required for further investigation of the link between the ATPase activity of the FtsZ G105S mutant protein and the temperature-sensitivity of *ftsZ84* cell division.

Significant progress has also been made towards the reconstitution of the early divisome proteins into lipid vesicles. In future work, the purification of FtsA will be completed and the proteins will be labelled by the covalent attachment of a fluorescent dye for visualisation by fluorescence microscopy. Whereas the ZapA protein contains a single native cysteine residue to which a dye will be attached, for the remaining proteins, a cysteine residue will be introduced by site-directed mutation. A surface residue will be targeted within a region of the protein not involved in protein-protein interactions, nucleotide binding or catalysis. A protocol for the production of lipid vesicles and for the insertion of the SMALP encapsulated membrane proteins will also be developed.

8.3 Final summary

Significant progress has been made with the development of an *in vivo* model of Z-ring formation and contraction based on the observed behaviour of the early cell division proteins *in vitro*. The mathematical model represents a module of a global model of cell division that will include explicit descriptions of: (i) the midcell localisation systems, (ii) membrane bending, (iii) peptidoglycan remodelling and (iv) outer membrane remodelling. The Z-ring formation and contraction module, referred to as *Critical Accumulation of Membrane FtsZ Fibres* or CAM-FF, has already proved useful in the identification of the order of efficiency of drug targets, and in the explanation of the temperature-sensitivity of the *ftsZ84* mutant.

An ATPase activity of the FtsZ84 protein was also observed in this work, following purification of the wild-type FtsZ and the FtsZ G105S proteins. Purification protocols were also established for the soluble protein ZapA, and for the membrane protein ZipA using styrene maleic acid as an alternative to detergent. The *ftsA* gene was cloned and the protein was expressed in *E. coli* C43 cells in preparation for its purification in future work. In addition to the work on bacterial cell division, a set of linear DNA molecules with defined length and GC

content was designed and produced using the *E. coli* K12 MG1655 genome as a sequence template. The DNA was found to be of sufficient purity and yield for the linear dichroism and dynamic light scattering experiments to follow. This will provide experimental evidence for the validation of theoretical analyses of the hysteresis of polymers in flow (212).

9 References

1. Anonymous. Less talk, more action. Nat Rev Microbiol. 2013;11(5):295.

2. Evans A. Causation and disease: A chronological journal: The Thomas Parran Lecture. Am J Epidemiol. 1978;108(4):249–58.

3. Wright GD. The antibiotic resistome: the nexus of chemical and genetic diversity. Nat Rev Microbiol. 2007;5(3):175–86.

4. Winau F, Westphal O, Winau R. Paul Ehrlich-in search of the magic bullet. Microbes Infect. 2004;6(8):786–9.

5. Aminov RI. A brief history of the antibiotic era: lessons learned and challenges for the future. Front Microbiol. 2010;1(1):134.

6. Bentley R. Different roads to discovery; Prontosil (hence sulfa drugs) and penicillin (hence beta-lactams). J Ind Microbiol Biotechnol. 2009;36(6):775–86.

7. Silver L. Challenges of antibacterial discovery. Clin Microbiol Rev. 2011;24(1):71–109.

8. Chopra I. The 2012 Garrod lecture: Discovery of antibacterial drugs in the 21st century. J Antimicrob Chemother. 2013;68(3):496–505.

9. Kohanski MA, Dwyer DJ, Collins JJ. How antibiotics kill bacteria: from targets to networks. Nat Rev Microbiol. 2010;8(6):423–35.

10. Den Blaauwen T, de Pedro MA, Nguyen-Distèche M, Ayala JA. Morphogenesis of rod-shaped sacculi. FEMS Microbiol Rev. 2008;32(2):321–44.

11. Typas A, Banzhaf M, Gross CA, Vollmer W. From the regulation of peptidoglycan synthesis to bacterial growth and morphology. Nat Rev Microbiol. 2011;10(2):123–36.

12. Den Blaauwen T. Prokaryotic cell division: Flexible and diverse. Curr Opin Microbiol. 2013;16(6):738–44.

13. Egan AJF, Vollmer W. The physiology of bacterial cell division. Ann N Y Acad Sci. 2013;1277:8–28.

14. Galli E, Gerdes K. FtsZ-ZapA-ZapB interactome of *Escherichia coli*. J Bacteriol. 2012;194(2):292–302.

15. Durand-Heredia JM, Yu HH, De Carlo S, Lesser CF, Janakiraman A. Identification and characterization of ZapC, a stabilizer of the FtsZ ring in *Escherichia coli*. J Bacteriol. 2011;193(6):1405–13.

16. Durand-Heredia J, Rivkin E, Fan G, Morales J, Janakiraman A. Identification of ZapD as a cell division factor that promotes the assembly of FtsZ in *Escherichia coli*. J Bacteriol. 2012;194(12):3189–98.

17. Pichoff S, Lutkenhaus J. Unique and overlapping roles for ZipA and FtsA in septal ring assembly in *Escherichia coli*. EMBO J. 2002;21(4):685–93.

18. Den Blaauwen T, Andreu JM, Monasterio O. Bacterial cell division proteins as antibiotic targets. Bioorg Chem. 2014;55:27–38.

19. Vollmer W, Seligman SJ. Architecture of peptidoglycan: more data and more models. Trends Microbiol. 2010;18(2):59–66.

20. Cabeen MT, Jacobs-Wagner C. Bacterial cell shape. Nat Rev Microbiol. 2005;3(8):601–10.

21. Vollmer W, Höltje JV. Morphogenesis of *Escherichia coli*. Curr Opin Microbiol. 2001;4(6):625–33.

22. Meyer P, Gutierrez J, Pogliano K, Dworkin J. Cell wall synthesis is necessary for membrane dynamics during sporulation of *Bacillus subtilis*. Mol Microbiol. 2010;76(4):956–70.

23. Gan L, Chen S, Jensen GJ. Molecular organization of Gram-negative peptidoglycan. Proc Natl Acad Sci U S A. 2008;105(48):18953–7.

24. Schleifer K, Kandler O. Peptidoglycan types of bacterial cell walls and their taxonomic implications. Bacteriol Rev. 1972;36(4):407–77.

25. Vollmer W, Blanot D, De Pedro MA. Peptidoglycan structure and architecture. FEMS Microbiol Rev. 2008;32(2):149–67.

26. Barreteau H, Kovač A, Boniface A, Sova M, Gobec S, Blanot D. Cytoplasmic steps of peptidoglycan biosynthesis. FEMS Microbiol Rev. 2008;32(2):168–207.

27. Bouhss A, Trunkfield AE, Bugg TDH, Mengin-Lecreulx D. The biosynthesis of peptidoglycan lipid-linked intermediates. FEMS Microbiol Rev. 2008;32(2):208–33.

28. Mohammadi T, van Dam V, Sijbrandi R, Vernet T, Zapun A, Bouhss A, et al. Identification of FtsW as a transporter of lipid-linked cell wall precursors across the membrane. EMBO J. 2011;30(8):1425–32.

29. Sham L, Butler E, Lebar M, Kahne D, Bernhardt T, Ruiz N. MurJ is the flippase of lipid-linked precursors for peptidoglycan biogenesis. Science. 2014;345(6193):220–2.

30. Den Blaauwen T, Aarsman MEG, Vischer NOE, Nanninga N. Penicillin-binding protein PBP2 of *Escherichia* coli localizes preferentially in the

lateral wall and at mid-cell in comparison with the old cell pole. Mol Microbiol. 2003;47(2):539–47.

31. Spratt BG. Distinct penicillin binding proteins involved in the division, elongation, and shape of *Escherichia coli* K12. Proc Natl Acad Sci U S A. 1975;72(8):2999–3003.

32. Spratt BG. Properties of the penicillin-binding proteins of *Escherichia coli* K12. Eur J Biochem. 1977;72(2):341–52.

33. Weiss D, Pogliano K, Carson M, Guzman L, Fraipont C, Nguyen-Distèche M, et al. Localization of the *Escherichia coli* cell division protein FtsI (PBP3) to the division site and cell pole. Mol Microbiol. 1997;25(4):671–81.

34. Suzuki H, Nishimura Y, Hirota Y. On the process of cellular division in *Escherichia coli*: A series of mutants of *E. coli* altered in the penicillin-binding proteins. Proc Natl Acad Sci U S A. 1978;75(2):664–8.

35. Schiffer G, Höltje JV. Cloning and characterization of PBP1C, a third member of the multimodular class A penicillin-binding proteins of *Escherichia coli*. J Biol Chem. 1999;274(45):32031–9.

36. Derouaux A, Wolf B, Fraiport C, Breukink E, Nguyen-Distèche M, Terrak M. The monofunctional glycosyltransferase of *Escherichia coli* localizes to the cell division site and interacts with penicillin-binding protein 3, FtsW, and FtsN. J Bacteriol. 2008;190(5):1831–4.

37. Hantke K, Braun V. Covalent binding of lipid to protein. Diglyceride and amide-linked fatty acid at the N-terminal end of the murein-lipoprotein of the *Escherichia coli* outer membrane. Eur J Biochem. 1973;34(2):284–96.

38. Dramsi S, Magnet S, Davison S, Arthur M. Covalent attachment of proteins to peptidoglycan. FEMS Microbiol Rev. 2008;32(2):307–20.

39. Van De Putte P, Van Dillewijn J, Roersch A. The selection of mutants of *Escherichia coli* with impaired cell division at elevated temperature. Mutat Res. 1964;106(2):121–8.

40. Hirota Y. Thermosensitive mutants of *E. coli* affected in the process of DNA synthesis and cellular division. Cold Spring Habor Symp Quant Biol [proceedings]. 1968;33:677–93.

41. Goehring NW, Beckwith J. Diverse paths to midcell: Assembly of the bacterial cell division machinery. Curr Biol. 2005;15(13):R514–26.

42. Allen JS, Filip CC, Gustafson RA, Allen RG, Walker JR. Regulation of bacterial cell division: Genetic and phenotypic analysis of temperature-sensitive, multinucleate, filament-forming mutants of *Escherichia coli*. J Bacteriol. 1974;117(3):978–86.

43. Addinall SG, Erfei B, Lutkenhaus J. FtsZ ring formation in *fts* mutants. J Bacteriol. 1996;178(13):3877–84.

44. Addinall SG, Cao C, Lutkenhaus J. Temperature shift experiments with an *ftsZ84(Ts)* strain reveal rapid dynamics of FtsZ localisation and indicate that the Z ring is required throughout septation and cannot reoccupy division sites once constriction has initiated. J Bacteriol. 1997;179(13):4277–84.

45. Bi EF, Lutkenhaus J. FtsZ ring structure associated with division in *Escherichia coli*. Nature. 1991;354:161–4.

46. Stricker J, Maddox P, Salmon ED, Erickson HP. Rapid assembly dynamics of the *Escherichia coli* FtsZ-ring demonstrated by fluorescence recovery after photobleaching. Proc Natl Acad Sci U S A. 2002;99(5):3171–5.

47. Anderson DE, Gueiros-Filho FJ, Erickson HP. Assembly dynamics of FtsZ rings in *Bacillus subtilis* and *Escherichia coli* and effects of FtsZ-regulating proteins. J Bacteriol. 2004;186(17):5775–81.

48. Chen Y, Erickson HP. Rapid *in vitro* assembly dynamics and subunit turnover of FtsZ demonstrated by fluorescence resonance energy transfer. J Biol Chem. 2005;280(23):22549–54.

49. Schmidt KL, Peterson ND, Kustusch RJ, Wissel MC, Graham B, Phillips GJ, et al. A predicted ABC transporter, FtsEX, is needed for cell division in *Escherichia coli*. J Bacteriol. 2004;186:785–93.

50. Corbin BD, Wang Y, Beuria TK, Margolin W. Interaction between cell division proteins FtsE and FtsZ. J Bacteriol. 2007;189(8):3026–35.

51. Wang L, Lutkenhaus J. FtsK is an essential cell division protein that is localised to the septum and induced as part of the SOS response. Mol Microbiol. 1998;29(3):731–40.

52. Chen J, Beckwith J. FtsQ, FtsL and FtsI require FtsK, but not FtsN, for co-localisation with FtsZ during *Escherichia coli* cell division. Mol Microbiol. 2001;42(2):395–413.

53. Chen J, Weiss D, Ghigo J, Beckwith J. Septal localization of FtsQ, an essential cell division protein in *Escherichia coli*. J Bacteriol. 1999;181(2):521–30.

54. Ghigo J, Weiss D, Chen J, Yarrow J, Beckwith J. Localization of FtsL to the *Escherichia coli* septal ring. Mol Microbiol. 1999;31(2):725–37.

55. Mercer K, Weiss D. The *Escherichia coli* cell division protein FtsW is required to recruit its cognate transpeptidase, FtsI (PBP3), to the division site. J Bacteriol. 2002;184(4):904–12.

56. Weiss D, Chen J, Ghigo J, Boyd D, Beckwith J. Localization of FtsI (PBP3) to the septal ring requires its membrane anchor, the Z ring, FtsA, FtsQ, and FtsL. J Bacteriol. 1999;181(2):508–20.

57. Aarsman MEG, Piette A, Fraipont C, Vinkenvleugel TMF, Nguyen-Distèche M, den Blaauwen T. Maturation of the *Escherichia coli* divisome occurs in two steps. Mol Microbiol. 2005;55(6):1631–45.

58. Goehring NW, Gueiros-Filho F, Beckwith J. Premature targeting of a cell division protein to midcell allows dissection of divisome assembly in *Escherichia coli*. Genes Dev. 2005;19(1):127–37.

59. Fraipont C, Alexeeva S, Wolf B, van der Ploeg R, Schloesser M, den Blaauwen T, et al. The integral membrane FtsW protein and peptidoglycan synthase PBP3 form a subcomplex in *Escherichia coli*. Microbiology. 2011;157(1):251–9.

60. Buddelmeijer N, Beckwith J. A complex of the *Escherichia coli* cell division proteins FtsL, FtsB and FtsQ forms independently of its localization to the septal region. Mol Microbiol. 2004;52(5):1315–27.

61. Geissler B, Margolin W. Evidence for functional overlap among multiple bacterial cell division proteins: Compensating for the loss of FtsK. Mol Microbiol. 2005;58(2):596–612.

62. RayChaudhuri D, Park JT. *Escherichia coli* cell-division gene *ftsZ* encodes a novel GTP-binding protein. Nature. 1992;359(6392):251–4.

63. De Boer P, Crossley R, Rothfield L. The essential bacterial cell-division protein FtsZ is a GTPase. Nature. 1992;359(6392):254–6.

64. Löwe J, Amos LA. Crystal structure of the bacterial cell-division protein FtsZ. Nature. 1998;391(6663):203–6.

65. Nogales E, Wolf SG, Downing KH. Structure of the alpha beta tubulin dimer by electron crystallography. Nature. 1998;391(6663):199–203.

66. Scheffers DJ, de Wit JG, den Blaauwen T, Driessen JM. GTP hydrolysis of cell division protein FtsZ: evidence that the active site is formed by the association of monomers. Biochemistry. 2002;41(2):521–9.

67. Scheffers DJ, de Wit JG, den Blaauwen T, Driessen JM. Substitution of a conserved aspartate allows cation-induced polymerization of FtsZ. FEBS Lett. 2001;494(1-2):34–7.

68. Mukherjee A, Lutkenhaus J. Dynamic assembly of FtsZ regulated by GTP hydrolysis. EMBO J. 1998;17(2):462–9.

69. Erickson HP, Anderson DE, Osawa M. FtsZ in bacterial cytokinesis: cytoskeleton and force generator all in one. Microbiol Mol Biol Rev. 2010;74(4):504–28.

70. Cordell SC, Robinson EJH, Lowe J. Crystal structure of the SOS cell division inhibitor SulA and in complex with FtsZ. Proc Natl Acad Sci U S A. 2003;100(13):7889–94.

71. Erickson HP, Taylor DW, Taylor KA, Bramhill D. Bacterial cell division protein FtsZ assembles into protofilament sheets and minirings, structural homologs of tubulin polymers. Proc Natl Acad Sci U S A. 1996;93(1):519–23.

72. Yu X, Margolin W. Ca2+-mediated GTP-dependent dynamic assembly of bacterial cell division protein FtsZ into asters and polymer networks *in vitro*. EMBO J. 1997;16(17):5455–63.

73. Bramhill D, Thompson CM. GTP-dependent polymerization of *Escherichia coli* FtsZ protein to form tubules. Proc Natl Acad Sci U S A. 1994;91(13):5813–7.

74. Chen Y, Bjornson K, Redick S, Erickson H. A rapid fluorescence assay for FtsZ assembly indicates cooperative assembly with a dimer nucleus. Biophys J. 2005;88(1):505–14.

75. González JM, Jiménez M, Vélez M, Mingorance J, Andreu JM, Vicente M, et al. Essential cell division protein FtsZ assembles into one monomer-thick ribbons under conditions resembling the crowded intracellular environment. J Biol Chem. 2003;278(39):37664–71.

76. Popp D, Iwasa M, Narita A, Erickson HP, Maéda Y. FtsZ condensates: An *in vitro* electron microscopy study. Biopolymers. 2009;91(5):340–50.

77. Huecas S, Llorca O, Boskovic J, Martín-Benito J, Valpuesta JM, Andreu JM. Energetics and geometry of FtsZ polymers: nucleated self-assembly of single protofilaments. Biophys J. 2008;94(5):1796–806.

78. Romberg L, Simon M, Erickson HP. Polymerization of FtsZ, a bacterial homolog of tubulin. J Biol Chem. 2001;276(15):11743–53.

79. Caplan MR, Erickson HP. Apparent cooperative assembly of the bacterial cell division protein FtsZ demonstrated by isothermal titration calorimetry. J Biol Chem. 2003;278(16):13784–8.

80. Rueda S, Vicente M, Mingorance J. Concentration and assembly of the division ring proteins FtsZ, FtsA, and ZipA during the *Escherichia coli* cell cycle. J Bacteriol. 2003;185(11):3344–51.

81. Pla J, Sánchez M, Palacios P, Vicente M, Aldea M. Preferential cytoplasmic location of FtsZ, a protein essential for *Escherichia coli* septation. Mol Microbiol. 1991;5(7):1681–6.

82. Lu C, Stricker J, Erickson HP. FtsZ from Escherichia coli, *Azotobacter vinelandii*, and *Thermotoga maritima*-quantitation, GTP hydrolysis, and assembly. Cell Motil Cytoskeleton. 1998;40(1):71–86.

83. González JM, Vélez M, Jiménez M, Alfonso C, Schuck P, Mingorance J, et al. Cooperative behavior of *Escherichia coli* cell-division protein FtsZ assembly involves the preferential cyclization of long single-stranded fibrils. Proc Natl Acad Sci U S A. 2005;102(6):1895–900.

84. Miraldi ER, Thomas PJ, Romberg L. Allosteric models for cooperative polymerization of linear polymers. Biophys J. 2008;95(5):2470–86.

85. Addinall S, Lutkenhaus J. FtsZ-spirals and -arcs determine the shape of the invaginating septa in some mutants of *Escherichia coli*. Mol Microbiol. 1996;22(2):231–7.

86. Fu G, Huang T, Buss J, Coltharp C, Hensel Z, Xiao J. *In vivo* structure of the *E. coli* FtsZ-ring revealed by photoactivated localization microscopy (PALM). PLoS One. 2010;5(9):1–16.

87. Sun Q, Margolin W. FtsZ dynamics during the division cycle of live *Escherichia coli* cells. J Bacteriol. 1998;180(8):2050–6.

88. Ma X, Ehrhardt DW, Margolin W. Colocalization of cell division proteins FtsZ and FtsA to cytoskeletal structures in living *Escherichia coli* cells by using green fluorescent protein. Proc Natl Acad Sci U S A. 1996;93(23):12998–3003.

89. Thanedar S, Margolin W. FtsZ exhibits rapid movement and oscillation waves in helix-like patterns in *Escherichia coli*. Curr Biol. 2004;14(13):1167–73.

90. Peters PC, Migocki MD, Thoni C, Harry EJ. A new assembly pathway for the cytokinetic Z ring from a dynamic helical structure in vegetatively growing cells of *Bacillus subtilis*. Mol Microbiol. 2007;64(2):487–99.

91. Jennings PC, Cox GC, Monahan LG, Harry EJ. Super-resolution imaging of the bacterial cytokinetic protein FtsZ. Micron. 2011;42(4):336–41.

92. Niu L, Yu J. Investigating intracellular dynamics of FtsZ cytoskeleton with photoactivation single-molecule tracking. Biophys J. 2008;95(4):2009–16.

93. Margolin W. The price of tags in protein localization studies. J Bacteriol. 2012;194(23):6369–71.

94. Swulius M, Jensen G. The helical MreB cytoskeleton in *Escherichia coli* MC1000/pLE7 is an artifact of the N-terminal yellow fluorescent protein tag. J Bacteriol. 2012;194(23):6382–6.

95. Rowlett V, Margolin W. 3D-SIM super-resolution of FtsZ and its membrane tethers in *Escherichia coli* cells. Biophys J. 2014;107(8):L17–20.

96. Strauss MP, Liew ATF, Turnbull L, Whitchurch CB, Monahan LG, Harry EJ. 3D-SIM super resolution microscopy reveals a bead-like arrangement for FtsZ and the division machinery: Implications for triggering cytokinesis. PLoS Biol. 2012;10(9):e1001389.

97. Holden SJ, Pengo T, Meibom KL, Fernandez Fernandez C, Collier J, Manley S. High throughput 3D super-resolution microscopy reveals *Caulobacter crescentus in vivo* Z-ring organization. Proc Natl Acad Sci U S A. 2014;111(12):4566–71.

98. Li Z, Trimble MJ, Brun Y V, Jensen GJ. The structure of FtsZ filaments *in vivo* suggests a force-generating role in cell division. EMBO J. 2007;26(22):4694–708.

99. Osawa M, Anderson DE, Erickson HP. Reconstitution of contractile FtsZ rings in liposomes. Science. 2008;320(5877):792–4.

100. Osawa M, Anderson DE, Erickson HP. Curved FtsZ protofilaments generate bending forces on liposome membranes. EMBO J. 2009;28(22):3476–84.

101. Osawa M, Erickson HP. Inside-out Z rings-constriction with and without GTP hydrolysis. Mol Microbiol. 2011;81(2):571–9.

102. Milam SL, Osawa M, Erickson HP. Negative-stain electron microscopy of inside-out FtsZ rings reconstituted on artificial membrane tubules show ribbons of protofilaments. Biophys J. 2012;103(1):59–68.

103. Maupin P, Pollard T. Arrangement of actin filaments and myosin-like filaments in the contractile ring and of actin-like filaments in the mitotic spindle of dividing HeLa cells. J Ultrastruct Mol Struct Res. 1986;94(1):92–103.

104. Lan G, Wolgemuth CW, Sun SX. Z-ring force and cell shape during division in rod-like bacteria. Proc Natl Acad Sci U S A. 2007;104(41):16110–5.

105. Erickson HP. Modeling the physics of FtsZ assembly and force generation. Proc Natl Acad Sci U S A. 2009;106(23):9238–43.

106. Lu C, Reedy M, Erickson HP. Straight and curved conformations of FtsZ are regulated by GTP hydrolysis. J Bacteriol. 2000;182(1):164–70.

107. Mingorance J, Tadros M, Vicente M, González JM, Rivas G, Vélez M. Visualization of single *Escherichia coli* FtsZ filament dynamics with atomic force microscopy. J Biol Chem. 2005;280(21):20909–14.

108. Li Y, Hsin J, Zhao L, Cheng Y, Shang W, Huang KC, et al. FtsZ protofilaments use a hinge-opening mechanism for constrictive force generation. Science. 2013;341(6144):392–5.

109. Hsin J, Gopinathan A, Huang KC. Nucleotide-dependent conformations of FtsZ dimers and force generation observed through molecular dynamics simulations. Proc Natl Acad Sci. 2012;109(24):9432–7.

110. Mingorance J, Rivas G, Vélez M, Gómez-Puertas P, Vicente M. Strong FtsZ is with the force: mechanisms to constrict bacteria. Trends Microbiol. 2010;18:348–56.

111. Denome SA, Elf PK, Henderson TA, Nelson DE, D YK. *Escherichia coli* mutants lacking all possible combinations of eight penicillin binding proteins: Viability, characteristics, and implications for peptidoglycan synthesis. J Bacteriol. 1999;181(13):3981–93.

112. Heidrich C, Ursinus A, Berger J, Schwarz H, Höltje J V. Effects of multiple deletions of murein hydrolases on viability, septum cleavage, and sensitivity to large toxic molecules in *Escherichia coli*. J Bacteriol. 2002;184(22):6093–9.

113. Daniel RA, Harry EJ, Errington J. Role of penicillin-binding protein PBP 2B in assemblyand functioning of the division machinery of *Bacillus subtilis*. Mol Microbiol. 2000;35(2):299–311.

114. Morlot C, Zapun A, Dideberg O, Vernet T. Growth and division of *Streptococcus pneumoniae*: localization of the high molecular weight penicillin-binding proteins during the cell cycle. Mol Microbiol. 2003;50(3):845–55.

115. Bailey M, Bisicchia P, Warren B, Sherratt D, Mannik J. Evidence for divisome localization mechanisms independent of the Min system and SlmA in *Escherichia coli*. PLOS Genet. 2014;10(8):e1004504.

116. Tsang M, Bernhardt TG. Guiding divisome assembly and controlling its activity. Curr Opin Microbiol. 2015;24:60–5.

117. Janion C. Inducible SOS response system of DNA repair and mutagenesis in *Escherichia coli*. Int J Biol Sci. 2008;4(6):338–44.

118. Huisman O, D'Ari R, Gottesman S. Cell-division control in *Escherichia coli*: specific induction of the SOS function SfiA protein is sufficient to block septation. Proc Natl Acad Sci U S A. 1984;81(14):4490–4.

119. Dajkovic A, Mukherjee A, Lutkenhaus J. Investigation of regulation of FtsZ assembly by SulA and development of a model for FtsZ polymerization. J Bacteriol. 2008;190(7):2513–26.

120. Chen Y, Milam SL, Erickson HP. SulA inhibits assembly of FtsZ by a simple sequestration mechanism. Biochemistry. 2012;51(14):3100–9.

121. Mukherjee A, Cao C, Lutkenhaus J. Inhibition of FtsZ polymerization by SulA, an inhibitor of septation in *Escherichia coli*. Proc Natl Acad Sci U S A. 1998;95(6):2885–90.

122. Mizusawa S, Gottesman S. Protein degradation in *Escherichia coli*: the *lon* gene controls the stability of SulA protein. Proc Natl Acad Sci U S A. 1983;80(2):358–62.

123. De Boer PA, Crossley RE, Rothfield LI. A division inhibitor and a topological specificity factor coded for by the minicell locus determine proper placement of the division septum in *E. coli*. Cell. 1989;56(4):641–9.

124. De Boer PA, Crossley RE, Rothfield LI. Central role for the *Escherichia coli minC* gene product in two different cell division-inhibition systems. Proc Natl Acad Sci U S A. 1990;87(3):1129–33.

125. Bi E, Lutkenhaus J. FtsZ regulates frequency of cell division in *Escherichia coli*. J Bacteriol. 1990;172(5):2765–8.

126. Lutkenhaus J. Assembly dynamics of the bacterial MinCDE system and spatial regulation of the Z-ring. Annu Rev Biochem. 2007;76:539–62.

127. Raskin DM, de Boer PA. Rapid pole-to-pole oscillation of a protein required for directing division to the middle of *Escherichia coli*. Proc Natl Acad Sci U S A. 1999;96(9):4971–6.

128. Hale C, Meinhardt H, de Boer P. Dynamic localisation cycle of the cell division regulator MinE in *Escherichia coli*. EMBO J. 2001;20(7):1563–72.

129. Hu Z, Lutkenhaus J. Topological regulation of cell division in *Escherichia coli* involves rapid pole to pole oscillation of the division inhibitor MinC under the control of MinD and MinE. Mol Microbiol. 1999;34(1):82–90.

130. Hu Z, Mukherjee A, Pichoff S, Lutkenhaus J. The MinC component of the division site selection system in *Escherichia coli* interacts with FtsZ to prevent polymerization. Proc Natl Acad Sci U S A. 1999;96(26):14819–24.

131. De Boer P, Crossley R, Hand A, Rothfield L. The MinD protein is a membrane ATPase required for the correct placement of the *Escherichia coli* division site. EMBO J. 1991;10(13):4371–80.

132. Hu Z, Saez C, Lutkenhaus J. Recruitment of MinC, an inhibitor of Z-ring formation, to the membrane in *Escherichia coli*: Role of MinD and MinE. J Bacteriol. 2003;185(1):196–203.

133. Szeto TH, Rowland SL, Rothfield LI, King GF. Membrane localization of MinD is mediated by a C-terminal motif that is conserved across eubacteria, archaea, and chloroplasts. Proc Natl Acad Sci U S A. 2002;99(24):15693–8.

134. Hu Z, Lutkenhaus J. A conserved sequence at the C-terminus of MinD is required for binding to the membrane and targeting MinC to the septum. Mol Microbiol. 2003;47(2):345–55.

135. Hu Z, Lutkenhaus J. Topological regulation of cell division in *E. coli*: Spatiotemporal oscillation of MinD requires stimulation of its ATPase by MinE and phospholipid. Mol Cell. 2001;7(6):1337–43.

136. Lackner LL, Raskin DM, De Boer PAJ. ATP-dependent interactions between *Escherichia coli* Min proteins and the phospholipid membrane *in vitro*. J Bacteriol. 2003;185(3):735–49.

137. Huang KC, Meir Y, Wingreen NS. Dynamic structures in *Escherichia coli*: spontaneous formation of MinE rings and MinD polar zones. Proc Natl Acad Sci U S A. 2003;100(22):12724–8.

138. Wu LJ, Errington J. Nucleoid occlusion and bacterial cell division. Nat Rev Microbiol. 2012;10(1):8–12.

139. Wu LJ, Errington J. Coordination of cell division and chromosome segregation by a nucleoid occlusion protein in *Bacillus subtilis*. Cell. 2004;117(7):915–25.

140. Bernhardt TG, de Boer P. SlmA, a nucleoid-associated, FtsZ binding protein required for blocking septal ring assembly over chromosomes in *E. coli*. Mol Cell. 2005 May 27;18(5):555–64.

141. Wu LJ, Ishikawa S, Kawai Y, Oshima T, Ogasawara N, Errington J. Noc protein binds to specific DNA sequences to coordinate cell division with chromosome segregation. EMBO J. 2009;28(13):1940–52.

142. Tonthat NK, Arold ST, Pickering BF, Van Dyke MW, Liang S, Lu Y, et al. Molecular mechanism by which the nucleoid occlusion factor, SlmA, keeps cytokinesis in check. EMBO J. 2011;30(1):154–64.

143. Tonthat NK, Milam SL, Chinnam N, Whitfill T, Margolin W, Schumacher MA. SlmA forms a higher-order structure on DNA that inhibits cytokinetic Z-ring formation over the nucleoid. Proc Natl Acad Sci U S A. 2013;110(26):10586–91.

144. Cho H, McManus HR, Dove SL, Bernhardt TG. Nucleoid occlusion factor SlmA is a DNA-activated FtsZ polymerization antagonist. Proc Natl Acad Sci U S A. 2011;108(9):3773–8.

145. Du S, Lutkenhaus J. SlmA antagonism of FtsZ assembly employs a two-pronged mechanism like MinCD. PLoS Genet. 2014;10(7):e1004460.

146. Mercier R, Petit M, Schbath S, Robin S, El Karoui M, Boccard F, et al. The MatP/*matS* site-specific system organizes the terminus region of the *E. coli* chromosome into a macrodomain. Cell. 2008;135(3):475–85.

147. Espéli O, Borne R, Dupaigne P, Thiel A, Gigant E, Mercier R, et al. A MatP–divisome interaction coordinates chromosome segregation with cell division in *E. coli*. EMBO J. 2012;31(14):3198–211.

148. Schaffner-Barbero C, Martín-Fontecha M, Chacón P, Andreu JM. Targeting the assembly of bacterial cell division protein FtsZ with small molecules. ACS Chem Biol. 2012;7(2):269–77.

149. Anderson DE, Kim MB, Moore JT, O'Brien TE, Sorto NA, Grove CI, et al. Comparison of small molecule inhibitors of the bacterial cell division protein FtsZ and identification of a reliable cross-species inhibitor. ACS Chem Biol. 2012;7(11):1918–28.

150. Läppchen T, Hartog AF, Pinas VA, Koomen GJ, den Blaauwen T. GTP analogue inhibits polymerization and GTPase activity of the bacterial protein FtsZ without affecting its eukaryotic homologue tubulin. Biochemistry. 2005;44(21):7879–84.

151. Läppchen T, Pinas VA, Hartog AF, Koomen GJ, Schaffner-Barbero C, Andreu JM, et al. Probing FtsZ and tubulin with C8-substituted GTP analogs reveals differences in their nucleotide binding sites. Chem Biol. 2008;15(2):189–99.

152. Läppchen T. Synthesis of GTP analogues and evaluation of their effect on the antibiotic target FtsZ and its eukaryotic homologue tubulin. University of Amsterdam; 2007.

153. Sorto NA, Painter PP, Fettinger JC, Tantillo DJ, Shaw JT. Design and synthesis of mimics of the T7-loop of FtsZ. Org Lett. 2013;15(11):2700–3.

154. Ohashi Y, Chijiiwa Y, Suzuki K, Takahashi K, Nanamiya H, Sato T, et al. The lethal effect of a benzamide derivative, 3-methoxybenzamide, can be suppressed by mutations within a cell division gene, *ftsZ*, in *Bacillus subtilis*. J Bacteriol. 1999;181(4):1348–51.

155. Haydon DJ, Stokes NR, Ure R, Galbraith G, Bennett JM, Brown DR, et al. An inhibitor of FtsZ with potent and selective anti-staphylococcal activity. Science. 2008;321(5896):1673–5.

156. Tan CM, Therien AG, Lu J, Lee SH, Caron A, Gill CJ, et al. Restoring methicillin-resistant *Staphylococcus aureus* susceptibility to β-lactam antibiotics. Sci Transl Med. 2012;4(126):126ra35.

157. Andreu JM, Schaffner-Barbero C, Huecas S, Alonso D, Lopez-Rodriguez ML, Ruiz-Avila LB, et al. The antibacterial cell division inhibitor PC190723 is an FtsZ polymer-stabilizing agent that induces filament assembly and condensation. J Biol Chem. 2010;285(19):14239–46.

158. Elsen NL, Lu J, Parthasarathy G, Reid JC, Sharma S, Soisson SM, et al. Mechanism of action of the cell-division inhibitor PC190723: Modulation of FtsZ assembly cooperativity. J Am Chem Soc. 2012;134(30):12342–5.

159. Matsui T, Yamane J, Mogi N, Yamaguchi H, Takemoto H, Yao M, et al. Structural reorganization of the bacterial cell-division protein FtsZ from *Staphylococcus aureus*. Acta Crystallogr Sect D Biol Crystallogr. 2012;68(9):1175–88.

160. Kaul M, Mark L, Zhang Y, Parhi AK, LaVoie EJ, Pilch DS. An FtsZ-targeting prodrug with oral antistaphylococcal efficacy *in vivo*. Antimicrob Agents Chemother. 2013;57(12):5860–9.

161. Adams DW, Wu LJ, Czaplewski LG, Errington J. Multiple effects of benzamide antibiotics on FtsZ function. Mol Microbiol. 2011;80(1):68–84.

162. Stokes NR, Baker N, Bennett JM, Berry J, Collins I, Czaplewski LG, et al. An improved small-molecule inhibitor of FtsZ with superior *in vitro* potency, drug-likeproperties, and *in vivo* efficacy. Antimicrob Agents Chemother. 2013;57(1):317–25.

163. Wang J, Galgoci A, Kodali S, Herath K, Jayasuriya H, Dorso K, et al. Discovery of a small molecule that inhibits cell division by blocking FtsZ, a novel therapeutic target of antibiotics. J Biol Chem. 2003;278(45):44424–8.

164. Park Y, Grove C, Gonzalez-Lopez M, Urgaonkar S, Fettinger J, Shaw J. Synthesis of (-)-viriditoxin: A 6,6'-binaphthopyran-2-one that targets the bacterial cell division protein FtsZ. Angew Chemie - Int Ed. 2011;50(16):3730–3.

165. Rai D, Singh JK, Roy N, Panda D. Curcumin inhibits FtsZ assembly: an attractive mechanism for its antibacterial activity. Biochem J. 2008;410(1):147–55.

166. Duggirala S, Nankar RP, Rajendran S, Doble M. Phytochemicals as inhibitors of bacterial cell division protein FtsZ: Coumarins are promising candidates. Appl Biochem Biotechnol. 2014;174(1):283–96.

167. Domadia PN, Bhunia A, Sivaraman J, Swarup S, Dasgupta D. Berberine targets assembly of *Escherichia coli* cell division protein FtsZ. Biochemistry. 2008;47(10):3225–34.

168. Beuria TK, Santra MK, Panda D. Sanguinarine blocks cytokinesis in bacteria by inhibiting FtsZ assembly a bundling. Biochemistry. 2005;44(50):16584–93.

169. Domadia P, Swarup S, Bhunia A, Sivaraman J, Dasgupta D. Inhibition of bacterial cell division protein FtsZ by cinnamaldehyde. Biochem Pharmacol. 2007;74(6):831–40.

170. Margalit DN, Romberg L, Mets RB, Hebert AM, Mitchison TJ, Kirschner MW, et al. Targeting cell division: small-molecule inhibitors of FtsZ GTPase perturb cytokinetic ring assembly and induce bacterial lethality. Proc Natl Acad Sci U S A. 2004;101(38):11821–6.

171. Ruiz-Avila LB, Huecas S, Artola M, Vergoñós A, Ramírez-Aportela E, Cercenado E, et al. Synthetic inhibitors of bacterial cell division targeting the GTP-binding site of FtsZ. ACS Chem Biol. 2013;8(9):2072–83.

172. Singh P, Jindal B, Surolia A, Panda D. A rhodanine derivative CCR-11 inhibits bacterial proliferation by inhibiting the assembly and GTPase activity of FtsZ. Biochemistry. 2012;51(27):5434–42.

173. Tsao D, Sutherland AG, Jennings L, Rush TI, Alvarez J, Ding W, et al. Discovery of novel inhibitors of the ZipA/FtsZ complex by NMR fragment screening coupled with structure-based design. Bioorganic Med Chem. 2006;14(23):7953–61.

174. Kenny C, Ding W, Kelleher K, Benard S, Dushin E, Sutherland A, et al. Development of a fluorescence polarization assay to screen for inhibitors of the FtsZ/ZipA interaction. Anal Biochem. 2003;323(2):224–33.

175. Sutherland AG, Alvarez J, Ding W, Foreman KW, Kenny H, Labthavikul P, et al. Structure-based design of carboxybiphenylindole inhibitors of the ZipA–FtsZ interaction. Org Biomol Chem. 2003;1(23):4138–40.

176. Hale CA, de Boer PAJ. Direct binding of FtsZ to ZipA, an essential component of the septal ring structure that mediates cell division in *E. coli*. Cell. 1997;88(2):175–85.

177. RayChaudhuri D. ZipA is a MAP-Tau homolog and is essential for structural integrity of the cytokinetic FtsZ ring during bacterial cell division. EMBO J. 1999;18(9):2372–83.

178. Liu Z, Mukherjee A, Lutkenhaus J. Recruitment of ZipA to the division site by interaction with FtsZ. Mol Microbiol. 1999;31(6):1853–61.

179. Moy FJ, Glasfeld E, Mosyak L, Powers R. Solution structure of ZipA, a crucial component of *Escherichia coli* cell division. Biochemistry. 2000;39(31):9146–56.

180. Mosyak L, Zhang Y, Glasfeld E, Haney S, Stahl M, Seehra J, et al. The bacterial cell-division protein ZipA and its interaction with an FtsZ fragment revealed by X-ray crystallography. EMBO J. 2000;19(13):3179–91.

181. Pichoff S, Lutkenhaus J. Tethering the Z ring to the membrane through a conserved membrane targeting sequence in FtsA. Mol Microbiol. 2005;55(6):1722–34.

182. Addinall SG, Lutkenhaus J. FtsA is localized to the septum in an FtsZ-dependent manner. J Bacteriol. 1996;178(24):7167–72.

183. Karimova G, Dautin N, Ladant D. Interaction network among *Escherichia coli* membrane proteins involved in cell division as revealed by bacterial two-hybrid analysis. J Bacteriol. 2005;187(7):2233–43.

184. Bork P, Sander C, Valencia A. An ATPase domain common to prokaryotic cell cycle proteins, sugar kinases, actin, and hsp70 heat shock proteins. Proc Natl Acad Sci U S A. 1992;89(16):7290–4.

185. Lara B, Rico AI, Petruzzelli S, Santona A, Dumas J, Biton J, et al. Cell division in cocci: Localization and properties of the *Streptococcus pneumoniae* FtsA protein. Mol Microbiol. 2005;55(3):699–711.

186. Feucht A, Lucet I, Yudkin MD, Errington J. Cytological and biochemical characterization of the FtsA cell division protein of *Bacillus subtilis*. Mol Microbiol. 2001;40(1):115–25.

187. Van den Ent F, Amos LA, Löwe J. Prokaryotic origin of the actin cytoskeleton. Nature. 2001;413(6851):39–44.

188. Loose M, Mitchison TJ. The bacterial cell division proteins FtsA and FtsZ self-organize into dynamic cytoskeletal patterns. Nat Cell Biol. 2014;16(1):38–46.

189. Haefner JW. Models of systems. Modeling biological systems: Principles and applications. 1997. p. 3–15.

190. Doucet P, Sloep P. Working with models. Mathematical modeling in the life sciences. 1992. p. 275–97.

191. Doucet P, Sloep P. Constructing models. Mathematical modeling in the life sciences. 1992. p. 300–23.

192. Mogilner A, Wollman R, Marshall WF. Quantitative Modeling in Cell Biology: What Is It Good for? Dev Cell. 2006;11(3):279–87.

193. Oosawa F, Kasai M. A theory of linear and helical aggregations of macromolecules. J Mol Biol. 1962;4:10–21.

194. Allard JF, Cytrynbaum EN. Force generation by a dynamic Z-ring in *Escherichia coli* cell division. Proc Natl Acad Sci U S A. 2009;106(1):145–50.

195. Lan G, Daniels BR, Dobrowsky TM, Wirtz D, Sun SX. Condensation of FtsZ filaments can drive bacterial cell division. Proc Natl Acad Sci U S A. 2009;106(1):121–6.

196. Surovtsev I V., Morgan JJ, Lindahl PA. Kinetic modeling of the assembly, dynamic steady state, and contraction of the FtsZ ring in prokaryotic cytokinesis. PLoS Comput Biol. 2008;4(7):e1000102.

197. Zhang Z, Morgan JJ, Lindahl PA. Mathematical model for positioning the FtsZ contractile ring in *Escherichia coli*. J Math Biol. 2014;68(4):911–30.

198. Loose M, Fischer-Friedrich E, Ries J, Kruse K, Schwille P. Spatial regulators for bacterial cell division self-organize into surface waves *in vitro*. Science. 2008;320(5877):789–92.

199. Meinhardt H, de Boer PA. Pattern formation in *Escherichia coli*: a model for the pole-to-pole oscillations of Min proteins and the localization of the division site. Proc Natl Acad Sci U S A. 2001;98(25):14202–7.

200. Ma XL, Margolin W. Genetic and functional analyses of the conserved C-terminal core domain of *Escherichia coli* FtsZ. J Bacteriol. 1999;181(24):7531–44.

201. Haney SA, Glasfeld E, Hale C, Keeney D, He Z, De Boer P. Genetic analysis of the *Escherichia coli* FtsZ-ZipA interaction in the yeast two-hybrid system. Characterization of FtsZ residues essential for the interactions with ZipA and with FtsA. J Biol Chem. 2001;276(15):11980–7.

202. Hale CA, De Boer PAJ. Recruitment of ZipA to the septal ring of *Escherichia coli* is dependent on FtsZ and independent of FtsA. J Bacteriol. 1999;181(1):167–76.

203. Lu C, Stricker J, Erickson HP. Site-specific mutations of FtsZ - effects on GTPase and *in vitro* assembly. BMC Microbiol. BioMed Central; 2001;1:7.

204. Marcelo F, Huecas S, Ruiz-Ávila LB, Cañada FJ, Perona A, Poveda A, et al. Interactions of bacterial cell division protein FtsZ with C8-substituted guanine nucleotide inhibitors. A combined NMR, biochemical and molecular modeling perspective. J Am Chem Soc. 2013;135(44):16418–28.

205. Phoenix P, Drapeau G. Cell division control in *Escherichia coli* K-12: Some properties of the *ftsZ84* mutations and suppression of this mutation by the product of a newly identified gene. J Bacteriol. 1988;170(9):4338–42.

206. Stricker J, Erickson HP. *In vivo* characterisation of *Escherichia coli ftsZ* mutants: Effects on Z-ring structure and function. J Bacteriol. 2003;185(16):4796–805.

207. RayChaudhuri D, Park JT. A point mutation converts *Escherichia coli* FtsZ septation GTPase to an ATPase. J Biol Chem. 1994;269(37):22941–4.

208. Oliva MA, Trambaiolo D, Löwe J. Structural insights into the conformational variability of FtsZ. J Mol Biol. 2007;373(5):1229–42.

209. Mohammadi T, Ploeger GEJ, Verheul J, Comvalius AD, Martos A, Alfonso C, et al. The GTPase activity of *Escherichia coli* FtsZ determines the magnitude of the FtsZ polymer bundling by ZapA *in vitro*. Biochemistry. 2009;48(46):11056–66.

210. Knowles TJ, Finka R, Smith C, Lin YP, Dafforn T, Overduin M. Membrane proteins solubilized intact in lipid containing nanoparticles bounded by styrene maleic acid copolymer. J Am Chem Soc. 2009;131(22):7484–5.

211. Orwick-Rydmark M, Lovett JE, Graziadei A, Lindholm L, Hicks MR, Watts A. Detergent-free incorporation of a seven-transmembrane receptor protein into nanosized bilayer lipodisq particles for functional and biophysical studies. Nano Lett. 2012;12(9):4687–92.

212. Ravi Prakash J. Micro and macro in the dynamics of dilute polymer solutions: Convergence of theory with experiment. Korea Aust Rheol J. 2009;21(4):245–68.

213. UK 5 year antimicrobial resistance strategy 2013 to 2018 [Internet]. Department of Health. 2013. Available from: https://www.gov.uk/government/publications/uk-5-year-antimicrobial-resistance-strategy-2013-to-2018

214. Centers for Disease Control and Prevention. Antibiotic resistance threats in the United States [Internet]. U.S. Department of Health and Human Servicesuman Services. 2013. Available from: http://www.cdc.gov/drugresistance/threat-report-2013/pdf/ar-threats-2013-508.pdf

215. Antimicrobial resistance: global report on surveillance 2014 [Internet]. WHO. 2014. Available from: http://www.who.int/drugresistance/documents/surveillancereport/en/

216. Surovtsev I V, Zhang Z, Lindahl PA, Morgan JJ. Mathematical modeling of a minimal protocell with coordinated growth and division. J Theor Biol. 2009;260(3):422–9.

217. Den Blaauwen T, Buddelmeijer N, Aarsman MEG, Hameete CM, Nanninga N. Timing of FtsZ assembly in *Escherichia coli*. J Bacteriol. 1999;181(17):5167–75.

218. Absolom DR, Lamberti F V, Policova Z, Zingg W, van Oss CJ, Neumann AW. Surface thermodynamics of bacterial adhesion. Appl Environ Microbiol. 1983;46(1):90–7.

219. Spelt JK, Absolom DR, Zingg W, van Oss CJ, Neumann AW. Determination of the surface tension of biological cells using the freezing front technique. Cell Biophys. 1982;4(2):117–31.

220. Yoneda M. Tension at the surface of sea-urchin egg: A critical examination of Cole's experiment. J Exp Biol. 1964;41:893–906.

221. Fischer-Friedrich E, Hyman A, Julicher F, Muller DJ, Helenius J. Quantification of surface tension and internal pressure generated by single mitotic cells. Sci Rep. 2014;4:6213.

222. Zlatanova J, Lindsay SM, Leuba SH. Single molecule force spectroscopy in biology using the atomic force microscope. Prog Biophys Mol Biol. 2000;74:37–60.

223. McAllister C, Karymov MA, Kawano Y, Lushnikov AY, Mikheikin A, Uversky VN, et al. Protein interactions and misfolding analyzed by AFM force spectroscopy. J Mol Biol. 2005;354(5):1028–42.

224. Margolin W. FtsZ and the division of prokaryotic cells and organelles. Nat Rev Mol Cell Biol. 2005 Nov;6(11):862–71.

225. Lu C, Erickson H. The straight and curved conformation of FtsZ protofilaments-evidence for rapid exchange of GTP into the curved protofilament. Cell Struct Funct. 1999;24(5):285–90.

226. Walker JM. Protein identification and analysis tools on the ExPASy server. The proteomics protocols handbook. 2005. p. 571–607.

A model of membrane contraction predicting initiation and completion of bacterial cell division

Claire E. Dow,[a,†] Alison Rodger,[*a,b], David I. Roper[c] and Hugo A. van den Berg[d]

***Integrative Biology*, 2013, 5(5):778-795**
Received 10th August 2012, Accepted 18th February 2013
First published on the web 21st February 2013
DOI: 10.1039/c3ib20273a

Bacterial cell division involves a complex and dynamic sequence of events whereby polymers of the protein FtsZ assemble at the division plane and rearrange to achieve the goal of contracting the cell membrane at the site of cell division, thus dividing the parent cell into two daughter cells. We present a mathematical model (which we refer to as CAM-FF: Critical Accumulation of Membrane-bound FtsZ Fibres) of the assembly of the contractile ring in terms of the accumulation of short linear polymers of FtsZ that associate and dissociate from the cell membrane. In prokaryotes, the biochemical function of FtsZ is thought to underpin the assembly and at least the initial kinetic force of ring contraction. Our model extends earlier work of Surovtsev *et al.* [*PLoS Computational Biology*, 2008, **4**, 7, e1000102] by adding (i) the kinetics of FtsZ accumulation on cell membrane anchor proteins and (ii) the physical forces required to deform the cell against its surface tension. Moreover, we provide a more rigorous treatment of intracellular diffusion and we revise some of the model parameter values in light of the experimental evidence now available. We derive a critical contraction parameter which links the chemical population dynamics of membrane-bound FtsZ molecules to the force of contraction. Using this parameter as a tool to predict the ability of the cell to initiate division, we are able to predict the division outcome in cells depleted of key FtsZ-binding proteins.

1 Introduction

Co-ordination of cell division, both temporally and spatially, is essential for the propagation of life through successive generations. A key event is the formation of a contractile ring, which is anchored to the cytoplasmic face of the cell membrane at the division plane. Following assembly, the ring contracts, drawing the membrane on opposite sides of the cell together. This divides the parent cell into two daughter cells.[1]

[a] *Molecular Organisation and Assembly in Cells Doctoral Training Centre, Coventry House, University of Warwick, Coventry, CV4 7AL, United Kingdom. E-mail: C.E.Dow@warwick.ac.uk*
[b] *Department of Chemistry and Warwick Centre for Analytical Science, University of Warwick, Coventry, CV4 7AL, United Kingdom*
[c] *School of Life Sciences, University of Warwick, Coventry, CV4 7AL, United Kingdom*
[d] *Mathematics Institute, University of Warwick, Coventry, CV4 7AL, United Kingdom*
[†] *The provision of funding by an EPSRC studentship through the MOAC Doctoral Training Centre is gratefully acknowledged*

In eukaryotic cells, contraction relies on the sliding force generated by the ATP-dependent interaction of the motor protein myosin and the structural actin filaments within a ring of polymeric actin fibres.[2] As yet no equivalent motor protein has been identified in prokaryotic cells.[3] Whereas in eukaryotes the major structural component is actin, in prokaryotes the ring consists primarily of a tubulin homologue, FtsZ,[4,5] and is referred to as the Z-ring.[6]

Although over two dozen additional proteins have hitherto been found to localise to the division site, evidence suggests that the assembly of the ring and the generation of contractile force are critically dependent on the protein FtsZ.[7] Indeed, purified FtsZ spontaneously forms linear head-to-tail polymers *in vitro*, as well as more complex structures, depending on experimental conditions.[8–11] Moreover, FtsZ is the only component of the division machinery that has homologues in almost all prokaryotic species so far analysed, including the minimal genome of *Mycoplasma genitalium*.[7] This suggests that the presence of FtsZ is a minimum requirement for division to occur. In addition, in *Escherichia coli*, FtsZ-deficient mutants show no indentation of the membrane, whereas mutation of other essential division genes results in some level of indentation even when full division fails.[12] In liposomes seeded with membrane-tethered FtsZ, Z-ring structures are apparent below regions of indented membrane.[13] These results suggest that the force of indentation is generated by FtsZ, at least initially.

Work reported by Surovtsev *et al.*[14] (which we shall refer to as the Surovtsev model) involved analysis of the assembly, maintenance, and contraction of the Z-ring based on kinetic parameters of FtsZ measured *in vitro*. Their model was the first to include the hydrolysis of GTP to GDP and the extension of linear polymers *via* head-to-tail annealing (see Figure 1B(iv)) in addition to polymer elongation by single FtsZ subunits, as used previously by Chen and Erickson[15] in a simpler model of FtsZ polymerisation. The Surovtsev model suggests that the Z-ring consists of long single-stranded FtsZ filaments that span the entire circumference of the cell and anneal head-to-tail to form closed polymers. There have been two mechanisms proposed for the contraction of a ring of such a structure: (i) a progressive increase in the lateral overlap of the two ends of the filament forming a spiral structure[16,17] or (ii) that proposed by Surovtsev *et al.*[14]: the progressive loss of FtsZ subunits following GTP hydrolysis with the open ends generated reannealing.

However, more recent evidence suggests that rather than being composed of long circular polymers, the Z-ring consists of shorter overlapping FtsZ filaments.[3,13] This remains consistent with the "Z-centric" hypothesis: that assembly and the force of constriction originate from FtsZ. In addition, our recent work determined the persistence length of FtsZ (*i.e.* the length over which the polymer naturally remains straight) to be 1.15 ± 0.25 μm.[18] This far exceeds previous estimates and makes it impossible for a single fibre to span the midcell circumference. Accordingly, the central aim of the present paper is to model the assembly of the Z-ring as a collection of shorter, membrane-bound, open filaments in the midcell region. Our model combines a substantial portion of the molecular kinetics developed by Surovtsev *et al.*[14], detailed here in Appendix A, but omits cyclisation as the driving force. We introduce diffusion of FtsZ into the midcell region as well as the interaction of FtsZ with membrane-bound anchor proteins, both additions to the Surovtsev model. Furthermore, we explicitly include the force exerted by

FtsZ polymers on the membrane. We also modify some parameter values in light of data determined since publication of the Surovtsev model in 2008.

Surovtsev *et al.* [19] have since incorporated their model of Z-ring assembly and contraction into a more complex model of protocell growth and division. They anticipate that the only viable path towards a whole-cell predictive model is *via* the collaborative development of individual modules to be added piecemeal to a global model. We present this work as a development of the Z-ring assembly and contraction module. Lan *et al.* [20] have modelled the deformation and inward growth of the bacterial cell wall originating from the small Z-ring force that deforms the cell with full division dependent on the remodelling of the peptidoglycan layer. We anticipate that this is complementary to our work and forms an additional module of the full cell division model. Our long-term goal is to link the current model with modules for: (i) membrane bending, (ii) the link to the outer membrane remodelling, and (iii) outer membrane remodelling.

§2 introduces the equations describing the dynamics of FtsZ polymerisation, much of which follows the work of Surovtsev *et al.* [14], and the concentration of FtsZ at the midcell membrane. §2 concludes with our new analysis of the force required for Z-ring contraction, leading to the definition of a key quantity which we call the *contraction parameter*. §3 shows that by implementing the wild-type parameter values, estimated from the current experimental literature, the model solutions are in accordance with the properties of the Z-ring measured *in vivo*. In §4 we show that the contraction parameter is a useful tool to predict the division outcome in cells, such as on depletion of the membrane-anchor proteins. §5 contains an analysis of the model assumptions.

2 Model

In the nascent daughter cell, FtsZ monomers are dispersed throughout the cytosol. [21] Formation of the Z-ring for the next cell division therefore requires polymerisation of FtsZ, polymer localisation at the midcell and polymer anchoring to the cell membrane. In the present model, which we refer to as CAM-FF: Critical Accumulation of Membrane-bound FtsZ Fibres, the cell is conceptually divided into three compartments: the midcell region, the adjoining cell caps, and the midcell membrane, as shown in Figure 1A. All FtsZ molecules are initially monomeric and dispersed within the cell caps and midcell compartments. A system of ordinary differential equations (ODEs) describes the changes in the concentrations of FtsZ molecules within the three compartments over time, as detailed in Appendix B. FtsZ molecules within the cell caps and the midcell region undergo the polymerisation and GTP hydrolysis reactions as shown in Figure 1B. Movement between these two compartments is by diffusion. Movement occurs from the midcell region to the midcell membrane when FtsZ molecules bind to anchor sites fixed to the membrane and *via* polymerisation reactions between membrane-bound FtsZ and free (unbound) FtsZ in the midcell region. The model explicitly accommodates the interaction of single FtsZ polymers with multiple membrane anchor sites as depicted in Figure 1C. Once bound to the membrane, the length of the polymer may increase by the addition of unbound FtsZ monomers and polymers but we assume that polymerisation reactions do not occur between membrane-bound FtsZ molecules due to the low density of anchor molecules on the membrane surface.

There is evidence of some polymerisation on the surface in the data from Mateos-Gil *et al.* [22] but this is at 40 times the density of the *in vivo* situation. GTP hydrolysis and polymer dissociation are assumed to occur within membrane-bound polymers in the same way as for free polymers. We do not include the lateral interaction of FtsZ polymers since, according to Erickson [23], when the subunit entropy contribution is considered, a contraction mechanism based on FtsZ polymer sliding is implausible. Thus the FtsZ:FtsZ lateral interactions are not expected to make an essential contribution to membrane contraction.

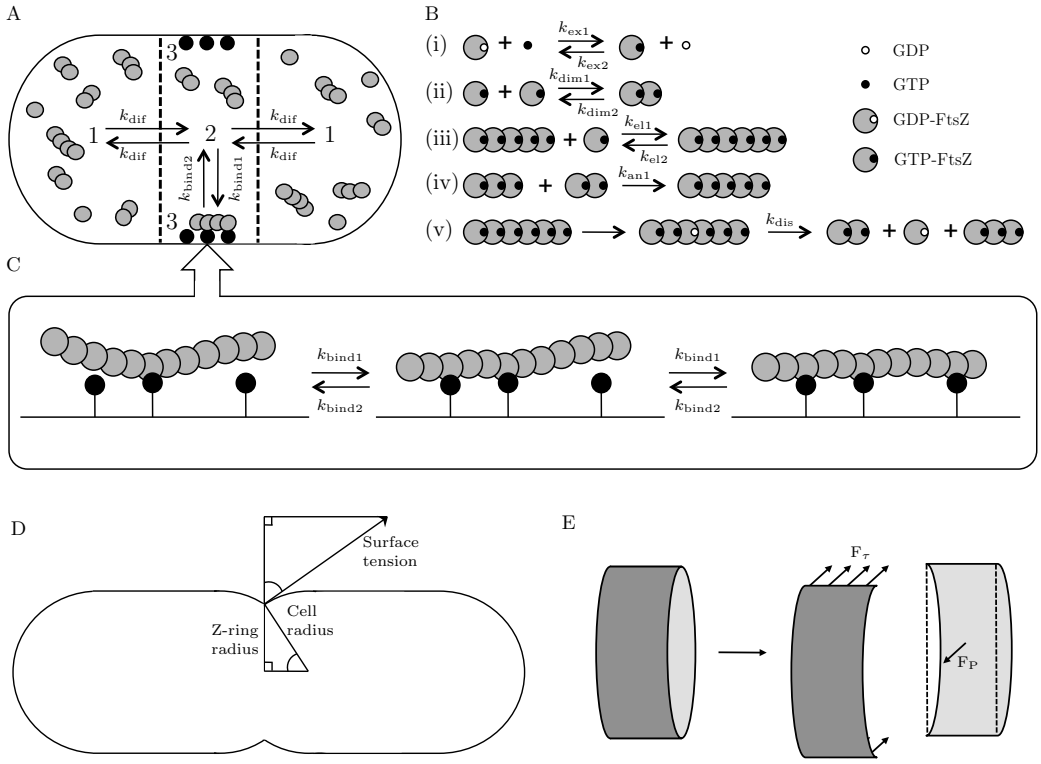

Fig. 1 Schematic diagram of the cell model used in this work. (A) The cell is conceptually divided into three compartments: the cell caps (1), the midcell (2), and the midcell membrane (3). FtsZ moves between the cell caps and the midcell regions by diffusion. Exchange between the midcell region and the midcell membrane is *via* the interaction of FtsZ with membrane anchor sites and subsequent polymerisation. (B) Using the notation of Surovtsev *et al.* [14], the chemical reactions in our model are: nucleotide exchange (i), dimerisation (ii), and elongation (iii) (reversible processes) and annealing (iv) (assumed to be irreversible in the absence of GTP hydrolysis) and polymer breakdown following GTP hydrolysis (v) (also irreversible). (C) Depending on the anchor density, an FtsZ polymer may bind to multiple anchor sites. As polymer length increases, the number of anchor connections increases thereby lowering the probability that the polymer will be released from the membrane. (D) Z-ring contraction pulls the membrane inwards against the outward force from the cell surface tension. (E) For the slice through the Z-ring, at equilibrium the horizontal force due to the ring tension (F_τ) is balanced by the internal pressure acting over the cross-sectional area of the slice (F_P).

2.1 FtsZ polymerisation and GTP hydrolysis: the Surovtsev model rewritten

The molecular kinetics of FtsZ polymerisation and GTP hydrolysis/dissociation summarised in Equations (1) to (6) are the rate equations as proposed by Surovtsev *et al.*[14]. FtsZ is a GTP/GDP-binding protein that interconverts GTP and GDP.[24] The nucleotide-binding site is exposed to the cytosol allowing for a bound nucleotide to be released, leaving the site open for another nucleotide to bind in nucleotide exchange. The relative concentrations of GTP-bound and GDP-bound FtsZ monomers therefore depend on the relative concentrations of GTP and GDP in the cytosol. In CAM-FF, all FtsZ monomers are initially GDP-bound reflecting the starting point for some *in vitro* experiments[25] and the depolymerisation of the Z-ring in the previous cell division event.[21] The rates of nucleotide exchange for monomeric FtsZ in solution are given by

$$R_{\mathrm{ex1}} = k_{\mathrm{ex1}}\,[\mathrm{GTP}]\,Z_{\mathrm{D}} \quad \text{and} \quad R_{\mathrm{ex2}} = k_{\mathrm{ex2}}\,[\mathrm{GDP}]\,Z_{\mathrm{T}}\,, \tag{1}$$

where Z_{D} and Z_{T} are the concentrations of GDP-bound and GTP-bound FtsZ monomers, respectively. In the GTP-bound state, FtsZ molecules polymerise rapidly *in vitro* forming head-to-tail subunit chains.[10] In CAM-FF, the rates of dimerisation and elongation of GTP-bound FtsZ are given by forward and reverse rates,

$$R_{\mathrm{dim1}} = k_{\mathrm{dim1}}\,Z_{\mathrm{T}}^2\,, \quad R_{\mathrm{dim2}} = k_{\mathrm{dim2}}\,Z_2 \tag{2}$$

and

$$R^i_{\mathrm{el1}} = k_{\mathrm{el1}}\,Z_{\mathrm{T}}\,Z_i\,, \quad R^i_{\mathrm{el2}} = k_{\mathrm{el2}}\,Z_{i+1}\,, \tag{3}$$

respectively, where Z_2 is the concentration of FtsZ dimers and Z_i is the concentration of FtsZ polymers of length i subunits. We assume the rate of elongation does not depend on the length i. The rates of dimerisation and elongation of GDP-bound FtsZ are assumed to be zero.[10] We assume the forward rates of dimerisation and elongation to be equal; for the corresponding dissociation, the rate constant has been found to be higher for the dissociation of FtsZ dimers than for the dissociation of FtsZ polymers.[26] This is reflected in the values of the rate constants k_{dim2} and k_{el2}, see §3.

Polymer length can also increase by annealing reactions, in which a polymer of length i is formed by the annealing of a polymer of length j to a polymer of length $i-j$. This occurs with rate

$$R^i_{\mathrm{an1}} = k_{\mathrm{an}} \sum_{j=2}^{i-2} \frac{1+\delta_{j\,i-j}}{2}\,Z_j\,Z_{i-j}\,, \tag{4}$$

and the removal of polymers due to annealing is given by

$$R^i_{\mathrm{an2}} = k_{\mathrm{an}}\,Z_i \sum_{j=2}^{i_{\mathrm{max}}-i} (1+\delta_{i\,j})\,Z_j\,, \tag{5}$$

where i_{max} is the maximum length polymer that can form in the model. In principle, the model should allow for arbitrarily long filaments, *i.e.* $i_{\mathrm{max}} \to \infty$, but for the purpose of calculation a cut-off value is selected that is sufficiently large such that the results do not depend on the value chosen. We do not include reverse rates

for the annealing reaction since we assume that depolymerisation does not occur in the absence of GTP hydrolysis.

On polymerisation, a GTPase active site is formed when a catalytic aspartate residue of one subunit inserts into the GTP-binding pocket of the adjacent subunit.[27,28] Once polymerised, the nucleotide state of an FtsZ subunit may therefore switch from GTP-bound to GDP-bound. *In vitro*, depletion of GTP leads to net depolymerisation, which suggests that the GDP-bound polymers are unstable.[10] Surovtsev *et al.*[14] assumed that upon GTP hydrolysis, the GDP-bound subunit dissociates from the intact polymers on either side instantaneously. Since this does not account for the 20-50% of FtsZ subunits in polymers in the GDP-bound form, we use the following equivalent rate equation:

$$R^i_{\mathrm{dis}} = (i-1)\, k_{\mathrm{dis}} Z_i \ , \tag{6}$$

where a polymer of length i has $i-1$ GTPase active sites. However, instead of the hydrolysis rate of 0.15 s^{-1} as used by Surovtsev *et al.*[14], to account for the rate of dissociation of FtsZ following hydrolysis, we use the value of k_{cat} from Romberg and Mitchison[25] of 4.5 min^{-1} per FtsZ to give $k_{\mathrm{dis}} = 0.075\ \mathrm{s}^{-1}$. The rate constant k_{dis} is equal for all GTPase active sites since it has been shown that all monomer interfaces are equally competent for hydrolysis.[22] The significance of the change in the model is that we now account for the time spent by FtsZ subunits within polymers in the GDP-bound state following hydrolysis, prior to dissociation.

2.2 Novel features of our membrane contraction model

2.2.1 FtsZ diffusion. In CAM-FF, we consider the change in the midcell concentration due to diffusion from the cell caps to the midcell for FtsZ molecules of length i to be given by

$$R^i_{\mathrm{cm}} = k_{\mathrm{dif}}(Z^{\mathrm{cc}}_i - Z^{\mathrm{mid}}_i)/V_{\mathrm{mid}} \ , \tag{7}$$

and that for the diffusion from the midcell to the cell caps to be

$$R^i_{\mathrm{mc}} = k_{\mathrm{dif}}(Z^{\mathrm{mid}}_i - Z^{\mathrm{cc}}_i)/V_{\mathrm{cc}} \ , \tag{8}$$

where k_{dif} is the diffusion constant, which is assumed to be equal for all values of i, and V_{cc} and V_{mid} are the volumes of the cell caps and midcell compartments, respectively. The rate of diffusion defined in Equations (7) and (8) applies to all polymer lengths and for both GDP- and GTP-bound FtsZ monomers.

The process of diffusion without any other factor will ensure a uniform concentration of FtsZ throughout the cell. To model the accumulation of FtsZ at the midcell and the physical attachment that confers a pinching force, we introduce to our model a compartment corresponding to the midcell membrane.

2.2.2 Membrane binding: Interaction of FtsZ polymers with multiple binding sites. To anchor to the cell membrane *in vivo*, FtsZ interacts directly with the membrane-binding proteins proteins ZipA and FtsA.[29] The anchoring means that if the Z-ring constricts, it exerts a pinching force on the cell membrane.

The rate of attachment of the FtsZ polymers within the midcell compartment is given by

$$R^i_{\text{bind1}} = i k_{\text{bind1}} Z^{\text{mid}}_i \left(\frac{10^{21} B}{N_{\text{A}} V_{\text{bnd}}} - \left(Z^{\text{bnd}}_{\text{D}} + Z^{\text{bnd}}_{\text{T}} + \sum_{j=2}^{i_{\max}} S(j) Z^{\text{bnd}}_j \right) \right) , \tag{9}$$

for $i \geq 2$, where B is the total number of binding sites, V_{bnd} is the volume of the midcell membrane compartment, N_{A} is Avogadro's number and $S(j)$ is the expected number of binding sites occupied by a polymer of length j. Multiplication by i reflects the number of potential anchor binding sites along an FtsZ polymer of length i. GDP- and GTP-bound monomers may bind to the midcell membrane with rates given by

$$R^{\text{D}}_{\text{bind1}} = k_{\text{bind1}} Z^{\text{mid}}_{\text{D}} \left(\frac{10^{21} B}{N_{\text{A}} V_{\text{bnd}}} - \left(Z^{\text{bnd}}_{\text{D}} + Z^{\text{bnd}}_{\text{T}} + \sum_{j=2}^{i_{\max}} S(j) Z^{\text{bnd}}_j \right) \right) \tag{10}$$

and

$$R^{\text{T}}_{\text{bind1}} = k_{\text{bind1}} Z^{\text{mid}}_{\text{T}} \left(\frac{10^{21} B}{N_{\text{A}} V_{\text{bnd}}} - \left(Z^{\text{bnd}}_{\text{D}} + Z^{\text{bnd}}_{\text{T}} + \sum_{j=2}^{i_{\max}} S(j) Z^{\text{bnd}}_j \right) \right) , \tag{11}$$

respectively. Release from the membrane is given by

$$R^i_{\text{bind2}} = k_{\text{bind2}} p_1(i) Z^{\text{bnd}}_i \quad \text{for } i \geq 2 , \tag{12}$$

where $p_1(i)$ is the fraction of polymers of length i expected to be attached to the membrane by a single binding site only. For GDP- and GTP-bound monomers, the rates of release are given by

$$R^{\text{D}}_{\text{bind2}} = k_{\text{bind2}} Z^{\text{bnd}}_{\text{D}} \quad \text{and} \quad R^{\text{T}}_{\text{bind2}} = k_{\text{bind2}} Z^{\text{bnd}}_{\text{T}} , \tag{13}$$

respectively. On release, polymers return to the midcell soluble population.

To determine $p_1(i)$, the binding of polymers to multiple binding sites is modelled as a Markov chain with a fixed number of binding sites available. We assume that the anchor proteins interact with single FtsZ subunits allowing a polymer of length i subunits to potentially form i membrane interactions.

At equilibrium, the fraction of polymers bound to a single binding site is given by

$$f^j_1 = \frac{j}{\kappa(1+\frac{1}{\kappa})^j - \kappa} , \tag{14}$$

where j is the number of binding sites available and κ is the dissociation constant. A full derivation of Equation (14) is given in Appendix C. Since each anchor interacts with a single FtsZ subunit within the polymer, the probability that j binding sites are available to a polymer of length i is given by

$$\mathrm{P}(j \text{ sites}) = \binom{i}{j} \frac{\mathrm{P}_a^j (1-\mathrm{P}_a)^{i-j}}{1-(1-\mathrm{P}_a)^i} \,, \tag{15}$$

where P_a is the probability that one FtsZ subunit is adjacent to a binding site. This equation is derived by conditioning the binomial distribution on at least one binding site being available, since for a molecule in the membrane-bound fraction, this condition is satisfied. The fraction expected to be attached by a single anchor is the expectation of fractions for all values of j from 1 to i:

$$p_1(i) = \sum_{j=1}^{i} \binom{i}{j} \frac{\mathrm{P}_a^j (1-\mathrm{P}_a)^{i-j}}{1-(1-\mathrm{P}_a)^i} \cdot \frac{j}{\kappa(1+\frac{1}{\kappa})^j - \kappa} \,. \tag{16}$$

Since a polymer is held on the membrane until the final FtsZ-anchor interaction is broken, adjustment of the rate of release using the fraction of polymers in the singly-bound state accounts for the binding to multiple sites.

The binding rate is proportional to the number of available binding sites. The available number depends on the total number of binding sites and the number of occupied binding sites, which itself depends on the membrane-bound FtsZ population. The expected number of sites occupied by a chain of length i is given by

$$S(i) = \frac{\mathrm{P}_a\, i}{1-(1-\mathrm{P}_a)^i} \,, \tag{17}$$

which is again conditional on at least one site being occupied by a membrane-bound polymer.

2.2.3 Polymerisation of membrane-bound FtsZ. For membrane-bound monomeric FtsZ, we assume that nucleotide exchange occurs as for soluble FtsZ, *cf.* Equation (1). The extension of membrane-bound FtsZ polymers occurs by interaction with unbound, soluble FtsZ in the midcell region. By analogy to Equations (2) and (3) for soluble FtsZ, the rates of dimerisation and elongation of membrane-bound FtsZ are given by

$$R_{\mathrm{dim1\_bnd}} = k_{\mathrm{dim1}}\, Z_{\mathrm{T}}^{\mathrm{mid}}\, Z_{\mathrm{T}}^{\mathrm{bnd}} \,, \quad R_{\mathrm{dim2\_bnd}} = k_{\mathrm{dim2}}\, Z_2^{\mathrm{bnd}} \tag{18}$$

and

$$R^i_{\mathrm{el1\_bnd}} = k_{\mathrm{el1}}\, Z_{\mathrm{T}}^{\mathrm{mid}}\, Z_i^{\mathrm{bnd}} \,, \quad R^i_{\mathrm{el2\_bnd}} = k_{\mathrm{el2}}\, Z_{i+1}^{\mathrm{bnd}} \,, \tag{19}$$

respectively. For the reverse reactions, it is assumed that a GTP-bound FtsZ monomer returns to the midcell region while the shortened polymer (which is a GTP-bound monomer in the case of the reverse of dimerisation) remains bound to the midcell membrane. The rate of polymer annealing is given by

$$R^i_{\mathrm{an1\_bnd}} = k_{\mathrm{an}} \sum_{j=2}^{i-2} Z_j^{\mathrm{bnd}}\, Z_{i-j}^{\mathrm{mid}} \,, \tag{20}$$

with the removal of polymers due to annealing given by

$$R^i_{\text{an2\_bnd}} = k_{\text{an}} Z_i^{\text{mid}} \sum_{j=2}^{i_{\max}-i} Z_j^{\text{bnd}} , \tag{21}$$

and

$$R^i_{\text{an2\_mid}} = k_{\text{an}} Z_i^{\text{bnd}} \sum_{j=2}^{i_{\max}-i} Z_j^{\text{mid}} , \tag{22}$$

for the midcell region and midcell membrane, respectively. The Kronecker delta used in Equations (4) and (5) for the annealing reactions of soluble FtsZ is not required since the double-counted combinations for the soluble case are no longer equivalent in the case of interaction of a membrane-bound population with a soluble population. As for soluble FtsZ, the annealing reactions are assumed to be irreversible. The value of rate constants for dimerisation, elongation, and annealing are assumed in the model to be equal to those for reactions between soluble FtsZ.

2.2.4 Hydrolysis of membrane-bound polymers. The GDP-bound subunit and the shorter polymer(s), generated by the polymer cleavage that follows a hydrolysis/dissociation event, may remain bound to the membrane or may return to the soluble midcell compartment, depending on their attachment to adjacent binding sites. For a parent polymer of length i', the probability that any subunit is adjacent to a binding site is given by

$$\text{P(site adjacent} \mid i') = \frac{\text{P}_a}{1-(1-\text{P}_a)^{i'}} . \tag{23}$$

Therefore, for a polymer of length i, formed as a result of a hydrolysis/dissociation reaction, the probability that the polymer returns to the midcell compartment is the probability that none of the i subunits is adjacent to a binding site which is given by

$$\text{P}_i\text{(no sites} \mid i') = \left(1 - \frac{\text{P}_a}{1-(1-\text{P}_a)^{i'}}\right)^i . \tag{24}$$

The probability that a polymer remains in the membrane-bound fraction is therefore $[1-\text{P}_i\text{(no sites} \mid i')]$. It is assumed that the fraction of those with at least one adjacent binding site will join the population of membrane-bound polymers of length i. The interaction of FtsZ with FtsA or ZipA does not affect the rate of GTP hydrolysis *in vitro*.[30,31] Therefore, the rate of dissociation of membrane-bound polymers remains as given by Equation (6) for soluble FtsZ in § 2.1.

We do not directly account for the potential of membrane-bound polymers to reanneal after fragmentation. However, the increased likelihood that a GTP hydrolysis/dissociation event occurring towards either end of the FtsZ polymer results in permanent loss of subunits from the polymer, compared to a GTP hydrolysis/dissociation event in the centre of the polymer, as found by Mateos-Gil *et al.* [22], is accounted for in CAM-FF. By calculation of the number of binding sites available to the polymer fragments produced on dissociation, smaller polymers are less likely to be bound to an anchor and so are more likely to move back to the soluble fraction with loss from the Z-ring. Although fragments that remain bound do not reanneal, they are available for reannealing to free (unbound) FtsZ polymers and remain within the Z-ring compartment.

2.2.5 Tension in the Z-ring. Two key properties govern Z-ring contraction. The first is the total tension of the Z-ring, τ_Z, defined in terms of the cell surface tension and the radius of the Z-ring as contraction proceeds. The second is the maximum tension the Z-ring can withstand, $\hat{\tau}$, at a given radius, ς, based on the population of FtsZ polymers assembled and the force of the interaction between FtsZ and the membrane anchor. The analysis shown in Appendix D, in which the components of the cell surface tension and the forces acting on the Z-ring are considered as in Figure 1D and Figure 1E respectively, shows that τ_Z, the total tension of the Z-ring during contraction, is given by

$$\tau_Z = \tau_0 \left(1 + \frac{2r}{\omega}\rho\sqrt{1-\rho^2}\right) , \tag{25}$$

where τ_0 is the cell surface tension, ω is the width of the Z-ring, and $\rho = \varsigma/r$ is the dimensionless ratio of the radius of the Z-ring during contraction, ς, to the radius of the Z-ring before contraction, r. For the sake of simplicity, the parameters τ_0 and ω are assumed to be constant throughout the contraction process.

As shown in Appendix D, the maximum tension the Z-ring can withstand $\hat{\tau}$ is given by

$$\hat{\tau} = F\,\frac{\mathrm{P}_a l_0}{\omega r}\,.\,\frac{\bar{i}^2 N_Z}{\rho} , \tag{26}$$

where F is proportional to the force of the interaction of FtsZ with a single anchor site, l_0 is the length of one FtsZ subunit, $\bar{i}$ is the average number of subunits per polymer, and N_Z is the total number of polymers bound to the membrane.

In the model, the sign of $\frac{\mathrm{d}}{\mathrm{d}t}(\varsigma)$ agrees with that of $(\tau_Z - \hat{\tau})$ because it is assumed that this difference will drive the contraction. The precise functional form of the relationship depends on the molecular mechanism of contraction, which remains to be elucidated. In the absence of detailed data, a simple linear relationship is proposed:

$$\frac{\mathrm{d}}{\mathrm{d}t}\varsigma = \vartheta_0\,(\tau_Z - \hat{\tau}) , \tag{27}$$

where ϑ_0 is a constant. Substituting the total ring tension and maximum sustainable tension, defined in Equations (25) and (26) respectively, gives an ODE for the rate of change of the dimensionless ratio ρ, the size of the ring relative to its starting size:

$$\frac{\mathrm{d}}{\mathrm{d}t}\rho = \vartheta\left(\alpha\left(1+\gamma\rho\sqrt{1-\rho^2}\right) - \frac{\bar{i}^2 N_Z}{\rho}\right) , \tag{28}$$

where

$$\vartheta \triangleq \frac{\vartheta_0 F \mathrm{P}_a l_0}{\omega r} , \quad \alpha \triangleq \frac{\tau_0 \omega r}{F \mathrm{P}_a l_0} , \quad \text{and} \quad \gamma \triangleq \frac{2r}{\omega} . \tag{29}$$

Left implicit in this parametrisation are the details of membrane bending energy and the molecular reorganisation that occurs concomitantly with the contraction. A full model of bacterial cell division would complement CAM-FF with a membrane remodelling module. Contraction corresponds to the rate of change of ρ being negative. Therefore, contraction proceeds if and only if

$$\bar{i}^2 N_Z > \alpha\rho\,(1+\gamma\rho\sqrt{1-\rho^2}) . \tag{30}$$

The ability of the cell to divide thus depends on the value of the *contraction parameter*:

$$\chi \triangleq \bar{i}^2 N_Z \,. \tag{31}$$

Initially, $\rho = 1$ and contraction therefore begins when $\chi > \alpha$. Numerical solution of the system of ODEs, given in full in Appendix B, allows determination of χ under various biological scenarios and prediction of the ability of cells to initiate and sustain division (since Equation (30) also tells us if contraction stops).

Since the average length of polymers $\bar{i}$ is squared in the calculation of the contraction parameter, for a given number of FtsZ subunits bound to the membrane, a smaller number of longer polymers are expected to collectively exert a stronger contractile force than a larger number of shorter polymers.

3 Estimation of wild-type rate constants

Surovtsev *et al.* [14] selected rate constants based on the best available experimental data. However, we use a lower value of $[\text{FtsZ}]_{\text{Total}}$. Based on the 15,000 molecules of FtsZ per cell found by Lu *et al.* [32], making $[\text{FtsZ}]_{\text{Total}} = 12\ \mu\text{M}$. Although lower values for the number of FtsZ molecules have been found,[33,34] we have chosen to use the highest of the recorded numbers and the full cell volume to calculate the corresponding concentration. The effective volume available to the FtsZ will be lower than the cell volume, making our choice a reasonable "average" that ensures the FtsZ concentration exceeds the critical concentration for polymerisation.[35] We retain the values used by Surovtsev *et al.* [14] for [GTP], [GDP] and $i_{\max}$. The value of $i_{\max} = 150$ subunits is consistent with the average length of FtsZ polymers measured *in vitro* using transmission electron microscopy of 23 subunits.[36] We have ensured that this is sufficiently large that the results are independent of its value. An increase in the value to $i_{\max} = 200$ does not change the predicted average lengths of free and membrane-bound FtsZ polymers, the predicted number of membrane-bound FtsZ molecules nor the predicted percentage of FtsZ incorporation into the Z-ring. We also follow Surovtsev *et al.* [14] in representing the cell as a cylinder with radius 0.4 μm, length 4 μm, and midcell region width 0.1 μm. In contrast to them, we include the whole midcell slice, as shown in Figure 2, not just a region of depth 8 nm. The volumes of the cell caps and midcell regions are therefore $V_{\text{cc}} = 2.0\ \mu\text{m}^3$ and $V_{\text{mid}} = 0.05\ \mu\text{m}^3$ respectively. For the midcell radius of 0.4 μm and the midcell width of 0.1 μm, this corresponds to a midcell membrane surface area of 0.25 μm^2. The depth of the midcell membrane was set to 4 nm (the size of an FtsZ subunit) giving a volume $V_{\text{bnd}} = 1.0 \times 10^{-3}\ \mu\text{m}^3$. As the diffusion constant D of ovalbumin, which is of similar size to FtsZ, is 78 $\mu\text{m}^2\text{s}^{-1}$,[37] we use this value for the diffusion constant of FtsZ. Fick's Law gives the flux across the diffusion area A equal to $\frac{AD}{L}\Delta C$ where ΔC is the concentration difference between the two compartments and L is the distance between the midpoint of the two compartments, in this case 1 μm. In our model, the flux in equivalent units is given by $k_{\text{dif}}(Z_i^{\text{cc}} - Z_i^{\text{mid}})$, Equation (7), whence $k_{\text{dif}}\Delta C = \frac{AD}{L}\Delta C$. Therefore, $k_{\text{dif}} = \frac{AD}{L}$. The value for the diffusion area A is given by the bounding area of the midcell slice, $2\pi r^2$, see Figure 2, giving $k_{\text{dif}} \approx 78\ \mu\text{m}^3\text{s}^{-1}$. This is equal to the original value of the diffusion constant D since the diffusion distance is taken as 1 μm and the area of the boundaries of the slice are approximately equal to 1 μm^2 for a radius

of 0.4 μm.

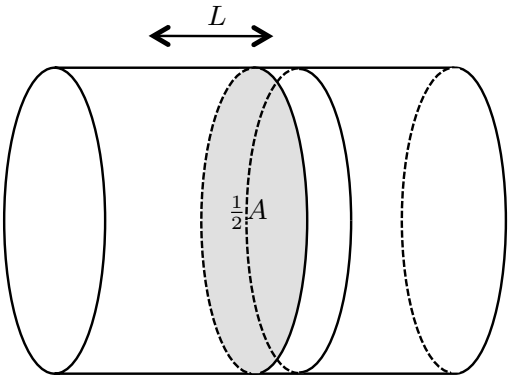

Fig. 2 The rate constant for the diffusion of FtsZ from the cell caps into the midcell region, k_{dif}, is estimated using Fick's Law assuming diffusion through area A along a path of length L.

A key parameter in our model is the fraction of membrane-bound FtsZ polymers which are in the singly-bound state. This depends on the probability that a subunit is adjacent to a binding site, P_a, and on the dissociation constant κ. We assume the two anchor interactions (ZipA and FtsA) have the same binding strength. The FtsEX complex may play an additional anchoring role since FtsX is an integral membrane protein and is linked to FtsZ via the soluble protein FtsE.[38,39] However, the role of FtsEX in cell division is unclear and key data are missing, such as the number of molecules per cell. The anchoring role of FtsEX has, for now, been omitted. The experimental literature cites the number of molecules per cell for ZipA and FtsA as 1500 and 740, respectively[33] and using fluorescent-labelled ZipA, Stricker *et al.*[40] found that approximately 30% of the cell complement of ZipA localises to the Z-ring *in vivo*. Therefore, it is assumed that 30% of the cell complement of anchors are found in the midcell membrane compartment. By dividing the surface area of the membrane into a grid of squares 4 nm $\times$ 4 nm, P_a is given by the proportion of grid squares occupied by 30% of the total number of anchor proteins. This gives $P_a = 0.043$. The wild-type dissociation constant of 0.2 μM for the FtsZ-ZipA (and hence the other) interactions was used to give κ.[41] Figure 3 shows $p_1(i)$, the fraction of polymers expected to be attached to the membrane by a single binding site only, for $P_a = 0.043$ and $\kappa = 0.2$ μM. The high proportion of polymers that remain in the singly-bound state for shorter lengths reflects the observation that although an FtsZ polymer of length i has the potential to form i FtsZ:anchor interactions, ZipA interacts with FtsZ substoichiometrically.[42] The interaction data presented by Martos *et al.*[42] show that oligomers of FtsZ, up to hexamers, bind to a single ZipA molecule. This is reflected in the model as the predicted number of anchor proteins occupied by FtsZ oligomers at the membrane is 1 for an FtsZ monomer, up to 1.11 for a hexamer.

Fluorescence recovery after photobleaching (FRAP) experiments have shown the half life of recovery of fluorescence in the Z-ring for wild-type FtsZ in *E. coli* to be 30 sec.[40] Since the recovery of fluorescence in the bleached patch of the Z-ring is exponential, the observed rate of recovery is given by $\ln 2/t_{1/2}$. For a half life of recovery of 30 seconds, the corresponding observed rate of release from the membrane is 0.023 s^{-1}. Since the steady state of Z-ring assembly has been reached

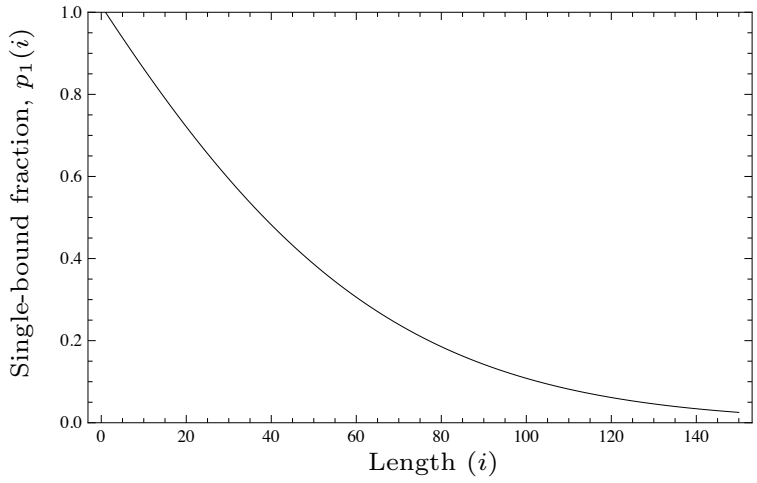

Fig. 3 The fraction of membrane-bound polymers expected to be attached by a single FtsZ-anchor interaction, as a function of polymer length for $P_a = 0.043$ and $\kappa = 0.2\ \mu$M.

prior to the photobleaching, it follows that $k_{\text{bind2}} p_1(\bar{i})$ (see Equations (12) and (16)) equals 0.023 s^{-1} (where $\bar{i}$ is the average membrane-bound polymer length at equilibrium). With the dissociation constant κ fixed at 0.2 μM, it follows that the lower bounds of k_{bind1} and k_{bind2} are 0.142 $\mu M^{-1} s^{-1}$ and 0.0284 s^{-1}, respectively.

For the wild-type parameter values as shown in Table 1, the NDSolve function of Wolfram *Mathematica* 8 was used to numerically solve the ODEs as provided in Appendix B. As described in Appendix E, including both the diffusion of FtsZ into the midcell region in a more physically realistic manner and an explicit model of membrane binding, prevents the truncation artefact arising in the Surovtsev model where long polymers accumulate thus increasing the concentrations of large polymers up to $i_{\max}$. CAM-FF predicts that the average FtsZ polymer length for the membrane-bound population is 14 subunits, which is considerably lower than in the Surovtsev model.[14] The average membrane-bound FtsZ polymer length of 14 subunits for the total of 504 polymers membrane-bound at equilibrium, gives a total polymer length of 29.3 μm. This is sufficient to span the circumference over 11 times. This overlap of short FtsZ filaments on the membrane is consistent with the hypothesis that Z-ring formation proceeds by overlap of short FtsZ polymers.[13] In the wild-type, our model predicts that the average polymer length at equilibrium for soluble FtsZ is 4 subunits in both the cell caps and midcell regions.

In the Surovtsev model, 80% of the cell complement of FtsZ was found at the midcell due to the enforced confinement to this region.[14] In CAM-FF, the percentage incorporation of FtsZ into the membrane-bound Z-ring is predicted to be 28%, in accordance with the value measured experimentally of 30–35%.[40,44]

Figure 4 shows the value of the contraction parameter χ over time for the wild type. The contraction parameter increases reaching its maximum value on formation of the Z-ring.

Table 1 Wild-type parameter values

Parameter	Wild-type value	Units	Reference
$[\mathrm{FtsZ}]_{\mathrm{Total}}$	20	μM	14
[GTP]	90	μM	14
[GDP]	10	μM	14
B	672	-	33
P_a	0.043	-	14,33
κ	0.2	μM	41
i_{max}	150	-	14
k_{ex1}	0.01	$\mu\mathrm{M}^{-1}\mathrm{s}^{-1}$	14,26,43
k_{ex2}	0.005	$\mu\mathrm{M}^{-1}\mathrm{s}^{-1}$	14,26,43
k_{dim1}	4	$\mu\mathrm{M}^{-1}\mathrm{s}^{-1}$	14,26
k_{dim2}	40	s^{-1}	14,26
k_{el1}	4	$\mu\mathrm{M}^{-1}\mathrm{s}^{-1}$	14,26
k_{el2}	0.4	s^{-1}	14,26
k_{an}	4	$\mu\mathrm{M}^{-1}\mathrm{s}^{-1}$	14,26
k_{dis}	0.15	s^{-1}	25
k_{dif}	78	$\mu\mathrm{m}^3\mathrm{s}^{-1}$	37
k_{bind1}	0.142	$\mu\mathrm{M}^{-1}\mathrm{s}^{-1}$	40,41
k_{bind2}	0.0284	s^{-1}	40,41

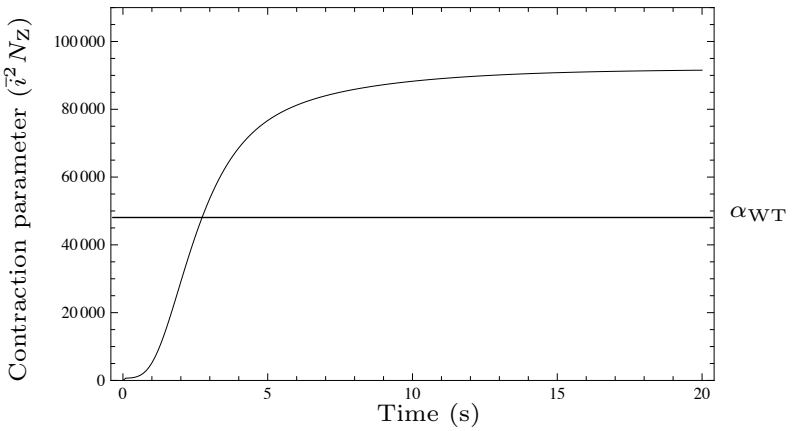

Fig. 4 The contraction parameter χ increases to a maximum value on formation of the Z-ring. Parameter values as shown in Table 1.

4 The contraction parameter predicts division outcome

The key parameter in CAM-FF is the contraction parameter χ which is a useful tool to predict the ability of cells to initiate and continue Z-ring contraction. Once contraction is initiated, the evolution of both the contraction parameter and the contraction threshold determines whether Z-ring constriction proceeds to completion. For the Z-ring radius to continue to decrease, χ must remain greater than $\alpha\rho\,(1+\gamma\rho\sqrt{1-\rho^2})$. If the width of the Z-ring is assumed to be constant during contraction, γ is constant at 8 (*cf.* Equation (29)) and the contraction threshold is a function of ρ, the dimensionless ratio of the radius of the Z-ring at time t to the initial radius. The plot of χ vs ρ is given in Figure 5 for the wild-type case. CAM-FF predicts three possible division outcomes: (i) division proceeds to completion, (ii) division is initiated but stalls prior to completion and (iii) division is not initiated. These scenarios are highlighted in Figure 5, on the assumption that the contraction parameter χ remains constant throughout the division process. The value of the initiation threshold α is currently unknown. Therefore, using the wild-type parameters, the value of α is set on the assumption that the wild-type contraction parameter value χ is sufficient to allow full division with the capacity to lose 15% of its value before division behaviour is affected. In Figure 5, the initiation threshold α is set to 20,000. The value of α determines the peak of the threshold curve or the "completion threshold".

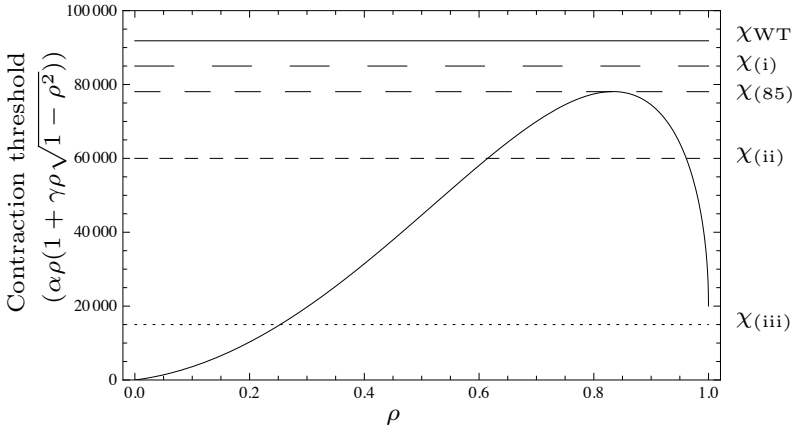

Fig. 5 The contraction threshold value varies as the radius of the Z-ring decreases. Using the wild-type value of the contraction parameter χ_{WT} and the 85% tolerance limit χ_{85}, for the parameter values in Table 1, $\alpha = 20{,}000$. $\gamma = 8$. Since the contraction parameter χ must exceed the contraction threshold at all values of the radius ratio from 1 to 0 for contraction to proceed, the model predicts three division outcomes: $\chi_{(\mathrm{i})}$ division proceeds to completion, $\chi_{(\mathrm{ii})}$ division is initiated but stalls prior to completion and $\chi_{(\mathrm{iii})}$division is not initiated.

4.1 Predicting division behaviour in cells depleted of FtsA or ZipA

Deletion of an anchor protein in CAM-FF alters the values of B, the total number of membrane-binding anchors, P_a, the probability that one FtsZ subunit is adjacent to a binding site and the initiation threshold α. Anchor deletion results in an increase in the initiation threshold value α from the assigned wild-type value since $\alpha \propto 1/\mathrm{P}_a$. The underlying reason for this behaviour can be understood from Equation (26). The maximum tension the ring may withstand, $\hat{\tau}$, is proportional to P_a so

in the deletion mutant, $\hat{\tau}$ is smaller than in the wild-type for a given population of membrane-bound FtsZ. It is therefore less likely that the condition for contraction is met *i.e.* that $\hat{\tau} > \tau_Z$ for lower values of P_a, see Equation (27), and the threshold α is correspondingly increased, see Equation (29).

If FtsA is depleted, as shown in Figure 6C ($B = 450$, $P_a = 0.029$), we expect the initiation threshold to increase to $\alpha = 29,665$ and outcome (ii) is predicted: division is initiated but stalls prior to completion. The predicted average membrane-bound FtsZ polymer length remains at 14 subunits but the percentage incorporation falls to 21%. Experimental data for a mutant with FtsA depleted show that the Z-ring is still formed, indentations are observed above the Z-ring but division is prevented,[45] in accord with the model prediction that division is initiated but later arrested.

The loss of ZipA changes the parameters to $B = 222$, $P_a = 0.014$, and the effect is shown in Figure 6D. The initiation threshold increases to $\alpha = 61,429$ and the equilibrium value of the contraction parameter falls below the initiation threshold. Outcome (iii) is therefore predicted: division is not initiated. The average membrane-bound FtsZ polymer length is increased slightly to 15 subunits and the percentage incorporation is less than half that of the wild-type at 12%. Following induced ZipA depletion in *E. coli*, cells are no longer able to divide and appear completely smooth.[45] The model thus explains the outcome of ZipA deletion.

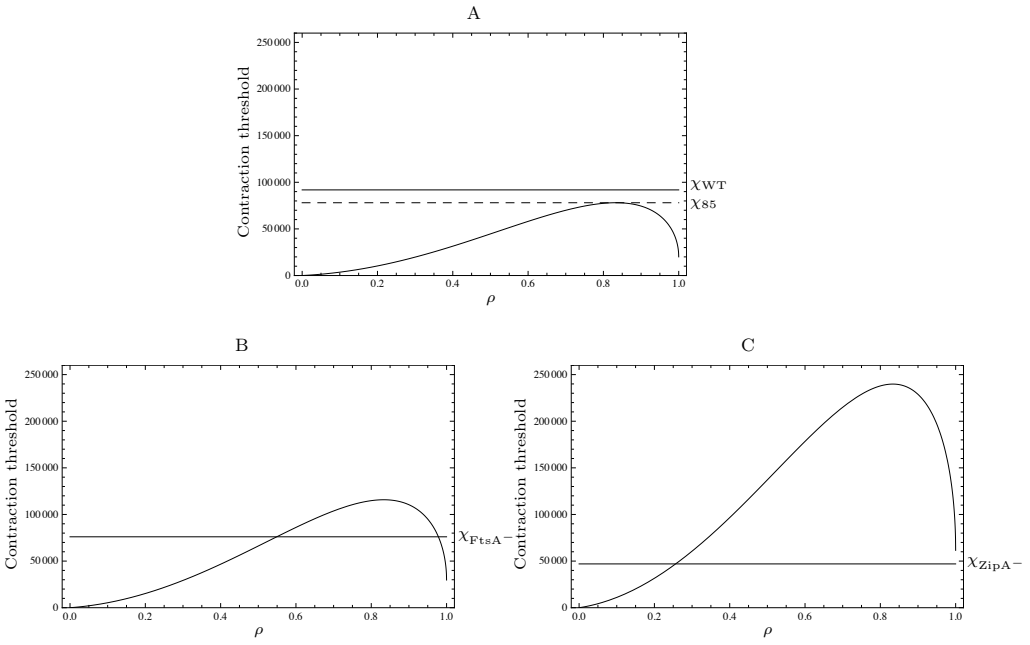

Fig. 6 The effect of anchor deletion. (A) The wild-type value of the contraction parameter χ_{WT} is shown for $B = 672$, $P_a = 0.043$; χ_{85} indicates the 15% tolerance threshold used to set $\alpha = 20,000$. (B) For the deletion of FtsA ($B = 450$, $P_a = 0.029$, $\alpha = 29,655$), division is initiated but stalls prior to completion. (C) For the deletion of ZipA ($B = 222$, $P_a = 0.014$, $\alpha = 61,429$), division is not initiated. All other parameters as shown in Table 1.

5 Analysis of model assumptions

5.1 Membrane-binding

Although CAM-FF accurately predicted the ability of the cell to divide in the absence of either one of the anchor proteins, more subtle features may become apparent if we acknowledge that the interaction of FtsZ with each protein is likely to differ, including the value of the dissociation constant κ, the force of the interaction F, and the strength of the interaction of the anchor protein with the cell membrane. It was assumed in the calculation of the maximum tension sustainable by the Z-ring that the weak point is the interaction of FtsZ with the anchor protein. While this seems plausible for the transmembrane protein ZipA,[45] whether this is the case for FtsA is less clear since FtsA is a peripheral membrane protein.[29] An additional anchoring role may be provided by the FtsEX complex.[38] Here, the weak point may be the interaction between FtsE and FtsX. The fact that the model predicts the behaviour of depletion mutants supports our assumptions.

5.2 Polymerisation and dissociation rates

We (and Surovtsev *et al.*[14]) assumed (i) the rate of polymerisation of GDP-bound FtsZ is zero, and (ii) the GTP hydrolysis event results in the dissociation of an FtsZ subunit, thus breaking two FtsZ-FtsZ interfaces. In reality, there may be some level of polymerisation of GDP-bound FtsZ and the hydrolysis event may disrupt only the FtsZ-FtsZ interface containing the bound nucleotide resulting in the dissociation of the parent polymer into two shorter polymers, without the loss of the GDP-bound subunit. Whereas Surovtsev *et al.*[14] assumed that the dissociation of the GDP-bound subunit is instantaneous (thus all subunits in FtsZ polymers were assumed to be GTP-bound), we assigned the rate constant of FtsZ dissociation (following GTP hydrolysis) in accordance with the GTP turnover measured by Romberg and Mitchison[25]. Although in CAM-FF all FtsZ subunits within polymers are GTP-bound, the reduced rate constant, relative to the Surovtsev model, accounts for the time spent in the GDP-bound state following GTP hydrolysis.

We also assumed that the rate of GTP hydrolysis/dissociation is equal for soluble and membrane-bound FtsZ and that the rate of nucleotide exchange for FtsZ subunits within polymers is zero. According to structural studies by Oliva *et al.*[46], and molecular modelling by Mingorance *et al.*[47], the active site is non-occluded leaving the nucleotide free to exchange with the cytosol from within FtsZ polymers. However, Chen and Erickson[48] found no evidence of nucleotide exchange within FtsZ polymers and Huecas *et al.*[49] reported that while exchange can occur, disassembly occurs first. Therefore our assumption is in keeping with the latest experimental evidence. We do not explicitly include the role of the putative bundling and stabilising (reduced GTPase activity) proteins that also localise to the Z-ring such as the ZapA orthologue YgfE in *E. coli*,[50,51] since at this point in time, experimental data to refine the model are not available. Thus we are implicitly assuming that they are behaving as required.

5.3 Regulation of FtsZ localisation

In CAM-FF, we assumed that FtsZ interacts with anchor proteins within the midcell region only, even though the midcell membrane contains only 30% of the total cell complement of anchors. *In vivo*, this apparently unrealistic assumption is made valid by additional systems that operate to regulate the localisation of Z-rings allowing formation at the midcell only.[6]

5.4 Changes in fibre geometry as contraction proceeds

In CAM-FF, we assume that the contraction parameter value χ remains constant throughout the division process. This is unlikely to be true for the later stages of cell division since as the radius decreases, the values of V_{mid} and V_{bnd} also change. The properties of the membrane-bound FtsZ population, including the components of the contraction parameter: the average membrane-bound polymer length and the number of membrane-bound polymers, may also vary. However, it is anticipated that the assumption of constant χ is reasonable for the initial stages of division which actually determines the prediction of division outcome since the peak of the threshold curve *i.e.* the "completion threshold" is early in the division process at $\rho = 0.833$, independent of the value of α.

Finally, a single diffusion constant for all lengths of FtsZ polymer was used. Extension of the current approximation of diffusion to a spatially continuous model may remove the artefact of the rapid assembly time observed compared to that measured *in vivo*. Our model predicts that the assembly of the Z-ring is complete within 5 sec, as does the Surovtsev model.[14] However, the assembly time measured in *E. coli in vivo* is 1 min.[52,53]

5.5 Dynamics of contraction

Whenever the maximal Z-ring tension that can physically be sustained by the population of FtsZ polymers assembled is less than that required to maintain a given radius, the Z-ring radius is expected to expand under the force of the cell surface tension. Conversely, whenever the maximum tension sustainable in the Z-ring exceeds the tension required to maintain a given Z-ring radius, we assume that cell constriction proceeds. The relationship between the rate of change of the Z-ring radius and the difference in the maximal tension and the required tension was assumed to be linear, as shown in Figure 7A. Depending on the molecular mechanism, it is conceivable that the true form of the relationship is non-linear, *e.g.* proportional to $(\tau_Z - \hat{\tau})^3$ as in Figure 7B, or a higher-order power. For the current analysis, the prediction of division outcome is based on the sign of $(\tau_Z - \hat{\tau})$. Therefore, this assumption only concerns the the rate of change of the radius.

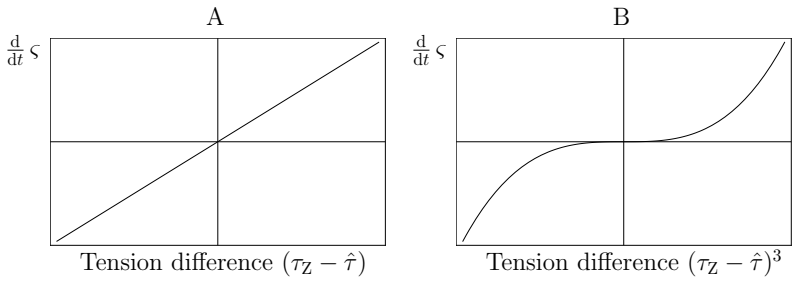

Fig. 7 Relationship between the rate of change of the Z-ring radius ς and the difference in calculated tensions. (A) In the presented model the relationship is assumed to be linear $\frac{\mathrm{d}}{\mathrm{d}t}\varsigma = \vartheta_0(\tau_Z - \hat{\tau})$. (B) The true form may be a higher order power *e.g.* $\frac{\mathrm{d}}{\mathrm{d}t}\varsigma = \vartheta_0(\tau_Z - \hat{\tau})^3$.

6 Discussion and conclusions

The model presented, CAM-FF: Critical Accumulation of Membrane-bound FtsZ Fibres, integrates the observed assembly behaviour of FtsZ *in vitro* with the hypothesis that the Z-ring is a molecular assembly of short open polymers that bind to the membrane *via* linking proteins, rather than the extremely long cyclic polymers, assumed in earlier work of Surovtsev *et al.* [14]. The division of the cell into distinct compartments and the introduction of diffusion of FtsZ between the cell caps and the midcell region, along with explicitly modelling the attachment of FtsZ polymers to membrane anchors, have been shown to be sufficient to prevent the truncation artefact that arises in the Surovtsev model. CAM-FF was further extended by representing the forces of adherence of FtsZ polymers to the cell membrane and their additional role in the generation and support of tension during contraction of the midcell region. This analysis linked the chemical population dynamics of membrane-bound FtsZ polymers to the force of contraction *via* the definition of the contraction parameter χ, a useful parameter in the prediction of the ability of cells to initiate and complete cell division.

We used CAM-FF to analyse the effect of reducing the concentrations of membrane-anchoring proteins to understand how their absence inhibits cell division by reducing the number of FtsZ polymers and the percentage of FtsZ molecules in the cell that bind to the membrane. Cell division is still initiated if FtsA, the lower concentrated anchor, is depleted but division stalls before completion. The cells show no sign of even initiating cell division if the more prevalent anchor ZipA is removed. Thus we effectively model whether division occurs or not. More work is required to accurately model the timescale of cell division. In particular a more complicated analysis of diffusion is required, though currently the experimental parameters are not available.

CAM-FF is silent on the molecular mechanism of Z-ring contraction except to consider the force required for it. At the molecular level, we implied this constriction as being driven by thermodynamic fluctuations. Biochemically analogous processes, such as the contraction of mammalian skeletal muscle, have previously been modelled by a Brownian ratchet mechanism whereby the movement of a motor protein along the actin fibre due to thermal fluctuation becomes unidirectional when coupled to a non-equilibrium chemical reaction.[54] For the contraction of skeletal muscle, the directionality arises from the conformational changes of the

motor protein due to its nucleotide-binding state, where the chemical hydrolysis of the nucleotide is far from equilibrium.[55] While no equivalent motor protein has hitherto been identified in prokaryotes, the existence of an as yet undiscovered motor protein is neither proposed nor repudiated in the assumption of a relationship between the difference in calculated tensions and the rate of change of the Z-ring radius. In the absence of a motor protein, the contraction mechanism is nonetheless coupled to a non-equilibrium process by the continual binding and release of FtsZ polymers, dependent on the rate of GTP-hydrolysis. It seems *prima facie* plausible that the release and rebinding of FtsZ polymers could create a ratchet mechanism whereby local fluctuations become locked in place by the adjacent binding of further FtsZ polymers.

The presence of multiple membrane anchors may provide a ratchet-type mechanism whereby *e.g*. ZipA, and potentially the FtsEX complex, are tightly anchored within the membrane but FtsA is more weakly bound and so may be released and rebound during thermal fluctuations, either from the FtsZ or from the cell membrane. Interestingly, FtsA is an ATPase[56] suggesting a possible means of chemical coupling to drive unidirectional contraction. The state of the bound nucleotide may affect the interaction of FtsA with FtsZ or the cell membrane or both. In CAM-FF, we couple the thermal fluctuations of the Z-ring radius to the non-equilibrium hydrolysis of GTP by FtsZ *via* the rate constant ϑ_0, Equation (28).

An additional role of the Z-ring that is not included in this work is the recruitment of peptidoglycan remodelling enzymes on the outside of the inner cell membrane.[6] As the Z-ring contracts, the peptidoglycan remodelling process potentially creates a physical barrier to any subsequent re-expansion of the Z-ring. This barrier formation process would be a positive feedback loop contributing to unidirectional contraction by consolidating the progress made thus far. The mechanics of the bacterial cell wall during division have been modelled by Lan *et al.*[20] in a complementary study. We assume that the contraction parameter is constant at the initial stages of division which is satisfactory for the prediction of incomplete cell division but to be fully confident of the prediction of division, the cell wall must also be considered.

We have established a framework for the further investigation of the effect of modifications to the biochemical properties of FtsZ and its membrane binding on the initiation and completion of cell division. Application of such a framework will not only improve our understanding of the biological process itself, but may also be applied to the optimisation of anti-biotic drug design. Potential drug interactions may be tested for efficacy *in silico* by identification of their effect on key processes of the system. This model may also now be applied to a global model of cell division as proposed by Surovtsev *et al.*[19].

A ODEs as defined by Surovtsev *et al.* [14]

The change in concentrations of FtsZ molecules over time was given by Surovtsev *et al.* [14] in terms of the following rate equations:

$$\frac{\mathrm{d}}{\mathrm{d}t}Z_{\mathrm{D}} = -R_{\mathrm{ex1}} + R_{\mathrm{ex2}} + R^2_{\mathrm{hyd}} + R^2_{\mathrm{hyd\_cyc}} + \xi \sum_{j=3}^{i_{\max}} \left(R^j_{\mathrm{hyd}} + R^j_{\mathrm{hyd\_cyc}}\right), \tag{A.1}$$

$$\frac{\mathrm{d}}{\mathrm{d}t}Z_{\mathrm{T}} = R_{\mathrm{ex1}} - R_{\mathrm{ex2}} - 2R_{\mathrm{dim1}} + 2R_{\mathrm{dim2}} - R^2_{\mathrm{el1}} + \xi R^2_{\mathrm{el2}} - \xi \sum_{j=3}^{i_{\max}-1} \left(R^j_{\mathrm{el1}} - R^j_{\mathrm{el2}}\right) + R^2_{\mathrm{hyd}} + \xi R^3_{\mathrm{hyd}} + \xi \sum_{j=4}^{i_{\max}} \frac{2}{j-1} R^j_{\mathrm{hyd}} + R^2_{\mathrm{hyd\_cyc}}, \tag{A.2}$$

$$\frac{\mathrm{d}}{\mathrm{d}t}Z_2 = R_{\mathrm{dim1}} - R_{\mathrm{dim2}} - R^2_{\mathrm{el1}} + \xi R^2_{\mathrm{el2}} - R^2_{\mathrm{an2}} - R^2_{\mathrm{cyc1}} + R^2_{\mathrm{cyc2}} - R^2_{\mathrm{hyd}} + \frac{1}{2}\xi R^3_{\mathrm{hyd}} + \xi \sum_{j=4}^{i_{\max}} \frac{2}{j-1} R^j_{\mathrm{hyd}} + \xi R^3_{\mathrm{hyd\_cyc}}, \tag{A.3}$$

$$\frac{\mathrm{d}}{\mathrm{d}t}Z_3 = \frac{1}{\xi} R^2_{\mathrm{el1}} - R^2_{\mathrm{el2}} - R^3_{\mathrm{el1}} + R^3_{\mathrm{el2}} - R^3_{\mathrm{an2}} - R^3_{\mathrm{cyc1}} + R^3_{\mathrm{cyc2}} - R^3_{\mathrm{hyd}} + \frac{1}{3} R^4_{\mathrm{hyd}} + \sum_{j=5}^{i_{\max}} \frac{2}{j-1} R^j_{\mathrm{hyd}} + R^4_{\mathrm{hyd\_cyc}}, \tag{A.4}$$

$$\frac{\mathrm{d}}{\mathrm{d}t}Z_i = R^{i-1}_{\mathrm{el1}} - R^{i-1}_{\mathrm{el2}} - R^i_{\mathrm{el1}} + R^i_{\mathrm{el2}} + R^i_{\mathrm{an1}} - R^i_{\mathrm{an2}} - R^i_{\mathrm{cyc1}} + R^i_{\mathrm{cyc2}} - R^i_{\mathrm{hyd}} + \frac{1}{i} R^{i+1}_{\mathrm{hyd}} + \sum_{j=i+2}^{i_{\max}} \frac{2}{j-1} R^j_{\mathrm{hyd}} + R^{i+1}_{\mathrm{hyd\_cyc}}, \qquad i = 4 \ldots i = i_{\max} - 2, \tag{A.5}$$

$$\frac{\mathrm{d}}{\mathrm{d}t}Z_{i_{\max}-1} = R^{i_{\max}-2}_{\mathrm{el1}} - R^{i_{\max}-2}_{\mathrm{el2}} - R^{i_{\max}-1}_{\mathrm{el1}} + R^{i_{\max}-1}_{\mathrm{el2}} + R^{i_{\max}-1}_{\mathrm{an1}} - R^{i_{\max}-1}_{\mathrm{cyc1}} + R^{i_{\max}-1}_{\mathrm{cyc2}} - R^{i_{\max}-1}_{\mathrm{hyd}} + \frac{1}{i_{\max}-1} R^{i_{\max}}_{\mathrm{hyd}} + R^{i_{\max}}_{\mathrm{hyd\_cyc}}, \tag{A.6}$$

$$\frac{\mathrm{d}}{\mathrm{d}t}Z_{i_{\max}} = R^{i_{\max}-1}_{\mathrm{el1}} - R^{i_{\max}-1}_{\mathrm{el2}} + R^{i_{\max}}_{\mathrm{an1}} - R^{i_{\max}}_{\mathrm{cyc1}} + R^{i_{\max}}_{\mathrm{cyc2}} - R^{i_{\max}}_{\mathrm{hyd}} \tag{A.7}$$

and

$$\frac{\mathrm{d}}{\mathrm{d}t} Z_i^{\mathrm{cyc}} = R_{\mathrm{cyc1}}^i - R_{\mathrm{cyc2}}^i - R_{\mathrm{hyd\_cyc1}}^i \,. \tag{A.8}$$

ξ is the ratio of the midcell volume to the cytosol volume.

To allow polymers to form closed rings, the forward and reverse cyclisation rates are given by

$$R_{\mathrm{cyc1}}^i = k_{\mathrm{cyc1}}(i)\, Z_i \,,\; R_{\mathrm{cyc2}}^i = k_{\mathrm{cyc2}}\, Z_i^{\mathrm{cyc}} \,, \tag{A.9}$$

where the forward rate constant is dependent on the polymer length i and is given by

$$k_{\mathrm{cyc1}}(i) = k_{\mathrm{cyc1}}\, e^{-(i-i_0)^2/\sigma^2} \,, \tag{A.10}$$

where i_0 is the length at which the cyclisation rate is optimal and σ is the width of the distribution of rates. The rate of GTP hydrolysis for cyclic polymers is given by

$$R_{\mathrm{hyd\_cyc}}^i = i\, k_{\mathrm{hyd}}\, Z_i^{\mathrm{cyc}} \,, \tag{A.11}$$

where cyclic polymers of length i have i GTPase active sites.

B ODEs of CAM-FF

The change in concentration of FtsZ molecules within the cell caps over time is given by

$$\frac{\mathrm{d}}{\mathrm{d}t} Z_{\mathrm{D}}^{\mathrm{cc}} = -R_{\mathrm{ex1}} + R_{\mathrm{ex2}} + \sum_{j=2}^{i_{\max}} R_{\mathrm{dis}}^j + R_{\mathrm{mc}}^{\mathrm{D}} \,, \tag{B.1}$$

$$\begin{aligned}\frac{\mathrm{d}}{\mathrm{d}t} Z_{\mathrm{T}}^{\mathrm{cc}} = {} & R_{\mathrm{ex1}} - R_{\mathrm{ex2}} - 2R_{\mathrm{dim1}} + 2R_{\mathrm{dim2}} - \sum_{j=2}^{i_{\max-1}} (R_{\mathrm{el1}}^j - R_{\mathrm{el2}}^j) \\ & + R_{\mathrm{dis}}^2 + \sum_{j=3}^{i_{\max}} \frac{2}{j-1} R_{\mathrm{dis}}^j + R_{\mathrm{mc}}^{\mathrm{T}} \,,\end{aligned} \tag{B.2}$$

$$\begin{aligned}\frac{\mathrm{d}}{\mathrm{d}t} Z_2^{\mathrm{cc}} = {} & R_{\mathrm{dim1}} - R_{\mathrm{dim2}} - R_{\mathrm{el1}}^2 + R_{\mathrm{el2}}^2 - R_{\mathrm{an2}}^2 - R_{\mathrm{dis}}^2 + \frac{1}{2} R_{\mathrm{dis}}^3 \\ & + \sum_{j=4}^{i_{\max}} \frac{2}{j-1} R_{\mathrm{dis}}^j + R_{\mathrm{mc}}^2 \,,\end{aligned} \tag{B.3}$$

$$\begin{aligned}\frac{\mathrm{d}}{\mathrm{d}t} Z_i^{\mathrm{cc}} = {} & R_{\mathrm{el1}}^{i-1} - R_{\mathrm{el2}}^{i-1} - R_{\mathrm{el1}}^i + R_{\mathrm{el2}}^i + R_{\mathrm{an1}}^i - R_{\mathrm{an2}}^i - R_{\mathrm{dis}}^i \\ & + \frac{1}{i} R_{\mathrm{dis}}^{i+1} + \sum_{j=i+2}^{i_{\max}} \frac{2}{j-1} R_{\mathrm{dis}}^j + R_{\mathrm{mc}}^i \,, \\ & i = 3 \ldots i = i_{\max} - 2 \,,\end{aligned} \tag{B.4}$$

$$\frac{\mathrm{d}}{\mathrm{d}t} Z^{\mathrm{cc}}_{i_{\max}-1} = R^{i_{\max}-2}_{\mathrm{el1}} - R^{i_{\max}-2}_{\mathrm{el2}} - R^{i_{\max}-1}_{\mathrm{el1}} + R^{i_{\max}-1}_{\mathrm{el2}} + R^{i_{\max}-1}_{\mathrm{an1}} - R^{i_{\max}-1}_{\mathrm{dis}} + \frac{1}{i_{\max}-1} R^{i_{\max}}_{\mathrm{dis}} + R^{i_{\max}-1}_{\mathrm{mc}} \tag{B.5}$$

and

$$\frac{\mathrm{d}}{\mathrm{d}t} Z^{\mathrm{cc}}_{i_{\max}} = R^{i_{\max}-1}_{\mathrm{el1}} - R^{i_{\max}-1}_{\mathrm{el2}} + R^{i_{\max}}_{\mathrm{an1}} - R^{i_{\max}}_{\mathrm{dis}} + R^{i_{\max}}_{\mathrm{mc}} \,. \tag{B.6}$$

For the midcell compartment the change in concentration of FtsZ molecules over time is given by

$$\begin{aligned}\frac{\mathrm{d}}{\mathrm{d}t} Z^{\mathrm{mid}}_{\mathrm{D}} = &-R_{\mathrm{ex1}} + R_{\mathrm{ex2}} + \sum_{j=2}^{i_{\max}} R^{j}_{\mathrm{dis}} + R^{\mathrm{D}}_{\mathrm{cm}} \\ &- R^{\mathrm{D}}_{\mathrm{bind1}} + \frac{V_{\mathrm{bnd}}}{V_{\mathrm{mid}}} R^{\mathrm{D}}_{\mathrm{bind2}} \\ &+ \frac{V_{\mathrm{bnd}}}{V_{\mathrm{mid}}} \sum_{j=2}^{i_{\max}} \mathrm{P}_1(\text{no sites} \mid i' = j) R^{j}_{\mathrm{dis\_bnd}} \,,\end{aligned} \tag{B.7}$$

$$\begin{aligned}\frac{\mathrm{d}}{\mathrm{d}t} Z^{\mathrm{mid}}_{\mathrm{T}} = &\, R_{\mathrm{ex1}} - R_{\mathrm{ex2}} - 2R_{\mathrm{dim1}} + 2R_{\mathrm{dim2}} - \frac{V_{\mathrm{bnd}}}{V_{\mathrm{mid}}} R_{\mathrm{dim1\_bnd}} \\ &+ \frac{V_{\mathrm{bnd}}}{V_{\mathrm{mid}}} R_{\mathrm{dim2\_bnd}} - \sum_{j=2}^{i_{\max-1}} (R^{j}_{\mathrm{el1}} - R^{j}_{\mathrm{el2}}) \\ &- \frac{V_{\mathrm{bnd}}}{V_{\mathrm{mid}}} \sum_{j=2}^{i_{\max-1}} (R^{j}_{\mathrm{el1\_bnd}} - R^{j}_{\mathrm{el2\_bnd}}) + R^{2}_{\mathrm{dis}} \\ &+ \sum_{j=3}^{i_{\max}} \frac{2}{j-1} R^{j}_{\mathrm{dis}} + R^{\mathrm{T}}_{\mathrm{cm}} - R^{\mathrm{T}}_{\mathrm{bind1}} + \frac{V_{\mathrm{bnd}}}{V_{\mathrm{mid}}} R^{\mathrm{T}}_{\mathrm{bind2}} \\ &+ \frac{V_{\mathrm{bnd}}}{V_{\mathrm{mid}}} \mathrm{P}_1(\text{no sites} \mid i' = 2) R^{2}_{\mathrm{dis\_bnd}} \\ &+ \frac{V_{\mathrm{bnd}}}{V_{\mathrm{mid}}} \sum_{j=3}^{i_{\max}} \frac{2}{j-1} \mathrm{P}_1(\text{no sites} \mid i' = j) R^{j}_{\mathrm{dis\_bnd}} \,,\end{aligned} \tag{B.8}$$

$$\begin{aligned}\frac{\mathrm{d}}{\mathrm{d}t} Z^{\mathrm{mid}}_{2} = &\, R_{\mathrm{dim1}} - R_{\mathrm{dim2}} - R^{2}_{\mathrm{el1}} + R^{2}_{\mathrm{el2}} - R^{2}_{\mathrm{an2}} - R^{2}_{\mathrm{an2\_mid}} - R^{2}_{\mathrm{dis}} \\ &+ \frac{1}{2} R^{3}_{\mathrm{dis}} + \sum_{j=4}^{i_{\max}} \frac{2}{j-1} R^{j}_{\mathrm{dis}} + R^{2}_{\mathrm{cm}} - R^{2}_{\mathrm{bind1}} \\ &+ \frac{V_{\mathrm{bnd}}}{V_{\mathrm{mid}}} R^{2}_{\mathrm{bind2}} + \frac{1}{2} \cdot \frac{V_{\mathrm{bnd}}}{V_{\mathrm{mid}}} \mathrm{P}_2(\text{no sites} \mid i' = 3) R^{3}_{\mathrm{dis\_bnd}} \\ &+ \frac{V_{\mathrm{bnd}}}{V_{\mathrm{mid}}} \sum_{j=4}^{i_{\max}} \frac{2}{j-1} \mathrm{P}_2(\text{no sites} \mid i' = j) R^{j}_{\mathrm{dis\_bnd}} \,,\end{aligned} \tag{B.9}$$

$$\frac{\mathrm{d}}{\mathrm{d}t}Z_i^{\mathrm{mid}} = R_{\mathrm{el1}}^{i-1} - R_{\mathrm{el2}}^{i-1} - R_{\mathrm{el1}}^{i} + R_{\mathrm{el2}}^{i} + R_{\mathrm{an1}}^{i}$$
$$- R_{\mathrm{an2}}^{i} - R_{\mathrm{an2\_mid}}^{i} - R_{\mathrm{dis}}^{i} + \frac{1}{i}R_{\mathrm{dis}}^{i+1} + \sum_{j=i+2}^{i_{\max}} \frac{2}{j-1}R_{\mathrm{dis}}^{j}$$
$$+ R_{\mathrm{cm}}^{i} - R_{\mathrm{bind1}}^{i} + \frac{V_{\mathrm{bnd}}}{V_{\mathrm{mid}}}R_{\mathrm{bind2}}^{i}$$
$$+ \frac{1}{i}.\frac{V_{\mathrm{bnd}}}{V_{\mathrm{mid}}}\mathrm{P}_i(\text{no sites} \mid i' = i+1)R_{\mathrm{dis\_bnd}}^{i+1}$$
$$+ \frac{V_{\mathrm{bnd}}}{V_{\mathrm{mid}}}\sum_{j=i+2}^{i_{\max}} \frac{2}{j-1}\mathrm{P}_i(\text{no sites} \mid i' = j)R_{\mathrm{dis\_bnd}}^{j}\,,$$
$$i = 3 \ldots i = i_{\max} - 2\,, \tag{B.10}$$

$$\frac{\mathrm{d}}{\mathrm{d}t}Z_{i_{\max}-1}^{\mathrm{mid}} = R_{\mathrm{el1}}^{i_{\max}-2} - R_{\mathrm{el2}}^{i_{\max}-2} - R_{\mathrm{el1}}^{i_{\max}-1} + R_{\mathrm{el2}}^{i_{\max}-1} + R_{\mathrm{an1}}^{i_{\max}-1}$$
$$- R_{\mathrm{dis}}^{i_{\max}-1} + \frac{1}{i_{\max}-1}R_{\mathrm{dis}}^{i_{\max}} + R_{\mathrm{cm}}^{i_{\max}-1}$$
$$- R_{\mathrm{bind1}}^{i_{\max}-1} + \frac{V_{\mathrm{bnd}}}{V_{\mathrm{mid}}}R_{\mathrm{bind2}}^{i_{\max}-1}$$
$$+ \frac{1}{i_{\max}-1}\cdot\frac{V_{\mathrm{bnd}}}{V_{\mathrm{mid}}}\mathrm{P}_{i_{\max}-1}(\text{no sites} \mid i' = i_{\max})R_{\mathrm{dis\_bnd}}^{i_{\max}} \tag{B.11}$$

and

$$\frac{\mathrm{d}}{\mathrm{d}t}Z_{i_{\max}}^{\mathrm{mid}} = R_{\mathrm{el1}}^{i_{\max}-1} - R_{\mathrm{el2}}^{i_{\max}-1} + R_{\mathrm{an1}}^{i_{\max}} - R_{\mathrm{dis}}^{i_{\max}} + R_{\mathrm{mc}}^{i_{\max}}$$
$$- R_{\mathrm{bind1}}^{i_{\max}} + \frac{V_{\mathrm{bnd}}}{V_{\mathrm{mid}}}R_{\mathrm{bind2}}^{i_{\max}}\,, \tag{B.12}$$

where V_{mid} and V_{bnd} are the volume of the midcell and the midecell membrane compartments, respectively. A volume is used for the midcell membrane compartment rather than a surface area so that the concentrations of membrane-bound molecules are in equivalent dimensions to the cell caps and midcell concentrations, and so the global rate constants may be applied.

For the midcell membrane, the change in concentration of FtsZ molecules over time is given by

$$\frac{\mathrm{d}}{\mathrm{d}t}Z_{\mathrm{D}}^{\mathrm{bnd}} = \frac{V_{\mathrm{mid}}}{V_{\mathrm{bnd}}}R_{\mathrm{bind1}}^{\mathrm{D}} - R_{\mathrm{bind2}}^{\mathrm{D}} - R_{\mathrm{ex1}} + R_{\mathrm{ex2}}$$
$$+ \sum_{j=2}^{i_{\max}}(1 - \mathrm{P}_1(\text{no sites} \mid i' = j))R_{\mathrm{dis\_bnd}}^{j}\,, \tag{B.13}$$

$$\frac{\mathrm{d}}{\mathrm{d}t}Z_{\mathrm{T}}^{\mathrm{bnd}} = \frac{V_{\mathrm{mid}}}{V_{\mathrm{bnd}}}R_{\mathrm{bind1}}^{\mathrm{T}} - R_{\mathrm{bind2}}^{\mathrm{T}} + R_{\mathrm{ex1}} - R_{\mathrm{ex2}} - R_{\mathrm{dim1\_bnd}}$$
$$+ R_{\mathrm{dim2\_bnd}} + (1 - \mathrm{P}_1(\text{no sites} \mid i' = 2))R_{\mathrm{dis\_bnd}}^{2}$$
$$+ \sum_{j=3}^{i_{\max}} \frac{2}{j-1}(1 - \mathrm{P}_1(\text{no sites} \mid i' = j))R_{\mathrm{dis\_bnd}}^{j}\,, \tag{B.14}$$

$$\frac{\mathrm{d}}{\mathrm{d}t} Z_2^{\mathrm{bnd}} = \frac{V_{\mathrm{mid}}}{V_{\mathrm{bnd}}} R^2_{\mathrm{bind1}} - R^2_{\mathrm{bind2}} + R_{\mathrm{dim1\_bnd}} - R_{\mathrm{dim2\_bnd}} - R^2_{\mathrm{el1\_bnd}} + R^2_{\mathrm{el2\_bnd}} - R^2_{\mathrm{an2\_bnd}} - R^2_{\mathrm{dis\_bnd}} + \frac{1}{2} \cdot (1 - \mathrm{P}_2(\text{no sites} \mid i' = 3)) R^3_{\mathrm{dis\_bnd}} + \sum_{j=4}^{i_{\max}} \frac{2}{j-1} (1 - \mathrm{P}_i(\text{no sites} \mid i' = j)) R^j_{\mathrm{dis\_bnd}} \,, \tag{B.15}$$

$$\frac{\mathrm{d}}{\mathrm{d}t} Z_{\mathrm{i}}^{\mathrm{bnd}} = \frac{V_{\mathrm{mid}}}{V_{\mathrm{bnd}}} R^i_{\mathrm{bind1}} - R^i_{\mathrm{bind2}} + R^{i-1}_{\mathrm{el1\_bnd}} - R^{i-1}_{\mathrm{el2\_bnd}} - R^i_{\mathrm{el1\_bnd}} + R^i_{\mathrm{el2\_bnd}} + R^i_{\mathrm{an1\_bnd}} - R^i_{\mathrm{an2\_bnd}} - R^i_{\mathrm{dis\_bnd}} + \frac{1}{i} \cdot (1 - \mathrm{P}_i(\text{no sites} \mid i' = i+1)) R^{i+1}_{\mathrm{dis\_bnd}} + \sum_{j=i+2}^{i_{\max}} \frac{2}{j-1} (1 - \mathrm{P}_i(\text{no sites} \mid i' = j)) R^j_{\mathrm{dis\_bnd}} \,, \quad i = 3 \ldots i = i_{\max} - 2 \,, \tag{B.16}$$

$$\frac{\mathrm{d}}{\mathrm{d}t} Z^{\mathrm{bnd}}_{i_{\max}-1} = \frac{V_{\mathrm{mid}}}{V_{\mathrm{bnd}}} R^{i_{\max}-1}_{\mathrm{bind1}} - R^{i_{\max}-1}_{\mathrm{bind2}} + R^{i_{\max}-2}_{\mathrm{el1\_bnd}} - R^{i_{\max}-2}_{\mathrm{el2\_bnd}} - R^{i_{\max}-1}_{\mathrm{el1\_bnd}} + R^{i_{\max}-1}_{\mathrm{el2\_bnd}} + R^{i_{\max}-1}_{\mathrm{an1\_bnd}} - R^{i_{\max}-1}_{\mathrm{dis\_bnd}} + \frac{1}{i_{\max}-1} \cdot (1 - \mathrm{P}_{i_{\max}-1}(\text{no sites} \mid i' = i_{\max})) R^{i_{\max}}_{\mathrm{dis\_bnd}} \tag{B.17}$$

and

$$\frac{\mathrm{d}}{\mathrm{d}t} Z^{\mathrm{bnd}}_{i_{\max}} = \frac{V_{\mathrm{mid}}}{V_{\mathrm{bnd}}} R^{i_{\max}}_{\mathrm{bind1}} - R^{i_{\max}}_{\mathrm{bind2}} + R^{i_{\max}-1}_{\mathrm{el1\_bnd}} - R^{i_{\max}-1}_{\mathrm{el2\_bnd}} + R^{i_{\max}}_{\mathrm{an1\_bnd}} - R^{i_{\max}}_{\mathrm{dis\_bnd}} \,. \tag{B.18}$$

The average polymer length $\bar{i}$, the total number of FtsZ polymers N_{Z}, and the total FtsZ concentration Z_{tot} are tracked over time for each compartment given by

$$\bar{i} = \sum_{i=1}^{i_{max}} i Z_i \Bigg/ \sum_{i=1}^{i_{max}} Z_i \,, \tag{B.19}$$

$$N_{\mathrm{Z}} = V_{\mathrm{bnd}} \frac{N_{\mathrm{A}}}{10^{21}} \sum_{i=1}^{i_{max}} Z_i \tag{B.20}$$

and

$$Z_{\mathrm{tot}} = \sum_{i=1}^{i_{max}} i Z_i \,, \tag{B.21}$$

respectively, where Z_1 includes both GDP- and GTP-bound monomers and N_{A} is Avogadro's number.

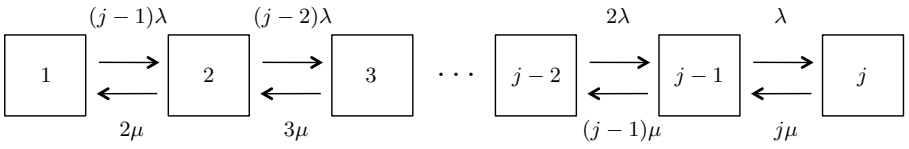

Fig. C 1 Binding to multiple sites. As multiple binding sites are available to a single polymer chain, binding is modelled as a Markov chain where j is the maximum number of binding sites available. λ is the rate of association of FtsZ and a binding site and μ is the rate of dissociation.

C Attachment to multiple binding sites

The attachment of an FtsZ polymer to multiple binding sites has been modelled as a Markov chain with state variables x_1 to x_j, where j is the maximum number of binding sites available to the chain. This is illustrated in Figure C 1.

A transition event up the chain is given by the rate of attachment per binding site and the number of free binding sites remaining. Conversely, a transition event down the chain is given by the rate of release per binding site and the number of sites currently occupied. At equilibrium, the rates of the forward and reverse transition events for x_{j-1} and x_j are equal,

$$j\,\mu\,x_j = \lambda\,x_{j-1}\ . \tag{C.1}$$

For the subsequent pair in the chain, x_{j-2} and x_{j-1},

$$(j-1)\,\mu\,x_{j-1} + \lambda\,x_{j-1} = 2\lambda\,x_{j-2} + j\,\mu\,x_j\ . \tag{C.2}$$

As $j\,\mu\,x_j$ and $\lambda\,x_{j-1}$ are equal then

$$(j-1)\,\mu\,x_{j-1} = 2\lambda\,x_{j-2}\ , \tag{C.3}$$

and

$$x_{j-2} = \frac{(j-1)}{2}\,\kappa x_{j-1}\ , \tag{C.4}$$

where $\kappa = \mu/\lambda$. Continuing in this way for the pair x_{j-3} and x_{j-2} gives

$$x_{j-3} = \frac{(j-2)}{3}\,\kappa x_{j-2}\ , \tag{C.5}$$

and for any subsequent pair this can be generalised to

$$x_{j-\ell} = \frac{(j-\ell+1)}{\ell}\,\kappa x_{j-\ell+1}\ , \tag{C.6}$$

where expression is in terms of the previous term in the sequence. To derive $x_{j-\ell}$ in terms of x_j and κ, each term from $\ell = 1$ is considered. As $x_{j-1} = j\,\kappa x_j$, then substituting into (C.4) for x_{j-2} gives

$$x_{j-2} = j\,\frac{(j-1)}{2}\,\kappa^2 x_j\ . \tag{C.7}$$

Continuing for x_{j-3} gives

$$x_{j-3} = j\,\frac{(j-1)}{2}\cdot\frac{(j-2)}{3}\,\kappa^3 x_j\ , \tag{C.8}$$

so this can be generalised to give $x_{j-\ell}$ in terms of x_j,

$$x_{j-\ell} = \binom{j}{\ell} \kappa^{\ell} x_j \, . \tag{C.9}$$

Of interest to the dissociation rate is the fraction of polymers in the singly-bound state. Therefore, this fraction is given by x_1/x_{T} where x_1 can be given by substituting $j-\ell = 1$,

$$x_1 = \binom{j}{j-1} \kappa^{j-1} x_j \, , \tag{C.10}$$

which simplifies to

$$x_1 = j\,\kappa^{j-1} x_j \, . \tag{C.11}$$

If x_{T} is the sum of all values of $x_{j-\ell}$ for $\ell = 0$ to $\ell = j-1$ then

$$x_{\mathrm{T}} = \left[\sum_{\ell=0}^{j-1} \binom{j}{\ell} \kappa^{\ell} \right] x_j \, . \tag{C.12}$$

By the binomial theorem, this is equal to

$$((1+\kappa)^j - \kappa^j) x_j \, . \tag{C.13}$$

Therefore, taking the value of x_1 from Equation (C.11), as a fraction of x_{T} given in Equation (C.13), the fraction of polymers expected to be bound by a single binding site when j binding sites are available is given by

$$f_1^j = \frac{j\,\kappa^{j-1} x_j}{((1+\kappa)^j - \kappa^j) x_j} \, , \tag{C.14}$$

which cancels and rearranges to give

$$f_1^j = \frac{j}{\kappa(1+\frac{1}{\kappa})^j - \kappa} \, , \tag{C.15}$$

as given in Equation (14) of §2.2.2.

D Forces acting on the Z-ring

The contraction process draws the cell membrane inwards, against the outward force from the cell surface tension. The aim of this model is to define the tension of the Z-ring during contraction and the maximum tension the Z-ring can withstand at a given ring radius. Figure D1 shows the components of the cell surface tension τ_0 as the ring constricts. The Z-ring is modelled as a cylinder with length ω and initial radius r. During contraction, the radius of the cylinder decreases where ς is defined as the Z-ring radius at time t of contraction, and ρ is the dimensionless ratio of the contraction radius to the initial radius, $\rho = \varsigma/r$. As can be seen in Figure D1, this ratio is equal to $\sin\beta$. As the ring contracts, the angle β decreases from $\pi/2$ to 0.

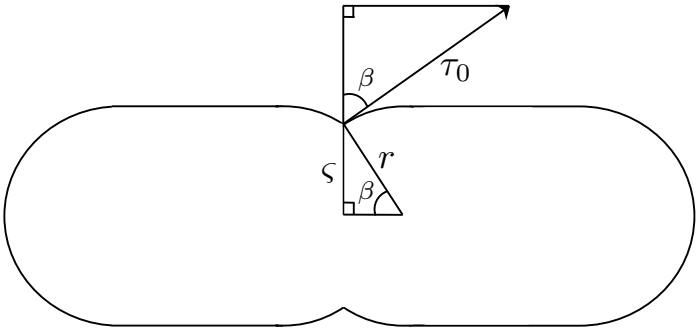

Fig. D 1 Membrane indentation on Z-ring contraction. Z-ring contraction pulls the membrane inwards against the outward force from the cell surface tension τ_0. ς is the radius of the Z-ring at time t of contraction and r is the radius of the Z-ring prior to contraction.

The angle β also corresponds to the angle of the tangent to the indented cell surface, with respect to the vertical. This tangent is the resultant of the cell surface tension. Since the pinching tension τ_{p} balances the vertical component of the surface tension τ_0 at equilibrium, the pinching tension is given by $\tau_0 \cos\beta$. To define τ_{p} in terms of the Z-ring radius, since $\sin\beta = \rho$, the pinching tension is also given by

$$\tau_{\mathrm{p}} = \tau_0 \sqrt{1-\rho^2}\,. \tag{D.1}$$

Since the surface tension acts on both the right and left sides of the cell indentation, the total pinching tension is equal to $2\tau_{\mathrm{p}}$. This acts around the circumference of the Z-ring so the pinching force generated is $4\pi\varsigma\,\tau_{\mathrm{p}}$. This force results in an additional internal pressure over the Z-ring surface area given by

$$\mathrm{P_p} = \frac{4\pi\varsigma\,\tau_{\mathrm{p}}}{2\pi\varsigma\,\omega}\,, \tag{D.2}$$

which simplifies to

$$\mathrm{P_p} = 2\frac{\tau_p}{\omega}\,. \tag{D.3}$$

To determine the Z-ring tension during contraction τ', the forces acting on either side of a vertical slice through the ring are considered, as shown in Figure D2. The magnitude of the force due to ring tension is given by this tension acting over the length of the two edges created by the slice. At equilibrium, this is balanced by the force of the internal pressure over the cross-sectional area. Therefore

$$2\omega\tau' = 2\varsigma\,\omega \mathrm{P_p}\,, \tag{D.4}$$

and substituting for $\mathrm{P_p}$ given in Equation (D.3) and expressing in terms of the dimensionless ratio ρ,

$$\tau' = \frac{2r}{\omega}\rho\,\tau_{\mathrm{p}}\,. \tag{D.5}$$

If the total Z-ring tension is given by the original cell surface tension plus the additional contraction tension τ' then

$$\tau_{\mathrm{Z}} = \tau_0\left(1+\frac{2r}{\omega}\rho\sqrt{1-\rho^2}\right)\,. \tag{D.6}$$

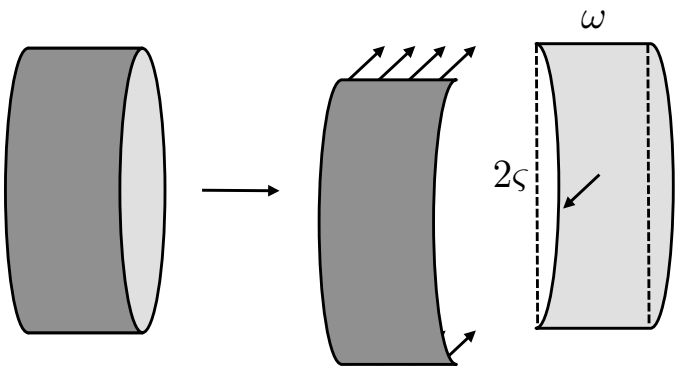

Fig. D 2 Forces acting on the Z-ring. For the slice through the Z-ring, at equilibrium the horizontal force due to the ring tension is balanced by the internal pressure acting over the cross-sectional area of the slice.

This is the first key property of the contraction model, the total tension of the Z-ring in terms of the cell surface tension and the radius of the Z-ring during contraction, as given in Equation (25) of §2.2.5.

The second key property is the maximum tension the Z-ring can withstand at a given radius, based on the assembled population of FtsZ polymers. To calculate this tension, a transverse line through the Z-ring is considered. As shown in Figure D3 for polymers bound to the membrane, for a polymer of length l, the probability that the transverse line intersects the polymer is

$$\mathrm{P}(\text{polymer hit} \mid l) = \frac{h}{2\pi\varsigma}\,, \tag{D.7}$$

where $h = l\sin\varphi$. As angle φ may take any value from 0 to π, the probability that a polymer of length l is intersected by the transverse line is given by

$$\mathrm{P}(\text{polymer hit} \mid l) = \int_0^\pi \frac{l}{2\pi\varsigma}\sin\varphi\,\mathrm{dF}(\varphi)\,. \tag{D.8}$$

If φ is uniform over $[0\,,\,\pi]$ then

$$\mathrm{P}(\text{polymer hit} \mid l) = \int_0^\pi \frac{l}{2\pi\varsigma}\sin\varphi\,\frac{1}{\pi}\,\mathrm{d}\varphi\,, \tag{D.9}$$

which simplifies to

$$\mathrm{P}(\text{polymer hit} \mid l) = \frac{l}{\pi^2\varsigma}\,, \tag{D.10}$$

since $\int_0^\pi \sin\varphi\,\mathrm{d}\varphi\ = 2$.

To extend this to all polymers, the probability that a polymer molecule is intersected is given by

$$\mathrm{P}(\text{polymer hit}) = \frac{l_0}{\pi^2\varsigma}\sum_{i=1}^{\infty} i\,\mathrm{P}_i, \tag{D.11}$$

where l_0 is the length of one FtsZ subunit, i is the number of subunits in the polymer and P_i is the probability that a polymer has length i subunits. The value of the summation is determined by the population of FtsZ molecules assembled at the Z-ring and bound to the membrane *via* anchors. The probability that a selected

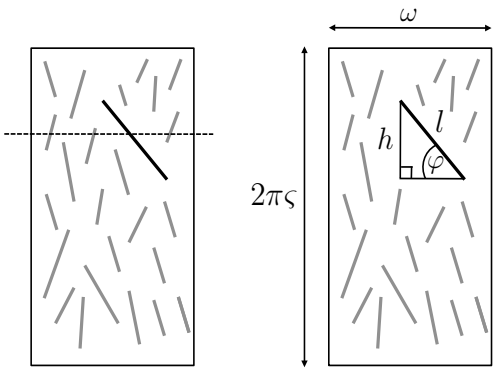

Fig. D 3 FtsZ polymers accumulated at the Z-ring. For a polymer of length l within the Z-ring, the probability that a transverse line intersects is given by $h/2\pi\varsigma$.

polymer has length i subunits is given by the concentration of polymers of length i, divided by the total polymer concentration,

$$\mathrm{P}_i = Z_i \Big/ \sum_{i=1}^{\infty} Z_i \,. \tag{D.12}$$

Multiplying by the number of subunits, and summing for all values of i gives the average polymer length. Therefore,

$$\sum_{i=1}^{\infty} i\mathrm{P}_i = \sum_{i=1}^{\infty} iZ_i \Big/ \sum_{i=1}^{\infty} Z_i = \bar{i}\,, \tag{D.13}$$

and

$$\mathrm{P}(\text{polymer hit}) = \frac{l_0\,\bar{i}}{\pi^2\varsigma}\,. \tag{D.14}$$

Since

$$N_{\mathrm{Z}} \triangleq \sum_{i=1}^{\infty} N_i\,, \tag{D.15}$$

the expectation of the number of polymers intersected by the transverse line is given by

$$\mathbb{E}(\text{number of polymers hit}) = \sum_{i=1}^{\infty} \frac{l_0\,\bar{i}}{\pi^2\varsigma} N_i = \frac{l_0\,\bar{i} N_{\mathrm{Z}}}{\pi^2\varsigma}\,. \tag{D.16}$$

To calculate the tension through the transverse line, the number of anchors and the maximum force sustainable per anchor is considered. For a polymer intersected by the transverse line, the expectation of the number of anchor sites on one side of the line is given by the number of subunits within the polymer and the probability that a subunit is adjacent to an anchor binding site. Therefore

$$\mathbb{E}(\text{anchors} \mid i) = \frac{1}{2}\mathrm{P}_a\, i\,, \tag{D.17}$$

where the correction factor of

$$\frac{1}{1-(1-\mathrm{P}_a)^i}\,, \tag{D.18}$$

used previously, has been omitted since this tends to 1 for increasing values of i. The force sustainable, perpendicular to the transverse line is then proportional to the number of anchors and depends on the angle φ so

$$\mathbb{E}(\text{max force} \mid i) \propto \mathbb{E}(\text{anchors} \mid i) \frac{1}{\pi} \int_0^{\pi} \sin\varphi \, \mathrm{d}\varphi \, . \tag{D.19}$$

Evaluating the integral and substituting for $\mathbb{E}(\text{anchors} \mid i)$ from Equation (D.17) gives

$$\mathbb{E}(\text{max force} \mid i) \propto \frac{\mathrm{P}_a \, i}{\pi} \, , \tag{D.20}$$

and for any polymer intersected,

$$\mathbb{E}(\text{max force}) \propto \frac{\mathrm{P}_a \, \bar{i}}{\pi} \, . \tag{D.21}$$

This is the expectation of the maximum force sustainable for a single polymer. For the total number of polymers intersected by the transverse line from Equation (D.16), the total maximum force is given by

$$\mathbb{E}(\text{max force of line}) \propto \frac{\mathrm{P}_a \, \bar{i}}{\pi} \, . \, \frac{l_0 \, \bar{i} N_{\mathrm{Z}}}{\pi^2 \varsigma} = \frac{\mathrm{P}_a \, l_0}{\pi^3 \, r} \, . \, \frac{\bar{i}^2 N_{\mathrm{Z}}}{\rho} \, . \tag{D.22}$$

The expectation of the maximum tension in the line is then given by the expectation of the maximum force of the line divided by the line length ω,

$$\mathbb{E}(\text{max tension of line}) \propto \frac{\mathrm{P}_a \, l_0}{\pi^3 \omega r} \, . \, \frac{\bar{i}^2 N_{\mathrm{Z}}}{\rho} \, . \tag{D.23}$$

On the assumption that the attachment to the anchor is the weak point, the maximum tension $\hat{\tau}$ is given by,

$$\hat{\tau} = F \frac{\mathrm{P}_a \, l_0}{\omega r} \, . \, \frac{\bar{i}^2 N_{\mathrm{Z}}}{\rho} \, , \tag{D.24}$$

where F is proportional to the force of the interaction of FtsZ and a single anchor site and accounts for the factor of $1/\pi^3$.

E CAM-FF resolves the truncation artefact of the Surovtsev model[14]

CAM-FF is based on the conceptual division of the cell into three compartments. Surovtsev *et al.* [14] assumed that FtsZ monomers and dimers are dispersed throughout the cell but that polymers of length $i \geq 3$ subunits are located exclusively in the midcell region. However, the two regions were not modelled as separate compartments. Instead, the concentrations of polymers of length $i \geq 3$ were scaled by a factor ξ, the ratio of the midcell volume to the cytosol volume, and reactions proceeded between all the molecules in the system. The Surovtsev ODEs, provided in Appendix A, included terms for nucleotide exchange, dimerisation, elongation, annealing, polymer cyclisation, and GTP hydrolysis reactions, with the factor ξ used to account for any "interfacial" reaction. For example, the increase in the

trimer concentration due to dimer elongation was scaled to be 1000 times larger than the corresponding decrease in the dimer concentration.

The scaling factor ξ on the modelled population of FtsZ engenders a truncation artefact: long open polymers accumulate with increasing concentrations towards $i_{\max}$, as shown in Figure E1A. Increasing the value of $i_{\max}$ then shifts the increase in concentration to greater values of i. As a result, the average open polymer length depends on $i_{\max}$. For example, for $i_{\max} = 150$, the average open polymer length is 62 subunits whereas for $i_{\max} = 200$, the average open polymer length is 70 subunits. At such high concentrations of polymers, the value of $i_{\max}$ is not sufficiently high to avoid truncation artefacts, due to their confinement to the midcell region. As can be seen in Figure E1, the artefact is not observed for any of the three compartments in CAM-FF. The average polymer length for the membrane-bound population is considerably lower than in the Surovtsev model[14], at 14 subunits for $i_{\max} = 150$ and if the maximum length is increased to $i_{\max} = 200$, the average membrane-bound polymer length remains at 14 subunits. Thus $i_{\max} = 150$ is sufficiently high to avoid the truncation artefact. Surovtsev *et al.*[14] acknowledge that the value for $i_{\max}$ was fixed at 150 due to limitations of the software used. However, CAM-FF shows that including (i) the diffusion of FtsZ into the midcell region, in a more physically realistic manner, and (ii) an explicit model of FtsZ membrane binding, prevents the truncation artefact and the formation of polymers as long as those in the Surovtsev model[14]. The formation of long polymers was due to the artificial increase in the FtsZ concentration with the confinement to the midcell volume.

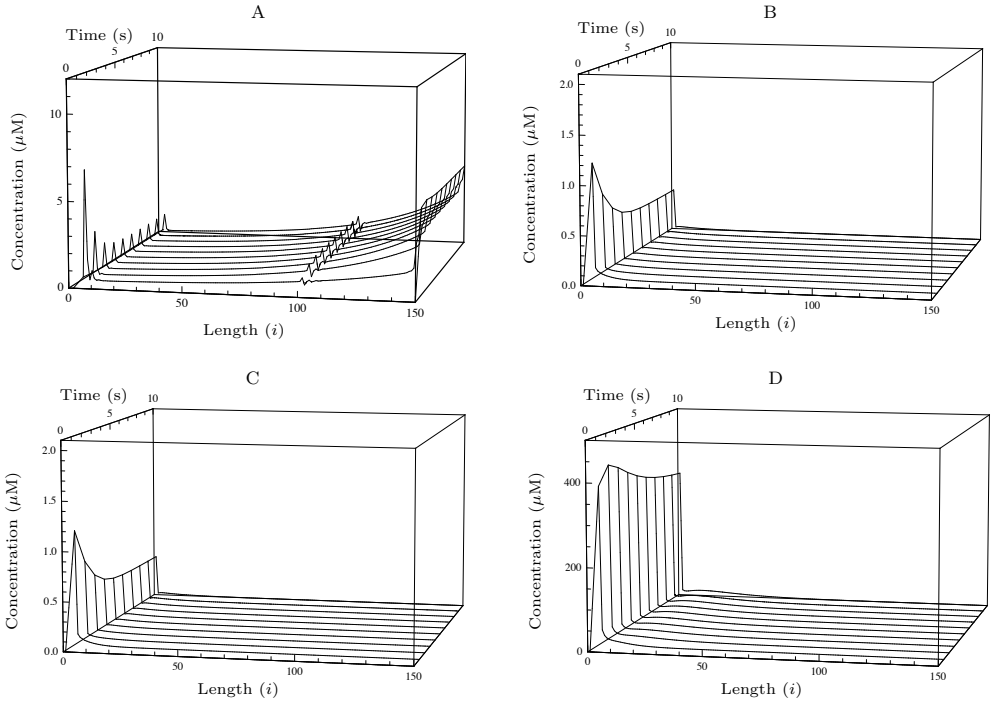

Fig. E 1 The effect of FtsZ diffusion between the cell caps and midcell compartments. FtsZ polymer concentrations are plotted for length *i* at different time points. Inclusion of FtsZ diffusion between the cell caps and the midcell region removes the accumulation of long open polymers seen in the Surovtsev model.[14] (A) The concentration of open FtsZ polymers in the "*in vivo*" Surovtsev model, $\xi = 0.001$, $\sigma = 0.5$, $k_{\text{cyc1}} = 60\,\text{s}^{-1}$, $k_{\text{cyc2}} = 0.4\,\text{s}^{-1}$. (B) The concentration of FtsZ polymers in the cell caps in CAM-FF. (C) The concentration of FtsZ polymers in the midcell region in CAM-FF. (D) The concentration of FtsZ polymers in the midcell membrane compartment in CAM-FF. All parameter values as shown in Table 1.

References

1 D. Bramhill, *Annual review of cell and developmental biology*, 1997, **13**, 395–424.

2 P. Maupin and T. Pollard, *Journal of ultrastructure and molecular structure research*, 1986, **94**, 92–103.

3 Z. Li, M. Trimble, Y. Brun and G. Jensen, *The EMBO journal*, 2007, **26**, 4694–4708.

4 E. Bi and J. Lutkenhaus, *Nature*, 1991, **354**, 161–164.

5 J. Löwe and L. Amos, *Nature*, 1998, **391**, 203–206.

6 P. de Boer, *Current opinion in microbiology*, 2010, **13**, 730–737.

7 J. Lutkenhaus and S. Addinall, *Annual review of biochemistry*, 1997, **66**, 93–116.

8 D. Bramhill and C. Thompson, *Proc. Natl. Acad. Sci. USA*, 1994, **91**, 5813–5817.

9 H. Erickson, D. Taylor, K. Taylor and D. Bramhill, *Proc. Natl. Acad. Sci. USA*, 1996, **93**, 519–523.

10 A. Mukherjee and J. Lutkenhaus, *The EMBO Journal*, 1998, **17**, 462–469.

11 C. Lu and H. Erickson, *Cell Structure and Function*, 1999, **24**, 285–290.

12 P. Taschner, P. Huls, E. Pas and C. Woldringh, *Journal of bacteriology*, 1988, **170**, 1533–1540.

13 M. Osawa, D. Anderson and H. Erickson, *Science*, 2008, **320**, 792–794.

14 I. Surovtsev, J. Morgan and P. Lindahl, *PLoS computational biology*, 2008, **4**, e1000102.

15 Y. Chen and H. Erickson, *Journal of Biological Chemistry*, 2005, **280**, 22549–22554.

16 I. Hörger, E. Velasco, G. Mingorance, J. Rivas, P. Tarazona and M. Vélez, *Physical Review E: Statistical, Nonlinear, and Soft Matter Physics*, 2008, **77**, 011902.

17 I. Hörger, E. Velasco, G. Rivas, M. Vélez and P. Tarazona, *Biophysical Journal: Biophysical Letters*, 2008, **94**, L81–L83.

18 D. Turner, I. Portman, T. Dafforn, A. Rodger, D. Roper, C. Smith and M. Turner, *Biophysical Journal*, 2012, **102**, 731–738.

19 I. Surovtsev, Z. Zhang, P. Lindahl and J. Morgan, *Journal of Theoretical Biology*, 2009, **260**, 422–429.

20 G. Lan, C. Wolgemuth and S. Sun, *Proc. Natl. Acad. Sci. USA*, 2007, **104**, 16110–16115.

21 W. Margolin, *Nature Reviews Molecular Cell Biology*, 2005, **6**, 862–871.

22 P. Mateos-Gil, A. Paez, I. Hörger, G. Rivas, M. Vicente, P. Tarazona and M. Vélez, *Proc. Natl. Acad. Sci. USA*, 2012, **109**, 8133–8138.

23 H. Erickson, *Proc. Natl. Acad. Sci. USA*, 2009, **106**, 9238–9243.

24 D. RayChaudhuri and J. T. Park, *Nature*, 1992, **359**, 251–254.

25 L. Romberg and T. Mitchison, *Biochemistry*, 2004, **43**, 282–288.

26 Y. Chen, K. Bjornson, S. Redick and H. Erickson, *Biophys. J.*, 2005, **88**, 505–514.

27 D. Scheffers, J. de Wit, T. den Blaauwen and A. Driessen, *Biochemistry*, 2002, **41**, 521–529.

28 D. Scheffers, J. de Wit, T. den Blaauwen and A. Driessen, *FEBS letters*, 2001, **494**, 34–37.

29 S. Pichoff and J. Lutkenhaus, *Molecular Microbiology*, 2005, **55**, 1722–1734.

30 Z. Liu, A. Mukherjee and J. Lutkenhaus, *Molecular Microbiology*, 1999, **31**, 1853–1861.

31 T. Beuria, S. Mullapudi, E. Mileykovskaya, M. Sadasivam, W. Dowhan and W. Margolin, *Journal of Biological Chemistry*, 2009, **284**, 14079–14086.

32 C. Lu, J. Stricker and H. Erickson, *Cell Motil Cytoskeleton*, 1998, **40**, 71–86.

33 S. Rueda, M. Vicente and J. Mingorance, *Journal of bacteriology*, 2003, **185**, 3344–3351.

34 J. Pla, M. Sánchez, P. Palacios, M. Vicente and M. Aldea, *Molecular Microbiology*, 1991, **5**, 1681–1686.

35 M. Caplan and H. Erickson, *Journal of Biological Chemistry*, 2003, **278**, 13784–8.

36 L. Romberg, M. Simon and H. Erickson, *J. Biol. Chem.*, 2001, **276**, 11743–11753.

37 C. Culbertson, S. Jacobson and J. Ramsey, *Talanta*, 2002, **56**, 365–373.

38 B. Corbin, Y. Wang, T. Beuria and W. Margolin, *Journal of Bacteriology*, 2007, **189**, 3026–3035.

39 K. Schmidt, N. Peterson, R. Kustusch, M. Wissel, B. Graham, G. Phillips and D. Weiss, *Journal of Bacteriology*, 2004, **186**, 785–793.

40 J. Stricker, P. Maddox, E. Salmon and H. Erickson, *Proc. Natl. Acad. Sci. USA*, 2002, **99**, 3171–3175.

41 S. Haney, E. Glasfeld, C. Hale, D. Keeney, Z. He and P. de Boer, *Journal of Biological Chemistry*, 2001, **276**, 11980–11987.

42 A. Martos, C. Alfonso, López-Navajas, R. Ahijado-Guzmán, J. Mingorance, A. Minton and G. Rivas, *Biochemistry*, 2010, **49**, 10780–10787.

43 A. Mukherjee, K. Dai and J. Lutkenhaus, *Proc. Natl. Acad. Sci. USA*, 1993, **90**, 1053–1057.

44 D. Anderson, F. Gueiros-Filho and H. Erikson, *Journal of Bacteriology*, 2004, **186**, 5775–5781.

45 C. Hale and P. De Boer, *Journal of Bacteriology*, 1999, **181**, 167–176.

46 M. Oliva, S. Cordell and J. Löwe, *Nature structural & molecular biology*, 2004, **11**, 1243–1250.

47 J. Mingorance, S. Rueda, P. Gómez Puertas, A. Valencia and M. Vicente, *Molecular Microbiology*, 2001, **41**, 83–91.

48 Y. Chen and H. Erickson, *Biochemistry*, 2009, **48**, 6664–6673.

49 S. Huecas, C. Schaffner-Barbaero, W. García, H. Yébenes, J. Palacios, J. Díaz, M. Menédez and J. Andreu, *Journal of Biological Chemistry*, 2007, **282**, 37515–37528.

50 E. Small, R. Marrington, A. Rodger, D. Scott, K. Sloan, D. Roper, T. Dafforn and S. Addinall, *Journal of Molecular Biology*, 2007, **369**, 210–221.

51 R. Pacheco-Gómez, X. Cheng, M. Hicks, C. Smith, D. Roper, S. Addinall, A. Rodger and T. Dafforn, *Biochemical Journal*, 2013, **449**, 795–802.

52 Q. Sun and W. Margolin, *Journal of bacteriology*, 1998, **180**, 2050–2056.

53 T. Den Blaauwen, N. Buddelmeijer, M. Aarsman, C. Hameete and N. Nanninga, *Journal of bacteriology*, 1999, **181**, 5167–5175.

54 R. Astumian, *Science*, 1997, **276**, 917–922.

55 R. Astumian and I. Derenyi, *Eur. Biophys. J.*, 1998, **27**, 474–489.

56 A. Feucht, I. Lucet, M. Yudkin and J. Errington, *Molecular microbiology*, 2001, **40**, 115–125.

Glossary of notation and terminology used in the description of CAM-FF

Terms are given in the order in which they appear in the text.

Midcell region	A central cylindrical section of the cell with width 100 nm, as if the cell is sliced at both edges of the Z-ring.
Cell caps	All regions of the cell outside of the midcell region slice.
Midcell membrane	The membrane surrounding the cylindrical midcell region slice.
Elongation	The addition of a single FtsZ monomer to an FtsZ polymer of length i to form a polymer of length $i+1$, where i is greater than or equal to 2.
Annealing	The binding of a polymer of length i to a polymer of length j to form a polymer of length $i+j$, where i and j are greater than or equal to 2.
[GDP]	The concentration of GDP in the cell caps and the midcell region.
[GTP]	The concentration of GTP in the cell caps and the midcell region.
$i_{\max}$	The maximum length of an FtsZ polymer, in subunits.
$Z_{\mathrm{D}}^{\mathrm{mid}}$	The concentration of GDP-bound FtsZ monomers in the midcell region.
$Z_{\mathrm{D}}^{\mathrm{bnd}}$	The concentration of GDP-bound FtsZ monomers on the midcell membrane.
$Z_{\mathrm{D}}^{\mathrm{cc}}$	The concentration of GDP-bound FtsZ monomers in the cell caps.
$Z_{\mathrm{T}}^{\mathrm{mid}}$	The concentration of GTP-bound FtsZ monomers in the midcell region.
$Z_{\mathrm{T}}^{\mathrm{bnd}}$	The concentration of GTP-bound FtsZ monomers on the midcell membrane.
$Z_{\mathrm{T}}^{\mathrm{cc}}$	The concentration of GTP-bound FtsZ monomers in the cell caps.
Z_i^{mid}	The concentration of FtsZ polymers of length i in the midcell region, for $2 \leq i \leq i_{\max}$.
Z_i^{bnd}	The concentration of FtsZ polymers of length i on the midcell membrane, for $2 \leq i \leq i_{\max}$.
Z_i^{cc}	The concentration of FtsZ polymers of length i in the cell caps, for $2 \leq i \leq i_{\max}$.
R_{ex1}	The rate of exchange of GDP for GTP by monomeric FtsZ.
k_{ex1}	The rate constant for the exchange of GDP for GTP by monomeric FtsZ.
R_{ex2}	The rate of exchange of GTP for GDP by monomeric FtsZ.

k_{ex2}	The rate constant for the exchange of GTP for GDP by monomeric FtsZ.
R_{dim1}	The rate of dimerisation of FtsZ.
k_{dim1}	The rate constant for the dimerisation of FtsZ.
R_{dim2}	The rate of the reverse of dimerisation i.e. the dissociation of an FtsZ dimer to two FtsZ monomers.
k_{dim2}	The rate constant for the dissociation of FtsZ dimers.
R^i_{el1}	The rate of elongation of an FtsZ polymer of length i to form an FtsZ polymer of length $i+1$.
k_{el1}	The rate constant for the FtsZ elongation reaction.
R^i_{el2}	The rate of the reverse of elongation i.e. the dissociation of an FtsZ polymer of length $i+1$ to form an FtsZ polymer of length i and an FtsZ monomer.
k_{el2}	The rate constant for the dissociation of the terminal FtsZ monomer from an FtsZ polymer.
R^i_{an1}	The rate of annealing of FtsZ polymers i.e. the formation of an FtsZ polymer of length i form an FtsZ polymer of length j and an FtsZ polymer of length $i-j$.
R^i_{an2}	The rate of loss of FtsZ polymers of length i due to annealing reactions.
k_{an}	The rate constant for the annealing reaction.
R^i_{dis}	The rate of dissociation of FtsZ polymers of length i following GTP hydrolysis, where both GTP hydrolysis and the subsequent FtsZ dissociation are captured by a single rate constant.
k_{dis}	The rate constant for the hydrolysis and dissociation reaction.
R^i_{cm}	The rate of diffusion of FtsZ polymers of length i from the cell caps to the midcell region.
R^i_{mc}	The rate of diffusion of FtsZ polymers of length i from the midcell region to the cell caps.
k_{dif}	The rate constant for the diffusion of FtsZ, which is assumed to be independent of the length of the FtsZ polymer.
V_{mid}	The volume of the midcell region, given by the volume of a cylinder with radius equal to the cell radius (r) and length equal to the width of the Z-ring (ω).
V_{bnd}	The volume of the midcell membrane, where the membrane depth is taken to be the length of a single FtsZ monomer (l_0).

V_{cc}	The volume of the cell caps, where the cell is represented as a cylinder with radius r and length 4 μm.
$R^{\mathrm{D}}_{\mathrm{bind1}}$	The rate of membrane binding of GDP-bound FtsZ monomers in the midcell region.
$R^{\mathrm{T}}_{\mathrm{bind1}}$	The rate of membrane binding of GTP-bound FtsZ monomers in the midcell region.
R^{i}_{bind1}	The rate of membrane binding of an FtsZ polymer of length i in the midcell region.
k_{bind1}	The rate constant for the binding of an FtsZ subunit to a membrane anchor protein.
B	The total number of ZipA and FtsA molecules in the cell.
$S(i)$	The expected number of membrane anchor sites occupied by a polymer of length i.
κ	The equilibrium constant for the interaction of FtsZ with a membrane anchor protein.
$R^{\mathrm{D}}_{\mathrm{bind2}}$	The rate of dissociation of GDP-bound FtsZ monomers from the midcell membrane.
$R^{\mathrm{T}}_{\mathrm{bind2}}$	The rate of dissociation of GTP-bound FtsZ monomers from the midcell membrane.
R^{i}_{bind2}	The rate of dissociation of an FtsZ polymer of length i from the midcell membrane.
k_{bind2}	The rate constant for the dissociation of an FtsZ subunit from a membrane anchor protein.
P_a	The probability that a 4 nm $\times$ 4 nm grid square on the midcell membrane surface contains a membrane anchor protein, on the assumption that 30% of the total number of ZipA and FtsA molecules in the cell (B) are localised to the midcell membrane.
$p_1(i)$	The fraction of FtsZ polymers of length i expected to be attached to the membrane by a single anchor site.
τ_{Z}	The total tension of the Z-ring.
τ_0	The cell surface tension.
$\hat{\tau}$	The maximum tension the Z-ring can withstand.
ς	The Z-ring radius.
r	The cell radius.

ρ	The Z-ring radius as a fraction of the cell radius i.e. ς/r.
ω	The width of the Z-ring.
l_0	The length of an FtsZ subunit.
F	A constant proportional to the force of the interaction of FtsZ with a single membrane anchor protein.
ϑ_0	The rate constant for the change in the Z-ring radius length for a difference in the total Z-ring tension (τ_Z) and the maximum tension the Z-ring can withstand ($\hat{\tau}$).
$\bar{i}$	The average length of membrane-bound FtsZ polymers at equilibrium.
N_Z	The total number of membrane-bound FtsZ polymers at equilibrium.
χ	The contraction parameter value, which is defined as equal to $\bar{i}^2/N_Z$.
α	The initiation threshold for contraction, which is defined as equal to $\tau_0\omega r/F\mathrm{P}_a l_0$.
γ	A constant which is defined as equal to $2r/\omega$.
ϑ	The rate constant for the change in the Z-ring radius fraction (ρ), which is defined as equal to $\vartheta_0 F\mathrm{P}_a l_0/\omega r$.

Biological insights from a simulation model of the critical FtsZ accumulation required for prokaryotic cell division

Claire E. Dow[1], Hugo A. van den Berg[2], David I. Roper[3], Alison Rodger[4,5*]

[1] Molecular Organisation and Assembly in Cells Doctoral Training Centre, Senate House, University of Warwick, Coventry, CV4 7AL, United Kingdom

[2] Mathematics Institute, University of Warwick, Coventry, CV4 7AL, United Kingdom

[3] School of Life Sciences, University of Warwick, Coventry, CV4 7AL, United Kingdom

[4] Department of Chemistry, University of Warwick, Coventry, CV4 7AL, United Kingdom

[5] Warwick Analytical Science Centre, University of Warwick, Coventry, CV4 7AL, United Kingdom

[*]Corresponding author. Email: a.rodger@warwick.ac.uk

Biochemistry, 2015, 54 (24), pp 3803–3813

DOI: 10.1021/acs.biochem.5b00261

Publication Date (Web): June 1, 2015

Funding support statement

This work was supported by an EPSRC-funded studentship to CD through the MOAC Doctoral Training Centre (Grant number EP/F500378/1).

Abbreviations

CAM-FF	Critical Accumulation of Membrane-bound FtsZ Fibres
ATP	Adenosine-5'-triphosphate
GDP	Guanosine-5'-diphosphtae
GMP	Guanosine-5'-monophosphtae
GTP	Guanosine-5'-triphosphtae

Running Title (50 characters incl. spaces):

CAM-FF accurately predicts cell division outcome

ABSTRACT

A simulation model of prokaryotic Z-ring assembly, based on the observed behaviour of FtsZ *in vitro* as well as on *in vivo* parameters, is used to integrate critical processes in cell division. According to the model, the cell's ability to divide depends on a "contraction parameter" (χ) that links the force of contraction to the dynamics of FtsZ. This parameter accurately predicts the outcome of division. Evaluating the GTP binding strength, the FtsZ polymerization rate, and the intrinsic GTP hydrolysis/dissociation activity, we find that inhibition of GTP-FtsZ binding is an inefficient anti-bacterial target. Furthermore, simulations indicate that the temperature-sensitivity of the *ftsZ84* mutation arises from the conversion of FtsZ to a dual-specificity NTPase. Finally, the sensitivity to temperature of the rate of ATP hydrolysis, over the critical temperature range, leads us to conclude that the *ftsZ84* mutation affects the turnover rate of the Z-ring much less strongly than previously reported.

INTRODUCTION

Cytokinesis is the final step in cell division, the process whereby the parent cell divides into two daughter cells each containing a complete copy of the genome. Although cytokinesis forms an attractive target for antibacterial drug design, success to date has been hampered by a lack of understanding of the interplay of the relevant factors. A key stage in prokaryotes is the formation of a contractile ring, composed of fibres of the cytoskeletal protein FtsZ, at the division plane.[1] This so-called Z-ring is anchored to the cytoplasmic face of the cell membrane by the direct interaction of FtsZ with the membrane-binding proteins ZipA and FtsA.[2] These proteins constitute the structural scaffold for the recruitment of various additional proteins to form the complete "divisome" complex, which includes the enzymes required for peptidoglycan synthesis and remodelling. Following assembly, the Z-ring contracts, drawing the membrane on opposite sides of the cell together. For recent reviews see Typas et al., Egan and Vollmer, and den Blaauwen.[3–5]

Despite extensive work since the discovery in 1991 that FtsZ is the major component of the contractile ring,[6] the mechanism driving the assembly and contraction of the Z-ring as well as the link between protein function and cellular phenotype remain poorly understood. Translation of the activity of FtsZ measured *in vitro* to its function *in vivo* is critical to further our understanding of cytokinesis.

We have developed a model of this key phase of cell division[7] and showed that the results are consistent with the division behaviour observed following the loss of expression of FtsA or ZipA, two components of the *Escherichia coli* divisome complex. This strongly suggests that the simulation model is a reliable tool to probe the early stages of cytokinesis which critically depend on the Z-ring and its membrane interactions. Here we explore how various perturbations of the system, such as mutations, which are represented in the model as changes of various biochemical and biophysical parameters, affect the initiation and completion of cell division. In each case, the predictions correspond with observed phenomena (up to absolute magnitudes of timescales, as will be explained further below), and can be used to evaluate which components are likely to constitute effective drug targets. We refer to our model as CAM-FF: *Critical Accumulation of Membrane-bound FtsZ Fibres*. After summarising the key aspects of the model, we review the wild-type behaviour, which forms our reference point, followed by analysis of:

1. A reduction in the measured rate of GTP hydrolysis by:
    (a) a reduction in the intrinsic rate of GTP hydrolysis/dissociation;
    (b) a reduction in the GTP binding strength;
    (c) a reduction in the FtsZ polymerisation rate.
2. Depletion or overexpression of anchor proteins.
3. Overexpression of FtsZ.
4. The *ftsZ84* mutant that has a significantly reduced FtsZ GTPase activity, combined with the introduction of ATPase activity.

Finally, we discuss the implications of our simulations for antibacterial agents.

EXPERIMENTAL PROCEDURES

We develop and apply CAM-FF to a range of different bacteria whose cell-division phenotype has yet to be explained. CAM-FF takes as its point of departure the "Z-centric hypothesis" (*viz.*, assembly of the Z-ring and the force of its constriction originate from FtsZ) and extends earlier work by Surovtsev *et al.*[8] Key assumptions are (i) no dependence of Z-ring formation on the cyclisation of FtsZ polymers into closed rings (*cf.* Surovtsev *et al.*,[8]), (ii) the addition of the diffusion of FtsZ into the midcell region, and (iii) the interaction of FtsZ polymers with membrane-binding proteins.

The removal of FtsZ polymer cyclisation followed from our recent work to determine the persistence length of FtsZ, *i.e.* the length scale below which the polymer molecule is essentially straight, which is 1.15 ± 0.25 μm;[9] since mature *E. coli* have a circumference of approximately 2.5 μm, *in vivo* FtsZ most probably forms short linear chains rather than rings curved around the circumference of the cell.

The cell is conceptually divided into three compartments: (1) the cell caps, (2) the midcell region, and (3) the midcell membrane, as shown in Figure 1A. FtsZ molecules within the cell caps and the midcell region undergo polymerisation and GTP hydrolysis reactions, as shown in Figure 1B, and movement between these two compartments is by diffusion with rate constant k_{dif}. Movement occurs from the midcell region to the midcell membrane when FtsZ molecules bind directly to anchor proteins fixed to the membrane or by polymerisation reactions to membrane-bound FtsZ. We account for the interaction of single FtsZ polymers with multiple membrane anchor proteins as depicted in Figure 1C. This depends on the dissociation constant of the FtsZ:anchor interaction, $\kappa = k_{\mathrm{bind2}} / k_{\mathrm{bind1}}$, and the density of anchor proteins on the membrane. Using the midcell membrane surface area and the number of

anchor proteins available, this anchor density is expressed as a probability that a bound FtsZ monomer is adjacent to, and consequently binding to, a binding site, P_a. As polymer length increases, the number of anchor connections increases, thereby lowering the probability that the polymer will be released from the membrane. Figure 1D shows the fraction of polymers predicted to be singly-bound to the membrane and thereby susceptible to release on dissociation at the anchor site.

CAM-FF accounts for the physical forces required to deform the cell against its surface tension. We assume that the pinching tension generated on Z-ring contraction depends on: (i) the population of FtsZ polymers accumulated in the Z-ring; (ii) the number of membrane protein:FtsZ interactions; and (iii) the force of this interaction. If the calculated maximum tension of the Z-ring exceeds the tension required to oppose the surface tension at a given radius, then we assume that a "black-box" mechanism will result in contraction of the ring and thus a decrease in the Z-ring and midcell diameter with time *i.e.* cell division may proceed (this black box could be a ratchet mechanism driven by thermal fluctuations, possibly assisted by a motor component, or by a conformational change in FtsZ on GTP hydrolysis). Figure 1E summarises the key variables in the force model.

The assumptions made in CAM-FF are listed below. For any biological system that is consistent with these assumptions, the model predictions are valid. Brief assessments or justifications are provided in parentheses.

1. The rate of polymerisation of GDP-bound FtsZ is zero. (Although GDP-bound FtsZ has been shown to polymerise, the equilibrium constant is significantly lower than for GTP[10] and was assumed to equal 0 in the original Surovtsev model.[8])

2. GTP hydrolysis occurs within membrane-bound FtsZ polymers in the same way as for free polymers. (This is plausible in the absence of evidence to the contrary.)

3. The dissociation of the FtsZ polymer following GTP hydrolysis proceeds at rate k_{dis} = 0.075 s^{-1}. (The value of k_{cat} from Romberg and Mitchison of 4.5 min^{-1} leads to this value.[11])

4. All lengths of FtsZ polymer diffuse at the same rate. (Failure of this assumption to hold may account in part for the too-rapid assembly of the Z-ring that CAM-FF predicts if, in fact, longer polymers diffuse more slowly than monomers/oligomers.)

5. The number of membrane anchor proteins, *B*, amounts to 30% of the cell complement of ZipA and FtsA. (Stricker *et al.* found that at equilibrium, approximately 30% of the cell complement of ZipA was localised to the Z-ring.[12])

6. Min and nucleoid occlusion systems were functional, permitting binding of FtsZ polymers in the midcell region only. (This is valid in the wild-type scenario but may not hold in certain mutants.)

7. FtsZ polymers do not grow longer than a given length. (We verified that increasing the value of above 150 subunits does not affect the model output appreciably.)

8. The initiation threshold value α is 20,000; the wild-type contraction parameter value χ is sufficient to allow full division with the capacity to lose 15% of its value before division behaviour is affected. (The initiation threshold is set such that the maximum value of the threshold plot as shown in Figure 2, the division completion threshold, CT, is 85% of the wild-type parameter value χ.)

9. The value of χ is constant. (We consider this to be reasonable for the initial stages of division which determine the division outcome since the peak of the threshold curve is reached early in the division process (ρ = 0.833), independent of the value of the initiation threshold α.)

10. If the calculated maximum tension of the Z-ring exceeds the tension required to oppose the cell surface tension at a given radius, the Z-ring diameter will decrease over time.

RESULTS

Model overview

In essence, in CAM-FF a complex system of biochemical and biophysical interactions is captured by a single index, the *contraction parameter*, χ, which links the population of membrane-bound FtsZ molecules to the force of constriction, and which can be used to predict the cell's ability to divide. It is given by

$$\chi = \overline{i}^2 N_z, \qquad (1)$$

where $\overline{i}$ is the average number of FtsZ subunits in the membrane-bound polymers and N_z is the total number of membrane-bound FtsZ polymers. The key result is that, in order to initiate contraction of the Z-ring, the value of χ must exceed the initiation threshold α which is given by

$$\alpha = \frac{\tau_0 \omega r}{F \mathrm{P_a} I_0}, \qquad (2)$$

where τ_0 is the cell surface tension, ω is the width of the Z-ring, r is the radius of the Z-ring before contraction, F is proportional to the force of the interaction of FtsZ with a single membrane anchor site, $\mathrm{P_a}$ represents the surface density of the membrane-bound proteins ZipA and FtsA (*i.e.* the probability that an FtsZ subunit is adjacent to an anchor on the membrane), and I_0 is the length of one FtsZ subunit.

Following initiation, in order for the Z-ring to continue to contract, the following condition applies:

$$\chi > \alpha\rho\left(1+\frac{2r}{\omega}\rho\sqrt{1-\rho^2}\right), \qquad (3)$$

where ρ is the dimensionless ratio of the radius of the Z-ring at any time point relative to the original radius r. As contraction proceeds, ρ decreases from 1 to 0. A plot of the contraction threshold as a function of ρ is given in Figure 2. Since the contraction parameter χ must exceed the contraction threshold at all values of the radius ratio from 1 to 0 for contraction to proceed, three outcomes are possible:

(i) division proceeds to completion;

(ii) division is initiated but stalls prior to completion; and

(iii) division is not initiated.

These outcomes are indicated schematically in Figure 2. The maximum value of the threshold plot can be regarded as the *division completion threshold*. Despite a number of simplifications, CAM-FF makes accurate predictions of cell division behaviour.[7] However, the estimates of timescales of the process, while correct in terms of relative ordering, are too short, for reasons that are discussed below. The model has been implemented in *Mathematica 8* as detailed in our previous paper.[7] In this paper we present the predicted wild-type behaviour and the predicted effects of various perturbations to key biochemical parameters and contrast those predictions with available experimental data.

Wild-type model predictions

The predicted populations of membrane-bound FtsZ at equilibrium according to CAM-FF are summarised in Table 1. The average bound polymer length ($\bar{i}$), the percentage of the FtsZ population incorporated into the Z-ring, the total number of membrane-bound FtsZ polymers (N_z), and the value of χ at equilibrium are shown, as well as the predicted division outcome. Using the wild-type parameter values as listed in Table 2, the average membrane-bound polymer length is predicted to be 14 subunits, with 28% of the cell complement of FtsZ predicted to be

membrane-bound at equilibrium. This is in accordance with the values measured experimentally of 30 – 35%.[12,13]

CAM-FF predicts a significantly faster Z-ring formation time (5 s) than is observed experimentally (1 min)[14,15] which is a consequence of assuming a single diffusion constant for all lengths of FtsZ polymer and of using the rates as measured *in vitro*, without accounting for the inhibitory effect of the cell environment viscosity and crowding (see Experimental Procedures). Accounting for this effect would slow down Z-ring assembly without materially affecting the prediction of cell division outcome. Since insufficient data are currently available to constrain these processes and our main interest is in relative orderings, we retain the simplest assumptions rather than incorporating *ad hoc* adjustments, accepting an order of magnitude timescale error.

Measurement of the GTPase activity of FtsZ alone cannot predict cell division

The experimental observation that an FtsZ mutant has a reduced rate of GTP hydrolysis can be attributed to a number of different causes, including (i) a reduced rate constant of the hydrolysis/dissociation reaction, (ii) a reduced binding efficiency of GTP, or (iii) a reduced rate of FtsZ polymerisation, since the GTPase active site is formed at the interface of two FtsZ subunits within the polymer. The same net effect in the cell would be obtained with lower FtsZ or GTP concentrations. The advantage of a mathematical model such as CAM-FF is these various scenarios can be explored independently.

As summarised in Table 1, a decrease in the rate of GTP hydrolysis/dissociation (with no other concomitant changes) results in increases of the average bound-polymer length, the percentage incorporation, and the value of the contraction parameter as well as a decrease in the number of membrane-bound FtsZ polymers. An increase in the rate of GTP hydrolysis has the opposite effects. Since the initiation threshold value α is by assumption independent of the rate of GTP hydrolysis, Equation (2), CAM-FF indicates that a loss-of-GTPase-

function mutation in FtsZ does not reduce the ability of the cell to initiate contraction and may even render the cell better able to divide as the equilibrium value of the contraction parameter increases. Conversely, an increase in the rate of hydrolysis reduces the ability of the cell to divide.

The above prediction is corroborated by the behaviour of curcumin (1,7-bis-(4-hydroxy-3-methoxy-phenyl)hepta-1,6-diene-3,5-dione), an antibacterial phenolic compound that is present in turmeric.[16] Curcumin's effect is to inhibit growth of *E. coli* and *Bacillus subtilis* cell cultures. Its mode of action is *via* direct binding to FtsZ and disruption of FtsZ polymerisation and bundling. The binding of curcumin results in an increase in GTP turnover and in the rate of FtsZ depolymerisation.[16] This may be due to a direct increase in the GTP hydrolysis reaction, induced by the change in FtsZ secondary structure on curcumin binding. Alternatively, the increase in GTP turnover may be due to a steric hindrance on polymer bundling (which is not explicitly represented in our model). Such a steric hindrance has the same effect as a direct increase of the GTP hydrolysis/dissociation rate in CAM-FF compared to the wild-type case, since polymer bundling has been shown to decrease the intrinsic rate of GTP hydrolysis by FtsZ.[17] An increase in the GTP hydrolysis/dissociation rate constant in CAM-FF reduces χ and inhibits cell division. Such a mechanism of increased GTP turnover may also deplete the cell's supply of GTP, which further reduces the accumulation of FtsZ polymers.

If taken to its logical extreme, the effect of an extreme reduction of the intrinsic hydrolysis rate, all else being equal, would seem to be that cell division is maximally expedited (*i.e.* maximum cell division when there is no GTPase activity). However, this overlooks the fact that reduced hydrolysis also results in the accumulation of longer polymers. Given the persistence length of FtsZ, ~1 μm,[9] such accumulation will impede cell division. Moreover, while reduced GTP hydrolysis promotes Z-ring formation, the Z-ring must depolymerise later in the cycle and a complete loss of GTPase activity would arrest this process. It is unlikely that an

extreme perturbation to the hydrolysis rate could arise without some accompanying effect on GTP binding and FtsZ polymerisation.

The analysis suggests a possible function of the FtsZ-interacting protein ZapA. It has been clear for some time that ZapA slows down GTP hydrolysis when ZapA is added to FtsZ *in vitro.*[18,19] At a mixing ratio of 4:1 ZapA:FtsZ, the GTPase actvity is reduced by ~50%.[19] However, the mechanism of slowing remains unclear. Our analysis suggests that by reducing the rate of GTP hydrolysis, ZapA promotes the formation of longer polymers and reduces the time taken for the cell to reach the critical contraction threshold, thus accelerating cell division once Z-ring formation has started.

As summarised in Table 1, either reduced GTP binding strengths or reduced FtsZ polymerisation rates lead to the formation of shorter polymers. These factors inhibit the formation of the Z-ring and reduce its contraction ability, which is similar to the effect of increasing the GTPase activity of FtsZ. Expression of the reduction of activity as a percentage of the wild-type value allows a direct comparison. Although a significant reduction to GTP binding can adversely affect cell division, CAM-FF suggests that the effect is relatively small and so competitive inhibition of GTP binding to FtsZ would be an ineffective strategy for the development of targeted antibacterial drugs (Figure 3).

The predicted modest effect of a reduction in GTP binding may explain why C8-substituted guanine, guanosine, guanosine 5'-monophosphate (GMP) and guanosine 5'-triphosphates have been found to be ineffective antibacterial agents against *E. coli*, despite the C8-substituted GTP analogues displaying strong inhibition of FtsZ polymerisation *in vitro* [20,21] by competition for the GTP binding site. It should be noted that the lack of toxicity was not due to low intracellular accumulation, nor to the absence of conversion of the analogue to the inhibitory triphosphate form.[20]

Compared with inhibition of GTP binding, reduction of FtsZ polymerisation affects the contraction parameter more strongly and so

would be predicted to be a more effective approach to arrest cell division. The differential change of χ, with respect to a change in the input parameter, gives a quantitative measure of the sensitivity of the system to perturbation of a specific biochemical interaction. To express the sensitivity as a dimensionless measure, which allows direct comparison of the different input paramaters, we use a sensitivity coefficient given by $p\Delta\chi/(\chi\Delta p)$ as a relative measure, where p is the value of the parameter. For example, for the GTP-binding constant, using the value of χ obtained for the parameter values of 99% of the wild-type GTP-binding rate constant (p = 0.0099 $\mu M^{-1}s^{-1}$, χ = 91,796) and 101% of the wild-type GTP-binding rate constant (p = 0.0101 $\mu M^{-1}s^{-1}$, χ = 91,874.7) to approximate the sensitivity of the wild-type system to changes to the rate of GTP binding, the sensitivity coefficient is given by (0.01×78.7)/(91,835.9×0.0002) = 0.043. By comparison, the sensitivity coefficient for FtsZ polymerisation is 1.035 which indicates that rational drug design effort should be focussed on the FtsZ:FtsZ interaction rather than on the inhibition of GTP binding. Indeed, Duggirala *et al.* recently reported the inhibitory effect of coumarin derviatives on *B. subtilis* growth with inhibition of FtsZ polymerisation observed *in vitro*.[22] *In silico* docking studies suggested the inhibitiory effect was due to binding of courmarin to residues of the T7 loop of FtsZ. This prevented FtsZ polymerisation by targetting the C-terminal end of the molecule, rather than via competitive inhibition of GTP binding at the N-terminal domain.

Predicting the effect of anchor protein deletion

In CAM-FF it is assumed that ZipA and FtsA have equivalent effects in anchoring FtsZ to the membrane and the total number of anchor proteins is given by the parameter *B*. The experimental literature cites the number of molecules per cell for ZipA and FtsA as 1500 and 740, respectively,[23] and according to Stricker *et al.* approximately 30% of the cell complement of ZipA localises to the Z-ring *in vivo*.[12] On the assumption that 30% of the cell complement of anchor proteins is located at the midcell, the wild-type value of *B* we have used is 672.

The effect of removing the contribution from either ZipA or FtsA (mimicking a deletion mutant) is summarised in Table 1. Upon deletion of ZipA, P_a is reduced by 67% corresponding to a total number of anchor proteins of 740 (FtsA only), with 30% located on the midcell membrane to give the number of membrane anchor proteins B = 222. The consequence is that the initiation threshold increases substantially so cells are predicted to be unable to initiate contraction in the absence of ZipA. This prediction is corroborated by the experimental observation that ZipA is essential for cell division to occur, even though the Z-ring does form in the absence of ZipA.[24] Thus, CAM-FF accurately predicts the outcome of ZipA depletion.

The lack of division of a ZipA-deletion mutant might suggest ZipA as an antibiotic target. However, the development of small molecule inhibitors has met with limited success. Targeting protein-protein interactions with small molecules remains a challenge due to the relatively large interaction area of the ZipA-FtsZ protein surfaces.[25] Inhibitors discovered by screening [26] and computational methods [27] often have affinities that are too low for therapeutic use but provide lead compounds for development. Figure 4 shows the equilibrium value of the contraction parameter for reductions of the number of ZipA available for FtsZ-membrane anchoring. Between approximately 5% and 85% of the wild-type level of ZipA availability, cells are able to initiate division but contraction will stall prior to completion. Conversely, for an increase in the expression of ZipA, the average membrane-bound polymer length is fairly stable, whereas the percentage incorporation increases, as does the number of membrane-bound FtsZ polymers, and so cell division is facilitated. The sensitivity coefficient for the effect of the number of ZipA binding sites available on the value of the contraction parameter χ is 0.204.

Upon deletion of less abundant FtsA, P_a reduces by 33% (corresponding to a total number of anchor proteins of 1500). CAM-FF predicts that χ reaches the initiation threshold but that contraction stalls

prior to completion. This is consistent with observations that FtsA-depleted cells exhibit indentations above the Z-ring, indicating that contraction is initiated, but division does not occur[24]. ZipA-depleted cells (discussed above), by contrast, appear completely smooth[24], indicating that contraction is not even being initiated.

Overexpression of FtsZ

If FtsZ is overexpressed, CAM-FF predicts increases of the average bound-polymer length and the percentage incorporation of FtsZ into the Z-ring, but a decrease in the number of bound FtsZ polymers. The χ-value indicates that the cells are better able to divide compared to the wild-type. However, FtsZ overexpression also affects assumption 6 (the confinement of membrane-bound FtsZ polymers to the midcell by the Min system – see Experimental Procedures) which is no longer valid: membrane-bound FtsZ will also be found at the cell poles. For example, at 2.7-fold over-expression of FtsZ in *E. coli*, the "minicell phenotype" is induced, in which divisions occur at the cell poles, in addition to the normal midcell divisions. As a closely similar phenotype follows deletion of the Min operon, it appears reasonable to suppose that control by the Min system is overwhelmed at increased concentrations of FtsZ. Furthermore, since the function of MinC is to antagonise the polymerisation activity of FtsZ,[28] the phenotype observed on loss of the intrinsic GTPase activity in FtsZ, which promotes polymerisation, somewhat resembles the loss of the Min system. In FtsZ over-expression studies, it was found that once the concentration of FtsZ reaches twelve times the wild-type value, all divisions are inhibited and cells become filamentous.[29]

The predicted average membrane-bound polymer length of 36 subunits for 3-fold FtsZ over-expression corresponds to an average polymer length of ~0.14 μm which is of the order of the cell radius. In view of the persistence length of FtsZ,[9] such long polymers are not anticipated to occur in *E. coli* as they would not bend to form the Z-ring. The

behaviour of FtsZ when assumption 6 breaks down has not yet been built into the model.

Temperature-sensitivity of the *ftsZ84* mutation

The GTPase activity of the FtsZ84 (FtsZ-G105S) mutant protein is approximately one-tenth of the wild-type protein, due to its strongly reduced affinity for GTP.[30] So far it has not been clear why cells bearing the *ftsZ84* mutation appear to divide normally at 30°C but are unable to divide at 42°C, particularly since the GTPase activity appears to be temperature-insensitive over this range.[30,31] Translation of the activity of the FtsZ84 protein measured *in vitro* into CAM-FF parameters allows us to explore the biochemical mechanism underlying this temperature-sensitivity.

According to RayChaudhuri and Park, the FtsZ84 mutant protein also catalyses the hydrolysis of ATP, a function not present in the wild-type protein.[31] Filter retention assays with radio-labelled nucleotides showed that the binding affinity of the mutant protein for ATP is approximately 30 times lower than the affinity of the wild-type protein for GTP.[31] The concentration of nucleotides within the cell is known to vary with growth conditions,[32,33] but according to Bennett *et al.*, in *E. coli* the concentration of ATP is approximately twice that of GTP and the concentrations of ADP and GDP are approximately equal.[34] At 42°C the mutant has a similar level of ATPase and GTPase activity whereas at 30°C the ATPase activity is a third of that of the GTPase.[31]

To model the behaviour of *ftsZ84*, we applied a 30-fold reduction in the rate of nucleotide triphosphate (NTP) binding, as well as a range of different increases in the concentration of the pool of activating nucleotides (since the measured concentrations of ATP vary), as indicated in Table 1, and different ranges of NTPase rates of the FtsZ84 protein to account for changes in the ATPase activity as a function of temperature. We assumed that the binding affinities and rates of polymerisation of FtsZ84 are equal for the ATP- and GTP-bound proteins and not temperature-sensitive. These assumptions imply that the

proportion of active sites in the ATP- and GTP-bound states correspond to the relative concentrations of ATP and GTP in the nucleotide pool. In view of the linearity of the rate terms in the kinetic equations, we can use a weighted average of the hydrolysis/dissociation rate constants as the effective rate constant $k_{\mathrm{dis\_eff}}$, based on the relative concentrations of the two activating nucleotides. For example, with an ATP:GTP ratio of 2:1 and a 2-fold reduction to the rate of ATP hydrolysis, the effective NTPase rate is 0.05 s^{-1} ((2/3) × 0.0375 + (1/3) × 0.075 s^{-1}).

Thus, as summarised in Table 1 and shown in Figure 5, at 42°C we predict a reduction in the average length of the membrane-bound FtsZ polymers. This in turn results in a dramatic lowering of χ. The percentage of FtsZ that is membrane-bound is also reduced. CAM-FF therefore predicts that cell division is initiated but stalls prior to completion at 42°C. However, for the lower efficiency of the ATPase activity at 30°C, χ increases above the completion threshold in all ATP:GTP ratios but with a 3-fold reduction in activity relative to the wild-type.

In sum, CAM-FF predicts that cell division occurs at lower temperatures due to the reduction in the ATPase activity of the mutant FtsZ84 protein. The precise point at which the division thresholds are no longer reached depends on the relative concentrations of nucleotides and the true intrinsic rates of hydrolysis/dissociation. The solutions shown in Figure 5 are based on current experimental estimates of the parameters and it is hoped representative of a biologically relevant scenario. CAM-FF also predicts that the introduction of a second mutation into the *ftsZ84* gene that reduces the intrinsic rate of hydrolysis, such as “T7 synergy loop” mutations, would restore cell division behaviour at the currently non-permissive temperature.

Furthermore, CAM-FF predicts that an increase in the concentration of FtsZ would restore cell division. Indeed, it has been shown that the introduction, at low copy numbers, of a plasmid containing the *ftsQ*, *ftsA*, and *ftsZ84* genes leads to recovery of cell division in *ftsZ84* cells but the introduction of the same plasmid with *ftsQ*

and *ftsA* only did not restore division.[35] These findings suggest that the recovery effect is due to increased levels of the FtsZ84 protein.

In summary, CAM-FF predicts that the average bound polymer length is 24 subunits for a 2-fold increase in FtsZ84 concentration and 80 subunits for a 3-fold increase. However, as was the case for wild-type FtsZ overexpression, excess expression of FtsZ threatens to invalidate a key assumption of CAM-FF. The possible breakdown of assumption 6 ties in with the experiemental observation that introduction of a high copy number plasmid to *ftsZ84* cells results in the inhibition of cell division as the Min and nucleoid occlusion systems are overwhelmed and membrane-binding is no longer restricted to the midcell.[35]

Division activity in *ftsZ84* is restored by increased gene dosage of ZipA at the non-permissive temperature,[36] in agreement with the simulation results summarised in Table 1. An increase in the number of membrane anchor proteins decreases the threshold value α and has a small effect on χ. With the value of the wild-type threshold α as above and the number of ZipA molecules per cell increased 3-fold, CAM-FF predicts that the completion threshold is reached and the cell is able to initiate division.

The effect of the *ftsZ84* mutation on Z-ring turnover is less pronounced than previously measured

Two key parameters in CAM-FF are the rate constants for membrane association (k_{bind1}) and dissociation (k_{bind2}) of FtsZ. Since these values are not available, we estimated them from the equilibrium binding constant for the FtsZ-ZipA interaction ($\kappa = 2$ μM)[10] and measurements of the half-life of fluorescence recovery (30 s)[12] when membrane-bound FtsZ-GFP is photobleached. The observed off-rate in the FRAP experiment corresponds to k_{bind2} multiplied by $p_1(\bar{i})$, the fraction of polymers in the singly-bound state (p_1) for the average polymer length at equilibrium $(\bar{i})$. Figure 1D shows how the fraction of polymers in the singly-bound state decreases for longer polymers (since more FtsZ:anchor interactions

retain the FtsZ polymer at the membrane). Cell conditions that increase the average polymer length lead to a decrease in $p_1(\bar{i})$ and therefore lower the rate of release from the membrane, and increase the fluorescence recovery time as k_{bind2} is constant. It is therefore predicted that a decrease in the intrinsic rate of GTP hydrolysis, which increases the average polymer length, will lead to an increase in the half-life of recovery.

On the assumption that the constants determined from WT data apply to the *ftsZ84* mutant, CAM-FF predicts only a minor increase in the half life of recovery for the *ftsZ84* mutant at the permissive temperature: 30 seconds for an ATP:GTP ratio of 2:1, 32 seconds for a ratio of 3:1 and 33 seconds for a ratio of 4:1. This is in contrast to the large increase observed by Stricker *et al.* and Anderson *et al.*[12,13] A minor increase in the percentage incorporation of FtsZ into the ring is also observed. However, this increase is considerably smaller than the values of up to ~65% that were reported by Stricker *et al.*[12] This discrepancy could be due to the fact that different growth conditions were used in their experiments, which affects the values of the rates of NTP hydrolysis as well as the concentrations of available nucleotides and of FtsZ.[33]

DISCUSSION

A simulation model of cytokinesis that includes kinetics and mid-cell membrane binding and contraction allows us to generate predictions of the *in vivo* properties of the Z-ring such as the average bound-polymer length, the percentage of FtsZ incorporation into the Z-ring, and whether a cell will initiate and/or complete cytokinesis. Our predictions accord well with experimental data, leading us to believe that the model, *Critical Accumulation of Membrane-bound FtsZ Fibres* (CAM-FF), adequately captures the dynamics of the processes occurring *in vivo*. The key output of CAM-FF is the contraction parameter χ which links the force of Z-ring contraction to the dynamics of the intracellular population of membrane-bound FtsZ. This χ-value is to be compared to threshold values for

initiation and completion to predict a cell division outcome. Interrogation of CAM-FF yields insights in the underlying mechanistic basis for observed behaviours. In the case of the *ftsZ84* mutation, model analysis suggests that the loss of division behaviour at 42°C is due to the ATPase activity acquired by the mutant FtsZ protein which increases the concentration of the pool of activating nucleotides (GTP and ATP). However, at lower temperatures where the ATPase activity is reduced, a functional Z-ring is able to form and contract. Moreover, the low turnover rate observed for the FtsZ84-ring *in vivo* may reflect changes in experimental conditions rather than be a true effect of the mutation.

While the explanation of the temperature-sensitivity of the *ftsZ84* mutant addresses some of the questions around cell division and cell behaviour observed in the laboratory, the key goal of our model is to understand bacterial cell division sufficiently well to determine which components pose the most effective targets for anti-bacterial agents. Our analysis suggests that targeting the binding of GTP to FtsZ using a competitive inhibitor is an inefficient method of blocking cell division. By contrast, targeting the polymerisation of FtsZ or the availability of ZipA or FtsA binding sites were shown to be considerably more effective. In sum, CAM-FF predicts that the order of efficiency of the possible drug targets as follows: FtsZ polymerisation > ZipA/FtsA availability > GTP-binding.

The model predicts which of three division outcomes prevails as a function of parameter values. In those cases where the model predicts that division can initiate but not complete, the filamentous phenotype is observed in the laboratory. The predicted cell phenotype is an important consideration in antibiotic development. Whereas induction of the filamentous phenotype leads to cell lysis following treatment with β-lactam antibiotics such as cephalexin,[37,38] induction of the filamentous phenotype has also been shown to inhibit phagocytosis by macrophages, where access to the filament pole was a crucial factor.[39] Furthermore, the filamentation process is thought to contribute to bacterial virulence in infections of *Legionella pneumophilia* (legionnaires' disease),[39] *E. coli*

(urinary tract infection),[40] and *Salmonella* (food poisoning).[37] The possibility of inducing dormant states such as those found in *Mycobacterium tuberculosis* infection, in which the organism survives in filamentous form within macrophages [41] may constitute a form of evasion of host defenses. Moreover, pools of dormant filamentous cells may reinitiate division upon removal of the antibiotic. This has been described as a "negative post-antibiotic effect", where the rate of growth of the bacteria is rapid after the removal of an antibiotic as the filamentous cells simultaneously divide.[42] Indirect evidence for this hypothesis is provided by the phenomenon of a resurgence of urinary tract infection following withdrawal of antibiotics.[40]

The CAM-FF model makes no assumptions about the molecular mechanism of Z-ring contraction and requires only that *some* minimal force is required for contraction, perhaps generated by a conformational switch in FtsZ itself on GTP hydrolysis,[43–45] which depends on the interaction of FtsZ polymers with the membrane, where the pulling force on the membrane is considered to be proportional to the number of membrane interactions. To our knowledge, no motor protein has yet been found to associate with FtsZ and it is conceivable that contraction might proceed without the intervention of such a motor, by means of a non-equilibrium process involving the continual binding and release of FtsZ polymers, dependent on the rate of GTP-hydrolysis. The release and rebinding of FtsZ polymers in the Z-ring would effectively create a ratchet mechanism whereby local fluctuations become locked in place by the adjacent binding of further FtsZ polymers. Multiple membrane anchors may play a role in the ratchet, *e.g.* ZipA is tightly anchored within the membrane whereas FtsA is more weakly bound and so is readily released and rebound during thermal fluctuations of the Z-ring or of the cell membrane. Interestingly, FtsA is an ATPase [46] which suggests a possible means of chemical coupling to drive unidirectional contraction. The state of the bound nucleotide may affect the interaction of FtsA with FtsZ or the cell membrane or both.

An additional role of the Z-ring that is not included in the model is the recruitment of peptidoglycan remodeling enzymes on the outside of the inner cell membrane.[47] As the Z-ring contracts, the peptidoglycan remodeling process creates a physical barrier to any subsequent re-expansion of the Z-ring which consolidates the progress made thus far and acts as another ratchet. The contribution of the cell wall to division will be considered in future modeling studies. Furthermore, as described in assumption 6 in Experimental Procedures, in CAM-FF the Min and nucleoid occlusions systems are captured in a simplified form by permitting binding of FtsZ to the ZipA/FtsA at the midcell only. This assumption limits CAM-FF to consideration of the effectiveness of inhibitors of the system such as inhibition of GTP-binding and FtsZ polymerisation, and activation of the GTPase activity of FtsZ. For factors that promote FtsZ polymerisation, CAM-FF requires extension to include the factors that validate assumption 6. For example, the antibacterial benzamide PC190723 has been reported as a promoter of FtsZ polymerisation in *Staphylococcus aureus* [48–50] and mulitple FtsZ rings and arcs are observed in PC190723-treated Methicillin-Resistent *S. aureus.*[51] While CAM-FF in its current form provides insight into various inhibitors of polymerisation, those factors which promote polymerisation require explicit consideration of the Min and nucleoid occlusion systems.

In conclusion, although certain aspects of the biological process have been simplified in our model and the molecular mechanism of the contraction process remains to be elucidated, analysis of the contraction parameter already allows us to make organism-level predictions based on the biochemical activity of FtsZ measured *in vitro*. The model simulations present a relatively cost-effective way of generating novel biological ideas, *e.g.* the biochemical mechanism of temperature-sensitivity of *ftsZ84*. This is particularly important for FtsZ since specific small molecule inhibitors, commonplace in the laboratory for the study of the structural FtsZ homolgue tubulin, are absent. This lack limits the study of the effect of loss of a particular function of FtsZ experimentally. The search for

potential drug interactions may be aided by evaluation of target efficacy *in silico*.

REFERENCES

1. Bramhill, D. (1997) Bacterial cell division. *Annu. Rev. Cell Dev. Biol.* 13, 395–424.

2. Pichoff, S. and Lutkenhaus, J. (2005) Tethering the Z ring to the membrane through a conserved membrane targeting sequence in FtsA. *Mol. Microbiol.* 55, 1722–1734.

3. Typas, A., Banzhaf, M., Gross, C. A. and Vollmer, W. (2011) From the regulation of peptidoglycan synthesis to bacterial growth and morphology. *Nat. Rev. Microbiol.* 10, 123–136.

4. Egan, A. J. F. and Vollmer, W. (2013) The physiology of bacterial cell division. *Ann. N. Y. Acad. Sci.* 1277, 8–28.

5. Den Blaauwen, T. (2013) Prokaryotic cell division: Flexible and diverse. *Curr. Opin. Microbiol.* 16, 738–744.

6. Bi, E. F. and Lutkenhaus, J. (1991) FtsZ ring structure associated with division in *Escherichia coli*. *Nature* 354, 161–164.

7. Dow, C. E., Rodger, A., Roper, D. I. and van den Berg, H. A. (2013) A model of membrane contraction predicting initiation and completion of bacterial cell division. *Integr. Biol. (Camb).* 5, 778–795.

8. Surovtsev, I. V., Morgan, J. J. and Lindahl, P. A. (2008) Kinetic modeling of the assembly, dynamic steady state, and contraction of the FtsZ ring in prokaryotic cytokinesis. *PLoS Comput. Biol.* 4, e1000102.

9. Turner, D. J., Portman, I., Dafforn, T. R., Rodger, A., Roper, D. I., Smith, C. J. et al. (2012) The mechanics of FtsZ fibers. *Biophys. J.* 102, 731–738.

10. Haney, S. A., Glasfeld, E., Hale, C., Keeney, D., He, Z. and De Boer, P. (2001) Genetic analysis of the *Escherichia coli* FtsZ-ZipA interaction in the yeast two-hybrid system. Characterization of FtsZ residues essential for the interactions with ZipA and with FtsA. *J. Biol. Chem.* 276, 11980–11987.

11. Romberg, L. and Mitchison, T. J. (2004) Rate-limiting guanosine 5'-triphosphate hydrolysis during nucleotide turnover by FtsZ, a prokaryotic tubulin homologue involved in bacterial cell division. *Biochemistry* 43, 282–288.

12. Stricker, J., Maddox, P., Salmon, E. D. and Erickson, H. P. (2002) Rapid assembly dynamics of the *Escherichia coli* FtsZ-ring demonstrated by fluorescence recovery after photobleaching. *Proc. Natl. Acad. Sci. U. S. A.* 99, 3171–3175.

13. Anderson, D. E., Gueiros-Filho, F. J. and Erickson, H. P. (2004) Assembly dynamics of FtsZ rings in *Bacillus subtilis* and *Escherichia coli* and effects of FtsZ-regulating proteins. *J. Bacteriol.* 186, 5775–5781.

14. Sun, Q. and Margolin, W. (1998) FtsZ dynamics during the division cycle of live *Escherichia coli* cells. *J. Bacteriol.* 180, 2050–2056.

15. Den Blaauwen, T., Buddelmeijer, N., Aarsman, M. E. G., Hameete, C. M. and Nanninga, N. (1999) Timing of FtsZ assembly in *Escherichia coli*. *J. Bacteriol.* 181, 5167–5175.

16. Rai, D., Singh, J. K., Roy, N. and Panda, D. (2008) Curcumin inhibits FtsZ assembly: an attractive mechanism for its antibacterial activity. *Biochem. J.* 410, 147–155.

17. Marrington, R., Small, E., Rodger, A., Dafforn, T. R. and Addinall, S. G. (2004) FtsZ fiber bundling is triggered by a conformational change in bound GTP. *J. Biol. Chem.* 279, 48821–48829.

18. Small, E., Marrington, R., Rodger, A., Scott, D. J., Sloan, K., Roper, D. et al. (2007) FtsZ Polymer-bundling by the *Escherichia coli* ZapA orthologue, YgfE, involves a conformational change in bound GTP. *J. Mol. Biol.* 369, 210–221.

19. Pacheco-Gómez, R., Cheng, X., Hicks, M., Smith, C., Roper, D., Addinall, S. et al. (2013) Tetramerisation of ZapA is required for FtsZ bundling. *Biochem. J.* 449, 795–802.

20. Läppchen, T. (2007) Synthesis of GTP analogues and evaluation of their effect on the antibiotic target FtsZ and its eukaryotic homologue tubulin. University of Amsterdam.

21. Marcelo, F., Huecas, S., Ruiz-Ávila, L. B., Cañada, F. J., Perona, A., Poveda, A. et al. (2013) Interactions of bacterial cell division protein FtsZ with C8-substituted guanine nucleotide inhibitors. A combined NMR, biochemical and molecular modeling perspective. *J. Am. Chem. Soc.* 135, 16418–16428.

22. Duggirala, S., Nankar, R. P., Rajendran, S. and Doble, M. (2014) Phytochemicals as inhibitors of bacterial cell division protein FtsZ: Coumarins are promising candidates. *Appl. Biochem. Biotechnol.* 174, 283–296.

23. Rueda, S., Vicente, M. and Mingorance, J. (2003) Concentration and assembly of the division ring proteins FtsZ, FtsA, and ZipA during the *Escherichia coli* cell cycle. *J. Bacteriol.* 185, 3344–3351.

24. Hale, C. A. and De Boer, P. A. J. (1999) Recruitment of ZipA to the septal ring of *Escherichia coli* is dependent on FtsZ and independent of FtsA. *J. Bacteriol.* 181, 167–176.

25. Fry, D. C. (2006) Protein-protein interactions as targets for small molecule drug discovery. *Biopolymers* 84, 535–552.

26. Tsao, D., Sutherland, A. G., Jennings, L., Rush, T. I., Alvarez, J., Ding, W. et al. (2006) Discovery of novel inhibitors of the ZipA/FtsZ complex by NMR fragment screening coupled with structure-based design. *Bioorganic Med. Chem.* 14, 7953–7961.

27. Rush, T. S., Grant, J. A., Mosyak, L. and Nicholls, A. (2005) A shape-based 3-D scaffold hopping method and its application to a bacterial protein-protein interaction. *J. Med. Chem.* 48, 1489–1495.

28. Hu, Z., Mukherjee, A., Pichoff, S. and Lutkenhaus, J. (1999) The MinC component of the division site selection system in *Escherichia coli* interacts with FtsZ to prevent polymerization. *Proc. Natl. Acad. Sci. U. S. A.* 96, 14819–14824.

29. Ward, J. E. and Lutkenhaus, J. (1985) Overproduction of FtsZ induces minicell formation in E. coli. *Cell* 42, 941–949.

30. RayChaudhuri, D. and Park, J. T. (1992) *Escherichia coli* cell-division gene *ftsZ* encodes a novel GTP-binding protein. *Nature* 359, 251–254.

31. RayChaudhuri, D. and Park, J. T. (1994) A point mutation converts *Escherichia coli* FtsZ septation GTPase to an ATPase. *J. Biol. Chem.* 269, 22941–22944.

32. Bagnara, A. and Finch, L. (1973) Relationships between intracellular contents of nucleotides and 5-phosphoribosyl 1-pyrophosphate in Escherichia coli. *Eur. J. Biochem.* 36, 422–427.

33. Gaal, T., Bartlett, M. S., Ross, W., Turnbough, C. L. and Gourse, R. L. (1997) Transcription regulation by initiating NTP concentration: rRNA synthesis in bacteria. *Science* 278, 2092–2097.

34. Bennett, B. D., Kimball, E. H., Gao, M., Osterhout, R., Van Dien, S. J. and Rabinowitz, J. D. (2009) Absolute metabolite concentrations and implied enzyme active site occupancy in *Escherichia coli*. *Nat. Chem. Biol.* 5, 593–599.

35. Phoenix, P. and Drapeau, G. (1988) Cell division control in *Escherichia coli* K-12: Some properties of the *ftsZ84* mutations and suppression of this mutation by the product of a newly identified gene. *J. Bacteriol.* 170, 4338–4342.

36. RayChaudhuri, D. (1999) ZipA is a MAP-Tau homolog and is essential for structural integrity of the cytokinetic FtsZ ring during bacterial cell division. *EMBO J.* 18, 2372–2383.

37. Chung, H. S., Yao, Z., Goehring, N. W., Kishony, R., Beckwith, J. and Kahne, D. (2009) Rapid beta-lactam-induced lysis requires successful assembly of the cell division machinery. *Proc. Natl. Acad. Sci. U. S. A.* 106, 21872–21877.

38. Kohanski, M. A., Dwyer, D. J. and Collins, J. J. (2010) How antibiotics kill bacteria: from targets to networks. *Nat. Rev. Microbiol.* 8, 423–435.

39. Möller, J., Luehmann, T., Hall, H. and Vogel, V. (2012) The race to the pole: How high-aspect ratio shape and heterogeneous environments limit phagocytosis of filamentous *Escherichia coli* bacteria by macrophages. *Nano Lett.* 12, 2901–2905.

40. Justice, S. S., Hunstad, D. A., Seed, P. C. and Hultgren, S. J. (2006) Filamentation by *Escherichia coli* subverts innate defenses during urinary tract infection. *Proc. Natl. Acad. Sci. U. S. A.* 103, 19884–19889.

41. Gengenbacher, M. and Kaufmann, S. H. E. (2012) *Mycobacterium tuberculosis*: Success through dormancy. *FEMS Microbiol. Rev.* 36, 514–532.

42. MacKenzie, F. and Gould, I. (1993) The post-antibiotic effect. *J. Antimicrob. Chemother.* 32, 519–537.

43. Lu, C. and Erickson, H. (1999) The straight and curved conformation of FtsZ protofilaments-evidence for rapid exchange of GTP into the curved protofilament. *Cell Struct. Funct.* 24, 285–290.

44. Lu, C., Reedy, M. and Erickson, H. P. (2000) Straight and curved conformations of FtsZ are regulated by GTP hydrolysis. *J. Bacteriol.* 182, 164–170.

45. Li, Y., Hsin, J., Zhao, L., Cheng, Y., Shang, W., Huang, K. C. et al. (2013) FtsZ protofilaments use a hinge-opening mechanism for constrictive force generation. *Science* 341, 392–395.

46. Feucht, A., Lucet, I., Yudkin, M. D. and Errington, J. (2001) Cytological and biochemical characterization of the FtsA cell division protein of *Bacillus subtilis*. *Mol. Microbiol.* 40, 115–125.

47. De Boer, P. A. (2010) Advances in understanding *E. coli* cell fission. *Curr. Opin. Microbiol.* 13, 730–737.

48. Haydon, D. J., Stokes, N. R., Ure, R., Galbraith, G., Bennett, J. M., Brown, D. R. et al. (2008) An inhibitor of FtsZ with potent and selective anti-staphylococcal activity. *Science* 321, 1673–1675.

49. Andreu, J. M., Schaffner-Barbero, C., Huecas, S., Alonso, D., Lopez-Rodriguez, M. L., Ruiz-Avila, L. B. et al. (2010) The antibacterial cell division inhibitor PC190723 is an FtsZ polymer-stabilizing agent that induces filament assembly and condensation. *J. Biol. Chem.* 285, 14239–14246.

50. Elsen, N. L., Lu, J., Parthasarathy, G., Reid, J. C., Sharma, S., Soisson, S. M. et al. (2012) Mechanism of action of the cell-division inhibitor PC190723: Modulation of FtsZ assembly cooperativity. *J. Am. Chem. Soc.* 134, 12342–12345.

51. Tan, C. M., Therien, A. G., Lu, J., Lee, S. H., Caron, A., Gill, C. J. et al. (2012) Restoring methicillin-resistant *Staphylococcus aureus* susceptibility to β-lactam antibiotics. *Sci. Transl. Med.* 4, 126ra35.

52. Mukherjee, A., Dai, K. and Lutkenhaus, J. (1993) *Escherichia coli* cell division protein FtsZ is a guanine nucleotide binding protein. *Proc Natl Acad Sci U S A* 90, 1053–1057.

53. Chen, Y., Bjornson, K., Redick, S. and Erickson, H. (2005) A rapid fluorescence assay for FtsZ assembly indicates cooperative assembly with a dimer nucleus. *Biophys. J.* 88, 505–514.

54. Culbertson, C. T., Jacobson, S. C. and Michael Ramsey, J. (2002) Diffusion coefficient measurements in microfluidic devices. *Talanta* 56, 365–373.

Table 1: Model predictions for different cell characteristics at kinetic equilibrium. Unless stated otherwise, all input parameter values are as shown in Table 2. The wild-type input parameter values were used to set the initiation threshold value α to 20,000. $\bar{i}$: the average length of membrane-bound FtsZ polymers, %: the percentage of FtsZ that is membrane-bound, N_Z : the number of membrane-bound FtsZ polymers, χ: the contraction parameter, α: the initiation threshold, CT: the completion threshold.

Parameter	$\bar{i}$	%	N_Z	χ	α	CT	Division Outcome
Wild type	14	28	504	91,836	20,000	78,086	Complete
GTP hydrolysis: WT k_{dis} = 0.075 s^{-1}							
0.06 (80%)	15	30	485	112,470	20,000	78,086	Complete
0.053 (70%)	16	31	475	125,010	20,000	78,086	Complete
0.045 (60%)	18	33	461	142,634	20,000	78,086	Complete
0.038 (50%)	19	34	448	161,989	20,000	78,086	Complete
0.09 (120%)	12	26	519	76,877	20,000	78,086	Initiation
0.105 (140%)	11	24	531	65,671	20,000	78,086	Initiation
0.12 (160%)	10	22	542	56,756	20,000	78,086	Initiation
0.135 (180%)	9	21	551	49,717	20,000	78,086	Initiation
0.15 (200%)	9	20	559	43,987	20,000	78,086	Initiation
GTP binding: WT k_{ex1} = 0.01 $\mu M^{-1}s^{-1}$							
0.008 (80%)	13	27	505	90,773	20,000	78,086	Complete
0.006 (60%)	13	27	507	88,642	20,000	78,086	Complete
0.005 (50%)	13	27	509	86,634	20,000	78,086	Complete
0.004 (40%)	13	26	513	83,199	20,000	78,086	Complete
0.003 (30%)	12	26	520	76,753	20,000	78,086	Initiation
0.002 (20%)	11	24	534	63,432	20,000	78,086	Initiation
0.001 (10%)	8	18	572	34,802	20,000	78,086	Initiation
FtsZ polymerisation: WT k_{dim1} = k_{el1} = k_{an} = 4 $\mu M^{-1}s^{-1}$							
3 (75%)	11	24	528	67,721	20,000	78,086	Initiation
2 (50%)	9	20	559	43,097	20,000	78,086	Initiation
1 (25%)	6	14	603	18,867	20,000	78,086	No
Anchor deletion:							
ZipA: B = 222, P_a=0.014	15	12	504	46,978	61,429	239,836	No initiation
FtsA: B = 450, P_a=0.029	14	21	365	76,045	29,665	115,821	Initiation only

Table 1 continued:

Parameter	$\bar{i}$	%	N_Z	χ	α	CT	Division Outcome
FtsZ overexpression - wild-type:							
[FtsZ] = 24 μM (200%)	27	42	386	277,974	20,000	78,086	Complete
[FtsZ] = 36 μM (300%)	36	48	328	425,000	20,000	78,086	Complete
ZipA overexpression - wild-type:							
B = 1122, P_a=0.072 (200%)	12	35	741	103,349	11,944	46,633	Complete
B = 1572, P_a=0.101 (300%)	10	39	968	96,267	8,515	33,245	Complete
The *ftsZ84* mutation: $k_{ex1} = 3 \times 10^{-4}$ μM^{-1}s^{-1}							
ATP:GTP ratio = 2:1, [NTP] = 270 μM, [NDP] = 20 μM							
k_{dis_eff} = 0.075 s^{-1}	7	16	584	27,328	20,000	78,086	Initiation only
k_{dis_eff} = 0.05 s^{-1}	11	24	532	65,672	20,000	78,086	Initiation only
k_{dis_eff} = 0.042 s^{-1}	13	27	509	88,161	20,000	78,086	Complete
ATP:GTP ratio = 3:1, [NTP] = 360 μM, [NDP] = 20 μM							
k_{dis_eff} = 0.075 s^{-1}	8	19	566	38,547	20,000	78,086	Initiation only
k_{dis_eff} = 0.047 s^{-1}	14	28	505	92,914	20,000	78,086	Complete
k_{dis_eff} = 0.038 s^{-1}	16	32	477	128,136	20,000	78,086	Complete
ATP:GTP ratio = 4:1, [NTP] = 450 μM, [NDP] = 20 μM							
k_{dis_eff} = 0.075 s^{-1}	9	21	553	47,945	20,000	78,086	Initiation only
k_{dis_eff} = 0.045 s^{-1}	15	30	486	114,890	20,000	78,086	Complete
k_{dis_eff} = 0.035 s^{-1}	19	35	455	160,818	20,000	78,086	Complete
ftsZ84 recovery: $k_{ex1} = 3 \times 10^{-4}$ μM^{-1}s^{-1}, [NTP] = 270 μM, [NDP] = 20 μM, k_{dis_eff} = 0.075 s^{-1}							
ftsZ84 overexpression:							
[FtsZ84] = 24 μM (200%)	24	41	415	247,715	20,000	78,086	Complete
[FtsZ84] = 36 μM (300%)	80	70	218	1,390,710	20,000	78,086	Complete
ZipA overexpression *ftsZ84*:							
B = 1122, P_a=0.072 (200%)	7	24	897	39,085	11,944	46,633	Initiation only
B = 1572, P_a=0.101 (300%)	6	27	1215	37,631	8,515	33,245	Complete

Table 2: Wild-type parameter values

Parameter	Wild-type value	Units	Reference
$[FtsZ]_{Total}$	12	μM	Surovtsev *et al.*, 2008 [8]
[GTP]	90	μM	Surovtsev *et al.*, 2008 [8]
[GDP]	10	μM	Surovtsev *et al.*, 2008 [8]
B	672	–	Rueda *et al.*, 2003 [23]
P_a	0.043	–	Rueda *et al.*, 2003; Surovtsev *et al.*, 2008 [8,23]
κ	0.2	μM	Haney *et al.*, 2001 [10]
i_{max}	150	–	Surovtsev *et al.*, 2008 [8]
k_{ex1}	0.01	$\mu M^{-1}s^{-1}$	Mukherjee *et al.*, 1993; Chen *et al.*, 2005; Surovtsev *et al.*, 2008 [8,52,53]
k_{ex2}	0.005	$\mu M^{-1}s^{-1}$	Mukherjee *et al.*, 1993; Chen *et al.*, 2005; Surovtsev *et al.*, 2008 [8,52,53]
k_{dim1}	4	$\mu M^{-1}s^{-1}$	Chen *et al.*, 2005; Surovtsev *et al.*, 2008 [8,53]
k_{dim2}	40	s^{-1}	Chen *et al.*, 2005; Surovtsev *et al.*, 2008 [8,53]
k_{el1}	4	$\mu M^{-1}s^{-1}$	Chen *et al.*, 2005; Surovtsev *et al.*, 2008 [8,53]
k_{el2}	0.4	s^{-1}	Chen *et al.*, 2005; Surovtsev *et al.*, 2008 [8,53]
k_{an}	4	$\mu M^{-1}s^{-1}$	Chen *et al.*, 2005; Surovtsev *et al.*, 2008 [8,53]
k_{dis}	0.075	s^{-1}	Romberg and Mitchison, 2004 [11]
k_{dif}	78	$\mu M^{-3}s^{-1}$	Culbertson *et al.*, 2002 [54]
k_{bind1}	0.142	$\mu M^{-1}s^{-1}$	Haney *et al.*, 2001; Stricker *et al.*, 2002 [10,12]
k_{bind2}	0.0284	s^{-1}	Haney *et al.*, 2001; Stricker *et al.*, 2002 [10,12]

FIGURES

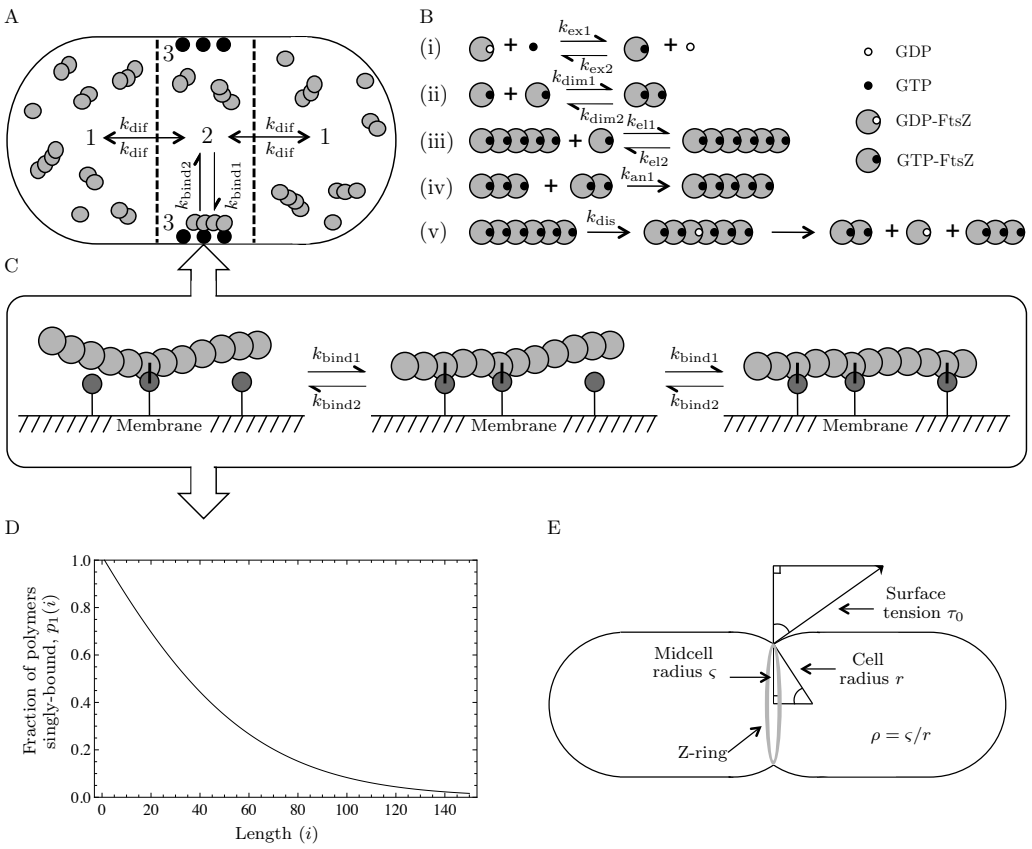

Figure 1:
Schematic diagram of the CAM-FF model. (A) The cell is conceptually divided into three compartments: (1) the cell caps; (2) the midcell; and (3) the midcell membrane. FtsZ moves between the cell caps and the midcell regions by diffusion. Exchange between the midcell region and the midcell membrane occurs on the interaction of FtsZ with membrane anchor sites and subsequent polymerisation. (B) Using the notation of Surovtsev *et al.*, (2008), the chemical reactions in our model are: (i) nucleotide exchange; (ii) dimerization; (iii) elongation; (iv) annealing; and (v) polymer breakdown following GTP hydrolysis (i-iii are reversible, iv-v are assumed to be irreversible). (C) Depending on the anchor density, an FtsZ polymer may bind to one or more anchor sites. (D) The fraction of membrane-bound polymers expected to be attached by a single FtsZ-anchor interaction, as a function of polymer length for anchor density P_a = 0.043 and equilibrium constant κ = 0.2 μM. (E) Z-ring contraction pulls the membrane inwards against the outward force from the surface-tension generated at the inner membrane.

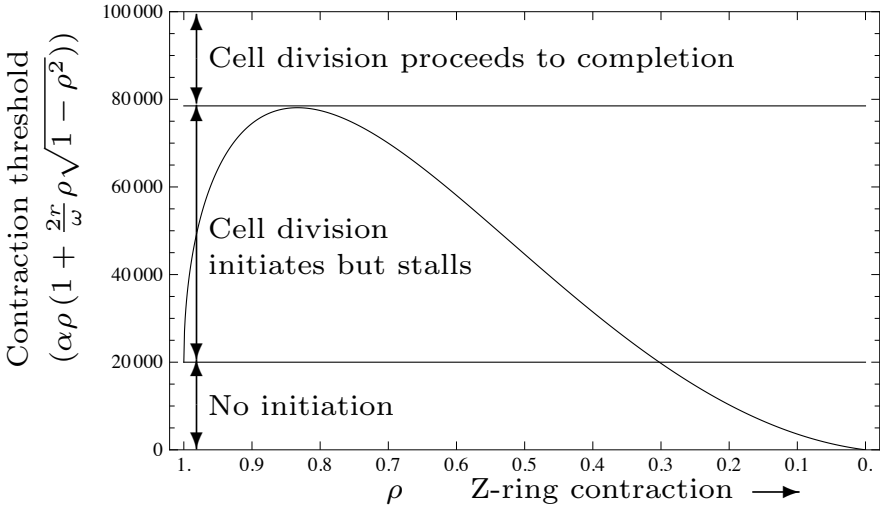

Figure 2:

The contraction threshold. The contraction threshold is shown as a function of ρ, the dimensionless ratio of the radius of the Z-ring to the original radius, *i.e.* contraction proceeds from ρ = 1 to ρ = 0. Parameter values are as follows: α = 20,000, r = 0.4 μm, ω = 0.1 μm.

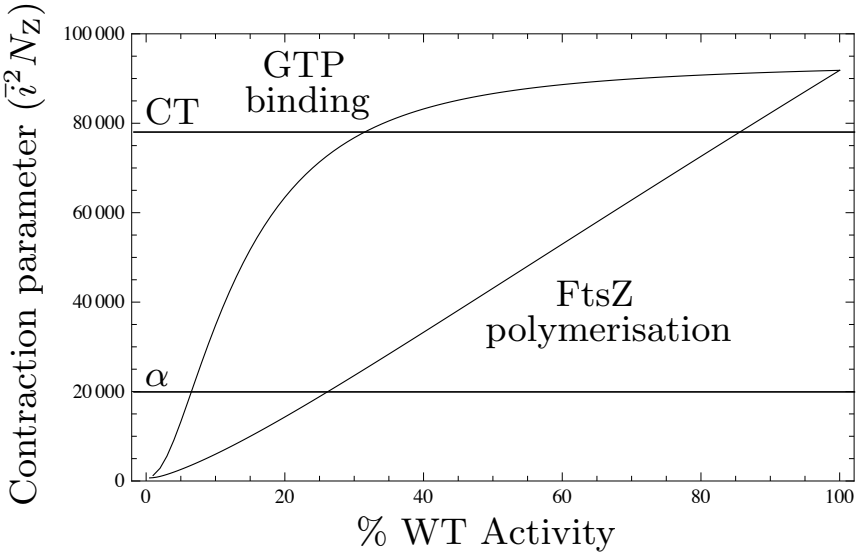

Figure 3:

Drug targeting: GTP binding vs FtsZ polymerization. Decreasing the rate of FtsZ polymerisation is a more efficient approach to prevention of cell division than inhibition of GTP binding. The initiation (α) and completion (CT) thresholds are shown. All other parameter values are as shown in Table 2.

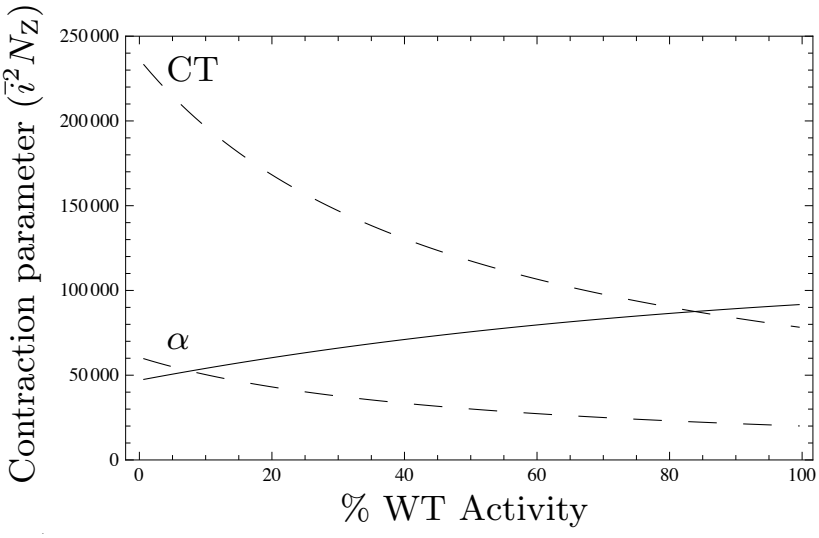

Figure 4:

Drug targeting: ZipA. Decreasing the number of ZipA binding sites available (solid line) is an effective approach to prevention of cell division. The initiation (α) and completion (CT) thresholds are shown (dashed lines). All other parameter values are as shown in Table 2.

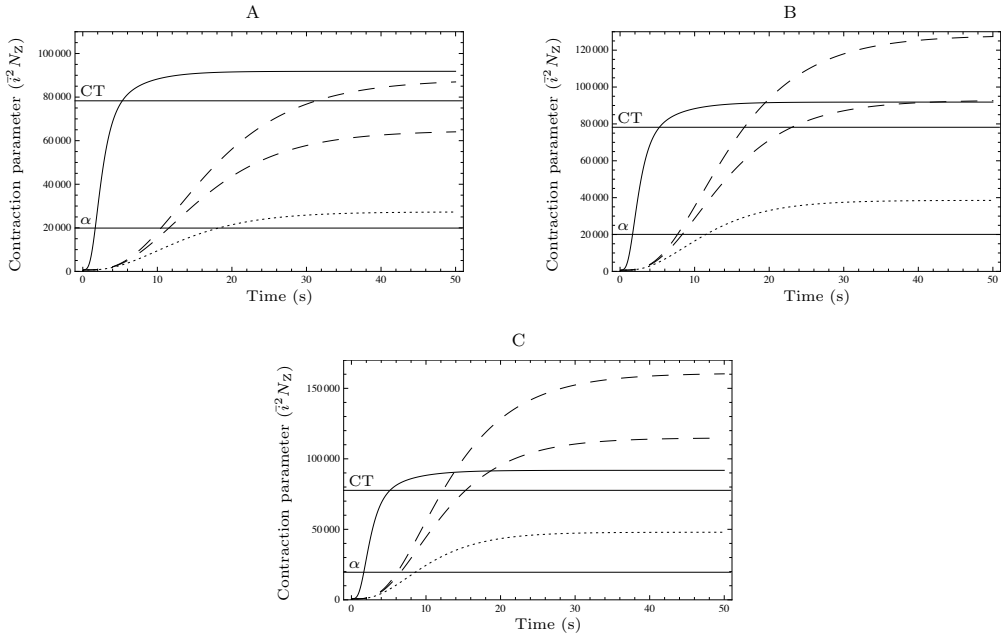

Figure 5:

ATP binding and hydrolysis by the ftsZ84 temperature-sensitive mutant. Solid line: Wild-type solution. All other plots $k_{ex1} = 3 \times 10^{-4}$ μM^{-1}s^{-1}. Dotted line: 42ºC, $k_{dis\_eff} = 0.075$ s^{-1}. Dashed lines correspond to reduced temperatures. Short dash: A 2-fold decrease in the rate of ATP hydrolysis. Long dash: A 3-fold decrease in the rate of ATP hydrolysis. (A) ATP:GTP ratio 2:1, [NTP] = 270 μM, [NDP] = 20 μM. (B) ATP:GTP to 3:1, [NTP] = 360 μM, [NDP] = 20 μM. (C) ATP:GTP to 4:1, [NTP] = 450 μM, [NDP] = 20 μM. All other parameters as shown in Table 2.

TOC GRAPHIC

For Table of Contents Only

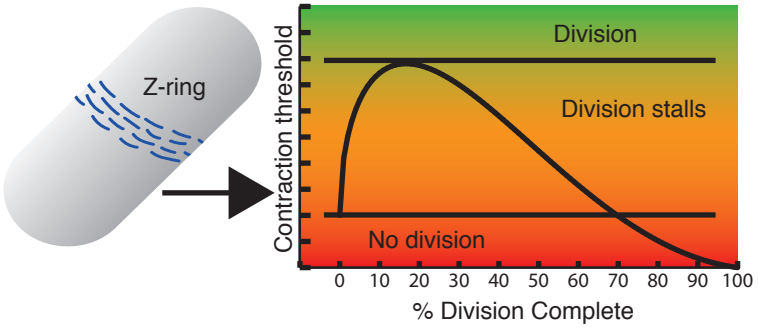

A significant ATPase activity of the mutant cell division protein FtsZ G105S/FtsZ84 from *Escherichia coli*.

Authors

Claire E Broughton[1], David I Roper[2], Alison Rodger[3,4]

Affiliations

1 Molecular Organisation and Assembly in Cells Doctoral Training Centre, Senate House, University of Warwick, Coventry, CV4 7AL, United Kingdom

2 School of Life Sciences, University of Warwick, Coventry, CV4 7AL, United Kingdom

3 Department of Chemistry, University of Warwick, Coventry, CV4 7AL, United Kingdom

4 Warwick Analytical Science Centre, University of Warwick, Coventry, CV4 7AL, United Kingdom

Abstract

We report the cloning and expression of an N-terminally polyhistidine-tagged FtsZ protein and the production of the wild-type and a G105S mutant to high purity. Analysis of the protein secondary structure using circular dichroism data and the secondary structure neural network (SSNN) software suggested that the G105S mutation did not induce any major structural reorganisation of the protein. Perhaps surprisingly, the FtsZ G105S mutant performs a significant ATPase activity that was not observed for the wild-type protein. The wild-type protein was active in polymerisation by GTP and formed long linear fibres that were visualised with electron microscopy and detected using linear dichroism. In contrast, the mutant protein formed aggregates or non-linear assemblies in the presence of either GTP or ATP. The formation of FtsZ aggregates in the presence of ATP *in vitro* may be relevant to the growth and temperature-sensitivity of the *ftsZ84* mutant cell *in vivo*.

Introduction

Understanding bacterial cell division is key to our ability to design and develop the antimicrobial drugs of the future. Our current arsenal of antimicrobials is becoming ineffective at an alarming rate due to bacterial resistance mechanisms. The FtsZ protein has been considered an antimicrobial drug target since the discovery in 1991 that it is the principle component of the midcell contractile ring in prokaryotes (1). This "Z-ring" pulls opposite sides of the cell membrane together in cytokinesis – the final step in the division of a parent cell into two daughter cells. There are over 20 proteins now known to localise to the midcell and to function during cell division – a set of proteins collectively termed the "divisome" (2). The complex assembles from just inside the plasma membrane when FtsZ self-assembles into polymers with structural organisation from the Zap proteins (3–5) and attachment to the membrane *via* interactions with ZipA and FtsA (6). This protein scaffold then recruits the enzymes that will hydrolyse and synthesise peptidoglycan on the opposite side of the plasma membrane. Further protein-protein interactions connect the scaffold to the outer membrane in Gram-negative bacteria such as *Escherichia coli*. This ensures that the entire cell wall is remodelled in a concerted manner. For recent reviews see (7–9). A simplified diagram of the divisome complex is shown in Figure 1.

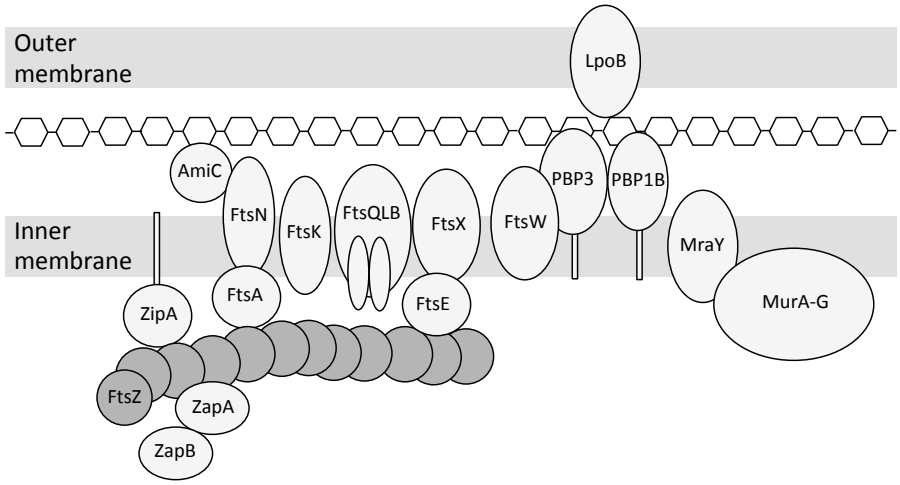

Figure 1: Simplified schematic of the divisome complex of proteins in *Escherichia coli*. Adapted from den Blaauwen *et al*., 2014 (10).

The *ftsZ* gene was originally identified as important to cell division with the isolation of mutant cells that were able to replicate and segregate DNA but were inactive in cell division (11,12). The *ftsZ* gene has since been found in almost all prokaryotic species (notable exceptions are the pathogens belonging to the phylum *Chlamydiae* (13)). The 40 kDa FtsZ protein is the prokaryotic structural homolog of eukaryotic tubulin, that is, the proteins have essentially the same three-dimensional fold, despite amino acid sequence similarity of only 10–18% (14,15). Like tubulin, FtsZ forms head-to-tail polymers on the addition of excess GTP *in vitro* and the proteins share almost identical phosphate-binding motifs – GGGTGTG in FtsZ compared to G/AGGTGSG in α-, β- and γ-tubulins (16). Numerous studies of the *in vitro* properties of FtsZ have now been documented. On polymerisation, a GTPase active site is formed when a catalytic aspartate residue (D212 in *E. coli*) of the T7 loop of the C-terminal domain of one subunit inserts into the N-terminal GTP-binding pocket of the adjacent subunit (17–19). The subsequent hydrolysis of GTP to GDP leads to polymer dissociation *in vitro* (20). It is thought that FtsZ polymers form the basic components of the Z-ring *in vivo* but the precise structure remains unclear (21).

We previously reported a mathematical model of Z-ring formation and contraction *in vivo* utilising the biophysical parameters of FtsZ polymerisation kinetics measured *in vitro* (22). We were intrigued by the reported ATPase activity of the FtsZ84 (FtsZ G105S) protein (23) and we employed the model to analyse the effect of an ATPase activity on cell division outcome in *ftsZ84* cells (24). The *ftsZ84* mutant was originally isolated by screening of cells that were able to replicate and segregate DNA, but were inactive in cell division under certain conditions (11,12). At 30 °C 80–95% of *E. coli* cells harbouring the *ftsZ84* mutation contain Z-rings that appear normal compared to wild-type cells. If the cells are transferred to fresh medium at 42 °C, loss of the Z-ring structure is rapid, even after just 1 and 2 minutes, only 2% and 1% of cells respectively contain Z-rings. Those cells undergoing constriction become blocked. If the cells are returned to 30 °C within 30 minutes, Z-rings do reform but only at sites at which Z-ring constriction had not begun before the original shift to 42 °C (25). At the non-permissive temperature of 42 °C, the FtsZ G105S protein is diffused throughout the cell (26) but the division defect can be compensated for by over-

expression of FtsZ G105S (27,28). The biochemical explanation for this temperature-sensitivity is still lacking.

Since the equivalent glycine residue is located close to the phosphates of the nucleotide, rather than the nitrogenous base, in the crystal structure of those FtsZ structures that have been determined to date, the measured ATPase activity has since been considered an artifact due to the presence of a contaminating protein. For example, using protein sequence alignment, the residue of interest in *E. coli* (G105) corresponds to G132 in the *Methanococcus jannaschii* FtsZ protein. Since the crystal structure of the *E. coli* protein is as yet unavailable, the key residue is highlighted in Figure 2 for the *M. jannaschii* FtsZ dimer (PDB 1W5B) (29). It is unclear how this mutation could result in a change to the nucleotide interaction behaviour of the binding site. Perhaps, the proximity of the G105 residue to the "arginine finger" residue (R169 in *M. jannaschii*, R142 in *E. coli*), a catalytic intermediate stabilising residue may be important (30).

We employed our mathematical model and found that the reported 2-fold increase in the ATPase activity of the FtsZ G105S protein at 43 °C compared to 30 °C could explain the temperature-sensitivity of the mutant cells (22,24). The availability of ATP as an additional substrate for polymerisation would lead to a largely increased pool of activating nucleotides for the mutant, compared to the wild-type which is activated by GTP only. At the permissive temperature, the rate of ATP hydrolysis is slow enough that Z-ring formation and contraction can proceed normally, despite the reduced affinity for nucleotide binding. However, the increase in ATPase activity at the non-permissive temperature causes rapid depolymerisation of the Z-ring (22,24). The question remained as to whether the reported ATPase activity was an artifact of a contaminating ATPase in the original study (23).

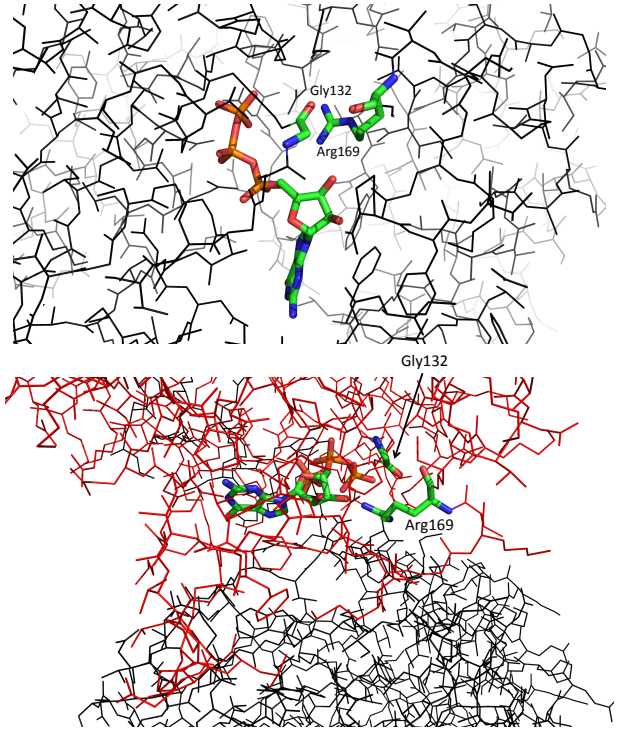

Figure 2: The GTPase active site of the FtsZ dimer from *Methanococcus jannaschii* (PDB 1W5B) (29). Glycine 132 in the *M. jannaschii* protein corresponds to glycine 105 in *Escherichia coli* FtsZ. The proximity of the mutated residue to the intermediate-stabilising residue arginine 169 in *M. jannaschii* (arginine 142 in *E. coli*) may be important. Two alternative views of the active site are shown. In (B) the N-terminal domain of an FtsZ monomer is shown in red, the C-terminal domain of the second monomer is shown in black.

We report here the cloning, mutagenesis, expression and purification of a wild-type N-terminal polyhistidine-tagged FtsZ and the corresponding FtsZ G105S mutant protein. We have undertaken a thorough biophysical characterisation of the two proteins to determine whether the mutation causes major structural changes and we measured a significant ATPase activity of the FtsZ G105S mutant protein. While the precise structural changes that can explain the biochemical mechanism are unclear, the FtsZ G105S mutant is an ATPase and further study is warranted to fully characterise the process.

Materials and Methods

All aqueous solutions were made with 18.2 MΩ.cm water obtained from a Millipore direct-Q water purifier. DNA primers were purchased from Integrated DNA Technologies. 2-(N-morpholino)ethanesulfonic acid (MES) buffer was purchased from MP Biomedicals. All other chemicals were purchased from Sigma unless otherwise stated.

FtsZ cloning

The *ftsZ* gene (locus b0095) was amplified from purifed *E. coli* K-12 W3110 genome (31) using FtsZ_forward (5' TTT GCG CAT ATG TTT GAA CCA ATG GAA CTT ACC AAT GAC 3') and FtsZ_reverse (5' CGC GGA TCC TTA ATC AGC TTG CTT ACG CAG GAA TGC TGG 3') primers and the Phusion® High-Fidelity DNA Polymerase enzyme (NEB). Briefly, the PCR reaction contained 1× Phusion® High-Fidelity DNA Polymerase GC buffer, 500 nM each primer, 200 μM each dNTP, 2 ng/μL genomic DNA template, 3% (v/v) DMSO and 1 unit Phusion® High-Fidelity DNA Polymerase enzyme in a final volume of 50 μL. The PCR mix was incubated at 98 °C for 30 seconds, followed by 30 cycles of: 10 seconds DNA denaturation at 98 °C, 30 seconds primer annealing at 62 °C, and 1 minute primer extension at 72 °C. After cycling, a final 10-minute extension at 72 °C was used. The PCR product was digested with restriction endonucleases NdeI and BamHI (NEB) and cloned into the vector pET15b (Novagen) that had been digested with the same two enzymes. Induction of expression from the cloned construct results in an FtsZ protein that has an additional 20 amino acid residues at the N-terminus. The additional sequence includes a polyhistidine purification tag. Success of the cloning was confirmed using separate DNA sequencing reactions (GATC Biotech) from both the T7 promoter (sequencing primer: 5' TAA TAC GAC TCA CTA TAG GGG 3') and the T7 terminator regions of the plasmid (sequencing primer: 5' GCT AGT TAT TGC TCA GCG G 3').

Site-directed mutagenesis

The G105S mutation was introduced into the pET15b-*ftsZ* plasmid using mismatched PCR. Forward (5' TGC TGC GGG TAT GAG TGG TGG TAC CGG 3') and reverse (5' CCG GTA CCA CCA CTC ATA CCC GCA GCA 3') primers were extended with *PfuUltra* High-Fidelity DNA Polymerase (Agilent) with the wild-type pET15b-*ftsZ* plasmid as the PCR template. Briefly, the PCR reaction contained 1× *PfuUltra* HF reaction buffer, 200 nM each primer, 200 μM each dNTP, 2 ng/μL pET15b-*ftsZ* template DNA, 3% (v/v) DMSO, 2.5 units *PfuUltra* High-Fidelity DNA Polymerase in a final volume of 50 μL. The PCR mix was incubated at 98 °C for 30 seconds, followed by 12 cycles of: 30 seconds DNA denaturation at 95 °C, 30 seconds primer annealing at 55 °C, and 8 minutes primer extension at 68 °C. After cycling, a final 10-minute extension at 68 °C was used. 10 units DpnI enzyme (NEB) was added and the PCR solution was incubated at 37 °C for 2 hours to cleave the wild-type pET15b-*ftsZ* template DNA. 8 μL digested PCR solution was used to transform 50 μL *E. coli* TOP10 cells (Invitrogen). The presence of the mutation was confirmed using DNA sequencing, as for the *ftsZ* cloning.

FtsZ expression and purification

10 mL LB containing 100 μg/mL ampicillin was inoculated with a fresh colony of transformed *E. coli* BL21(DE3) pLysS cells (Invitrogen) and grown overnight at 37 °C with shaking at 180 rpm. The overnight culture was used to inoculate 1 L LB (also containing ampicillin at 100 μg/mL) supplemented with 0.2% (w/v) glucose and the culture was incubated at 37 °C with shaking at 180 rpm until the optical density at 600 nm (1 cm pathlength) reached 0.6, compared to an LB blank. Protein expression was induced with the addition of 1 M isopropyl β-D-1-thiogalactopyranoside to a final concentration of 0.5 mM. The culture was then further incubated for 4 hours at 37 °C with shaking at 180 rpm. The cells were harvested by centrifugation at 12,000×g for 15 minutes at 4 °C. The cell pellet was stored at –20 °C.

The FtsZ purification protocol followed a combination of the methods used in the original purification studies of the FtsZ protein. That is, precipitation of FtsZ with ammonium sulfate followed by anion exchange and gel filtration chromatographies (16,17). We essentially followed the method of Mukherjee and Lutkenhaus (20) with the addition of an immobilised metal affinity chromatography (IMAC) step, since the FtsZ fusion protein used in this study also contains a polyhistidine tag. The cell pellet was thawed, resuspended in 20 mL FtsZ Buffer A (50 mM Tris-HCl, 50 mM KCl, 1 mM EDTA, 10% (v/v) glycerol, pH 7.9) and held on ice. Cells were lysed by sonication. The lysed cells were then centrifuged at 50,000×g for 45 minutes at 4 °C and the supernatant was collected. To precipitate FtsZ, 1.7 g ammonium sulfate was added per 10 mL supernatant to give a 30% saturated solution. The solution was stirred for 20 minutes at 4 °C and then centrifuged at 20,000×g for 10 minutes at 4 °C. The protein pellet was resuspended in 10 mL FtsZ Buffer A and dialysed against 3 × 1 L FtsZ Buffer A.

A 20 mL HiPrep 16/10 DEAE FF column (GE Healthcare) was used for anion exchange chromatography. The column was extensively washed with 100 mL 1 M NaCl, then with 100 mL 1 M NaOH and then with 100 mL 70% ethanol. The column was further cleared with 50 mL deionised water (dH_2O). Finally, the column was equilibrated with 100 mL FtsZ Buffer A and the protein was loaded. The column was washed with 100 mL FtsZ Buffer A then the protein was eluted over a gradient of increasing KCl concentration from 100% FtsZ Buffer A to 100% FtsZ Buffer B (50 mM Tris-HCl, 500 mM KCl, 1 mM EDTA, 10% (v/v) glycerol, pH 7.9) over 180 mL with a flow rate of 2 mL/min. FtsZ eluted from the column at a KCl concentration of 200–250 mM. 1.5 mL fractions were collected and fractions containing FtsZ were pooled. The protein was dialysed against 3 × 1 L IMAC Buffer A (25 mM HEPES, 0.5 M NaCl, 50 mM imidazole, pH 8) and was concentrated using a VivaSpin 20 10,000 MWCO PES membrane sample concentrator with centrifugation at 3,200×g at 4 °C.

A 5 mL HisTrap column (GE Healthcare) was used for immobilised metal affinity chromatography. The column was washed with 50 mL dH_2O, followed by 20 mL 50 mM EDTA. The EDTA was cleared with a further wash using 50 mL dH_2O. The resin was re-charged with 10 mg/mL $NiCl_2$ solution and

washed with 50 mL dH_2O. Finally, the primed column was equilibrated with 50 mL IMAC Buffer A and the protein was loaded. The column was washed with 40 mL IMAC Buffer A then the protein was eluted over a gradient of increasing imidazole concentration from 100% IMAC Buffer A to 100% IMAC Buffer B (25 mM HEPES, 0.5 M NaCl, 500 mM imidazole, pH 8) over 50 mL with a flow rate of 2 mL/min. 1.5 mL fractions were collected and fractions containing FtsZ were pooled. The protein was dialysed against 3 × 1 L FtsZ Gel Filtration Buffer (50 mM Tris-HCl, 0.15 M NaCl, pH 8) and was concentrated using a VivaSpin 20 10,000 MWCO PES membrane sample concentrator with centrifugation at 3,200 g at 4 °C.

The FtsZ was further purified using a HiPrep 26/60 Sephacryl S-300 HR (GE Healthcare) gel filtration column. The column was equilibrated with at least 2 column volumes of FtsZ Gel Filtration Buffer using a flow rate of 2 mL/min. After injection of the FtsZ solution, the flow rate was reduced to 1 mL/min and 3 mL fractions were collected. Fractions containing FtsZ were pooled and dialysed against 3 × 1 L FtsZ Buffer A. The purified protein was concentrated to ~20 mg/mL using a VivaSpin 20 10,000 MWCO PES membrane sample concentrator with centrifugation at 3,200×g at 4 °C. Samples were aliquoted and stored at –80 °C. Protein purity was assessed by sodium dodecyl sulphate polyacrylamide gel electrophoresis (SDS-PAGE), using 12% acrylamide resolving gels.

FtsZ concentration determination

Determination of the concentration of FtsZ can be problematic due to the absence of tryptophan for use of absorbance at 280 nm. For the Bradford assay, 2 µL protein sample was added to a pre-mixed solution containing 200 µL BioRad reagent and 800 µL dH_2O (32). After 5 minutes, the absorbance at 595 nm was measured relative to a blank containing buffer, dH_2O and BioRad reagent only. A standard curve was generated using bovine serum albumin standard solutions.

Linear dichroism

Linear dichroism (LD) measurements were performed at 20 °C using a Jasco J-815 spectropolarimeter adapted for LD spectroscopy. Samples were aligned in the light path using a custom-made, temperature-controlled Couette cell (Crystal Precision Optics, Rugby) (33,34). A cylindrical sample capillary, sealed at one end using Araldite® Rapid, rotates around a fixed, inserted quartz rod to create a shear force across the sample by laminar flow. The annular gap between the rod and the inner capillary wall is 250 μm. Samples of 50–100 μL are accommodated.

Data were collected using full wavelength scanning and single wavelength measurements using the Jasco software. For wavelength scans, a scanning speed of 100 nm/min was used. Baselines of data collected without sample alignment by flow were subtracted from the spectra. For the polymerisation assays, FtsZ was diluted into polymerisation buffer (50 mM MES, 50 mM KCl, 10 mM $MgCl_2$, pH 6.5) and polymerisation was initiated with the addition of GTP to a final concentration of 0.2 mM (35). The time taken to load and assemble the capillary LD unit and to start the analysis (dead time) was 15–30 seconds.

Circular dichroism

The CD spectrum of FtsZ was collected using a Jasco J-815 spectropolarimeter in a 0.1 cm path length cuvette. Data were collected for 180–280 nm using a wavelength scanning speed of 100 nm/min. Spectra presented are the average of 10 accumulations. For melting temperature analysis, data were collected every 5 °C from 20 to 100 °C using a temperature ramp of 1 °C/min. Samples were held at the required temperature for 2 minutes before data collection.

CD spectra were analysed using the secondary structure neural network (SSNN) software (36,37) allowing variation of the protein concentration scaling factor. SSNN1 was trained on the augmented CDDATA.(48+5) dataset which contains the CDDATA.48 reference dataset available from CDPro (38,39) and 5

additional spectra to represent 100% α-helical and 100% "random coil" proteins. The optimum protein concentration scaling factor was selected as that giving the lowest normalised root mean square deviation (NRMSD) between the measured spectrum and the modelled spectrum (36,37). CD spectra were also analysed using the analysis tools available through DichroWeb (40,41).

For comparison, the *E. coli* FtsZ amino acid sequence was input to SWISS-MODEL (42–44) to generate a three-dimensional structure, that was then analysed with DSSP (45,46) to give a secondary structure prediction. The secondary structure was also predicted from the amino acid sequence using JPred4 (47,48) and PSIPRED (49).

Dynamic light scattering

The distributions of protein particle sizes were measured using the Malvern Zetasizer Nano-S dynamic light scattering (DLS) instrument. To determine the viscosity of the polymerisation buffer, which is required as a variable for the calculation of particle size, latex spheres of known diameter were suspended in polymerisation buffer and their size measured on the instrument. The buffer viscosity was then calculated using,

$$\eta_{\text{buffer}} = \eta_{\text{water}} \frac{r_{\text{measured}}}{r_{\text{actual}}},$$

where r is the particle radius and η is the dynamic viscosity (50). The refractive index of the buffer was also measured using an Abbe 60/DR refractometer (Bellingham and Stanley, UK) and the value input to the Zetasizer software. Samples of FtsZ were diluted to 0.1 mg/mL in polymerisation buffer, to a final volume of 100 µL. Samples were equilibrated at 20 °C for 10 minutes. Seven repeats were performed per sample with each repeat consisting of 15 measurements of 30 seconds. For comparison, the three-dimensional structure of *E. coli* FtsZ from SWISS-MODEL was used as input to the HYDROPRO algorithm to calculate the predicted hydrodynamic radius (51,52).

Calculation of the Debye length

The Debye length λ_D gives a measure of the extent of the charge layer around a molecule in solution and it can be calculated from the solution constituents. The Debye length is given by,

$$\lambda_D = \sqrt{\frac{\varepsilon_0 \varepsilon_r k_B T}{2 N_A e^2 I}} \quad ,$$

where ε_0 is the permittivity of free space, ε_r is the dielectric constant of the solution, N_A is Avogadro's number, e is the elementary charge and I is the ionic strength of the solution (53) which is given by the sum for all ions in the solution,

$$I = \frac{1}{2} \sum_{i=1}^{n} c_i z_i^2 \quad ,$$

where c_i is the molar concentration of ion i, and z_i is the charge of ion i. For the polymerisation buffer, the ionic strength is 80 mM. According to theoretical analysis and experimental measurement, the dielectric constant of the polymerisation buffer will be less than that for water at 80, but it is likely to remain above 70 since the salt concentrations are relatively low (54). Using 75 as a reasonable estimate of the dielectric constant, the Debye length is 1.58 nm.

Electron microscopy

FtsZ samples were visualized using negative stain transmission electron microscopy. Carbon films on 400 copper mesh grids (Agar Scientific) were glow-discharged for 20 seconds at 10 mA. 10 μL protein sample was applied to the grid. After 1 minute, excess liquid was blotted and the grid was stained with 10 μL 1% uranyl acetate solution. After 1 minute excess liquid was blotted. Grids were imaged using the JOEL 2011 electron microscope and software.

NTP hydrolysis assays

The EnzChek® Phosphate Assay Kit (Life Technologies) was used to follow the release of inorganic phosphate from GTP catalysed by FtsZ (55). Reactions contained 0.4 mM 2-amino-6-mercapto-7-methylpurine riboside (MESG), 0.2 mM GTP or ATP, 0.1 units purine nucleoside phosphorylase enzyme (PNP) and various concentrations of FtsZ in 1× FtsZ polymerisation buffer. Since the NTP stock solutions were found to contain some free phosphate, all components of the reaction were added except the FtsZ and the absorbance at 360 nm was measured for at least 5 minutes to ensure that any free phosphate was turned over and the rate measured on addition of the protein was due to the NTPase activity of FtsZ. The absorbance at 360 nm was then set to zero prior to addition of the protein (or buffer control) and the absorbance was further measured for 1 hour at 20 °C. For calibration, standards of inorganic phosphate were incubated in the reaction mixture (without addition of FtsZ) for 30 minutes at room temperature. The absorbance at 360 nm was measured compared to a blank containing no inorganic phosphate.

Results

A combination of several purification techniques yields FtsZ protein of high purity

The *ftsZ* gene was successfully cloned into the pET15b vector. The absence of mutations in the wild-type sequence, possibly incurred during the cloning procedure, was confirmed by DNA sequencing. The introduction of a single nucleic acid substitution that results in the replacement of glycine at position 105 of the FtsZ amino acid sequence with a serine residue was also successful and was confirmed by DNA sequencing. The wild-type FtsZ and FtsZ G105S *E. coli* proteins were overexpressed and purified using a combination of ammonium sulfate precipitation and three different chromatography techniques, anion exchange, immobilised metal affinity chromatography and gel filtration.

Various FtsZ purification protocols have been documented in the literature. In the original reports of FtsZ purification in 1992, RayChaudhuri and Park used ammonium sulfate precipitation followed by anion exchange (16), and de Boer *et al*. used ammonium sulfate precipitation followed by anion exchange and gel filtration (17). Since then, various combinations of methods have been reported. Romberg *et al*. used ammonium sulfate precipitation only. They initially applied a 20% saturation and the protein precipitate was discarded. This was then followed by an increase to 26% saturation to precipitate the FtsZ (56). Similarly, Chen *et al*. used an initial 20% ammonium sulfate saturation step and the precipitate was discarded. An increase to 30% saturation then precipitated the FtsZ. In addition, the resuspended FtsZ precipitate was then further purified by anion exchange chromatography (57). Bramhill *et al*. used the original method of RayChaudhuri and Park of precipitation by 35% saturation of ammonium sulfate, followed by anion exchange chromatography (16,58,59). Mukherjee and Lutkenhaus included a final gel filtration step (20). In 2000, Rivas *et al*. used an alternative approach to the purification of FtsZ. The polymerisation and bundling of FtsZ was initiated with the addition of GTP and calcium ions to the protein solution. FtsZ bundles were then purified by sedimentation (60).

We used a combination of precipitation by 30% ammonium sulfate saturation and three different chromatography techniques to optimise the yield and purity of the FtsZ purification, a protocol that essentially followed that of Mukerjee and Lutkenhaus (20), with the addition of an immobilised metal affinity chromatography step to utilise the addition of the polyhistidine tag. Although the same protocol without IMAC will give a high level of purity for the native untagged FtsZ protein (20), we chose to use an N-terminal polyhistidine-tagged FtsZ to achieve a very high purity level and therefore to reduce the possibility that the measured NTPase activities are affected by contaminating proteins. We had previously shown that an N-terminally tagged wild-type FtsZ protein polymerised as for the wild type, whereas a C-terminally tagged FtsZ was inactive (unpublished data).

The method of GTP/calcium precipitation (60) was not applied in this work. Since the introduction of the FtsZ G105S mutation has previously been shown to inhibit the polymerisation activity of the protein (17,23,61), it was

anticipated that this method would be unsuitable for the purification of the FtsZ G105S mutant protein. In order to directly compare the results for the wild-type FtsZ and the FtsZ G105S proteins, the two samples were handled in the same way. Figures 3A and 3B show the SDS-PAGE separation of the wild-type FtsZ and FtsZ G105S preparations respectively.

The lack of tryptophan in FtsZ and the contribution of signal from any bound nucleotide render determination of the protein concentration using UV absorbance problematic. Therefore, the Bradford assay was used (32), as in previous FtsZ studies, with comparison to a bovine serum albumin standard curve (Figure 3C). In the analysis of the secondary structure of the FtsZ proteins using the SSNN software and the circular dichroism data (see below), the protein concentration scaling factor was varied and according to SSNN, the BioRad assay under-predicted the FtsZ concentration by a factor of 20%. This is in agreement with the 20% under-prediction of the BioRad assay found by Rivas *et al*. (60). The yield of purified FtsZ protein from the method described here is 110–120 mg/L culture.

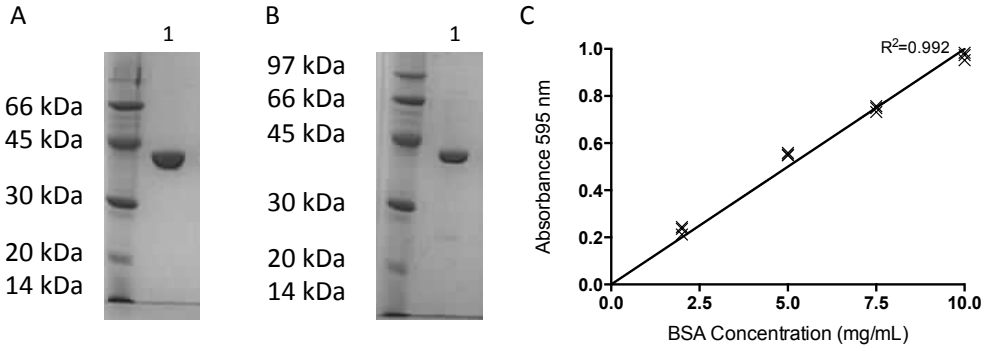

Figure 3: FtsZ purification and concentration determination. Purified proteins were separated using SDS-PAGE with 12% acrylamide resolving gels and stained with Coomassie Blue. Marker sizes are indicated. (A) Lane 1: Wild-type FtsZ. (B) Lane 1: FtsZ G105S. (C) Calibration curve for the Bradford assay (BioRad) using bovine serum albumin standards (Pathlength 1 cm).

FtsZ G105S has a significant ATPase activity that is absent in the wild-type protein

The release of inorganic phosphate was quantified using the EnzChek® Phosphate Assay Kit (Life Technologies) which utilises the assay originally developed by Webb (55). Inorganic phosphate (released by the NTPase activity of FtsZ) is consumed in the conversion of the substrate molecule MESG (2-amino-6-mercapto-7-methylpurine riboside) to ribose-1-phosphate and 2-amino-6-mercapto-7-methlpurine by the enzyme purine nucleoside phosphorylase (PNP). This results in a shift in the maximum absorbance from 330 nm to 360 nm. In the absence of added nucleotide, there was no increase in absorbance on addition of the FtsZ sample to the reaction mixture. This indicates that the protein sample does not contain free phosphates that would cause an over-estimation of the measured activity of FtsZ in the presence of nucleotide. In addition, once the reaction mixture had stabilised, in the absence of added protein, the signal did not significantly change over the time course of the experiment. The standard curve used for the conversion of the absorbance signal to a concentration of phosphate is shown in Figure 4A. As shown in Figure 4B, the wild-type FtsZ has a significant GTPase activity. Using the first 500 seconds to calculate the initial rate of reaction, the rate of phosphate (Pi) production is 0.70 ± 0.02 Pi/min/FtsZ. As expected, the wild-type FtsZ protein did not hydrolyse ATP.

As can be seen in Figure 4C, for the GTPase activity of the FtsZ G105S protein, there is a burst of phosphate release within the first 100–200 seconds of the experiment followed by an approximately linear production of phosphate over the remaining course of the experiment. For the linear regions, the rate of phosphate production is 12% of the rate seen for the wild-type at 0.087 ± 0.004 Pi/min/FtsZ. The initial burst of phosphate release, which is not seen in the ATP assay or for the wild type GTP assay, could suggest that the initial binding and then subsequent hydrolysis of GTP is functional. The much slower linear region for the FtsZ G105S protein compared to the wild-type, is consistent with the subsequent release of the GDP being slowed: after the initial activity, the rate slows since the subsequent binding of GTP requires the release of the GDP. As

shown in Figure 4D, significant ATPase activity (without the initial burst of its GTP behaviour) was measured for the FtsZ G105S protein that is absent in the wild-type protein. Using the first 500 seconds of the assays, the rate of production of phosphate from ATP by FtsZ G105S was 0.040 ± 0.003 Pi/min/FtsZ. This is 6% of the wild-type rate and half of the FtsZ G105S GTPase activity.

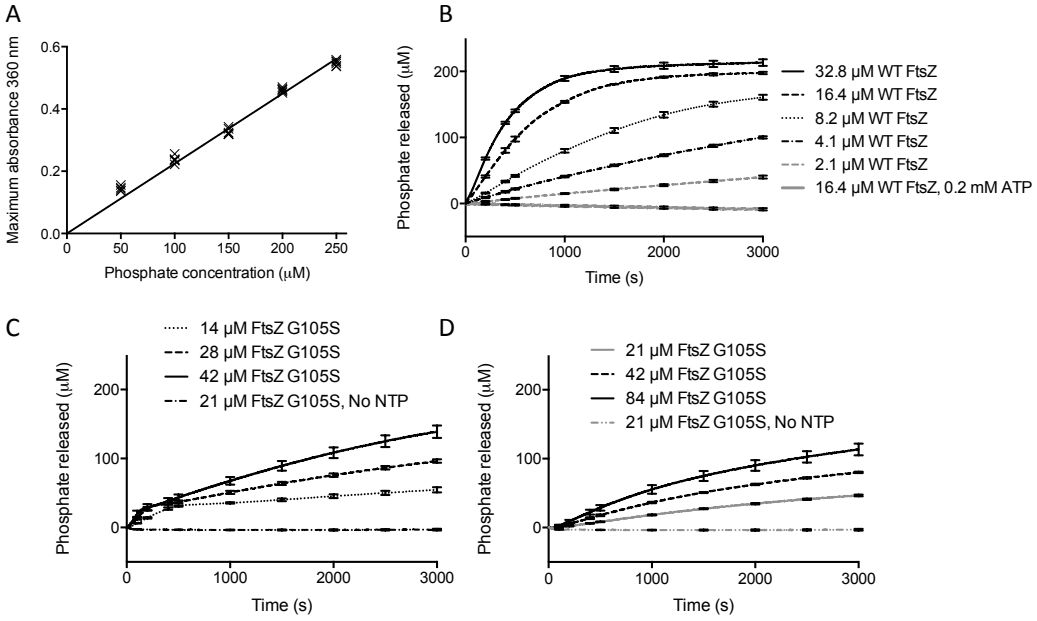

Figure 4: The NTPase activities of wild-type FtsZ and FtsZ G105S were measured using the EnzChek® phosphate assay protocol with measurement of the absorbance at 360 nm. (A) Standards of inorganic phosphate were used to calibrate the absorbance measurement. (B) Wild-type FtsZ GTPase activity. Note: The time course with no added nucleotide mapped onto the time course for 0.2 mM ATP as shown. (C) FtsZ G105S GTPase activity. (D) FtsZ G105S ATPase activity. For all assays, the NTP concentration was 0.2 mM.

FtsZ G105S forms aggregates on the addition of ATP

As can be seen in Figure 5A–C, wild-type FtsZ is polymerised into very long, straight fibres on addition of GTP. There is no difference between the micrographs for the presence and the absence of ATP, within the resolution of the experiment. As can be seen in Figure 5D, for FtsZ G105S, the protein solution appears to be the same or very similar to the wild-type protein. On the addition of GTP (Figure 5E), large aggregates of protein form of approximately 50–100 nm in diameter, rather than the fibres seen for wild-type FtsZ. On

addition of ATP (Figure 5F), aggregation into smaller particles is observed. Given the NTPase activity of the protein, both aggregates must create active sites following assembly.

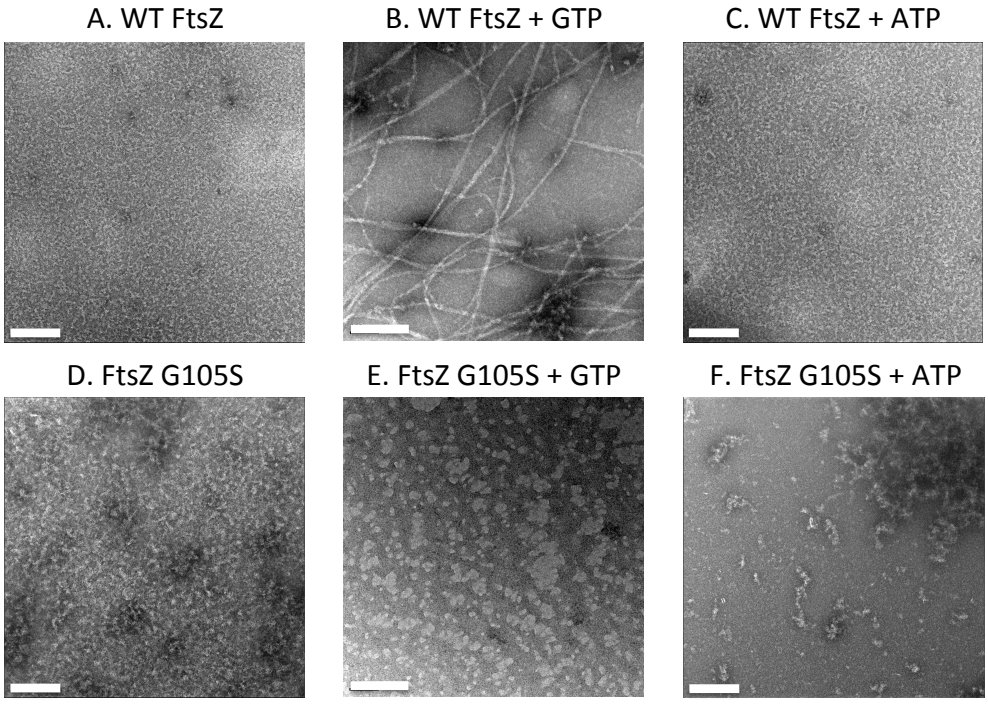

Figure 5: FtsZ polymerisation visualised by electron microscopy. 7.5 μM wild-type FtsZ or FtsZ G105S was incubated in polymerisation buffer at room temperature for 10 minutes prior to the addition of GTP or ATP to a final concentration of 0.2 mM. The scale bar indicates 400 nm (20,000× magnification) for A, C, D and F, and 200 nm (40,000× magnification) for B and E.

Biophysical characterisation of the wild-type FtsZ and FtsZ G105S proteins

Wild-type FtsZ is active in polymerisation but FtsZ G105S becomes aggregated in flow on the addition of GTP or ATP

Linear dichroism (LD) was used to confirm that the wild-type N-terminal polyhistidine-tagged FtsZ protein was active in polymerisation. LD is the difference in absorption of light polarised parallel to an orientation direction ($A_{\parallel}$) and light polarised perpendicular to the orientation direction ($A_{\perp}$). The magnitude of the LD signal is determined by the intensity of the absorbance, the orientation of the electronic transition with respect to the orientation axis, and the

degree of orientation of the sample. The reduced linear dichroism (LD^r) is pathlength- and concentration-independent and is given by:

$$LD^r = \frac{A_{\parallel} - A_{\perp}}{A} = \frac{3}{2} S(3\cos^2\alpha - 1) \ ,$$

where *A* is the absorbance of the sample under isotropic conditions, α is defined as the angle between the transition moment and the orientation axis, and *S* is a flow orientation parameter, which equals 1 for (the never achieved) perfect orientation and 0 for no orientation (62).

LD is an ideal technique to study the polymerisation of FtsZ. In the absence of nucleotide, FtsZ is roughly spherical and therefore does not align in flow (30). Once polymerised, the fibres align under flow and this organises the absorbing chromophores in the monomeric units. This results in a preferential absorption of one orientation of polarised light over the other (62,63).

As anticipated (35,64), prior to the addition of GTP, the wild-type FtsZ protein does not align in flow and the difference between the measured LD signal with flow and in the absence of flow was zero within experimental error. By way of contrast, as shown in Figure 6, when 7.5 μM wild-type FtsZ was polymerised by the addition of GTP (to a final concentration of 0.2 mM), the maximum signal is reached within the first minute. Depolymerisation of the protein occurred within 15 minutes with the signal returning to the baseline on depletion of the pool of available GTP by hydrolysis. Essentially no LD signal was measured between 300 nm and 350 nm for polymerised FtsZ. Since this is a non-absorbing region, this suggests that light scattering by FtsZ polymers is not an issue and the subtraction of a scattering contribution is not required. Wild-type FtsZ gave no LD signal on the addition of ATP (also at a final concentration of 0.2 mM). Therefore, wild-type FtsZ is not polymerised by ATP. For the FtsZ G105S protein, prior to the addition of nucleotide, the protein was stable but unaligned in flow. On addition of either GTP or ATP, the protein rapidly precipitated in the flow. This suggests that both nucleotides interact with FtsZ G105S protein causing it to aggregate.

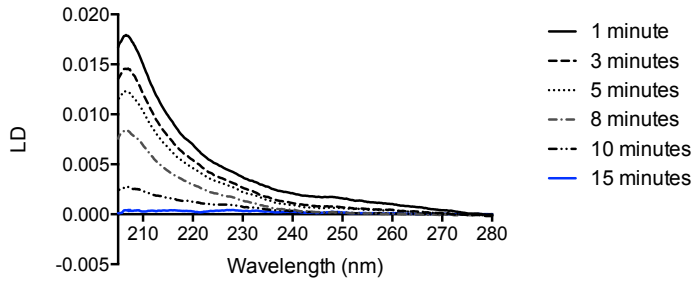

Figure 6: Far UV LD spectrum of wild-type FtsZ. 7.5 μM FtsZ after the addition of GTP to a final concentration of 0.2 mM.

The G105S mutation does not cause significant changes to the secondary structure of the FtsZ protein

Circular dichroism was used to confirm that the FtsZ proteins were correctly folded and to detect any major secondary structural changes between wild-type FtsZ and FtsZ G105S. As can be seen in Figure 7A, the wild-type FtsZ and FtsZ G105S spectra at 20 °C are essentially identical. Therefore, the presence of the G105S point mutation does not cause reorganisation of the protein secondary structure. The data were analysed using the secondary structure neural network (SSNN) software (36,37). SSNN creates a 40 × 40 self-organising map (SOM) of the circular dichroism spectra of 53 reference proteins and generates an intermediate, virtual spectrum at each of the remaining free nodes (SSNN1). Next, the known secondary structures from X-ray crystallography data are assigned to the corresponding nodes for the reference proteins and, using the same weighting as in SSNN1, secondary structures are generated at the virtual nodes (SSNN2). The CD spectrum of the "unknown" protein, in this case FtsZ, is then input and a modelled spectrum and secondary structure are predicted using the 5 best matching units (BMUs).

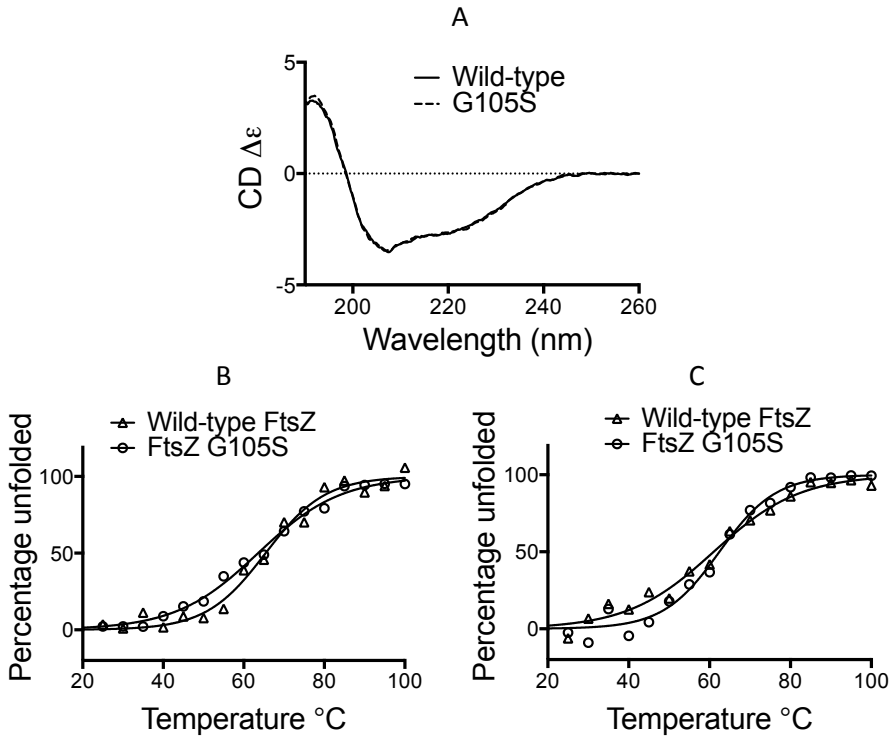

Figure 7: Analysis of the wild-type FtsZ and FtsZ G105S secondary structures using circular dichroism. (A) Far UV circular dichroism spectra corrected to be independent of protein concentration. (B) Analysis of the CD signal at 222 nm as a function of temperature. (C) Analysis of the CD signal at 195 nm as a function of temperature. In (B) and (C) data were fitted to a 4-parameter sigmoidal function using PRISM 6. Data are shown as percentage unfolded.

As can be seen in Table 1, the predictions for the wild-type FtsZ and FtsZ G105S secondary structures are almost identical. The modelled and measured spectra as well as the location of the best matching units in the SOM for wild-type FtsZ and FtsZ G105S are shown in Supplementary Information. The same 5 nodes were identified as the 5 BMUs for the wild-type FtsZ and FtsZ G105S spectra, although the order of winning matches was slightly different. If the nodes for the wild-type FtsZ fit are numbered 1–5, the order of the best matching nodes for the FtsZ G105S fit was 2, 1, 3, 5 and 4. The order affects the weighting applied in the calculation of the modelled spectrum and the secondary structure prediction. The NRMSD values for the modelled spectrum compared to the measured spectrum were 0.0303 and 0.0319 for the wild-type FtsZ and FtsZ G105S fits respectively. This is well below the "reasonable" quality cut off of 0.05 and close to the "good" range of < 0.03 (36,37).

Since the three-dimensional crystal structure of the FtsZ protein from *E. coli* is as yet unavailable, SWISS-MODEL was used to generate a three-dimensional model of the protein structure using the amino acid sequence (42–44). The best matching template was the FtsZ protein from *Pseudomonas aeruginosa* (PDB file: 1ofu.1.A) and the structural model was deemed acceptable based on the QMEAN4 and GMQE quality criteria (see Supplementary Information). The structure co-ordinates file includes residues 10–316 of the *E. coli* FtsZ protein. The co-ordinates were used to predict the secondary structure of the wild-type *E. coli* protein using DSSP (45,46). DSSP is also the secondary structure annotation programme used in the generation of the reference set for SSNN (36,37). The predicted secondary structure output from DSSP was further grouped as for the original CDDATA.48 reference dataset to give the six secondary structure categories predicted by SSNN. On the assumption that all residues outside of 10–316 (including the N-terminal polyhistidine tag sequence) were unordered, the secondary structure prediction is shown in Table 1. The structural NRMSD using the SSNN prediction and the SWISS-MODEL structure is 0.338 which is at the higher end of the range of NRMSD values from the original SSNN case study (36).

To account for the structure of the additional residues of FtsZ not included in the SWISS-MODEL structure, the co-ordinates from molecular dynamics (MD) simulations of wild-type *E. coli* FtsZ were used (unpublished data). Again, the atomic co-ordinates were input to DSSP to predict the secondary structure. For residues 10–316 the secondary structural assignments were very similar, particularly for the regions of α-helix and β-sheet. The variation between the two models is in the unordered or loop regions. For the additional sequence not included in the SWISS-MODEL structure, the protein is mostly unordered but there are additional distorted α-helical regions at residues 5–8 and 333–336. An additional α-helix is found at residues 369–377. As can be seen in Table 1, using the MD structure the proportion of α-helix increased slightly, and that of β-sheet regular and "other" decreased. The structural NRMSD was improved at 0.296.

A set of the secondary structure prediction programs available from DichroWeb (40,41) was also used to analyse the circular dichroism data for the

wild-type FtsZ. The predictions were similar to that of SSNN for SELCON3 (39,65) and CONTIN (66,67). However, CDsstr (68) predicted a slightly higher α-helical content, and a lower β-sheet content. The secondary structure predictions of JPred4 (47,48) and PSIPRED (49) from the wild-type FtsZ amino acid sequence were similar to that for the DSSP analysis of the SWISS-MODEL and the MD simulated structures. Both JPred4 and PSIPRED predicted α-helical content of 0.31. For β-strand content, JPred4 and PSIPRED predicted 0.17 and 0.13 respectively.

In general, the secondary structure analysis of the CD data under-predicted the α-helical content of FtsZ and over-predicted the proportion of β-sheet and turns compared to the structural models and the analysis of the FtsZ amino acid sequence. The structural models may represent the form of the protein when tightly packed such as in polymers or bundles, since they are derived from X-ray crystallography data. The CD data may reveal a different secondary structure of the protein monomer in solution. However, in previous work, in an analysis of the CD data for wild-type FtsZ monomers and wild-type FtsZ polymers, no significant difference was found in the secondary structures. A reduction in the CD signal for wavelengths 190–200 nm was reported but this was attributed to the scattering of light by FtsZ polymers (64).

For the temperature analysis, shown in Figures 7B and 7C, single-wavelength data were extracted from the full wavelength scans and were fitted to a 4-parameter sigmoidal curve using PRISM 6. The melting temperatures for loss of secondary structure using the CD signal at 222 nm were 61.0 ± 1.7 °C and 62.4 ± 1.2 °C for the wild-type FtsZ and the FtsZ G105S mutant respectively. For the signal at 195 nm, the melting temperatures were 65.4 ± 1.4 °C and 63.6 ± 1.0 °C for the wild-type FtsZ and the FtsZ G105S mutant respectively. According to the melt analysis there is no significant difference to the stability of the secondary structure with the introduction of the G105S mutation.

Table 1: Secondary structure predictions. Circular dichroism data were analysed with SSNN and the fitting programs available through DichroWeb (SEL3: SELCON3, CONT: CONTIN). SWISS-MODEL (SWIS-MOD) and MD simulated FtsZ structures were analysis using DSSP. The FtsZ primary sequence was analysed using JPred4 and PSIPRED (PSI).

Structure	WT FtsZ SSNN	FtsZ G105S SSNN	WT FtsZ CDsstr	WT FtsZ SEL3	WT FtsZ CONT	WT FtsZ SWIS-MOD	WT FtsZ MD	WT FtsZ JPred4	WT FtsZ PSI
α-helix regular	0.128	0.128	0.14	0.125	0.133	0.221	0.226	-	-
α-helix distorted	0.108	0.108	0.11	0.121	0.129	0.139	0.153	-	-
α-helix total	0.237	0.236	0.25	0.246	0.262	0.360	0.380	0.31	0.31
β-sheet regular	0.135	0.135	0.10	0.134	0.126	0.143	0.122	-	-
β-sheet distorted	0.098	0.099	0.07	0.090	0.085	0.050	0.052	-	-
β-sheet total	0.234	0.234	0.17	0.224	0.210	0.194	0.173	0.17	0.13
Turns	0.220	0.220	0.16	0.225	0.218	0.092	0.124	-	-
Other	0.309	0.309	0.42	0.300	0.309	0.355	0.323	0.52	0.57

Dynamic light scattering data hint at a relaxation of the FtsZ G105S protein structure

Dynamic light scattering was used to measure the hydrodynamic radius of wild-type FtsZ and FtsZ G105S to detect any major unfolding or aggregation of the protein on introduction of the point mutation. The refractive index of the polymerisation buffer was measured as 1.335. Using measurement of 100 nm latex spheres in water and in polymerisation buffer, the viscosity of the polymerisation buffer was measured as 1.1612 mPas. From the intensity data shown in Figure 8A, it can be seen that the wild-type FtsZ sample is of better quality compared to the FtsZ G105S sample as it contains a smaller proportion of large aggregates. For the FtsZ G105S protein sample, the size of the aggregates is smaller and there is a wider distribution of aggregate size compared to the FtsZ wild-type sample. However, since the intensity of scattered light is proportional to d^6 in the Rayleigh regime, where d is the scattering particle diameter, when the data are converted to particle volume or particle number, the presence of aggregates is negligible for both the wild-type FtsZ and FtsZ G105S protein

samples (69). This is also shown in the electron microscopy images of both samples (see Figures 5A and 5D) since little aggregation is observed in the absence of added nucleotide.

As can be seen in Figure 8B–D, there is a slight shift in the number distribution for FtsZ G105S compared to the wild-type protein. The wild-type FtsZ sample has a mean particle diameter of 7.1 nm, with a standard deviation of 2.0 nm. For FtsZ G105S the mean particle diameter is 8.8 nm, with a standard deviation of 2.3 nm. However, it should be noted that the determination of particle size becomes problematic when aggregates contribute to more than 50% of the scattering intensity, as may be the case for both samples, and the intensity from larger aggregates is certainly higher for the FtsZ G105S sample than for the wild-type protein. This causes an over-estimation of particle size so the increase in the scattering intensity from aggregates of FtsZ G105S may account for this shift rather than a change to the protein conformation on introduction of the mutation (69).

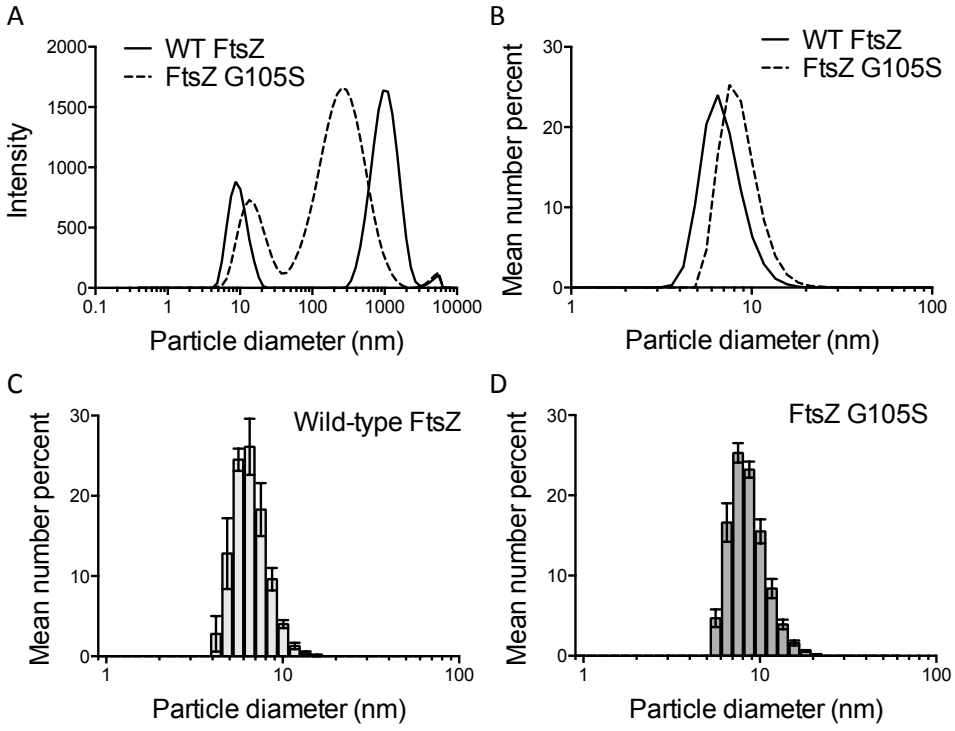

Figure 8: Dynamic light scattering data by particle size for the wild-type FtsZ and FtsZ G105S protein preparations. (A) Data by intensity. The averages of all measurements per sample were multiplied by the average count rate to allow direct comparison. (B–D) Data by number.

To predict the hydrodynamic diameter of the FtsZ protein, the atomic co-ordinates from the SWISS-MODEL structure of the wild-type FtsZ core and the MD-simulated wild-type FtsZ structures were submitted to the HYDROPRO program (51,52). The atomic co-ordinates are replaced by beads with a central position co-ordinate and a radius *a*. Each non-hydrogen atom may be replaced or a more coarse-grained approach can be chosen in which each amino acid residue is replaced by a single bead. The model may consider only the surface-exposed beads (shell model) or it may fill the entire protein volume (bead model). The model is then used to calculate the hydrodynamic properties of the protein (51,52). For the core FtsZ structure from SWISS-MODEL, HYDROPRO predicts a hydrodynamic radius of approximately 2.6 nm (model mode 1 – atomic-level, shell R_h = 2.590 nm, model mode 2 – residue-level, shell R_h = 2.572 nm, model mode 4 – residue-level, bead R_h = 2.598 nm). Therefore, the hydrodynamic diameter of the protein core is approximately equal to 5.3 nm. For the atomic co-ordinates from the MD-simulated structure, the prediction of the hydrodynamic radius from HYDROPRO is approximately 2.9 nm (model mode 1 – atomic-level, shell R_h = 2.974 nm, model mode 2 – residue-level, shell R_h = 2.879 nm, model mode 4 – residue-level, bead R_h = 2.884 nm). Therefore the hydrodynamic diameter is predicted to be around 5.8 nm.

By addition of the Debye length of 1.58 nm (see Materials and Methods) to the calculated hydrodynamic radius from HYDROPRO using the SWISS-MODEL structure, the hydrodynamic diameter of FtsZ is predicted to be 8.4 nm. For the MD-simulated structures, the hydrodynamic diameter of FtsZ is estimated as 9.0 nm.

Since the calculated values are just slightly higher than the mean sizes of the number distributions from the DLS experiments, it is reasonable then to suggest that the distributions of particle sizes shown in Figure 8 are those of a population of monomers. There may be some non-specific interactions that result in dimers, trimers *etc*. within the distribution since hydrodynamic radii are not additive. In accord with this, when the wild-type protein was diluted into buffer containing 50 mM Tris, which should shield some of the non-specific interactions, and 100 mM NaCl in the absence of divalent ions, there was

essentially no change to the size distribution. This suggests that the presence of non-specific interactions is minimal in the polymerisation buffer.

Discussion

In this work, the *ftsZ* gene was successfully cloned to produce an N-terminal polyhistidine-tagged FtsZ protein that was subsequently purified to a high level. Linear dichroism and electron microscopy were used to confirm that the wild-type FtsZ protein was active in polymerization; long protein fibres were formed on the addition of GTP to the buffer. The timescale of the depolymerisation, shown by loss of the LD signal, was similar to that observed in previous LD studies using the native, untagged *E. coli* FtsZ protein (35,64). For the enzyme activity assays, the time dependent release of phosphate was highly reproducible and the maximum concentration of 0.2 mM was reached, based on the total amount of GTP added to the reaction, within the timescale of the experiment for the higher concentrations of wild-type FtsZ. It is interesting to note that the release of phosphate from GTP continued on a longer timescale than the signal was maintained in the LD experiment. The FtsZ (7.5 μM) LD signal was lost after 15 minutes. Whereas, for a slightly higher concentration of FtsZ (8.2 μM), in the phosphate release assay after 15 minutes only around 40% of the total phosphate had been released and the assay was still in the linear phase. From the electron microscopy images (not shown), after 1 hour FtsZ polymers are still present in the solution, although they are shorter and considerably fewer in number. It may be that the kinetics of the polymerisation and depolymerisation are affected by the flow used in LD. However, in previous studies the LD signal was maintained on a similar timescale to the signal measured using right-angled light scattering which does not use flow to align the fibres (35,64).

Purification of the FtsZ G105S protein was achieved, using mutagenesis of the pET15b-*ftsZ* wild-type construct, and expression and purification of the mutant protein as for the wild-type. This work agrees with the original report (23) in that FtsZ G105S has impaired GTPase activity *in vitro*. We also did not detect a lag phase in the GTPase activity of wild-type FtsZ and we measured an ATPase activity that is not observed for the wild-type FtsZ protein. Our proteins

were purified through ammonium sulfate precipitation followed by three different chromatographic techniques, and according to the SDS-PAGE analysis, there is no evidence to suggest that the ATPase activity is due to contamination of the mutant protein sample compared to the wild-type sample, as the preparations were handled in the same way.

The inhibition data in the original report are interesting since azide and vanadate were shown to inhibit the ATPase activity of the G105S mutant protein but not the GTPase of wild-type FtsZ. In addition, AlF_4^- was shown to inhibit the wild-type GTPase but not the mutant ATPase. This suggested a different mechanism or active site. However, the effect of the inhibitors on the GTPase activity of the G105S mutant was not reported so a direct comparison cannot be made. In their study using radio-labelled nucleotides, both unlabelled GTP and unlabelled ATP inhibited the ATP hydrolysis activity of the FtsZ G105S protein suggesting that GTP and ATP do compete for the same site. The authors also reported that the mutant is more susceptible to tryptic digest, suggesting a more open conformation (23). The DLS data in this work hint at a slight increase in the size of the FtsZ protein on introduction of the G105S mutation but this was not conclusive.

There are a number of examples in the literature of GTP-binding proteins for which a mutation of the active site has produced a change in the nucleotide preference from GTP to XTP. This includes prokaryotic examples such as the SRP receptor homologue FtsY (70), the purine biosynthesis enzyme adenylosuccinate synthetase (71) and the polypeptide elongation factor EF-Tu (72) in *E. coli*, as well as eukaryotic examples such as human Rab5 (73) and yeast Ypt1p (74) which both mediate vesicle fusion events, and Ras p21 of the MAP kinase pathway (75). However, these examples differ from the FtsZ G105S mutation as the residues that were altered for the GTP to XTP switch directly bind to the guanine base of the GTP and the change in substrate preference can be explained by the change to the hydrogen bonding on replacement of the amino acid side chain of aspartate to asparagine.

In addition to the conversion of substrate preference from GTP to XTP, the substrate preference of the DEAD-box RNA helicase Hera (Heat resistant RNA-dependent ATPase) of *Thermus thermophilus* was altered by a single point

mutation that changed the preferred nucleotide from ATP to 8-oxo-ATP. However, in this case although 8-oxo-ATP was able to bind to the helicase, the native glutamate residue was required for communication between the Q-motif and the P-loop so the mutant was inactive (76). In another example, on mutation of an arginine residue to alanine or glutamate, the specificity for ATP is lost from *E. coli* ATP-dependent phosphofructo-1-kinase and the affinity increases for GTP and CTP. But again the arginine residue is in close proximity to the nucleotide within the binding site (77).

There are additional examples in the literature of a change in nucleotide preference for mutations of cyclic GMP or cyclic AMP dependent ion channels. For example, the mutation of an aspartate to an uncharged residue in a bovine rod cell cyclic nucleotide-gated (CNG) ion channel inverted the preference from cGMP to cAMP (78). In another study, 3 mutations were required to invert the preference of the CNG channel MlotiK1 from the plant root nodule bacterium *Mesorhizobium loti*. Interestingly, the reverse effect was observed to that in the bovine rod cell CNG channel, as the affinity for cAMP was reduced and that for cGMP was increased, when the native alanine residue was replaced by an aspartate residue. Again, the aspartate was shown to be directly hydrogen bonded to the base of the nucleotide in the crystal structure (79). Finally, rat guanylyl cyclase was converted to adenylyl cyclase by three mutations (80). Again, the specificity could be explained by the close proximity to the base of the nucleotide.

A significant example for direct comparison to the FtsZ case is the protein kinase casein kinase 2 (CK2) (81). The CK2α subunit is unusual as a protein kinase as it is able to use GTP as well as the usual ATP as the source of phosphate in the kinase reaction. It was noted that an absolutely conserved serine residue within CK2 is usually replaced with glycine in many other protein kinase enzymes. As for the serine residue in FtsZ G105S, it was not expected that this residue would affect nucleotide preference since the glycine-rich region in which the serine is found is next to the phosphates and not the base of the nucleotide. Unfortunately for the purposes of a direct comparison, the mutation reported for the *Xenopus laevis* CK2α protein (expressed in *E. coli*) is a double mutant of the conserved serine residue to glycine as well as a mutation of the preceding

tyrosine residue that is mutated to phenylalanine. Therefore, two hydroxyl groups are removed from the phosphate-binding region in this case. However, it is interesting to note that the apparent K_m for ATP binding increased significantly in the mutant but the effect on the K_m for GTP was reported to be insignificant. As for the G105S mutation in FtsZ, the presence of the hydroxylated residues in close proximity to the phosphates produces a dual-specificity NTPase that can utilise both ATP and GTP.

In contrast to the FtsZ case, for CK2α the absence of the hydroxylated residues resulted in a reduction in the enzyme activity as K_{cat} reduced for both ATP and GTP to 20% and 6% of the wild-type value respectively. For FtsZ G105S, the presence of the serine residue results in a loss of enzymatic activity for GTP hydrolysis. The authors of the CK2α work suggest that the serine residue could form a key hydrogen bond to one of the nucleotide phosphates or to another amino acid residue in the active site. Although the serine side chain is not adjacent to the nucleotide base, small conformational changes induced by the change in polarity may affect the specificity of nucleotide binding, although the precise mechanistic details remain unclear (81).

Conclusion

Importantly, we have shown that when FtsZ is purified to a high level, there is a significant ATPase activity of the mutant protein that is not measured in the wild-type protein. Our biophysical measurements suggested there was no change to the secondary structure of the protein, although there may be a relaxation of the structure shown by dynamic light scattering but this is not conclusive. Competition assays to measure the phosphate release with the addition of non-hydrolysable analogues of GTP and ATP will confirm whether the same active site is used by both nucleotides in the FtsZ G105S mutant. Further, repetition of the inhibition assays of the original work but with direct comparison of the GTPase and ATPase activities of the FtsZ G105S protein will also be useful. Introduction of another mutation to the protein to inhibit the hydrolysis activity such as D212A would also confirm that the ATPase activity is intrinsic to the FtsZ G105S protein, if both the GTPase and ATPase activities are

lost. Crosslinking of radio-labelled NTPs using UV-light followed by analysis using SDS-PAGE would also confirm that the ATPase is specific to the FtsZ protein and not the result of a contamination. The availability of a specific FtsZ inhibitor compound would also be useful. The authors of the original ATPase study used a polyclonal antibody raised to the purified protein, but this will also contain antibodies specific to any contaminating protein. Therefore, this cannot be used as evidence that the ATPase activity is not due to a contaminant. This is the reason we undertook several rounds of purification to prevent the presence of contaminants.

The next stage of this work is to explore the system further using molecular dynamics simulation. This will help elucidate the biochemical explanation of the change to the nucleotide specificity and would also allow us to determine if the FtsZ G105S structure is in a more open conformation compared to the wild-type protein, as suggested in the tryptic digest and the dynamic light scattering. X-ray crystallography data would be extremely useful, although currently the crystal structure of *E. coli* FtsZ remains elusive. Analysis of the effect of temperature on the GTPase and ATPase activities of the mutant protein will also be required for further investigation of the link between the ATPase activity of the FtsZ G105S mutant protein and the temperature-sensitivity of cell division.

Acknowledgments

Funding to CEB through the EPSRC-funded MOAC Doctoral Training Centre (Grant number EP/F500378/1) is gratefully acknowledged. Many thanks to Ian Hands-Portman from the School of Life Sciences Imaging Suite for training and assistance in use of the electron microscope.

References

1. Bi EF, Lutkenhaus J. FtsZ ring structure associated with division in *Escherichia coli*. Nature. 1991;354:161–4.

2. Den Blaauwen T, de Pedro MA, Nguyen-Distèche M, Ayala JA. Morphogenesis of rod-shaped sacculi. FEMS Microbiol Rev. 2008;32(2):321–44.

3. Galli E, Gerdes K. FtsZ-ZapA-ZapB interactome of *Escherichia coli*. J Bacteriol. 2012;194(2):292–302.

4. Durand-Heredia JM, Yu HH, De Carlo S, Lesser CF, Janakiraman A. Identification and characterization of ZapC, a stabilizer of the FtsZ ring in *Escherichia coli*. J Bacteriol. 2011;193(6):1405–13.

5. Galli E, Gerdes K. Spatial resolution of two bacterial cell division proteins: ZapA recruits ZapB to the inner face of the Z-ring. Mol Microbiol. 2010;76(6):1514–26.

6. Pichoff S, Lutkenhaus J. Unique and overlapping roles for ZipA and FtsA in septal ring assembly in *Escherichia coli*. EMBO J. 2002;21(4):685–93.

7. Typas A, Banzhaf M, Gross CA, Vollmer W. From the regulation of peptidoglycan synthesis to bacterial growth and morphology. Nat Rev Microbiol. 2011;10(2):123–36.

8. Den Blaauwen T. Prokaryotic cell division: Flexible and diverse. Curr Opin Microbiol. 2013;16(6):738–44.

9. Egan AJF, Vollmer W. The physiology of bacterial cell division. Ann N Y Acad Sci. 2013;1277:8–28.

10. Den Blaauwen T, Andreu JM, Monasterio O. Bacterial cell division proteins as antibiotic targets. Bioorg Chem. 2014;55:27–38.

11. Van De Putte P, Van Dillewijn J, Roersch A. The selection of mutants of *Escherichia coli* with impaired cell division at elevated temperature. Mutat Res. 1964;106(2):121–8.

12. Hirota Y, Jacob F, Ryter A, Buttin G, Nakai T. On the process of cellular division in *Escherichia coli*. I. Asymmetrical cell division and production of deoxyribonucleic acid-less bacteria. J Mol Biol. 1968;35(1):175–92.

13. Frandi A, Jacquier N, Théraulaz L, Greub G, Viollier PH. FtsZ-independent septal recruitment and function of cell wall remodelling enzymes in chlamydial pathogens. Nat Commun. 2014;5:4200.

14. Löwe J, Amos LA. Crystal structure of the bacterial cell-division protein FtsZ. Nature. 1998;391(6663):203–6.

15. Nogales E, Wolf SG, Downing KH. Structure of the alpha beta tubulin dimer by electron crystallography. Nature. 1998;391(6663):199–203.

16. RayChaudhuri D, Park JT. *Escherichia coli* cell-division gene *ftsZ* encodes a novel GTP-binding protein. Nature. 1992;359(6392):251–4.

17. De Boer P, Crossley R, Rothfield L. The essential bacterial cell-division protein FtsZ is a GTPase. Nature. 1992;359(6392):254–6.

18. Scheffers DJ, de Wit JG, den Blaauwen T, Driessen JM. GTP hydrolysis of cell division protein FtsZ: evidence that the active site is formed by the association of monomers. Biochemistry. 2002;41(2):521–9.

19. Scheffers DJ, de Wit JG, den Blaauwen T, Driessen JM. Substitution of a conserved aspartate allows cation-induced polymerization of FtsZ. FEBS Lett. 2001;494(1-2):34–7.

20. Mukherjee A, Lutkenhaus J. Dynamic assembly of FtsZ regulated by GTP hydrolysis. EMBO J. 1998;17(2):462–9.

21. González JM, Jiménez M, Vélez M, Mingorance J, Andreu JM, Vicente M, et al. Essential cell division protein FtsZ assembles into one monomer-thick ribbons under conditions resembling the crowded intracellular environment. J Biol Chem. 2003;278(39):37664–71.

22. Dow CE, Rodger A, Roper DI, van den Berg HA. A model of membrane contraction predicting initiation and completion of bacterial cell division. Integr Biol (Camb). 2013;5(5):778–95.

23. RayChaudhuri D, Park JT. A point mutation converts *Escherichia coli* FtsZ septation GTPase to an ATPase. J Biol Chem. 1994;269(37):22941–4.

24. Dow CE, van den Berg HA, Roper DI, Rodger A. Biological insights from a simulation model of the critical FtsZ accumulation required for prokaryotic cell division. Biochemistry. 2015;54(24):3803–13.

25. Addinall SG, Cao C, Lutkenhaus J. Temperature shift experiments with an *ftsZ84(Ts)* strain reveal rapid dynamics of FtsZ localisation and indicate that the Z ring is required throughout septation and cannot reoccupy division sites once constriction has initiated. J Bacteriol. 1997;179(13):4277–84.

26. Addinall SG, Erfei B, Lutkenhaus J. FtsZ ring formation in *fts* mutants. J Bacteriol. 1996;178(13):3877–84.

27. Phoenix P, Drapeau G. Cell division control in *Escherichia coli* K-12: Some properties of the *ftsZ84* mutations and suppression of this mutation by the product of a newly identified gene. J Bacteriol. 1988;170(9):4338–42.

28. Stricker J, Erickson HP. *In vivo* characterisation of *Escherichia coli ftsZ* mutants: Effects on Z-ring structure and function. J Bacteriol. 2003;185(16):4796–805.

29. Oliva MA, Cordell SC, Löwe J. Structural insights into FtsZ protofilament formation. Nat Struct Mol Biol. 2004;11(12):1243–50.

30. Oliva MA, Trambaiolo D, Löwe J. Structural insights into the conformational variability of FtsZ. J Mol Biol. 2007;373(5):1229–42.

31. Hayashi K, Morooka N, Yamamoto Y, Fujita K, Isono K, Choi S, et al. Highly accurate genome sequences of *Escherichia coli* K-12 strains MG1655 and W3110. Mol Syst Biol. 2006;2:2006.0007.

32. Bradford M. Rapid and sensitive method for quantification of microgram quantities of protein utilizing principle of protein-dye-binding. Anal Biochem. 1976;72:248–54.

33. Marrington R, Dafforn TR, Halsall DJ, Rodger A. Micro-volume couette flow sample orientation for absorbance and fluorescence linear dichroism. Biophys J. 2004;87(3):2002–12.

34. Marrington R, Dafforn TR, Halsall DJ, MacDonald JI, Hicks M, Rodger A. Validation of new microvolume Couette flow linear dichroism cells. Analyst. 2005;130(12):1608–16.

35. Pacheco-Gómez R, Roper DI, Dafforn TR, Rodger A. The pH dependence of polymerization and bundling by the essential bacterial cytoskeltal protein FtsZ. PLoS One. 2011;6(6):e19369.

36. Hall V, Nash A, Hines E, Rodger A. Elucidating protein secondary structure with circular dichroism and a neural network. J Comput Chem. 2013;34(32):2774–86.

37. Hall V, Sklepari M, Rodger A. Protein secondary structure prediction from circular dichroism spectra using a self-organizing map with concentration correction. Chirality. 2014;26(9):471–82.

38. Sreerama N, Woody RW. Estimation of protein secondary structure from circular dichroism spectra: comparison of CONTIN, SELCON, and CDSSTR methods with an expanded reference set. Anal Biochem. 2000;287(2):252–60.

39. Sreerama N, Venyaminov SY, Woody RW. Estimation of the number of alpha-helical and beta-strand segments in proteins using circular dichroism spectroscopy. Protein Sci. 1999;8(2):370–80.

40. Whitmore L, Wallace BA. DICHROWEB, an online server for protein secondary structure analyses from circular dichroism spectroscopic data. Nucleic Acids Res. 2004;32(Web Server Issue):W668–73.

41. Whitmore L, Wallace BA. Protein secondary structure analyses from circular dichroism spectroscopy: Methods and reference databases. Biopolymers. 2008;89(5):392–400.

42. Biasini M, Bienert S, Waterhouse A, Arnold K, Studer G, Schmidt T, et al. SWISS-MODEL: Modelling protein tertiary and quaternary structure using evolutionary information. Nucleic Acids Res. 2014;42:W252–8.

43. Arnold K, Bordoli L, Kopp J, Schwede T. The SWISS-MODEL workspace: A web-based environment for protein structure homology modelling. Bioinformatics. 2006;22(2):195–201.

44. Benkert P, Biasini M, Schwede T. Toward the estimation of the absolute quality of individual protein structure models. Bioinformatics. 2011;27(3):343–50.

45. Joosten RP, Te Beek TAH, Krieger E, Hekkelman ML, Hooft RWW, Schneider R, et al. A series of PDB related databases for everyday needs. Nucleic Acids Res. 2011;39:D411–9.

46. Kabsch W, Sander C. Dictionary of protein secondary structure: pattern recognition of hydrogen-bonded and geometrical features. Biopolymers. 1983;22(12):2577–637.

47. Drozdetskiy A, Cole C, Procter J, Barton G. JPred4: a protein secondary structure prediction server. Nucleic Acids Res. 2015;43(W1):W389–94.

48. Fox NK, Brenner SE, Chandonia JM. SCOPe: Structural classification of proteins-extended, integrating SCOP and ASTRAL data and classification of new structures. Nucleic Acids Res. 2014;42(D1):D304–9.

49. Buchan DWA, Minneci F, Nugent TCO, Bryson K, Jones DT. Scalable web services for the PSIPRED Protein Analysis Workbench. Nucleic Acids Res. 2013;41(W1):W340–8.

50. Gilroy E, Hicks M, Smith D, Rodger A. Viscosity of aqueous DNA solutions determined using dynamic light scattering. Analyst. 2011;136(20):4159–63.

51. Ortega A, Amorós D, García De La Torre J. Prediction of hydrodynamic and other solution properties of rigid proteins from atomic- and residue-level models. Biophys J. 2011;101(4):892–8.

52. García De La Torre J, Huertas ML, Carrasco B. Calculation of hydrodynamic properties of globular proteins from their atomic-level structure. Biophys J. 2000;78(2):719–30.

53. Becht NO, Malik DJ, Tarleton ES. Evaluation and comparison of protein ultrafiltration test results: Dead-end stirred cell compared with a cross-flow system. Sep Purif Technol. 2008;62(1):228–39.

54. Wang P, Anderko A. Computation of dielectric constants of solvent mixtures and electrolyte solutions. Fluid Phase Equilib. 2001;186(1-2):103–22.

55. Webb MR. A continuous spectrophotometric assay for inorganic phosphate and for measuring phosphate release kinetics in biological systems. Proc Natl Acad Sci U S A. 1992;89(11):4884–7.

56. Romberg L, Simon M, Erickson HP. Polymerization of FtsZ, a bacterial homolog of tubulin. J Biol Chem. 2001;276(15):11743–53.

57. Chen Y, Erickson HP. Rapid *in vitro* assembly dynamics and subunit turnover of FtsZ demonstrated by fluorescence resonance energy transfer. J Biol Chem. 2005;280(23):22549–54.

58. Erickson HP, Taylor DW, Taylor KA, Bramhill D. Bacterial cell division protein FtsZ assembles into protofilament sheets and minirings, structural homologs of tubulin polymers. Proc Natl Acad Sci U S A. 1996;93(1):519–23.

59. Bramhill D, Thompson CM. GTP-dependent polymerization of *Escherichia coli* FtsZ protein to form tubules. Proc Natl Acad Sci U S A. 1994;91(13):5813–7.

60. Rivas G, López A, Mingorance J, Ferrándiz MJ, Zorrilla S, Minton AP, et al. Magnesium-induced linear self-association of the FtsZ bacterial cell division protein monomer. The primary steps for FtsZ assembly. J Biol Chem. 2000;275(16):11740–9.

61. Lu C, Stricker J, Erickson HP. Site-specific mutations of FtsZ - effects on GTPase and *in vitro* assembly. BMC Microbiol. BioMed Central; 2001;1:7.

62. Rodger A, Marrington R, Geeves MA, Hicks M, de Alwis L, Halsall DJ, et al. Looking at long molecules in solution: what happens when they are subjected to Couette flow? Phys Chem Chem Phys. 2006;8:3161–71.

63. Rodger A, Rajendra J, Marrington R, Ardhammar M, Nordén B, Hirst J, et al. Flow oriented linear dichroism to probe protein orientation in membrane environments. Phys Chem Chem Phys. 2002;4:4051–7.

64. Marrington R, Small E, Rodger A, Dafforn TR, Addinall SG. FtsZ fiber bundling is triggered by a conformational change in bound GTP. J Biol Chem. 2004;279(47):48821–9.

65. Sreerama N, Woody RW. A self-consistent method for the analysis of protein secondary structure from circular dichroism. Anal Biochem. 1993;209(1):32–44.

66. Provencher SW, Glöckner J. Estimation of globular protein secondary structure from circular dichroism. Biochemistry. 1981;20(1):33–7.

67. Van Stokkum IH, Spoelder HJ, Bloemendal M, van Grondelle R, Groen FC. Estimation of protein secondary structure and error analysis from circular dichroism spectra. Anal Biochem. 1990;191(1):110–8.

68. Compton LA, Johnson WC. Analysis of protein circular dichroism spectra for secondary structure using a simple matrix multiplication. Anal Biochem. 1986;155(1):155–67.

69. Lorber B, Fischer F, Bailly M, Roy H, Kern D. Protein analysis by dynamic light scattering: methods and techniques for students. Biochem Mol Biol Educ. 2012;40(6):372–82.

70. Shan S, Walter P. Induced nucleotide specificity in a GTPase. Proc Natl Acad Sci U S A. 2003;100(8):4480–5.

71. Kang C, Sun N, Honzatko RB, Fromm HJ. Replacement of Asp333 with Asn by site-directed mutagenesis changes the substrate specificity of *Escherichia coli* adenylosuccinate synthetase from guanosine 5'-triphosphate to xanthosine 5'-triphosphate. J Biol Chem. 1994;269(39):24046–9.

72. Hwang YW, Miller DL. A mutation that alters the nucleotide specificity of elongation factor Tu, a GTP regulatory protein. J Biol Chem. 1987;262(27):13081–5.

73. Hoffenberg S, Nikolova L, Pan JY, Daniel DS, Wessling-Resnick M, Knoll BJ, et al. Functional and structural interactions of the Rab5 D136N mutant with xanthine nucleotides. Biochem Biophys Res Commun. 1995;215(1):241–9.

74. Jones S, Litt RJ, Richardson CJ, Segev N. Requirement of nucleotide exchange factor for Ypt1 GTPase mediated protein transport. J Cell Biol. 1995;130(5):1051–61.

75. Zhong JM, Chen-Hwang MC, Hwang YW. Switching nucleotide specificity of Ha-Ras p21 by a single amino acid substitution at aspartate 119. J Biol Chem. 1995;270(17):10002–7.

76. Strohmeier J, Hertel I, Diederichsen U, Rudolph M, Klostermeier D. Changing nucleotide specificity of the DEAD-box helicase Hera abrogates communication between the Q-motif and the P-loop. J Biol Chem. 2011;392(4):357–69.

77. Wang X, Kemp RG. Identification of residues of *Escherichia coli* phosphofructokinase that contribute to nucleotide binding and specificity. Biochemistry. 1999;38(14):4313–8.

78. Varnum MD, Black KD, Zagotta WN. Molecular mechanism for ligand discrimination of cyclic nucleotide-gated channels. Neuron. 1995;15(3):619–25.

79. Pessoa J, Fonseca F, Furini S, Morais-Cabral J. Determinants of ligand selectivity in a cyclic nucleotide-regulated potassium channel. J Gen Physiol. 2014;144(1):41–54.

80. Sunahara RK, Beuve A, Tesmer JJG, Sprang SR, Garbers DL, Gilman AG. Exchange of substrate and inhibitor specificities between adenylyl and guanylyl cyclases. J Biol Chem. 1998;273(26):16332–8.

81. Srinivasan N, Antonelli M, Jacob G, Korn I, Jedlicki A, Dhanaraj V, et al. Structural interpretation of site-directed mutagenesis and specificity of the catalytic subunit of protein kinase CK2 using comparative modelling. Protein Eng. 1999;12(2):119–27.

Supplementary Information

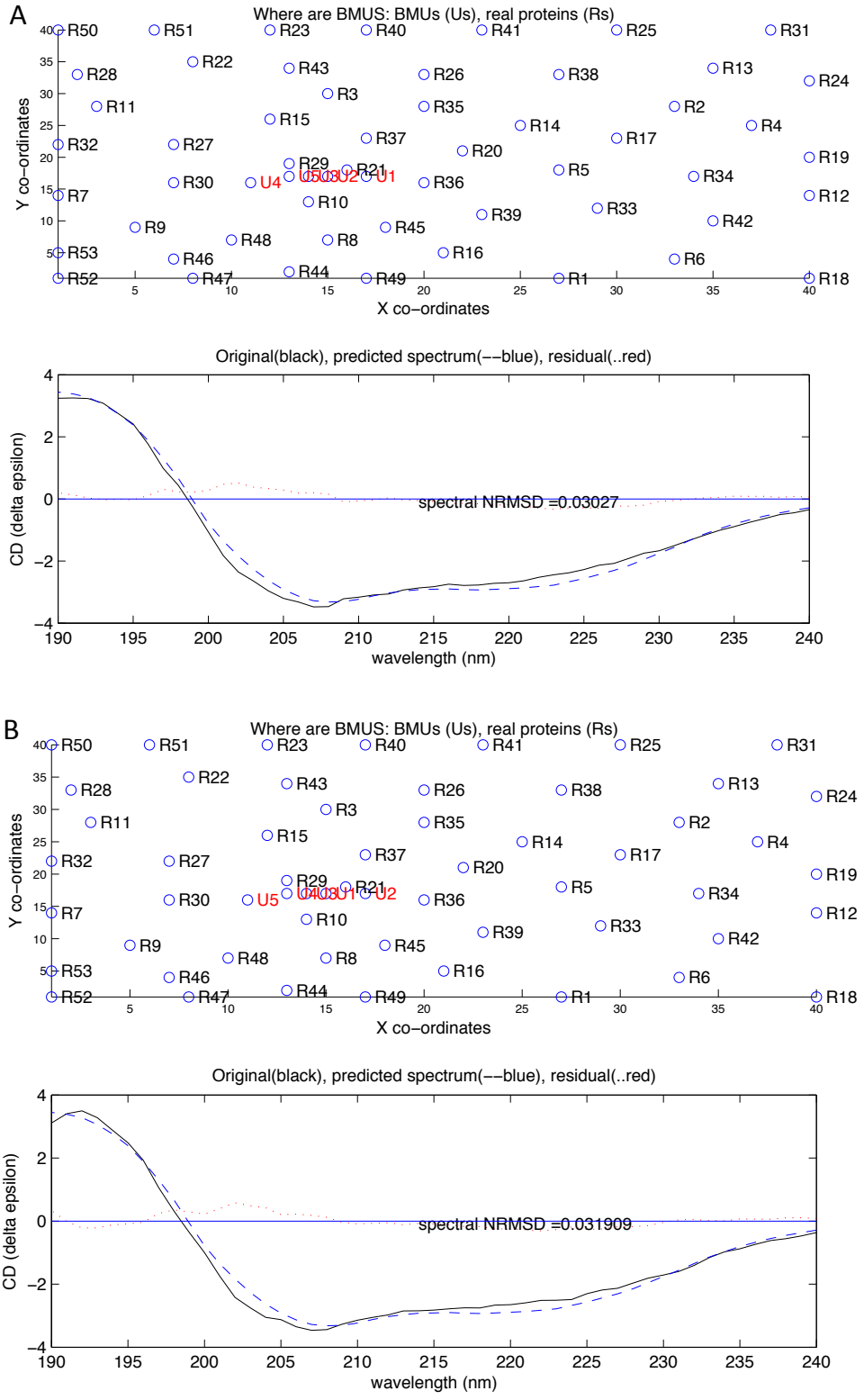

Figure S1: SSNN output from circular dichroism data analysis. Locations of the 5 BMUs are shown on the SOM as well as the modelled and measured CD spectra with residuals. (A) Wild-type FtsZ (B) FtsZ G105S.

```
Identities
217/382(57%)

Positives
267/382(69%)

Gaps
34/382(8%)

E. coli  10  DAVIKVIGVGGGGGNAVEHMVRERIEGVEFFAVNTDAQALRKTAVGQTIQIGSGITKGLGAGAN  73
             AVIKVIGVGGGGGNAV HM +  +EGVEF   NTDAQAL+  A    +Q+G G+TKGLGAGAN
P. aeru  11  TAVIKVIGVGGGGGNAVNHMAKNNVEGVEFICANTDAQALKNIAARTVLQLGPGVTKGLGAGAN  74

E. coli  74  PEVGRNAADEDRDALRAALEGADMVFIAAGMGGGTGTGAAPVVAEVAKDLGILTVAVVTKPFNF 137
             PEVGR AA EDR+ +   LEGADMVFI  GMGGGTGTGAAP++AEVAK++GILTVAVVT+PF F
P. aeru  75  PEVGRQAALEDRERISEVLEGADMVFITTGMGGGTGTGAAPIIAEVAKEMGILTVAVVTRPFPF 138

E. coli 138  EGKKRMAFAEQGITELSKHVDSLITIPNDKLLKVLGRGISLLDAFGAANDVLKGAVQGIAELIT 201
             EG+KRM  A++GI  L++ VDSLITIPN+KLL +LG+  SLL AF  A+DVL GAV+GI+++I
P. aeru 139  EGRKRMQIADEGIRALAESVDSLITIPNEKLLTILGKDASLLAAFAKADDVLAGAVRGISDIIK 202

E. coli 202  RPGLMNVDFADVRTVMSEMGYAMMGSGVASGEDRAEEAAEMAISSPLLEDIDLSGARGVLVNIT 265
             RPG++NVDFADV+TVMSEMG AMMG+G ASG +RA EA E AI +PLLED++L GARG+LVNIT
P. aeru 203  RPGMINVDFADVKTVMSEMGMAMMGTGCASGPNRAREATEAAIRNPLLEDVNLQGARGILVNIT 266

E. coli 266  AGFDLRLDEFETVGNTIRAFASDNATVVIGTSLDPDMNDELRVTVVATGIGMDKRPEITLVTN- 328
             AG DL L E+  VGN I  FAS++ATV +GT +D DM DEL VTVVATG+G      + +V N
P. aeru 267  AGPDLSLGEYSDVGNIIEQFASEHATVKVGTVIDADMRDELHVTVVATGLGARLEKPVKVVDNT 330

E. coli 329  ----------------------KQVQQPVMDRYQQHGMAPLTQEQKPVAKVVNDNAPQTAKEPDY 371
                                 + + +P + R Q HG A    +  P              + DY
P. aeru 331  VQGSAAQAAAPAQREQQSVNYRDLDRPTVMRNQSHGSAATAAKLNP------------QDDLDY 382

E. coli 372  LDIPAFLRKQAD 383
             LDIPAFLR+QAD
P. aeru 383  LDIPAFLRRQAD 394
```

Figure S2: BLASTP alignment of the *E. coli* FtsZ protein sequence and the sequence of the closest matching template identified by SWISS-MODEL, FtsZ from *P. aeruginosa*.

Model #02	File	Built with	Oligo-State	Ligands	GMQE	QMEAN4
	PDB	ProMod Version 3.70.	MONOMER	None	0.72	-0.93

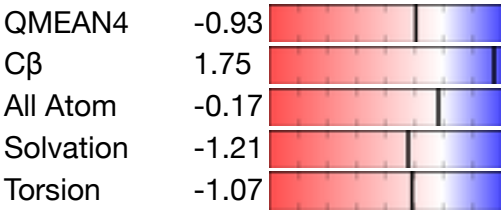

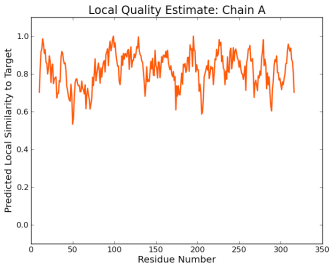

Template	Seq Identity	Oligo-state	Found by	Method	Resolution	Seq Similarity	Range	Coverage	Description
1ofu.1.A	66.56	hetero-oligomer	HHblits	X-ray	2.10Å	0.49	10 - 316	0.83	CELL DIVISION PROTEIN FTSZ

```
Target    MFEPME-LTNDAVIKVIGVGGGGGNAVEHMVRERIEGVEFFAVNTDAQALRKTAVGQTIQIGSGITKGLGAGANPEVGRN
1ofu.1.A  MFELVDNIAQTAVIKVIGVGGGGGNAVNHMAKNNVEGVEFICANTDAQALKNIAARTVLQLGPGVTKGLGAGANPEVGRQ

Target    AADEDRDALRAALEGADMVFIAAGMGGGTGTGAAPVVAEVAKDLGILTVAVVTKPFNFEGKKRMAFAEQGITELSKHVDS
1ofu.1.A  AALEDRERISEVLEGADMVFITTGMGGGTGTGAAPIIAEVAKEMGILTVAVVTRPFPFEGRKRMQIADEGIRALAESVDS

Target    LITIPNDKLLKVLGRGISLLDAFGAANDVLKGAVQGIAELITRPGLMNVDFADVRTVMSEMGYAMMGSGVASGEDRAEEA
1ofu.1.A  LITIPNEKLLTILGKDASLLAAFAKADDVLAGAVRGISDIIKRPGMINVDFADVKTVMSEMGMAMMGTGCASGPNRAREA

Target    AEMAISSPLLEDIDLSGARGVLVNITAGFDLRLDEFETVGNTIRAFASDNATVVIGTSLDPDMNDELRVTVVATGIGMDK
1ofu.1.A  TEAAIRNPLLEDVNLQGARGILVNITAGPDLSLGEYSDVGNIIEQFASEHATVKVGTVIDADMRDELHVTVVATGLGA--

Target    RPEITLVTNKQVQQPVMDRYQQHGMAPLTQEQKPVAKVVNDNAPQTAKEPDYLDIPAFLRKQAD
1ofu.1.A  ------------------------------------------------------------
```

Figure S3: SWISS-MODEL results analysis. The GMQE and QMEAN4 scores are acceptable.

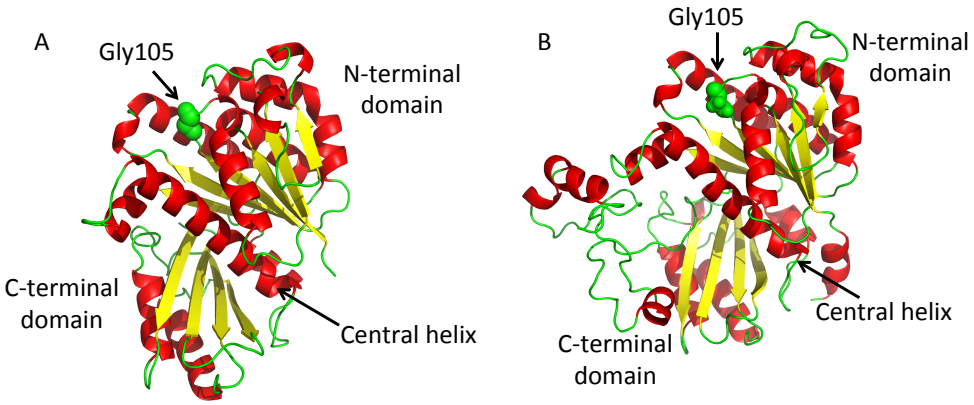

Figure S4: The modelled three-dimensional structure of the *E. coli* FtsZ protein coloured by secondary structure. Glycine 105 is highlighted. (A) SWISS-MODEL structure for residues 10–316. (B) Full-length FtsZ modelled using molecular dynamics simulation.

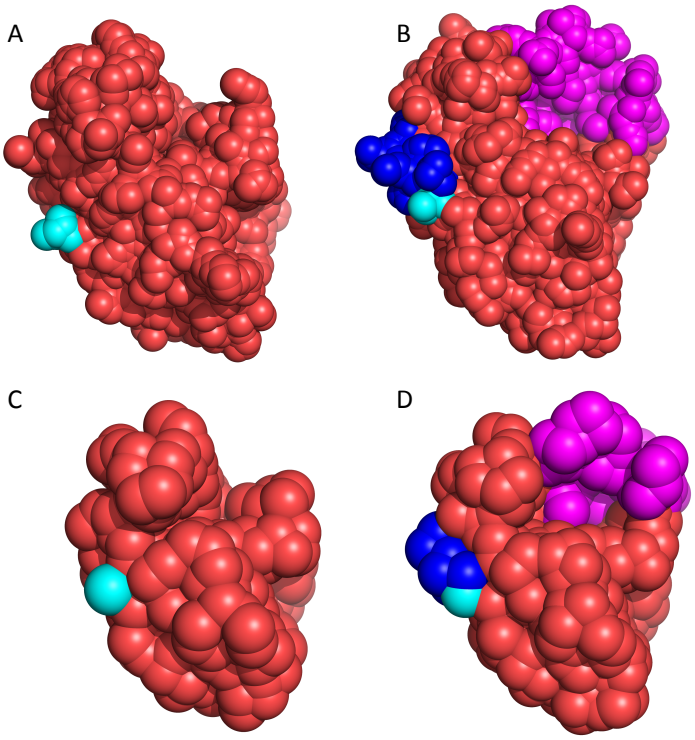

Figure S5: HYDROPRO primary structural models of FtsZ. The HYDROPRO program replaces non-hydrogen atoms from the structural PDB input file with a single bead in the atomistic mode and replaces each amino acid with a single bead in the coarse-grained residue mode. (A) The SWISS-MODEL derived FtsZ core containing residues 10 to 316 in atomistic mode. (B) The full length MD-simulated FtsZ protein in atomistic mode. (C) Residues 10 to 316 in residue mode. (D) Full-length FtsZ in residue mode. Additional N-terminal residues in the full-length structure are shown in blue. Aspartate 10 is shown in cyan for orientation. Additional C-terminal residues in the full-length structure are shown in magenta.

Table S1: Comparison of the secondary structure assignments of the SWISS-MODEL core structure of FtsZ (SM) and the molecular dynamics-simulated, full-length structure of FtsZ (MD) using DSSP. SSNN indicates the corresponding secondary structure classification of SSNN.

Residue	SM DSSP	SM SSNN	MD DSSP	MD SSNN
1			-	Unordered
2			-	Unordered
3			T	Turn
4			T	Turn
5			H	α-distorted
6			H	α-distorted
7			H	α-distorted
8			H	α-distorted
9			T	Turn
10	-	Unordered	T	Turn
11	-	Unordered	-	Unordered
12	-	Unordered	-	Unordered
13	E	β-distorted	E	β-distorted
14	E	β-regular	E	β-regular
15	E	β-regular	E	β-regular
16	E	β-regular	E	β-regular
17	E	β-regular	E	β-regular
18	E	β-distorted	E	β-distorted
19	H	α-distorted	H	α-distorted
20	H	α-distorted	H	α-distorted
21	H	α-regular	H	α-regular
22	H	α-regular	H	α-regular
23	H	α-regular	H	α-regular
24	H	α-regular	H	α-regular
25	H	α-regular	H	α-regular
26	H	α-regular	H	α-regular
27	H	α-regular	H	α-regular
28	H	α-regular	H	α-regular
29	H	α-regular	H	α-regular
30	H	α-distorted	H	α-distorted
31	H	α-distorted	H	α-distorted
32	T	Turn	T	Turn
33	T	Turn	T	Turn
34	-	Turn	-	Unordered
35	T	Turn	S	Unordered
36	T	Turn	S	Unordered
37	E	β-distorted	-	Unordered
38	E	β-regular	E	β-distorted
39	E	β-regular	E	β-regular
40	E	β-regular	E	β-regular
41	E	β-regular	E	β-regular
42	E	β-regular	E	β-regular

Residue	SM DSSP	SM SSNN	MD DSSP	MD SSNN
43	E	β-distorted	E	β-distorted
44	S	Unordered	-	Unordered
45	B	Unordered	S	Unordered
46	T	Unordered	G	α-distorted
47	G	α-distorted	G	α-distorted
48	G	α-distorted	G	α-distorted
49	G	α-distorted	-	Unordered
50	S	Turn	-	Unordered
51	S	Turn	-	Unordered
52	-	Unordered	-	Unordered
53	S	Unordered	T	Turn
54	-	Unordered	T	Turn
55	S	Unordered	S	Unordered
56	E	β-distorted	-	Unordered
57	E	β-regular	E	β-distorted
58	E	β-regular	E	β-regular
59	E	β-distorted	E	β-distorted
60	-	Unordered	-	Unordered
61	-	Unordered	-	Unordered
62	H	α-distorted	S	Unordered
63	H	α-distorted	S	Unordered
64	H	α-distorted	T	Turn
65	H	α-distorted	T	Turn
66	T	Turn	T	Turn
67	T	Turn	T	Turn
68	B	Unordered	T	Turn
69	-	Unordered	-	Unordered
70	-	Unordered	-	Unordered
71	S	Turn	T	Turn
72	S	Turn	T	Turn
73	-	Unordered	-	Unordered
74	H	α-distorted	H	α-distorted
75	H	α-distorted	H	α-distorted
76	H	α-regular	H	α-regular
77	H	α-regular	H	α-regular
78	H	α-regular	H	α-regular
79	H	α-regular	H	α-regular
80	H	α-regular	H	α-regular
81	H	α-regular	H	α-regular
82	H	α-regular	H	α-regular
83	H	α-regular	H	α-regular
84	T	α-distorted	T	α-distorted
85	H	α-regular	H	α-regular
86	H	α-regular	H	α-regular
87	H	α-regular	H	α-regular
88	H	α-regular	H	α-regular
89	H	α-regular	H	α-regular

Residue	SM DSSP	SM SSNN	MD DSSP	MD SSNN
90	H	α-regular	H	α-regular
91	H	α-distorted	H	α-distorted
92	H	α-distorted	H	α-distorted
93	T	Turn	T	Turn
94	T	Turn	T	Turn
95	-	Unordered	-	Unordered
96	S	Unordered	S	Unordered
97	E	β-distorted	E	β-distorted
98	E	β-regular	E	β-regular
99	E	β-regular	E	β-regular
100	E	β-regular	E	β-regular
101	E	β-regular	E	β-regular
102	E	β-regular	E	β-distorted
103	E	β-distorted	-	Unordered
104	T	Turn	-	Unordered
105	T	Turn	S	Unordered
106	S	Turn	S	Unordered
107	S	Turn	S	Unordered
108	H	α-distorted	H	α-distorted
109	H	α-distorted	H	α-distorted
110	H	α-regular	H	α-regular
111	H	α-regular	H	α-regular
112	H	α-regular	H	α-regular
113	H	α-regular	H	α-regular
114	H	α-regular	H	α-regular
115	H	α-regular	H	α-regular
116	H	α-regular	H	α-regular
117	H	α-regular	H	α-regular
118	H	α-regular	H	α-regular
119	H	α-regular	H	α-regular
120	H	α-regular	H	α-regular
121	H	α-distorted	H	α-regular
122	H	α-distorted	H	α-distorted
123	T	Turn	H	α-distorted
124	T	Turn	T	Turn
125	-	Unordered	-	Unordered
126	E	β-distorted	E	β-distorted
127	E	β-regular	E	β-regular
128	E	β-regular	E	β-regular
129	E	β-regular	E	β-regular
130	E	β-regular	E	β-regular
131	E	β-regular	E	β-regular
132	E	β-regular	E	β-regular
133	E	β-distorted	E	β-distorted
134	-	Unordered	-	Unordered
135	-	Unordered	-	Unordered
136	G	α-distorted	G	α-distorted

Residue	SM DSSP	SM SSNN	MD DSSP	MD SSNN
137	G	α-distorted	G	α-distorted
138	G	α-distorted	G	α-distorted
139	-	Unordered	-	Unordered
140	H	α-distorted	H	α-distorted
141	H	α-distorted	H	α-distorted
142	H	α-regular	H	α-regular
143	H	α-regular	H	α-regular
144	H	α-regular	H	α-regular
145	H	α-regular	H	α-regular
146	H	α-regular	H	α-regular
147	H	α-regular	H	α-regular
148	H	α-regular	H	α-regular
149	H	α-regular	H	α-regular
150	H	α-regular	H	α-regular
151	H	α-regular	H	α-regular
152	H	α-regular	H	α-distorted
153	H	α-distorted	H	α-distorted
154	H	α-distorted	T	Turn
155	T	Turn	T	Turn
156	T	Turn	T	Turn
157	-	Unordered	-	Unordered
158	S	Unordered	S	Unordered
159	E	β-distorted	E	β-distorted
160	E	β-regular	E	β-regular
161	E	β-regular	E	β-regular
162	E	β-regular	E	β-regular
163	E	β-regular	E	β-regular
164	E	β-distorted	E	β-distorted
165	H	α-distorted	H	α-distorted
166	H	α-distorted	H	α-distorted
167	H	α-regular	H	α-regular
168	H	α-regular	H	α-regular
169	H	α-regular	H	α-regular
170	H	α-regular	H	α-regular
171	H	α-distorted	H	α-distorted
172	H	α-distorted	H	α-distorted
173	G	α-distorted	G	α-distorted
174	G	α-distorted	G	α-distorted
175	G	α-distorted	G	α-distorted
176	-	Unordered	S	Unordered
177	-	Unordered	-	Unordered
178	H	α-distorted	H	α-distorted
179	H	α-distorted	H	α-distorted
180	H	α-regular	H	α-regular
181	H	α-regular	H	α-regular
182	H	α-regular	H	α-regular
183	H	α-regular	H	α-regular

Residue	SM DSSP	SM SSNN	MD DSSP	MD SSNN
184	H	α-regular	H	α-regular
185	H	α-regular	H	α-regular
186	H	α-regular	H	α-regular
187	H	α-regular	H	α-regular
188	H	α-regular	H	α-regular
189	H	α-regular	H	α-regular
190	H	α-regular	H	α-regular
191	H	α-regular	H	α-regular
192	H	α-regular	H	α-regular
193	H	α-regular	H	α-regular
194	H	α-regular	H	α-regular
195	H	α-regular	H	α-regular
196	H	α-regular	H	α-regular
197	H	α-regular	H	α-regular
198	H	α-regular	H	α-regular
199	H	α-regular	H	α-regular
200	H	α-distorted	H	α-distorted
201	H	α-distorted	H	α-distorted
202	S	Unordered	S	Unordered
203	-	Unordered	-	Unordered
204	S	Turn	-	Unordered
205	S	Turn	S	Unordered
206	S	Turn	S	Unordered
207	S	Turn	-	Unordered
208	-	Unordered	-	Unordered
209	-	Unordered	-	Unordered
210	H	α-distorted	H	α-distorted
211	H	α-distorted	H	α-distorted
212	H	α-regular	H	α-regular
213	H	α-regular	H	α-regular
214	H	α-regular	H	α-distorted
215	H	α-regular	H	α-distorted
216	H	α-distorted	T	Turn
217	H	α-distorted	T	Turn
218	T	Turn	S	Unordered
219	T	Turn	S	Unordered
220	-	Unordered	-	Unordered
221	E	β-distorted	E	β-distorted
222	E	β-regular	E	β-regular
223	E	β-regular	E	β-regular
224	E	β-regular	E	β-regular
225	E	β-regular	E	β-regular
226	E	β-regular	E	β-regular
227	E	β-regular	E	β-regular
228	E	β-regular	E	β-regular
229	E	β-regular	E	β-regular
230	E	β-regular	E	β-regular

Residue	SM DSSP	SM SSNN	MD DSSP	MD SSNN
231	E	β-distorted	E	β-distorted
232	S	Unordered	S	Unordered
233	T	Turn	T	Turn
234	T	Turn	T	Turn
235	H	α-distorted	H	α-distorted
236	H	α-distorted	H	α-distorted
237	H	α-regular	H	α-regular
238	H	α-regular	H	α-regular
239	H	α-regular	H	α-regular
240	H	α-regular	H	α-regular
241	H	α-regular	H	α-regular
242	H	α-regular	H	α-regular
243	H	α-distorted	H	α-regular
244	H	α-distorted	H	α-distorted
245	T	Unordered	H	α-distorted
246	-	Unordered	S	Unordered
247	G	α-distorted	T	Turn
248	G	α-distorted	T	Turn
249	G	α-distorted	S	Unordered
250	T	Turn	T	Turn
251	T	Turn	T	Turn
252	-	Unordered	S	Unordered
253	-	Unordered	S	Unordered
254	G	α-distorted	G	α-distorted
255	G	α-distorted	G	α-distorted
256	G	α-distorted	G	α-distorted
257	E	β-distorted	-	Unordered
258	E	β-regular	S	Unordered
259	E	β-regular	E	β-distorted
260	E	β-regular	E	β-regular
261	E	β-regular	E	β-regular
262	E	β-regular	E	β-regular
263	E	β-regular	E	β-regular
264	E	β-regular	E	β-regular
265	E	β-regular	E	β-regular
266	E	β-distorted	E	β-distorted
267	-	Unordered	-	Unordered
268	T	Turn	T	Turn
269	T	Turn	T	Turn
270	-	Unordered	-	Unordered
271	-	Unordered	-	Unordered
272	H	α-distorted	H	α-distorted
273	H	α-distorted	H	α-distorted
274	H	α-regular	H	α-regular
275	H	α-regular	H	α-regular
276	H	α-regular	H	α-regular
277	H	α-regular	H	α-regular

Residue	SM DSSP	SM SSNN	MD DSSP	MD SSNN
278	H	α-regular	H	α-regular
279	H	α-regular	H	α-regular
280	H	α-regular	H	α-regular
281	H	α-regular	H	α-regular
282	H	α-regular	H	α-distorted
283	H	α-regular	H	α-distorted
284	H	α-distorted	T	Turn
285	H	α-distorted	T	Turn
286	S	Unordered	S	Unordered
287	-	Unordered	-	Unordered
288	T	Turn	S	Unordered
289	T	Turn	S	Unordered
290	S	Unordered	S	Unordered
291	E	β-distorted	E	β-distorted
292	E	β-regular	E	β-regular
293	E	β-regular	E	β-regular
294	E	β-regular	E	β-regular
295	E	β-regular	E	β-regular
296	E	β-regular	E	β-regular
297	E	β-regular	E	β-regular
298	E	β-distorted	E	β-distorted
299	-	Unordered	-	Unordered
300	T	Turn	T	Turn
301	T	Turn	T	Turn
302	-	Unordered	-	Unordered
303	-	Unordered	S	Unordered
304	S	Unordered	S	Unordered
305	E	β-distorted	E	β-distorted
306	E	β-regular	E	β-regular
307	E	β-regular	E	β-regular
308	E	β-regular	E	β-regular
309	E	β-regular	E	β-regular
310	E	β-regular	E	β-regular
311	E	β-regular	E	β-distorted
312	E	β-regular	-	Unordered
313	E	β-regular	T	Turn
314	E	β-regular	T	Turn
315	E	β-distorted	T	Turn
316	-	Unordered	-	Unordered
317			-	Unordered
318			B	β-distorted
319			-	Unordered
320			-	Unordered
321			S	Unordered
322			-	Unordered
323			-	Unordered
324			-	Unordered

Residue	SM DSSP	SM SSNN	MD DSSP	MD SSNN
325			-	Unordered
326			-	Unordered
327			S	Unordered
328			-	Unordered
329			S	Unordered
330			S	Unordered
331			T	Turn
332			T	Turn
333			G	α-distorted
334			G	α-distorted
335			G	α-distorted
336			H	α-distorted
337			-	Unordered
338			-	Unordered
339			-	Unordered
340			-	Unordered
341			H	α-distorted
342			T	Turn
343			T	Turn
344			-	Unordered
345			-	Unordered
346			-	Unordered
347			-	Unordered
348			S	Unordered
349			-	Unordered
350			-	Unordered
351			S	Unordered
352			S	Unordered
353			-	Unordered
354			S	Unordered
355			S	Unordered
356			S	Unordered
357			-	Unordered
358			-	Unordered
359			-	Unordered
360			T	Turn
361			T	Turn
362			S	Unordered
363			-	Unordered
364			T	Turn
365			T	Turn
366			T	Turn
367			T	Turn
368			S	Unordered
369			H	α-distorted
370			H	α-distorted
371			H	α-regular

Residue	SM DSSP	SM SSNN	MD DSSP	MD SSNN
372			H	α-regular
373			H	α-regular
374			H	α-regular
375			H	α-regular
376			H	α-distorted
377			H	α-distorted
378			T	Turn
379			T	Turn
380			S	Unordered
381			-	Unordered
382			-	Unordered
383			-	Unordered

Production of DNA molecules of defined length and GC content for linear dichroism and light scattering experiments

Claire E. Broughton[†], Daniela P.C.A. Lobo[§], David I. Roper[‡], Jason Piper[∞], Ravi Jagadeeshan[¬], Alison Rodger[§,⊥,]*

† Molecular Organisation and Assembly in Cells Doctoral Training Centre, Senate House, University of Warwick, Coventry, CV4 7AL, United Kingdom

§ Department of Chemistry, University of Warwick, Coventry, CV4 7AL, United Kingdom

‡ School of Life Sciences, University of Warwick, Coventry, CV4 7AL, United Kingdom

∞ Systems Biology Doctoral Training Centre, Senate House, University of Warwick, Coventry, CV4 7AL, United Kingdom

¬ Department of Engineering, Clayton Campus, Monash University, Wellington Road, Clayton, Victoria 3800, Australia

⊥ Warwick Analytical Science Centre, University of Warwick, Coventry, CV4 7AL, United Kingdom

ABSTRACT

DNA has been used as a model polymer in many rheology studies. However, to date a limited set of molecules has been utilized including phage genomic DNA and bacterial extra-chromosomal constructs such as plasmids, fosmids and the bacterial artificial chromosome. We report the design of a series of DNA molecules from 0.5 kbp to 6 kbp with identical GC content, synthesized by PCR. The *Escherichia coli* genome was used as the template and the target regions were identified by full length scanning of the sequence. The targets were amplified and cloned into the plasmid vector pBluescript II KS+. Using the cloned vector as the template for a second PCR yielded DNA of the required length and GC content, at a concentration suitable for linear dichroism and light scattering experiments for the dilute regime and at the crossover into the semi-dilute regime at C^*.

INTRODUCTION

The experimental manipulation of DNA is clearly important in the field of molecular biology in gene cloning, DNA sequencing, and mutagenesis as well as for the toolbox of techniques for the study of DNA-protein interactions including oligonucleotide array chip technologies,[1] chromatin immuno-precipitation (ChIP)[2] (and their combination in ChIP-on-chip applications),[3] electrophoretic mobility shift assays (EMSA)[4] and DNA pulldown.[5] Spectroscopic techniques such as circular dichroism and linear dichroism can also be used to measure the interaction of DNA with proteins or with small

molecules such as ethidium bromide, DAPI and Hoechst dyes[6,7] and to probe secondary structure changes in the DNA.

An additional application of DNA is in the study of polymer physics and rheology. Polymer solutions are complex displaying both liquid- and solid-like behavior[8] and non-Newtonian characteristics[9]. Polymeric solutions often have flow-dependent viscosities and exhibit normal shear stress.[10] DNA as a model polymer has the advantage of being able to be produced in large quantities, with high sequence fidelity (*i.e.* fixed identity) by employing prokaryotic cells as DNA polymer "factories" or using PCR. The particular attraction of DNA polymers is that polymer length can be controlled down to a single base pair and monodisperse polymer solutions may be produced with relative ease.

The prediction of the viscosity and elasticity of polymer solutions is of considerable value to the chemical and petroleum industries, yet it remains challenging. One of the motivations of this work was to produce well-characterized DNA solutions to provide experimental reference points for theoretical work on polymer dynamics and coil-stretch hysteresis.[11] A side benefit of this work is that a detailed understanding of the physical properties of DNA is of importance to both molecular biologists, who use it in standard molecular biology applications and in synthetic biology. The overall aim is to connect the microscopic behavior of the polymer molecules with the macroscopic properties of the polymeric solution.[10]

We anticipate that our DNA could be used in several techniques currently employed in the study of DNA solution physics. This includes bulk rheology measurements,[12] microfluidics,[13–16] single-molecule imaging using fluorescent labelled DNA,[17,18] and mechanical manipulation with optical tweezers or

tethering.[18–20] These techniques may be applied for polymeric solutions across the concentration range including dilute solutions, such that the individual polymer molecules do not interact with each other and the solution viscosity is proportional to the polymer concentration,[21] semi-dilute solutions with concentrations falling between C^*, the point at which molecules begin to overlap and interact, and C^{**}, the transition point into the concentrated regime, in which polymer entanglements dominate the flow behaviour,[22] polymers are constricted to the limit of the unperturbed dimension[23] and the polymer chain dimensions become independent of concentration.[21] At the high concentration end of the scale, single molecule tracking has been used for DNA polymers within a background of unlabeled DNA for concentrations far in excess of C^{**}.[24,25]

The viscoelastic properties of a polymer solution vary between these different concentration regimes,[8] which are represented in Figure 1, and also within the semi-dilute regime which is further subdivided into the semi-dilute unentangled regime and the semi-dilute entangled regime. C_e indicates the point of transition and the onset of polymer entanglements, where chain motions are topologically constrained[22] and the power law relationship between the polymer concentration and the solution viscosity shifts from $\eta \sim c^{1.25}$ for semi-dilute unentangled polymers to $\eta \sim c^{4.5}$ for semi-dilute entangled polymers.[26]

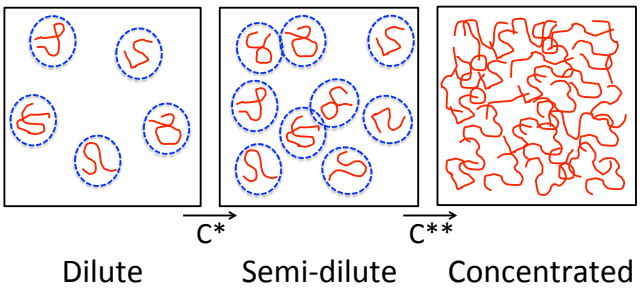

Figure 1. Concentration regimes of polymeric solutions. *C** is the concentration at which individual polymer molecules overlap and interact. Above *C*** the polymers form an entangled mesh of fibers. The macroscopic properties of the polymer solution will vary depending on the interactions between individual molecules.

Linear dichroism (LD) has the potential to be an ideal technique for the study of polymer behavior in flow.[27] LD is the difference in absorption of light polarised parallel to an orientation direction ($A_{\parallel}$) and light polarised perpendicular to the orientation direction ($A_{\perp}$). LD signal is determined by the intensity of the absorbance and the orientation of the electronic transition with respect to the orientation axis. The reduced linear dichroism is pathlength- and concentration- independent and is given by:

$$\mathrm{LD^r} = \frac{A_{\parallel} - A_{\perp}}{A} = \frac{3}{2} S(3\cos^2\alpha - 1) \ ,$$

where *A* is the absorbance of the sample under isotropic conditions, α is defined as the angle between the transition moment and the orientation axis, and *S* is a flow orientation parameter, which equals 1 for (the never achieved) perfect orientation and 0 for no orientation.[27]

Under Couette flow, the alignment of DNA molecules can be measured as the absorbing chromophores of the nitrogenous bases become ordered, resulting in a preferential absorption of one orientation of polarised light over the other for wavelengths in the UV-visible range.[27,28] Couette flow cells are available which take small solution volumes and show reduced light scattering, and measurements can be taken under tight temperature control.[6,29] Analysis of even smaller volumes using microfluidic LD systems is under development.

In previous LD studies of DNA, calf thymus DNA has been used,[6,29–31] as well as synthetic DNA,[32–36] and bacterial chromosomal DNA.[37] However, with these samples there was either no control over the polymer size or no control over GC content as in practice both calf thymus DNA and synthetic DNAs are polydisperse, and the bacterial DNA molecules are limited in size and GC content. The aim of this work was to design and produce monodisperse linear DNA molecules with known length and GC content to be used for polymer rheology work using linear dichroism and multiple-angle light scattering experiments.

EXPERIMENTAL SECTION

Materials. All aqueous solutions were made with 18.2 MΩ.cm water obtained from a Millipore direct-Q water purifier. DNA polymerase, restriction endonuclease, DNA ligase and calf intestinal alkaline phosphatase (CIP) enzymes were all purchased from New England Biolabs. PCR primers were purchased from Integrated DNA Technologies.

Design and amplification of target DNA sequences. *Escherichia coli* strain K12 MG1655 genomic DNA was used as the template source of DNA. The genome sequence (NCBI Reference Sequence: NC_000913.3) was scanned for regions of the required length that contain precisely the GC content selected, in this case 50%. Regions identified by the full genome scan were selected as the target DNA sequences. PCR primers were identical to at least the first 20 nucleotides of the target sequence (forward primer) and the reverse complement of at least the last 20 nucleotides (reverse primer) to give replication of the intervening sequence by PCR. An additional set of primers was designed to include a restriction endonuclease recognition site at each end of the target to allow cloning of the PCR product obtained. The target regions of the genome and the primer sequences are given in Table 1.

The target sequence was amplified using the Phusion® High-Fidelity DNA Polymerase according to the manufacturers instructions. Briefly, the PCR reaction contained 1× Phusion® GC buffer, 3% DMSO, 0.5 mM $MgCl_2$, 0.5 mM each restriction-encoded primer, 0.8 mM dNTPs, 100 ng *E. coli* genomic DNA and 2 units of Phusion® High-Fidelity DNA Polymerase. A series of annealing temperatures between 58 °C and 66 °C was tested to find the optimum conditions for each primer set. The optimum temperature is given in Table 1. For the PCR reaction, the polymerase was activated at 98 °C for 2 minutes. This was followed by 30 cycles of 10 seconds DNA denaturation at 98 °C, 1 minute primer annealing at the optimum temperature, and 30 seconds primer extension per kbp at 72 °C. After cycling, a final 10-minute extension at 72 °C was used. Where necessary, the PCR product was cleaned by gel extraction using 1.5% agarose gel electrophoresis and the QIAquick Gel Extraction kit according to the

manufacturer's instructions. Otherwise, the PCR product was cleaned with the QIAquick PCR Purification kit according to the manufacturer's instructions.

Table 1. Design of linear DNA target sequences with 50% GC content. Numbering of target region is as in NCBI Reference Sequence: NC_000913.3. Basic primers contain the sequence shown in black. Blue indicates the additional sequence added for restriction cloning.

Size (bp)	*E. coli* target region	Primers (5' to 3')	Anneal temp. (°C)	Cloning enzymes used
500	110,251–110,750	F: TTT GCG GGATCC CCATTTACTCCCAGCGTAAC R: TTT GCG AAGCTT ACTGATAACTTCATATTTCAACGAC	66	BamHI HindIII
1000	110,250–111,249	F: TTT GCG GGATCC GCCATTTACTCCCAGCGTAAC R: TTT GCG AAGCTT TCAAATAGCGAAAAATGTTGGGGG	60	BamHI HindIII
2000	111,491–113,490	F: TTT GCG GGATCC TGGCGCGTCTTATCAGGCCT R: TTT GCG AAGCTT ATGAGAACGTCTTTAAAACC	60	BamHI HindIII
3000	8,997–11,996	F: TTT CGC GAA TTC GAGAGCGAAGGGGCTATCGA R: TTT GCG AAG CTT TTTTTGTGCTTTTGCGCAGA	65	EcoRI HindIII
4000	110,070–114,069	F: TTT GCG GGATCC TTTGCTTCCGACCGAGTATC R: TTT GCG CTCGAG GCAGCATCGGCACATTCGAT	60	BamHI XhoI
5000	7,582–12,581	F: TTT GCG GAATTC ACGAAACTGCCCATTGACGT R: TTT GCG CTCGAG ATAACAGCTTCAGTTACCGG	66	EcoRI XhoI
6000	13,837–19,836	F: TTT GCG GAATTC GCTGACGACAAAACTGCTAT R: TTT GCG CTCGAG ATCTGAACATAAAACACTAT	66	EcoRI XhoI

Cloning of the target DNA. 2 µg PCR product was cleaved for 3 hours at 37 °C in a final volume of 30 µL with the appropriate restriction enzymes (given in Table 1) in 1× CutSmart® buffer. 1 µg of the vector pBluescript II KS+ was also cleaved in a separate digestion reaction with the same two enzymes under the

same conditions. 10 units of CIP were also added to the vector digest to remove the 5' phosphates from linearized DNA. This prevents the re-circularization of the plasmid vector in the later ligation reaction without insertion of the target DNA. The digested DNA was cleaned with the QIAquick PCR Purification kit according to the manufacturer's instructions.

Ligation reactions contained 1× T4 DNA ligase reaction buffer, 50 units of T4 DNA ligase and various ratios of vector DNA to PCR product DNA in a final volume of 20 μL. Typically 100 ng vector DNA and 250 ng PCR product DNA was successful. Ligations were incubated at room temperature overnight then 5 μL of the reaction mix was used to transform 50 μL *E. coli* TOP10 cell suspension. Cells were grown overnight at 37 °C on LB-agar plates supplemented with 100 μg/mL ampicillin and 40 μg/mL 5-bromo-4-chloro-3-indolyl-β-D-galactopyranoside (X-gal) for selection and screening of successful clones respectively. Single white colonies were picked and grown overnight at 37 °C with shaking at 180 rpm in 5 mL LB supplemented with 100 μg/mL ampicillin. Plasmid DNA was purified using the QIAPrep Spin Miniprep kit according to the manufacturer's instructions. Successful cloning was confirmed by detecting the release of the appropriately sized PCR product from the vector on digestion with the original restriction enzymes using 0.8% agarose gel electrophoresis. DNA sequencing reactions (GATC Biotech) from the T7 promoter (sequencing primer: 5' TAA TAC GAC TCA CTA TAG GGG 3') were also used to confirm successful cloning.

Amplification of cloned DNA. The cloned PCR product was used as the template for the production of highly concentrated, monodisperse DNA for LD and light scattering experiments. The PCR was repeated as previously using the basic primer set (shown in black in Table 1) and the cloned vector DNA was used as the template. The result is a PCR product that is the same size as the original target DNA with no additional sequence at the 5' and 3' ends. Once the production of the correctly sized DNA was confirmed using 0.8% gel electrophoresis, the PCR was scaled up to produce sufficient quantities of the target DNA.

RESULTS AND DISCUSSION

We considered various methods for the production of linear DNA for LD and dynamic light scattering experiments. We sought to improve the control over sequence length and sequence composition in comparison to the polymers utilized to date in the field of polymer rheology which includes: native, fragmented and concatenated λ-phage genomic DNA[20,25,38,39], T2 phage genomic DNA[40], T4 phage genomic DNA[41], and bacterial plasmids, fosmids and the bacterial artificial chromosome (BAC)[9,41,42]. The target size range for our work was 0.5 kbp to 6 kbp, which is suitable for replication by PCR. We chose to use an identical base composition for each polymer size to allow direct comparison in the temperature-controlled studies that will follow. For example, at the same GC content, a DNA molecule of 1000 bp contains exactly double the number of each base in a DNA molecule of size 500 bp. This will be important in melt analyses, since a GC base pair is held by 3 hydrogen bonds compared to the 2

hydrogen bonds of the AT pair. The entire *E. coli* genome sequence was scanned to identify regions that had precisely the required GC content for each size. For this work we chose a GC content of 50%. The limitation to the range of possible GC contents is the availability of sequences matching the desired GC composition within the template genome.

We considered using a single PCR reaction for the production of DNA of the required length using the *E. coli* genome as template. However, we found that the final PCR solution contained additional products and so required further clean-up or selection. Gel extraction of the original PCR was a possibility. However, this would have required the addition of ethidium bromide or another DNA dye, which would have remained as a contaminant in later work. We know that ethidium bromide causes stiffening of the DNA molecule from previous linear dichroism studies.[43] In addition, ethidium bromide contributes to the absorbance signal in the 260 nm region where we plan to probe the DNA LD. Thus the addition of dyes for DNA purification was particularly unattractive for the goals of this work.

Once the target sequence had been cloned, the possibility of using *E. coli* cells to produce a high concentration of plasmid/target DNA was investigated. However, the addition and subsequent removal of restriction endonuclease enzymes to release the required DNA, and the purification of the correct size became problematic. (Purification of the required DNA fragment from the digested plasmid by HPLC is currently under investigation.) We anticipated that once the PCR product had been cloned, a subsequent PCR reaction would give a cleaner product since the possibility of additional, less-specific primer recognition was reduced for the shorter template sequence. Scale-up of the PCR

using the cloned pBluescript II KS+ vector as the template was considered the most practical of the methods for the initial stages of this work. The strategy finally adopted to produce linear DNA of constant GC content is illustrated in Figure 2. The limitation on the size of DNA that may be produced by the method is the size limit of the PCR and the maximum insert that can be cloned into the pBS II KS+ vector. The maximum insert size for pBS II KS+ may be as low as 8 kbp.[44]

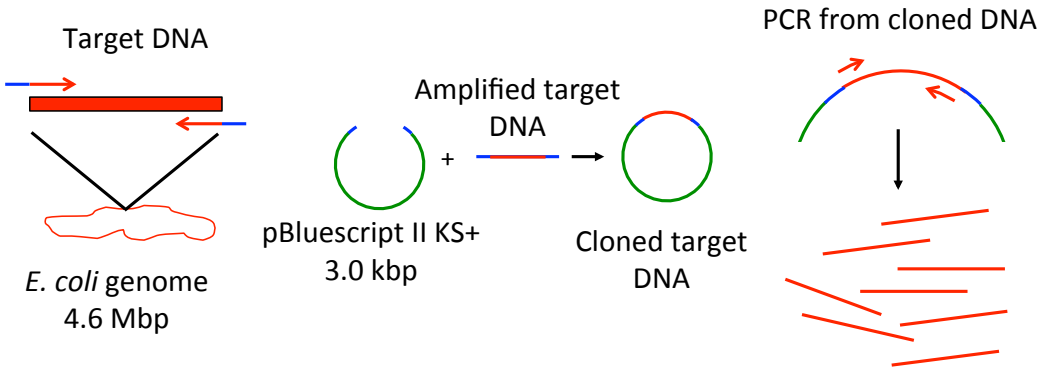

Figure 2. Synthesis strategy to produce monodisperse, linear DNA of defined length and GC content.

Example gel images obtained are shown in Figure 3. As can be seen in Figure 3A, the initial PCR using *E. coli* genomic DNA as the template does not produce a monodisperse product due to additional (less specific) primer annealing. An example of the confirmation of successful cloning is illustrated in Figure 3B for the 2 kbp product, where digestion with the appropriate restriction enzymes releases the cloned product of the correct size. Figure 3C shows the final monodisperse DNA produced using PCR amplification from the cloned vector DNA template for the 0.5 kbp.

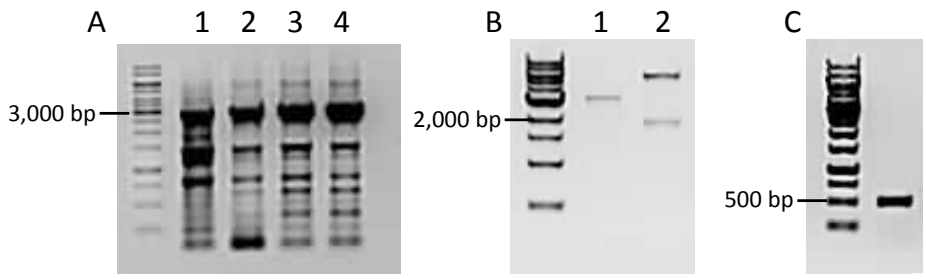

Figure 3. Example agarose gel electrophoresis images. (A) The initial PCR for the 3 kbp target using the *E. coli* genome as template. Lanes 1–4 used different annealing temperatures. (B) The confirmation of cloning success: lane 1 shows the uncut cloned vector and lane 2 shows the release of the 2 kbp fragment on digestion with the appropriate enzymes. (C) Monodisperse linear DNA produced by PCR using the cloned vector DNA as template.

The concentrations of DNA used for a good magnitude LD signal are in the region of 100–200 μM base concentration.[6,7,29,43] This must be compared to the value of C^* for the rheology studies and also to the concentrations yielded by the PCR method to determine whether the proposed DNA synthesis procedure is suitable. To calculate C^*, the length, diffusion constant and radius of gyration of the polymer molecule are used along with the molecular weight to give C^* in mg/mL.

Polymer theory predicts that for long linear polymers $D \sim 1/R_G \sim L^{-v}$, where D is the diffusion coefficient, R_G is the radius of gyration and L is the polymer length (μm) with $v \cong 0.558$.[42] The polymer length may be measured using fluorescent labeling and single molecule microscopy or it may be estimated based on previous measurements. We used a factor of 0.45 nm/base pair to calculate L as reported by Robertson *et al*.[42] The diffusion coefficient may then be calculated using $D \cong 2.5L^{-0.588}$, where the length is given in μm.[42]

The radius of gyration is then estimated using the Stokes-Einstein relation,

$$D = k_{\mathrm{B}}T/6\pi\eta R_{\mathrm{h}},$$

where k_{B} is the Boltzmann constant, T is the temperature in Kelvin, η is the dynamic viscosity of the solvent and R_{h} is the hydrodynamic radius. Substitution of the ratio of $\frac{R_{\mathrm{G}}}{R_{\mathrm{H}}} = 8/3\pi^{\frac{1}{2}}$ from the Zimm model[25,42] gives,

$$D = 4k_{\mathrm{B}}T/9\pi^{1.5}\eta R_{\mathrm{G}}.$$

From the calculation of the radius of gyration, the value of C^* as a mass concentration can be predicted using,

$$C^* \cong 3M/4\pi N_{\mathrm{A}}R_{\mathrm{G}}^3,$$

where M is the molecular weight (an average of 660 g/mol per base pair) and N_{A} is Avogadro's number.[45] C^* has been calculated for the DNA constructs and is given in Table 2. C^* represents the transition from the dilute phase to the semi-dilute phase where the molecules begin to interact. Therefore, the concentration of DNA in the experiments to determine the behavior of polymers in the dilute phase must not exceed C^*.

In the initial PCR scale up, without a thorough yield optimization, the DNA concentrations measured were in the range of 0.25–0.45 mg/mL. Using the average molecular weight of a single base of 330 g/mol, the typical concentrations of DNA for LD experiments of 100–200 μM correspond to 0.033–0.066 mg/mL. Therefore, the yield of DNA is suitable for the production of samples for LD, since the DNA can be diluted into the chosen solvent. The

concentration range used for LD is also lower than the smallest value of C^*, for the largest DNA construct of 6 kbp, at 0.210 mg/mL. The concentrations used for LD measurement in the DNA region of the spectrum can always be maintained as lower than this value. Therefore, the typical linear dichroism experimental setup is suitable for the study of polymer rheology in the dilute range.

Table 2. Calculated polymer contour length (L), diffusion constant (D), radius of gyration (R_G) and C^* using $\eta = 1.2$ mPas for DNA of given size.

Size (bp)	L (μm)	D ($\mu m^2 s^{-1}$)	R_G (μm)	C^* (mg/mL)
500	0.225	6.010	0.045	1.40
1000	0.45	3.998	0.068	0.825
2000	0.9	2.660	0.102	0.486
3000	1.35	2.096	0.130	0.357
4000	1.8	1.769	0.154	0.286
5000	2.25	1.552	0.176	0.241
6000	2.7	1.394	0.196	0.210

CONCLUSION

In this paper we describe a method which allows greater control of the sequence length and the base composition of DNA molecules than those previously used in the production of DNA for polymer rheology studies. We have produced a series of molecular lengths with identical GC content to allow the direct comparison of sizes in temperature-controlled linear dichroism and light scattering experiments to follow. The protocol provides an adequate yield to measure the behavior of polymers in the dilute regime and at the crossover into the semi-dilute regime at C^*.

The protocol may be extended to produce larger DNA molecules until the insert size becomes the limiting factor for cloning the product into the plasmid

vector. At this point, alternative vectors that can accommodate larger inserts could be tested including a fosmid vector or the bacterial artificial chromosome.[44] Alternatively, it may also be possible to produce larger constructs from the original shorter series by long multiple fusion PCR.[46] Restriction endonuclease-free systems[47,48] such as In-Fusion® HD[49] from Clontech or Cold fusion from BioCat may also be investigated, as well as homologous recombination based methods such as Gateway® and Red/ET cloning.[50] These were not necessary for our goals so were not attempted.

AUTHOR INFORMATION

Corresponding Author

* Email: a.rodger@warwick.ac.uk

Funding Sources

The authors declare no competing financial interest.

ACKNOWLEDGMENT

The financial support of this work through an EPSRC grant (EP/F500378/1) (CEB) through the MOAC Doctoral Training Centre is gratefully acknowledged.

REFERENCES

(1) Schena, M.; Shalon, D.; Davis, R.; Brown, P. *Science* **1995**, *270* (5325), 467–470.

(2) Pillai, S.; Dasgupta, P.; Chellappan, S. P. *Methods Mol. Biol.* **2009**, *523*, 323–339.

(3) Pillai, S.; Chellappan, S. *Methods Mol. Biol.* **2009**, *523*, 341–366.

(4) Hellman, L. M.; Fried, M. G. *Nat. Protoc.* **2007**, *2* (8), 1849–1861.

(5) Jutras, B. L.; Verma, A.; Stevenson, B. *Curr. Protoc. Microbiol.* **2012**, *24*, 1F1.1–1F1.16.

(6) Marrington, R.; Dafforn, T. R.; Halsall, D. J.; Rodger, A. *Biophys. J.* **2004**, *87* (3), 2002–2012.

(7) Rodger, A. *Methods Mol. Biol.* **2010**, *613*, 37–54.

(8) Sunthar, P. In *Rheology of Complex Fluids*; 2010; pp 171–191.

(9) Laib, S.; Robertson, R. M.; Smith, D. E. *Macromolecules* **2006**, *39* (12), 4115–4119.

(10) Rickgauer, J.; Smith, D. In *Soft matter characterisation*; 2008; pp 1139–1186.

(11) Ravi Prakash, J. *Korea Aust. Rheol. J.* **2009**, *21* (4), 245–268.

(12) Babcock, H.; Smith, D.; Hur, J.; Shaqfeh, E.; Chu, S. *Phys. Rev. Lett.* **2000**, *85* (9), 2018–2021.

(13) Juarez, G.; Arratia, P. E. *Soft Matter* **2011**, *7* (19), 9444.

(14) Hu, X.; Boukany, P.; Hemminger, O.; Lee, L. *Macromol. Mater. Eng.* **2011**, *296* (3-4), 308–320.

(15) Pipe, C. J.; McKinley, G. H. *Mech. Res. Commun.* **2009**, *36*, 110–120.

(16) Tegenfeldt, J. O.; Prinz, C.; Cao, H.; Huang, R. L.; Austin, R. H.; Chou, S. Y.; Cox, E. C.; Sturm, J. C. *Anal. Bioanal. Chem.* **2004**, *378* (7), 1678–1692.

(17) Chan, T. F.; Ha, C.; Phong, A.; Cai, D.; Wan, E.; Leung, L.; Kwok, P. Y.; Xiao, M. *Nucleic Acids Res.* **2006**, *34* (17), e113.

(18) Perkins, T. T.; Smith, D. E.; Larson, R. G.; Chu, S. *Science* **1995**, *268* (5207), 83–87.

(19) Meiners, J. C.; Quake, S. R. *Phys. Rev. Lett.* **2000**, *84* (21), 5014–5017.

(20) Smith, D. E.; Perkins, T. T.; Chu, S. *Macromolecules* **1996**, *29* (4), 1372–1373.

(21) Graessley, W. W. *Polymer (Guildf).* **1980**, *21*, 258–262.

(22) McKee, M. G.; Wilkes, G. L.; Colby, R. H.; Long, T. E. *Macromolecules* **2004**, *37* (5), 1760–1767.

(23) Imae, T. *Colloid Polym. Sci.* **1989**, *267*, 707–713.

(24) Perkins, T. T.; Smith, D. E.; Chu, S. *Science* **1994**, *264* (5160), 819–822.

(25) Smith, D. E.; Perkins, T. T.; Chu, S. *Phys. Rev. Lett.* **1995**, *75* (22), 4146–4149.

(26) Gupta, P.; Elkins, C.; Long, T. E.; Wilkes, G. L. *Polymer (Guildf).* **2005**, *46* (13), 4799–4810.

(27) Rodger, A.; Marrington, R.; Geeves, M. A.; Hicks, M.; de Alwis, L.; Halsall, D. J.; Dafforn, T. R. *Phys. Chem. Chem. Phys.* **2006**, *8*, 3161–3171.

(28) Nordén, B.; Rodger, A.; Dafforn, T. R. In *Linear Dichroism and circular dichroism*; 2010; pp 9–12.

(29) Marrington, R.; Dafforn, T. R.; Halsall, D. J.; MacDonald, J. I.; Hicks, M.; Rodger, A. *Analyst* **2005**, *130* (12), 1608–1616.

(30) Houssier, C.; Hardy, B.; Fredericq, E. *Biopolymers* **1974**, *13* (6), 1141–1160.

(31) Kubista, M.; Akerman, B.; Nordén, B. *Biochemistry* **1987**, *26* (14), 4545–4553.

(32) Moon, J.; Kim, S.; Sehlstedt, U.; Rodger, A.; Nordén, B. *Biopolymers* **1996**, *38* (5), 593–606.

(33) Ismail, M. A.; Sanders, K. J.; Fennell, G. C.; Latham, H. C.; Wormell, P.; Rodger, A. *Biopolymers* **1998**, *46* (3), 127–143.

(34) Coggan, D.; Haworth, I.; Bates, P.; Robinson, A.; Rodger, A. *Inorg. Chem.* **1999**, *38* (20), 4486–4497.

(35) Rodger, A.; Parkinson, A.; Best, S. *Eur. J. Inorg. Chem.* **2001**, *2001* (9), 2311–2316.

(36) Patel, K. K.; Plummer, E. A.; Darwish, M.; Rodger, A.; Hannon, M. J. *J. Inorg. Biochem.* **2002**, *91* (1), 220–229.

(37) Rittman, M.; Hoffmann, S. V; Gilroy, E.; Hicks, M. R.; Finkenstadt, B.; Rodger, A. *Phys. Chem. Chem. Phys.* **2012**, *14* (1), 353–366.

(38) Smith, D. E.; Babcock, H. P.; Chu, S. *Science* **1999**, *283* (5408), 1724–1727.

(39) Teixeira, R. E.; Babcock, H. P.; Shaqfeh, E. S. G.; Chu, S. *Macromolecules* **2005**, *38* (2), 581–592.

(40) LeDuc, P.; Haber, C.; Bao, G.; Wirtz, D. *Nature* **1999**, *399* (6736), 564–566.

(41) Pan, S.; Ahirwal, D.; Nguyen, D.; Sridhar, T.; Sunthar, P.; Ravi Prakash, J. *Macromolecules* **2014**, *47* (21), 7548–7560.

(42) Robertson, R. M.; Laib, S.; Smith, D. E. *Proc. Natl. Acad. Sci. U. S. A.* **2006**, *103* (19), 7310–7314.

(43) Nordén, B.; Rodger, A.; Dafforn, T. R. In *Linear Dichroism and circular dichroism*; 2010; pp 60–62.

(44) Brown, T. In *Gene cloning and DNA analysis*; 2010; pp 102–104.

(45) Ying, Q.; Chu, B. *Macromolecules* **1987**, *20* (2), 362–366.

(46) Shevchuk, N. A.; Bryksin, A. V; Nusinovich, Y. A.; Cabello, F. C.; Sutherland, M.; Ladisch, S. *Nucleic Acids Res.* **2004**, *32* (2), e19.

(47) Zuo, P.; Rabie, B. M. *Curr. Issues Mol. Biol.* **2010**, *12* (1one-step), 11–16.

(48) You, C.; Zhang, X. Z.; Zhang, Y. H. P. *Appl. Environ. Microbiol.* **2012**, *78* (5), 1593–1595.

(49) Raman, M.; Martin, K. *Nat. Methods* **2014**, *11* (9), 2014.

(50) Zhang, Y.; Muyrers, J. P.; Testa, G.; Stewart, A. F. *Nat. Biotechnol.* **2000**, *18* (12), 1314–1317.

Appendix A Cloning, overexpression and purification of *E. coli* ZapA

1 Introduction

Z-ring associated protein A or ZapA was initially discovered in *B. subtilis* by Gueiros-Filho and Losick in 2002 (1) in an overexpression screen for proteins that compensate the effects of excess MinD. Overexpression of MinD blocks FtsZ polymerisation throughout the cell and therefore inhibits cell division (1). The initial study of ZapA was extensive. Loss of the *zapA* gene was shown to be non-lethal and cell division was not inhibited. However, in combination with deletion of *ezrA* or *DivIVA* or in cells with reduced expression of FtsZ, division became severely inhibited. The ZapA protein was shown to localise to the midcell in the presence of FtsZ, with no dependence on later-acting proteins. A direct interaction of ZapA with FtsZ was also confirmed using affinity chromatography. ZapA promotes the polymerisation of GDP-bound FtsZ and increases the light scattered by polymers of GTP-bound FtsZ. Electron micrographs also showed branched networks of FtsZ in the presence of ZapA and GTP. A 20–30% reduction in the GTPase activity was also observed. Finally the authors identified the *Escherichia coli* ortholog YfgE, now referred to as *E. coli* ZapA (1).

In contrast to the lack of phenotype on the loss of ZapA in *B. subtilis*, deletion of the *zapA* gene in *Escherichia coli* has been shown to affect cell growth. Mohammadi *et al*. found that 11% of cells were filamentous on deletion of *zapA* (2). In addition, Galli and Gerdes found a 40% increase in cell length, and in 25% of the cells, the Z-ring was mislocalised on deletion of *zapA* (3). The interaction of *E. coli* ZapA with FtsZ to promote polymer bundling, and an associated loss of GTPase activity of 20–24% have also been demonstrated (2, 4).

The three-dimensional structure of the ZapA protein from *P. aeruginosa* was solved in 2004 using X-ray crystallography (5). Each monomer is relatively small containing only 104 amino acids. An N-terminal 2-stranded antiparallel β-sheet is followed by a short N-terminal α-helix. The long C-terminal α-helix then

protrudes away from the globular N-terminal domain. Monomers of ZapA interact via both the N-terminal domains and the C-terminal helices in parallel to form a dimer. Dimers further interact via the C-terminal helices to form antiparallel tetramers. The structure of the *P. aeruginosa* tetramer is given in Figure A1E. Both the *P. aeruginosa* and the *E. coli* ZapA proteins have been shown to exist in a dimer/tetramer equilibrium *in vitro* (4–6).

The conserved N-terminal domain of ZapA interacts with FtsZ (3, 5). According to the *P. aeruginosa* dimer crystal structure, two FtsZ polymers would be expected to run antiparallel as a double filament at each end of the tetramer structure. In support of this hypothesis, electron micrographs indicated that FtsZ double filaments were ordered by the addition of *E. coli* ZapA (2).

The current model includes ZapA tetramers that crosslink double FtsZ filaments in a "rungs of a ladder" structure. Since the concentration required for the tetramerisation of the *P. aeruginosa* protein was relatively high, it is suggested that ZapA binds to FtsZ as a dimer. Then, the increased concentration of ZapA within the Z-ring leads to tetramerisation and crosslinking of FtsZ fibres (5). In further support of the ladder model, Pacheco-Gomez *et al*. showed that a ZapA mutant that is unable to tetramerise but remains dimeric (ZapA I83E) is able to interact with FtsZ. However, the FtsZ bundling activity is lost and the reduction of the FtsZ GTPase is also not observed as for wild-type ZapA (6).

Although the *E. coli* ZapA protein was crystallised only a year following the publication of the *P. aeruginosa* structure (7), it was not until 2014 that the atomic resolution three-dimensional structure of the *E. coli* ZapA protein was published (8). Despite only 25% sequence identity to the *P. aeruginosa* protein, the overall structures are very similar. The ZapA crystal structures for *E. coli* are shown in Figure A1A–C. There were some key differences between the structures such as a more extensive stabilising interaction for the *E. coli* tetramer compared to the *P. aeruginosa* tetramer. This can be seen in Figure A1D–E. This may push the equilibrium in favour of the tetramer as the predominant species *in vivo* for *E. coli*. Six key residues of the ZapA:FtsZ interaction were identified in the N-terminal domain α-helix: Aspartate 22, arginine 24, asparagine 28, aspartate 32, aspartate 33 and aspartate 46 (8). The positions of the residues are shown in Figure A1C.

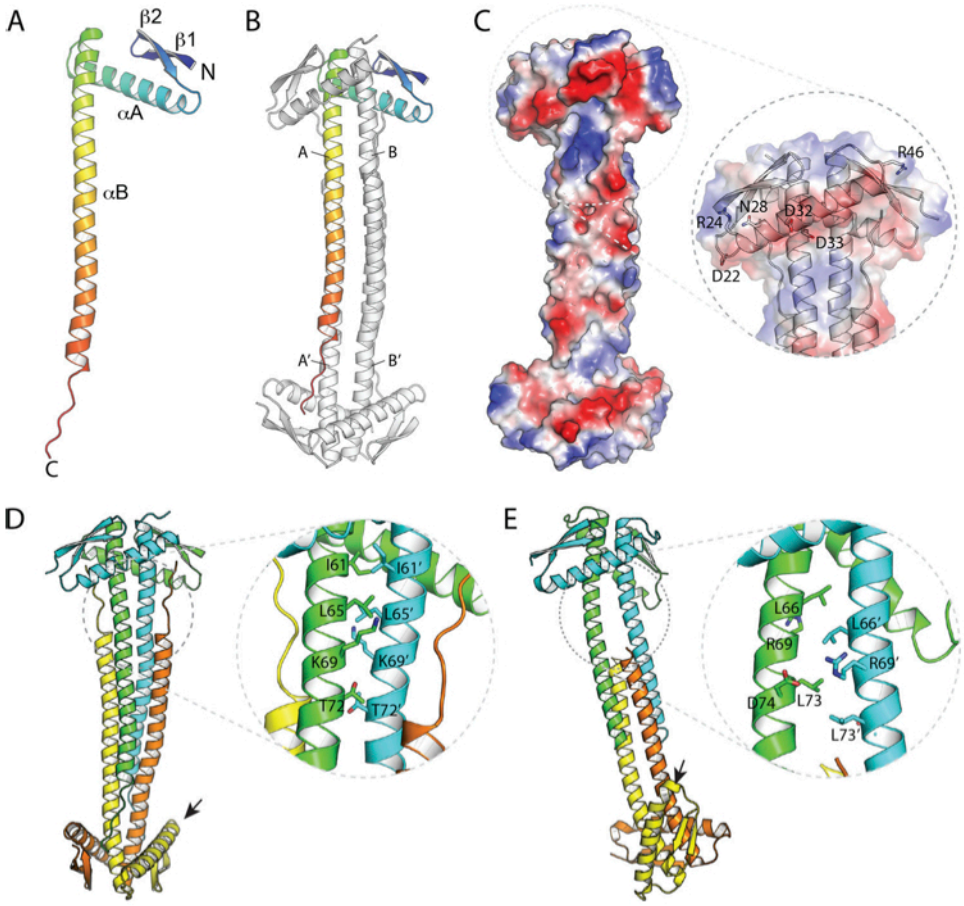

Figure A1: ZapA three-dimensional structures from X-ray crystallography. (A) *E. coli* monomer by secondary structure. (B) *E. coli* tetramer by secondary structure. (C) *E. coli* tetramer space-filled model with surface electrostatic charge. Blue indicates positive charge, red indicates negative charge. (D) *E. coli* tetramer by secondary structure with detail of the key dimerisation residues. (E) *P. aeruginosa* tetramer by secondary structure with detail of the key dimerisation residues for comparison (8).

The aim of this work was to produce a highly purified ZapA protein by immobilised metal affinity chromatography (IMAC) with subsequent removal of the polyhistidine tag. Mohammadi *et al*. reported that their his-tagged *E. coli* ZapA protein was inactive *in vivo* and that the polyhistidine tag affected the function of the protein *in vitro*. For example, native ZapA was shown to bundle FtsZ double filaments, whereas polyhistidine-tagged ZapA bundled single FtsZ filaments (2). Although Roach *et al.* reported that their polyhistidine-tagged ZapA was active (8), a construct of ZapA was chosen for this work that allows removal of the additional N-terminal residues. This will ensure that any measured effects can be attributed to the native protein. The ZapA protein

produced will be used for further crystallisation and co-crystallisation studies and for the reconstitution of the *E. coli* divisome in lipid vesicles.

2 *zapA* cloning

The *zapA* gene (locus b2910) was amplified from the *E. coli* K12 W3110 genome using ZapA_forward (5' TTT CGC GGT CTC CCA TGC ATC ACC ATC ACC ATC ACG AAA ACC TGT ATT TTC AGG GCA TGA TCA AGG CGA CGG ACA G 3') and ZapA_reverse (5' TTT CGC GGA TCC TTA AAA CTC TTT TCG CAG CC 3') primers and the Phusion® High-Fidelity DNA Polymerase enzyme (NEB). Briefly, the PCR reaction contained 1× Phusion® High-Fidelity DNA Polymerase GC buffer, 500 nM each primer, 200 μM each dNTP, 2 ng/μL genomic DNA template, 3% (v/v) DMSO and 1 unit Phusion® High-Fidelity DNA Polymerase enzyme in a final volume of 50 μL. The PCR mix was incubated at 98 °C for 30 seconds, followed by 30 cycles of: 10 seconds DNA denaturation at 98 °C, 30 seconds primer annealing at 61 °C, and 1 minute primer extension at 72 °C. After cycling, a final 10-minute extension at 72 °C was used. The PCR product was digested with restriction endonucleases BsaI and BamHI (NEB) and cloned into the vector pET28b (Novagen) that had been digested with NcoI and BamHI.

The additional sequence at the 5' end of the forward primer encodes six adjacent histidine residues and the tobacco etch virus (TEV) protease recognition site (ENLYFQG). The primers were designed such that following expression and purification of the protein using IMAC, the poly-histidine tag may be removed using TEV protease. This leaves a single additional glycine residue at the N-terminus of the ZapA protein. Success of the cloning was confirmed using separate DNA sequencing reactions (GATC Biotech) from both the T7 promoter (sequencing primer: 5' TAA TAC GAC TCA CTA TAG GGG 3') and the T7 terminator regions of the plasmid (sequencing primer: 5' GCT AGT TAT TGC TCA GCG G 3').

3 ZapA expression and purification

10 mL LB containing 25 μg/mL kanamycin was inoculated with a fresh colony of transformed *E. coli* BL21(DE3) cells and grown overnight at 37 °C with shaking at 180 rpm. The overnight culture was used to inoculate 1 L LB (also containing kanamycin at 25 μg/mL) supplemented with 0.2% (w/v) glucose and the culture was incubated at 37 °C with shaking at 180 rpm until the optical density at 600 nm (1 cm pathlength) reached 0.6, compared to an LB blank. Protein expression was induced with the addition of 1 M isopropyl-β-D-1-thiogalactopyranoside (IPTG) to a final concentration of 0.5 mM. The culture was then further incubated for 4 hours at 37 °C with shaking at 180 rpm. The cells were harvested by centrifugation at 12,000×g for 15 minutes at 4 °C. The cell pellet was stored at –20 °C.

The cell pellet was thawed, resuspended in 20 mL ZapA Buffer A (25 mM HEPES, 0.1 M NaCl, 10 mM imidazole, pH 8) and held on ice. Cells were lysed by sonication. The lysed cells were then centrifuged at 50,000×g for 45 minutes at 4 °C and the supernatant was collected. A 5 mL HisTrap column (GE Healthcare) was used for IMAC. The column was washed with 50 mL deionised water (dH_2O), followed by 20 mL 50 mM EDTA. The EDTA was cleared with a further wash using 50 mL dH_2O. The resin was re-charged with 10 mg/mL $NiCl_2$ solution and washed with 50 mL dH_2O. Finally, the primed column was equilibrated with 50 mL ZapA Buffer A and the protein was loaded. The column was washed with 40 mL ZapA Buffer A then the protein was eluted over a gradient of increasing imidazole concentration from 100% ZapA Buffer A to 100% ZapA Buffer B (25 mM HEPES, 0.5 M NaCl, 500 mM imidazole, pH 8) over 50 mL with a flow rate of 2 mL/min. 1.5 mL fractions were collected. Fractions containing ZapA were pooled. The protein concentration was determined using the Bradford protein assay (BioRad) and a bovine serum albumin standard curve, and 1 mg TEV protease was added per 200 mg ZapA. The solution was dialysed against 3 × 1 L ZapA buffer A then incubated at 4 °C overnight to allow removal of the poly-histidine tag.

The IMAC procedure was repeated for the cleaved protein but the flow through was collected as this contains the cleaved ZapA protein. The cleaved tag and the TEV protease are retained on the column. The TEV-cleaved protein was

dialysed against 3 × 1 L storage buffer (50 mM Tris-HCl, 50 mM KCl, 1 mM EDTA, 10% (v/v) glycerol, pH 7.9). The protein was concentrated to ~ 8 mg/mL using a VivaSpin 20 10,000 MWCO PES membrane sample concentrator with centrifugation at 3200×g at 4 °C. Samples were aliquoted and stored at –80 °C. Protein purity was assessed by sodium dodecyl sulphate polyacrylamide gel electrophoresis (SDS-PAGE), using 12% acrylamide resolving gels. As shown in Figure A2, the procedure outlined yields highly pure ZapA protein. The yield of purified ZapA protein from the method described here is 60–80 mg/L culture.

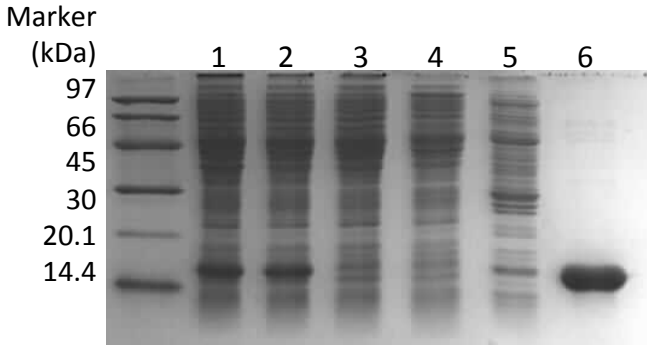

Figure A2: ZapA purification. The protocol outlined yields highly purified ZapA protein. Lane 1: whole cells, lane 2: soluble proteins, lane 3: cell membranes, lane 4: IMAC column flow through, lane 5: IMAC column wash, lane 6: eluted ZapA protein.

4 References

1. Gueiros-Filho FJ, Losick R (2002) A widely conserved bacterial cell division protein that promotes assembly of the tubulin-like protein FtsZ. *Genes Dev* 16(19):2544–2556.

2. Mohammadi T, et al. (2009) The GTPase activity of *Escherichia coli* FtsZ determines the magnitude of the FtsZ polymer bundling by ZapA *in vitro*. *Biochemistry* 48(46):11056–11066.

3. Galli E, Gerdes K (2012) FtsZ-ZapA-ZapB interactome of *Escherichia coli*. *J Bacteriol* 194(2):292–302.

4. Small E, et al. (2007) FtsZ Polymer-bundling by the *Escherichia coli* ZapA orthologue, YgfE, involves a conformational change in bound GTP. *J Mol Biol* 369(1):210–221.

5. Low HH, Moncrieffe MC, Löwe J (2004) The crystal structure of ZapA and its modulation of FtsZ polymerisation. *J Mol Biol* 341(3):839–852.

6. Pacheco-Gómez R, et al. (2013) Tetramerisation of ZapA is required for FtsZ bundling. *Biochem J* 449(3):795–802.

7. Addinall SG, et al. (2005) Expression, purification and crystallization of the cell-division protein YgfE from *Escherichia coli*. *Acta Crystallogr Sect F Struct Biol Cryst Commun* 61(3):305–307.

8. Roach EJ, Kimber MS, Khursigara CM (2014) Crystal structure and site-directed mutational analysis reveals key residues involved in *Escherichia coli* ZapA function. *J Biol Chem* 289(34):23276–23286.

Appendix B Cloning, overexpression and purification of *E. coli* ZipA

1 Introduction

FtsZ-interacting protein A or ZipA was originally identified in a screen for *E. coli* proteins that interact with FtsZ (1). In the Gammaproteobacteria, ZipA is an essential inner membrane protein that localises to the Z-ring simultaneously to FtsZ and remains at the midcell throughout cell constriction. ZipA acts as a Z-ring membrane anchoring protein (1, 2). On depletion of ZipA, cell division is inhibited and although a Z-ring is formed, its constriction is not initiated (3). The purified C-terminal domain of ZipA was shown to induce bundling of FtsZ polymers *in vitro* (4), without affecting the GTPase activity of FtsZ (5). In addition to its role as an FtsZ-anchor protein, *in vivo* ZipA is required for the midcell localisation of the late division proteins (6).

ZipA is a bitopic inner membrane protein with a short N-terminal periplasmic domain that contains residues 1–6 only. Residues 7 to 28 form the single transmembrane domain, which is followed by a highly charged region from residue 29 to residue 85. The region from residue 86 to residue 188 is referred to as the P/Q domain as it contains 31% proline and 23% glutamine and this domain is thought to form an extended, flexible linker that is perhaps important for controlling the distance from the inner membrane to the Z-ring. Residues 189 to 328 form the globular, cytoplasmic C-terminal domain which interacts with FtsZ (7).

The atomic-resolution structure of the C-terminal domain of *E. coli* ZipA has been solved by both X-ray crystallography and NMR spectroscopy (8, 9). The X-ray crystal structure of ZipA is shown in Figure B1 (9). A 6-stranded antiparallel β-sheet forms a 20-Å cavity in which the C-terminal tail of FtsZ binds. The crystal structure also revealed the key residues of FtsZ that are important in the binding interaction with ZipA. Isoleucine 374, phenylalanine 377 and leucine 378 were shown to be deeply buried in the hydrophobic cavity of ZipA. Aspartate 373 forms a capping hydrogen bond between its side chain and the backbone nitrogen of alanine 376 to stabilise the induced α-helical structure of the FtsZ C-terminal tail (9).

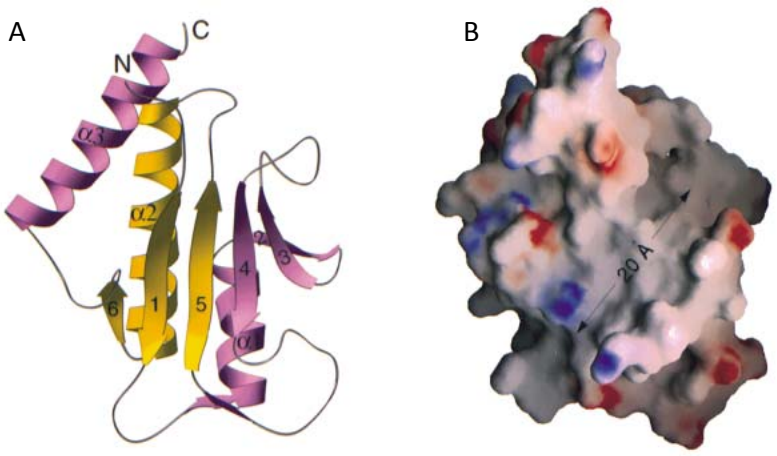

Figure B1: The structure of the C-terminal domain (residues 185–328) of *E. coli* ZipA. (A) ZipA displayed by secondary structure. (B) ZipA space-filling model with surface potential display. Blue indicates regions of negative charge and red indicates regions of positive charge. Arrow indicates the position of the FtsZ C-terminal tail binding cleft (9).

The essential role of ZipA became unclear when a single point mutation in *ftsA* (FtsA R286W) was shown to bypass the requirement for ZipA in *E. coli* (10). Overexpression of the late division protein FtsN, thought to be the key protein in the activation of Z-ring constriction and cell wall remodelling, was also found to bypass the requirement for ZipA (11). Although ZipA is required for the recruitment of the downstream cell division proteins, it was shown that only FtsA interacts with them directly (12).

A self-interaction of FtsA was revealed when its C-terminal membrane targeting sequence was removed and the protein formed rods in the cytoplasm (12). Interestingly, this self-interaction was found to occlude the 1C domain of FtsA, that directly interacts with FtsN (12). In a screen for mutations of *ftsA* that block the formation of cytoplasmic FtsA rods, several were found (including the *ftsA** mutation R286W) that complemented the deletion of the *ftsA* gene and bypassed the requirement for ZipA (13). The purified mutant FtsA proteins were also shown to have a reduced self-interaction in a bacterial two hybrid assay (11).

Pichoff *et al*. suggest that the essential role of ZipA is to antagonise the self-interaction of FtsA at the divisome, which allows FtsA to interact with FtsN. However, direct evidence for the inhibition of the FtsA self-interaction by ZipA is currently lacking. It should also be noted that in the absence of ZipA, the *ftsA* mutant cells were elongated. This suggests an additional role of ZipA in cell

division that is not compensated for by the loss of the FtsA self-interaction, such as the organisation or stabilisation of the Z-ring (13).

The aim of this work was to produce a highly purified ZipA protein using a styrene maleic acid (SMA) polymer to solubilise the membrane fraction, rather than a detergent. Encapsulation of the membrane protein into a styrene maleic acid lipid particle (SMALP) should retain the native lipid environment of the protein, and should provide a simple method to reconstitute the protein into a lipid vesicle. The buffer composition can be adjusted to stimulate the release of the SMA polymer from the particle (14, 15). The ZipA protein produced in this work will be used for crystallisation and co-crystallisation studies, for the reconstitution of the *E. coli* divisome in lipid vesicles and to investigate the use of the SMALP purification technique in polarised light spectroscopy of membrane proteins.

2 *zipA* cloning

The *zipA* gene (locus b2412) was amplified from the *E. coli* K12 W3110 genome using ZipA_forward (5' TTT GCG CAT ATG ATG CAG GAT TTG CGT CTG ATA TTA ATC 3') and ZipA_reverse (5' TTT GCG GGA TCC TCA GGC GTT GGC GTC TTT GAC TTC GCG GAT 3') primers and the Phusion® High-Fidelity DNA Polymerase enzyme (NEB). Briefly, the PCR reaction contained 1× Phusion® High-Fidelity DNA Polymerase GC buffer, 500 nM each primer, 200 μM each dNTP, 2 ng/μL genomic DNA template, 3% (v/v) DMSO and 1 unit Phusion® High-Fidelity DNA Polymerase enzyme in a final volume of 50 μL. The PCR mix was incubated at 98 °C for 30 seconds, followed by 30 cycles of: 10 seconds DNA denaturation at 98 °C, 30 seconds primer annealing at 67 °C, and 1 minute primer extension at 72 °C. After cycling, a final 10-minute extension at 72 °C was used. The PCR product was digested with restriction endonucleases NdeI and BamHI (NEB) and cloned into the vector pET15b (Novagen) that had been digested with the same two enzymes. On expression, the ZipA protein contains an additional 20 amino acid residues at the N-terminal (periplasmic) end including a polyhistidine purification tag. Success of the cloning was confirmed using separate DNA sequencing reactions (GATC Biotech) from both the T7 promoter (sequencing primer: 5' TAA TAC GAC

TCA CTA TAG GGG 3') and the T7 terminator regions of the plasmid (sequencing primer: 5' GCT AGT TAT TGC TCA GCG G 3').

3 ZipA expression and purification

10 mL LB containing 100 μg/mL ampicillin was inoculated with a fresh colony of transformed *E. coli* C43(DE3) cells and grown overnight at 37 °C with shaking at 180 rpm. The overnight culture was used to inoculate 1 L LB (also containing ampicillin at 100 μg/mL) supplemented with 0.2% (w/v) glucose and the culture was incubated at 37 °C with shaking at 180 rpm until the optical density at 600 nm (1 cm pathlength) reached 0.6, compared to an LB blank. Protein expression was induced with the addition of 1 M isopropyl-β-D-1-thiogalactopyranoside (IPTG) to a final concentration of 0.5 mM. The culture was then further incubated for 4 hours at 37 °C with shaking at 180 rpm. The cells were harvested by centrifugation at 12,000×g for 15 minutes at 4 °C. The cell pellet was stored at –20 °C.

The cell pellet was thawed, resuspended in 50 mL SMALP resuspension buffer (50 mM Tris, 50 mM NaCl, 2 mM EDTA, 5% (v/v) glycerol, pH 8) and held on ice. Cells were lysed by 4 passages through a chilled cell disruptor (Constant Systems Ltd) with ~30,000 psi pressure. The lysed cells were then centrifuged at 15,000×g for 30 minutes at 4 °C, to clear unbroken cells and cell debris, and the supernatant was collected. Membranes were collected with centrifugation at 125,000×g for 1 hour.

Membranes were resuspended in SMALP solubilisation buffer (50 mM Tris, 500 mM NaCl, 10% (v/v) glycerol, 2.5% (w/v) SMA, pH 8) to a concentration of 40 mg/mL. SMA was kindly provided by T. Dafforn, University of Birmingham. The slurry was stirred overnight at 4 °C. Unsolubilised material was removed by centrifugation at 125,000×g for 1 hour.

2.5 mL Ni Sepharose Fast Flow resin (GE Healthcare) was equilibrated with 10 mL SMALP buffer A (50 mM Tris, 500 mM NaCl, 10% (v/v) glycerol, pH 8) using the Proteus 1-step batch Midi Spin Column (Generon) with centrifugation at 750×g for 2 minutes. The equilibrated resin was mixed with the solubilised membrane solution and gently stirred at 4 °C for 2 hours. The flow

through was cleared from the resin using centrifugation of the column at 750×g for 2 minutes. The resin was washed with 5 × 20 mL SMALP buffer A and the protein was eluted with 2 × 5 mL SMALP buffer B (50 mM Tris, 500 mM NaCl, 10% (v/v) glycerol, 200 mM imidazole, pH 8). The solution was dialysed against 3 × 1 L SMALP buffer A. Protein purity was assessed by sodium dodecyl sulphate polyacrylamide gel electrophoresis (SDS-PAGE), using 12% acrylamide resolving gels. As shown in Figure B2, the procedure outlined yields purified ZipA protein with a concentration of ~2–3mg/mL. The yield of purified ZipA protein from the method described here is 20–30 mg/L culture.

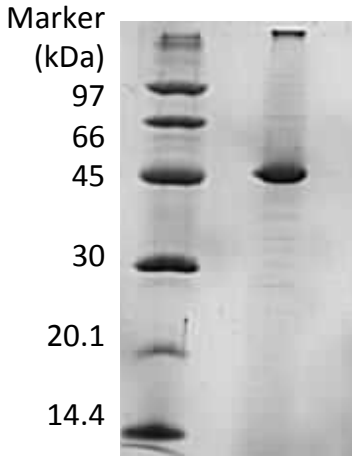

Figure B2: SMALP purification of the *E. coli* membrane protein ZipA. The final ZipA protein preparation purified by immobilised metal affinity chromatography.

4 References

1. Hale CA, de Boer PAJ (1997) Direct binding of FtsZ to ZipA, an essential component of the septal ring structure that mediates cell division in *E. coli*. *Cell* 88(2):175–185.

2. Hale C, Rhee A, de Boer P (2000) ZipA-induced bundling of FtsZ polymers mediated by an interaction between C-terminal domains. *J Bacteriol* 182(18):5153–5166.

3. Hale CA, De Boer PAJ (1999) Recruitment of ZipA to the septal ring of *Escherichia coli* is dependent on FtsZ and independent of FtsA. *J Bacteriol* 181(1):167–176.

4. RayChaudhuri D (1999) ZipA is a MAP-Tau homolog and is essential for structural integrity of the cytokinetic FtsZ ring during bacterial cell division. *EMBO J* 18(9):2372–2383.

5. Liu Z, Mukherjee A, Lutkenhaus J (1999) Recruitment of ZipA to the division site by interaction with FtsZ. *Mol Microbiol* 31(6):1853–1861.

6. Pichoff S, Lutkenhaus J (2002) Unique and overlapping roles for ZipA and FtsA in septal ring assembly in *Escherichia coli*. *EMBO J* 21(4):685–693.

7. Ohashi T, Hale C, de Boer P, Erickson H (2002) Structural evidence that the P/Q domain of ZipA is an unstructured, flexible tether between the membrane and the C-terminal FtsZ-binding domain. *J Bacteriol* 184(15):4313–4315.

8. Moy FJ, Glasfeld E, Mosyak L, Powers R (2000) Solution structure of ZipA, a crucial component of *Escherichia coli* cell division. *Biochemistry* 39(31):9146–9156.

9. Mosyak L, et al. (2000) The bacterial cell-division protein ZipA and its interaction with an FtsZ fragment revealed by X-ray crystallography. *EMBO J* 19(13):3179–3191.

10. Geissler B, Elraheb D, Margolin W (2003) A gain-of-function mutation in *ftsA* bypasses the requirement for the essential cell division gene *zipA* in *Escherichia coli*. *Proc Natl Acad Sci U S A* 100(7):4197–4202.

11. Pichoff S, Du S, Lutkenhaus J (2015) The bypass of ZipA by overexpression of FtsN requires a previously unknown conserved FtsN motif essential for FtsA-FtsN interaction supporting a model in which FtsA monomers recruit late cell division proteins to the Z ring. *Mol Microbiol* 95(6):971–987.

12. Weiss D (2015) Last but not least: new indights into how FtsN triggers constriction during *Escherichia coli* cell division. *Mol Microbiol* 95(6):903–909.

13. Pichoff S, Shen B, Sullivan B, Lutkenhaus J (2012) FtsA mutants impaired for self-interaction bypass ZipA suggesting a model in which FtsA's self-interaction competes with its ability to recruit downstream division proteins. *Mol Microbiol* 83(1):151–167.

14. Knowles TJ, et al. (2009) Membrane proteins solubilized intact in lipid containing nanoparticles bounded by styrene maleic acid copolymer. *J Am Chem Soc* 131(22):7484–7485.

15. Orwick-Rydmark M, et al. (2012) Detergent-free incorporation of a seven-transmembrane receptor protein into nanosized bilayer lipodisq particles for functional and biophysical studies. *Nano Lett* 12(9):4687–4692.

Appendix C Cloning and overexpression of *E. coli* FtsA

1 Introduction

FtsA is a member of a large family of ATPases that includes actin, hsp70 and MreB (1). FtsA is recruited to the midcell simultaneously to FtsZ (2). While the Z-ring still forms in its absence, FtsA is essential for the downstream recruitment of the late division proteins and is therefore essential to cell division. The Z-ring can form in the presence of either ZipA or FtsA but both are essential for downstream functions. In the absence of both ZipA and FtsA, the Z-ring does not form (3). For ZipA depletion, cells appear completely smooth whereas for FtsA depletion some cell constriction is observed (4).

The FtsA C-terminal tail contains a well-conserved amphipathic helix that acts as a membrane targeting sequence to tether FtsZ to the inner membrane. If FtsA lacks this tail, the protein forms rods in the cytoplasm (5). Similar to actin and MreB, FtsA has 4 domains. However, whereas actin and MreB contain domains 1A, 1B, 2A and 2B, in FtsA the 1B domain is missing. FtsA contains an additional domain 1C. The 2B domain is required for the interaction of FtsA with FtsZ (6) and the 1C domain is required for recruitment of the late division proteins (7).

Despite missing the 1B domain that is required for the polymerisation of actin and MreB (8), in crystallography studies using FtsA from *T. maritima*, when co-crystallised with ATP-γ-S, the FtsA crystal contained continuous protofilaments (9, 10). The position of the 1C domain was on the opposite side of the protein compared to the 1B domain of MreB, as shown in Figure C1. The nucleotide binding cleft is formed by the three domains 1A, 2A and 2B and is very similar to those of actin and other members of the family (8, 9).

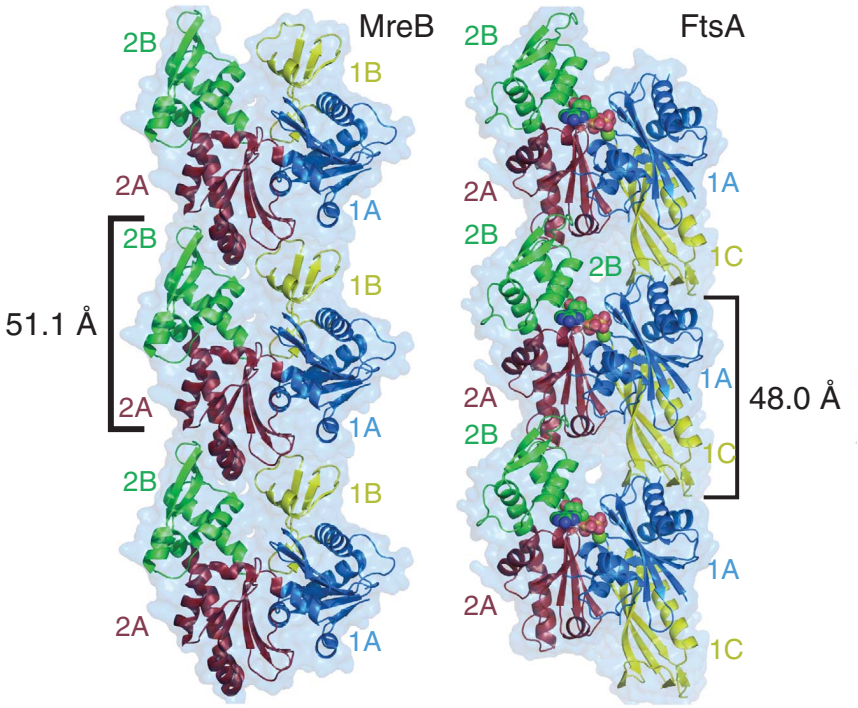

Figure C1: The protofilament structures of MreB and FtsA from *T. maritima*. Despite the difference in domain structure between FtsA and actin-like MreB, the protofilament structures are similar (8, 10).

The final essential cell division protein to localise to the midcell is FtsN and its arrival coincides with the appearance of cell constriction. This suggests that the recruitment of FtsN may act as a signal for the initiation of the constriction process (11, 12). Cytosolic N-terminal residues 4–6 of FtsN interact directly with FtsA, via domain 1C of FtsA, and it is suggested that this interaction forms a feedback mechanism to signal the completion of divisome assembly to FtsZ (13). Once recruited to the midcell by FtsA, the transmembrane domain of FtsN is thought to then mediate the dimerisation or oligomerisation of FtsN causing an initial low-level accumulation of FtsN at the midcell (11, 13). The accumulation of sufficient FtsN for cell division to proceed efficiently then requires the C-terminal, periplasmic domain of FtsN (11, 14) and the presence of the FtsI/FtsW complex at the midcell (11). It is thought that FtsN then mediates the activation of peptidoglycan remodelling and a contraction signal may be transduced to FtsZ via FtsA (11, 15).

The aim of this work was to produce a highly purified FtsA protein using a styrene maleic acid (SMA) polymer to solubilise the membrane fraction, rather

than a detergent. Encapsulation of the membrane protein into a styrene maleic acid lipid particle (SMALP) should retain the native lipid environment of the protein, and should provide a simple method to reconstitute the protein into a lipid vesicle. The buffer composition can be adjusted to stimulate the release of the SMA polymer from the particle (16, 17).

The FtsA protein produced in this work will be used for crystallisation an co-crystallisation studies, for the reconstitution of the *E. coli* divisome in lipid vesicles and to investigate the use of the SMALP purification technique in polarised light spectroscopy of membrane proteins.

2 *ftsA* cloning

The *ftsA* gene (locus b0094) was amplified from the *E. coli* K12 W3110 genome using FtsA_forward (5' TTT CGC GGT CTC CCA TGC ATC ACC ATC ACC ATC ACG AAA ACC TGT ATT TTC AGG GCA TGT CTG CAC AAC CCG TCG A 3') and FtsA_reverse (5' TTT CGC GGA TCC TTA AAA CTC TTT TCG CAG CC 3') primers and the Phusion® High-Fidelity DNA Polymerase enzyme (NEB). Briefly, the PCR reaction contained 1× Phusion® High-Fidelity DNA Polymerase GC buffer, 500 nM each primer, 200 μM each dNTP, 2 ng/μL genomic DNA template, 3% (v/v) DMSO and 1 unit Phusion® High-Fidelity DNA Polymerase enzyme in a final volume of 50 μL. The PCR mix was incubated at 98 °C for 30 seconds, followed by 30 cycles of: 10 seconds DNA denaturation at 98 °C, 30 seconds primer annealing at 62 °C, and 1 minute primer extension at 72 °C. After cycling, a final 10-minute extension at 72 °C was used. The PCR product was digested with restriction endonucleases BsaI and BamHI (NEB) and cloned into the vector pET28b (Novagen) that had been digested with NcoI and BamHI.

The additional sequence at the 5' end of the forward primer encodes six adjacent histidine residues and the tobacco etch virus (TEV) protease recognition site (ENLYFQG). The primers were designed such that following expression and purification of the protein using immobilised metal ion affinity chromatography (IMAC), the poly-histidine tag may be removed using TEV protease. This leaves a single additional glycine residue at the N-terminus of the FtsA protein. Success of the cloning was confirmed using separate DNA sequencing reactions (GATC

Biotech) from both the T7 promoter (sequencing primer: 5' TAA TAC GAC TCA CTA TAG GGG 3') and the T7 terminator regions of the plasmid (sequencing primer: 5' GCT AGT TAT TGC TCA GCG G 3').

3 FtsA expression

10 mL LB containing 25 μg/mL kanamycin was inoculated with a fresh colony of transformed *E. coli* C43(DE3) cells and grown overnight at 37 °C with shaking at 180 rpm. The overnight culture was used to inoculate 1 L LB (also containing kanamycin at 25 μg/mL) supplemented with 0.2% (w/v) glucose and the culture was incubated at 37 °C with shaking at 180 rpm until the optical density at 600 nm (1 cm pathlength) reached 0.6, compared to an LB blank. Protein expression was induced with the addition of 1 M isopropyl-β-D-1-thiogalactopyranoside (IPTG) to a final concentration of 0.5 mM. The culture was then further incubated for 4 hours at 37 °C with shaking at 180 rpm. The cells were harvested by centrifugation at 12,000×g for 15 minutes at 4 °C. The cell pellet was stored at –20 °C.

The cell pellet was thawed, resuspended in 50 mL SMALP resuspension buffer (50 mM Tris, 50 mM NaCl, 2 mM EDTA, 5% (v/v) glycerol, pH 8) and held on ice. Cells were lysed by 4 passages through a chilled cell disruptor (Constant Systems Ltd) with ~30,000 psi pressure. The lysed cells were then centrifuged at 15,000×g for 30 minutes at 4 °C, to clear unbroken cells and cell debris, and the supernatant was collected. Membranes were collected with centrifugation at 125,000×g for 1 hour.

The induction of expression of the FtsA protein was confirmed by sodium dodecyl sulphate polyacrylamide gel electrophoresis (SDS-PAGE), using 12% acrylamide resolving gels. Samples for whole cells, membranes and soluble proteins were analysed for *E. coli* C43(DE3) cells containing the pET28b-*ftsA* construct, compared to cells containing an "empty" pET28b control. As shown in Figure C2, for the *E. coli* C43(DE3)-pET28b-*ftsA* cells, an additional protein band is present in the whole cell and membrane fractions of the appropriate size for the 45 kDa FtsA protein. The next stages of this work are to solubilise the membrane with SMA and to purify the FtsA protein using IMAC.

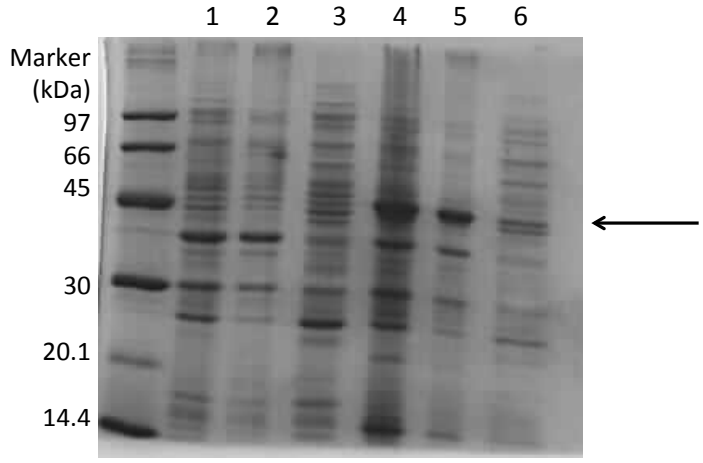

Figure C2: FtsA expression. Induction of protein expression from the pET28b-*ftsA* vector in *E. coli* C43(DE3) cells introduces an additional band of the correct size in the whole cell and cell membrane fractions compared to *E. coli* C43(DE3) containing an empty pET28b vector control. Arrow indicates the position of the additional band. Lanes 1–3 *E. coli* C43(DE3)-pET28b, lane 1: whole cells, lane 2: membranes, lane 3: soluble proteins. Lanes 4–6 *E. coli* C43(DE3)-pET28b-*ftsA*, lane 1: whole cells, lane 2: membranes, lane 3: soluble proteins.

4 References

1. Bork P, Sander C, Valencia A (1992) An ATPase domain common to prokaryotic cell cycle proteins, sugar kinases, actin, and hsp70 heat shock proteins. *Proc Natl Acad Sci U S A* 89(16):7290–7294.

2. Addinall SG, Lutkenhaus J (1996) FtsA is localized to the septum in an FtsZ-dependent manner. *J Bacteriol* 178(24):7167–7172.

3. Pichoff S, Lutkenhaus J (2002) Unique and overlapping roles for ZipA and FtsA in septal ring assembly in *Escherichia coli*. *EMBO J* 21(4):685–693.

4. Hale CA, De Boer PAJ (1999) Recruitment of ZipA to the septal ring of *Escherichia coli* is dependent on FtsZ and independent of FtsA. *J Bacteriol* 181(1):167–176.

5. Pichoff S, Lutkenhaus J (2005) Tethering the Z ring to the membrane through a conserved membrane targeting sequence in FtsA. *Mol Microbiol* 55(6):1722–1734.

6. Pichoff S, Lutkenhaus J (2007) Identification of a region of FtsA required for interaction with FtsZ. *Mol Microbiol* 64(4):1129–1138.

7. Corbin BD, Geissler B, Sadasivam M, Margolin W (2004) Z-ring-independent interaction between a subdomain of FtsA and late septation

proteins as revealed by a polar recruitment assay. *J Bacteriol* 186(22):7736–7744.

8. Van den Ent F, Amos LA, Löwe J (2001) Prokaryotic origin of the actin cytoskeleton. *Nature* 413(6851):39–44.

9. Van den Ent F, Löwe J (2000) Crystal structure of the cell division protein FtsA from *Thermotoga maritima*. *EMBO J* 19(20):5300–5307.

10. Szwedziak P, Wang Q, Freund SM, Löwe J (2012) FtsA forms actin-like protofilaments. *EMBO J* 31(10):2249–2260.

11. Gerding MA, et al. (2009) Self-enhanced accumulation of FtsN at division sites and roles for other proteins with a SPOR domain (DamX, DedD, and RlpA) in *Escherichia coli* cell constriction. *J Bacteriol* 191(24):7383–7401.

12. Weiss D (2015) Last but not least: new indights into how FtsN triggers constriction during *Escherichia coli* cell division. *Mol Microbiol* 95(6):903–909.

13. Busiek KK, Eraso JM, Wang Y, Margolin W (2012) The early divisome protein FtsA interacts directly through its 1c subdomain with the cytoplasmic domain of the late divisome protein FtsN. *J Bacteriol* 194(8):1989–2000.

14. Busiek K, Margolin W (2014) A role for FtsA in SPOR-independent localisation of the essential *Escherichia coli* cell division protein FtsN. *Mol Microbiol* 92(6):1212–1226.

15. Loose M, Mitchison TJ (2014) The bacterial cell division proteins FtsA and FtsZ self-organize into dynamic cytoskeletal patterns. *Nat Cell Biol* 16(1):38–46.

16. Knowles TJ, et al. (2009) Membrane proteins solubilized intact in lipid containing nanoparticles bounded by styrene maleic acid copolymer. *J Am Chem Soc* 131(22):7484–7485.

17. Orwick-Rydmark M, et al. (2012) Detergent-free incorporation of a seven-transmembrane receptor protein into nanosized bilayer lipodisq particles for functional and biophysical studies. *Nano Lett* 12(9):4687–4692.